

Effect of particle morphology on film cracking

Hesham Abdeldaim

Supervisor:

Prof. José M. Asua



Universidad
del País Vasco

Euskal Herriko
Unibertsitatea

2023

Acknowledgements

First, I would like to thank my supervisor Prof. José M. Asua for giving me the opportunity to do this PhD. Thank you for the guidance and support. You have been excellent role model to me. This work could never have been achieved without his support. Working under his supervision was a great opportunity for to grow as a chemist and person.

In addition, I would like to thank all the professors of the group for the discussions, suggestions and help. Specially, I also thank Ines for her kindness, patience and support.

I would like to gratefully thank Dr. Bernd Reck and Dr. Konrad Roschmann who provided me the opportunity to join their team as intern and for their support during these three months in BASF. I would like to thank other members of BASF company specially Dr. Roland Baumstark, Dr. Andreas Daiss, Dr. Hugo Vale and Dr. Svetlana Guriyanova. for their support and help.

Thanks to the Sgiker Services of the Basque Country for the support, Maite, Ana and Loli Martin for the TEM and AFM images, Dr. Amaia Agirre for the DSC, Dr. Daniel E. Martínez-Tong for AFM analysis. Thanks to Prof. Andrey Chuvilin, Dr. Edurne González and Noé González. For ESEM analysis. Thanks to Antje Polenz, Shirin koeber and Anna Nick from BASF for their assistance in the laboratory.

I would like to acknowledge the financial support of Industrial Liaison Program in Polymerization in Dispersed Media.



Thank you to all the members of the polymerization processes group and other groups in POLYMAT. I can tell with all my heart that THE BEST PART WAS KNOWING YOU. I will never forget the moments we shared inside and outside the lab. Remember you have a friend whenever you need. I will always remember your kindness.

Chapter 1. Introduction

Contents

1.1	Polymer coatings	1
1.2	Emulsion polymerization	4
1.3	Film formation of waterborne dispersions.....	14
1.4	Approaches to overcome film formation dilemma.....	22
1.5	Formation of cracks during drying of colloidal dispersions.....	24
1.6.	Thesis objectives	29
1.7.	Outline of the thesis	29
1.8.	References.....	32

Chapter 2. Cracking in films cast from soft core/hard shell waterborne polymer dispersions

Contents

2.1. Abstract.....	53
2.2. Experimental part.....	54
2.3. Results and discussion.....	58
2.4. Conclusions	77
2.5. References	79

Chapter 3. Modelling cracking during film formation of soft core/hard shell latexes

Contents

3.1. Abstract	82
3.2. Model description.....	83
3.3. Model validation.....	92
3.4. Conclusions	105
3.5. References.....	107

Chapter 4. blends of soft core-hard “shell” particles

Contents

4.1.	Abstract.....	109
4.2.	Introduction.....	110
4.3.	Experimental part.....	110
4.4.	Results and discussion.....	112
4.5.	Conclusions	126
4.6.	References	127

**Chapter 5. Internally reinforced soft core-hard shell
waterborne dispersions for high performance solvent-
free coatings**

Contents

5.1. Abstract.....	129
5.2. Introduction.....	130
5.3. Experimental part.....	133
5.4. Results and discussion.....	134
5.5. Conclusions.....	139
5.6. References.....	140

Chapter 6. Coarse graining modelling of the film formation from soft core-hard shell waterborne dispersions

Contents

6.1. Abstract.....	142
6.2. Model description	143
6.3. Model validation	146
6.4. Conclusions	159
6.5. References	160

Chapter 7. Soft core hard “shell” latex for industrial coatings applications

Contents

7.1. Abstract	162
7.2. Experimental part	163
7.3. Results of wood stains	168
7.4. Results of white paints	181
7.5. Conclusions	184
7.6. References.....	185

Chapter 8. Conclusions	187
-------------------------------	------------

Appendix I. Supporting information for Chapter 2	199
---	------------

Appendix II. Supporting information for Chapter 3	218
--	------------

Appendix III. Supporting information for Chapter 4	226
---	------------

Appendix IV. Supporting information for Chapter 5	228
--	------------

Chapter 1. Introduction

1.1 Polymer coatings

Polymer coatings (paints, varnishes, enamels, primers, inks...) are essential goods in modern life, as nearly every surface needs to be coated for decorative purposes or surface protection [1]. Accordingly, the global paints and coatings market size was USD 146.54 Billion (43.40 million tons) in 2018 and it is estimated to keep growing during the next decade to reach USD 236.11 billion by 2026 [2, 3].

From the economic point of view, protective coatings are the most important ones, as they are used to extend the lifetime of products and machinery. Important examples of surfaces that need protective coatings are steel to avoid the formation of rust or wood to protect it from weathering. Decorative coatings, on the other hand, are commonly used to improve the appeal of products to customers. The most relevant group in this category are decorative paints, due to their high production volume. Other important markets are paper coatings and inks, which are extensively used in packaging [1].

The basic formulation of a coating consists of a binder dispersion, fillers, pigments, and additives. The binder is a polymer that forms a matrix that holds the rest of the components of the coating, and it is responsible for the mechanical and barrier properties of the coating. It determines other important features such as the adhesion to the substrate, durability and gloss. A wide variety of polymer resins such as acrylic, epoxy, polyurethane or alkyds are used as binders. The fillers are cheap inorganic particles that are added to improve the mechanical

strength of the film and reduce the cost. The pigments are more expensive components that can be either organic or inorganic particles, responsible for the opacity and colour of the coating. The additives like rheology modifiers or thickeners are components added in small quantities to modify the properties of the coating. For the application as wet coating, all the ingredients are dispersed in a continuous liquid phase, which can be an organic solvent or water [4].

Traditionally coatings have been commercialized as organic solvent solutions [5, 6] but in the last decades, there have been a shift towards waterborne coatings. Generally, the solventborne coatings exhibit superior mechanical and water resistance properties, at the cost of emissions of volatile organic compounds (VOCs). The VOCs are low boiling point compounds such as acetone, ethyl acetate or aliphatic hydrocarbons. They are smelly, toxic and enhance the greenhouse effect that is causing global warming. For this reason, in the past years governmental regulations have become more restrictive towards the emission of VOCs [7, 8]. This has driven the coatings market towards greener alternatives, namely waterborne coatings. In a waterborne coating the continuous phase is water, therefore, they are low VOC or even VOC free, making them safer, cheaper, and easier to handle.

Although they are an environmentally friendly alternative, waterborne coatings have some drawbacks. In waterborne coatings, the polymer is not a water solution, but a colloidal dispersion. To keep the dispersion stability, the presence of surfactants or polymeric stabilizers is necessary, which increases the water sensitivity of the final coatings. Additionally, the film formation process limits the glass transition temperature (and therefore the hardness) of the polymers that can be used. The mechanical properties of waterborne coatings are typically not as good as those of solventborne coatings because of differences in the film formation process, which leads to poor cohesion in films cast from waterborne systems. Thus, solventborne coatings still dominate the

market in applications that require high mechanical strength. In order to complete the replacement from solventborne to waterborne products, the production of high performance waterborne coatings is required [6]. The importance of the film formation process will be discussed in more detail in Section 1.3 of this chapter.

Despite their disadvantages, waterborne coatings have a wide use in many applications, such as decorative and protective paints, paper coatings or inks. The most common polymers for waterborne coatings are fully acrylic copolymers, styrene-butadiene or styrene-acrylic copolymers and vinyl acetate copolymers. About 40% of the total production of emulsion polymers are acrylic (co)polymers. There are a large variety of acrylate and methacrylate monomers, such as methyl methacrylate (MMA), butyl methacrylate (BMA), butyl acrylate (BA), 2-ethylhexyl acrylate (2EHA) and so on. The copolymerization allows great flexibility in both the glass transition temperature and hydrophobicity of the copolymer. A very common formulation for decorative paint applications is a methyl methacrylate/ butyl acrylate copolymer, in a 50-50 weight ratio. Acrylic copolymers have excellent UV and water resistance, making them a good candidate for exterior applications, protective and industrial coatings such as industrial structures, machinery, metal containers, wood furniture, marine coatings or traffic marking coatings. In this introductory chapter, the processes of emulsion polymerization, which is the most relevant technique for the production of aqueous polymer dispersions, is first explained. Then, the film formation process and film cracking of waterborne dispersions are discussed. After that, the main approaches employed for the improvement of mechanical properties of films cast from waterborne dispersions are summarized. Finally, the motivation and outline of the thesis are presented.

1.2 Emulsion polymerization

Emulsion polymerization is the most important industrial procedure to synthesize waterborne polymer dispersions by free radical polymerization. The resulting product is a colloidal dispersion of polymer particles in water with particle sizes ranging between 50 and 1000 nm [9]. Emulsion polymerization is superior to solution polymerization in many aspects. From the environmental point of view, the use of water as dispersion medium is a great improvement compared to solution polymerization where organic solvents are used. Free radical polymerizations are very exothermic reactions, and an efficient heat removal is essential for safety and control of the process. When water is the dispersion medium, it is much easier to control the temperature during the process because of the lower viscosity of a polymer dispersion compared to a polymer solution and the high specific heat capacity of water.

Emulsion polymerization allows one to simultaneously obtain both high molar masses and high polymerization rates, due to its compartmentalized nature [10]. This feature is unique for emulsion polymerization (and related techniques), and it is very interesting from an industrial point of view. The growing radicals confined in different polymer particles are not able to terminate between them and therefore, they can grow for longer times (in the absence of chain transfer reactions, until a second radical enters the polymer particle). Furthermore, the viscosity of the latex does not depend on the molar mass of the polymer. That makes emulsion polymerization an ideal technique to obtain polymers with very high molar masses ($> 10^6$ g/mol).

However, colloidal dispersions are thermodynamically unstable and require surfactants to achieve kinetic stability. Surfactants are amphiphilic molecules that are located at the oil-water interface and prevent the aggregation of the polymer particles by steric or electrostatic repulsions

[11-13]. Electrostatic stabilization can also be achieved by incorporating functional monomers able to generate charges. Examples of these monomers are (meth)acrylic acid and sodium styrene sulfonate [14]. One of the main drawbacks of emulsion polymers is that the surfactants and stabilizing groups remain in the final products increasing the water sensitivity of the coating [15, 16]

The basic formulation for emulsion polymerization includes at least one vinyl monomer, a radical initiator, surfactant, and water. In addition, chain transfer agents (CTA) or crosslinkers can be employed to alter the molecular weight of the polymer. Usually, more than one monomer is copolymerized to achieve a product with the desired properties. The glass transition temperature (T_g) of a copolymer depends on the nature and the relative amount of the monomers in the formulation [17, 18].

For the creation of new (co)polymers by emulsion polymerization, understanding the process is crucial. During the polymerization process, the microstructure of the polymer is formed. This microstructure includes the molar mass and its distribution, the polymer composition and monomer sequence distribution (in the case of copolymers), branching and crosslinking, or gel. In addition, colloidal aspects such as particle morphology, particle size distribution and surface composition are critical. Each of these variables has a significant impact on the final properties of the polymer and, consequently, on the application. The process of emulsion polymerization is briefly explained in the section that follows.

1.2.1 Batch emulsion polymerization process

Although batch emulsion polymerization is rarely used in commercial practice, it is convenient to explain the complex processes that occur in emulsion polymerization because they

appear successively in different stages, typically called intervals [10, 19-22] which are shown in Figure 1.1 Semibatch (semicontinuous) emulsion polymerization where the processes occur simultaneously will be discussed later.

1.2.1.1 System before initiation

The initial charge of the reactor contains water, monomer, and surfactant. The water forms a continuous phase, in which a small amount of monomer is dissolved and the rest accumulates in monomer droplets. The surfactant adsorbs on the monomer droplets and also covers the water/air interface and dissolves in water. If the emulsifier concentration exceeds its saturation level, also known as critical micellar concentration (CMC), it forms aggregates called micelles that will be swollen with monomer. It is important to highlight that the concentration of monomer and surfactant in each phase is often at thermodynamic equilibrium and that the monomer and surfactant molecules will continuously diffuse, during the polymerization, across the different phases to maintain the equilibrium.

1.2.1.2 Interval I

The first interval of the emulsion polymerization (also known as nucleation) starts when the initiator is added to the reactor and radicals are generated. The initiators decompose into radicals when they are heated or undergo redox reactions. Common thermal initiators include persulfates, peroxides, and azo compounds. Typically, in emulsion polymerization, water-soluble initiators are used, thus, generating free radicals in the aqueous phase. These radicals are usually too hydrophilic to enter the micelles, so they react with the monomer in the aqueous phase, forming oligoradicals that became more and more hydrophobic as they grow.

After propagating with some monomer units, the oligoradicals can become surface active and enter the organic phase. The radical can enter into either a monomer droplet or a monomer swollen micelle, but because the total surface area of the micelles is about 3 orders of magnitude larger, the entry into the droplets is negligible. Once a radical enters the micelle, it rapidly propagates with the monomer forming a polymer particle. This mechanism to form new particles is called heterogeneous (or micellar) nucleation and is more likely to happen when the monomer has a low solubility in water, like styrene or butyl acrylate or when high surfactant concentrations are used [19, 20].

If the monomer has a relatively high water solubility (such as methyl methacrylate or vinyl acetate), the monomer concentration in the aqueous phase will be higher. Consequently, the polymerization rate in water will be faster, and the oligoradicals can grow long enough so that they become insoluble in water before entering in a micelle [23, 24]. When this happens, the growing chain precipitates and the emulsifier adsorbs on the precipitate stabilizing the new surface and creating a particle [25, 26]. This nucleation mechanism is called homogeneous nucleation. When the surfactant concentration is below the critical micellar concentration (CMC), homogenous nucleation is the only particle nucleation mechanism. In the presence of micelles, heterogeneous and homogenous mechanisms may coexist.

The particles that are formed through homogeneous or heterogeneous nucleation are very small and may be unstable, because the growth rate of their surface area might be higher than the adsorption rate of the surfactant molecules [27, 28]. These small particles called precursors can coagulate to form larger "mature" particles that are stable and will become the main locus of the polymerization [29]. The process in which stable polymer particles are generated from particle precursors is called coagulative nucleation [30]. During Interval I,

micelles disappear because they become polymer particles when a radical enters or are destroyed to provide emulsifier to the growing particles. Interval I finishes when all the micelles disappear. From this point, unless coagulation occurs, the number of particles in the system remains constant.

1.2.1.3 Interval II

During Interval II the system contains monomer droplets and polymer particles. In this interval, the monomer is being consumed in the polymer particles, and the diffusion from the monomer droplets (through the aqueous phase) keeps constant the monomer concentration in the polymer particles. For this reason, the polymerization rate (R_p , as defined in equation 1.1) is roughly constant during this interval [20, 22, 31]

$$R_p = k_p [M]_p \bar{n} \frac{N_p}{N_A \cdot V} \quad (\text{mol} \cdot \text{l}^{-1} \cdot \text{s}^{-1}) \quad (1.1)$$

where k_p is the propagation rate coefficient, $[M]_p$ is the monomer concentration in the polymer particles, \bar{n} is the average number of radicals per particle, N_p is the number of particles, N_A is Avogadro's number and V is the volume.

The average number of radicals per particle is the product of the radical entry, radical desorption, and bimolecular termination in the polymer particle. \bar{n} equals 0.5 in the Smith-Ewart limiting Case 2. For hydrophilic monomers with a high chain transfer to monomer rate such as vinyl acetate, the average number of radicals per particle is often lower than 0.5. Large particles and high radical generation rate often lead to $\bar{n} > 0.5$.

Similarly to the nucleation process, the radicals formed from the initiator are too hydrophilic to directly enter in the organic phase. Instead, they need to react with a certain amount of monomer units in the aqueous phase to reach a critical length where the growing oligomer is surface active and can enter into the polymer particle in an irreversible way [32]. The critical length is different according to the hydrophobicity of the initiator moiety and the monomer. In the case of copolymers (especially when water-soluble monomers such as acrylic or methacrylic acid are used), instead of a critical length a solubility parameter can be considered, which will depend on the copolymer composition and molar mass of the oligoradicals (controlled by the monomer concentrations in the aqueous phase and the reactivity ratios) [33].

The polymer particles grow in size while the number and the size of monomer droplets decrease until they disappear. The end of interval II comes when there is no any monomer droplet left. The length of this interval (in terms of monomer conversion) is dependent of the swelling capacity of the monomer by the polymer. Generally, the more water-soluble the monomer is, the higher is the swelling capacity [34].

1.2.1.4 Interval III

In Interval III, the system only contains polymer particles swollen with monomer. The monomer concentration in the particles decreases until polymerization is over. The polymerization rate can either decrease or increase. It can decrease because the monomer concentration in the particles decreases (see Equation 1.1), but on the other hand, the increase of the polymer concentration in the particles increases the viscosity inside of the particles, lowering the effective termination rate and increasing the radical concentration which accelerates the polymerization rate (gel effect).

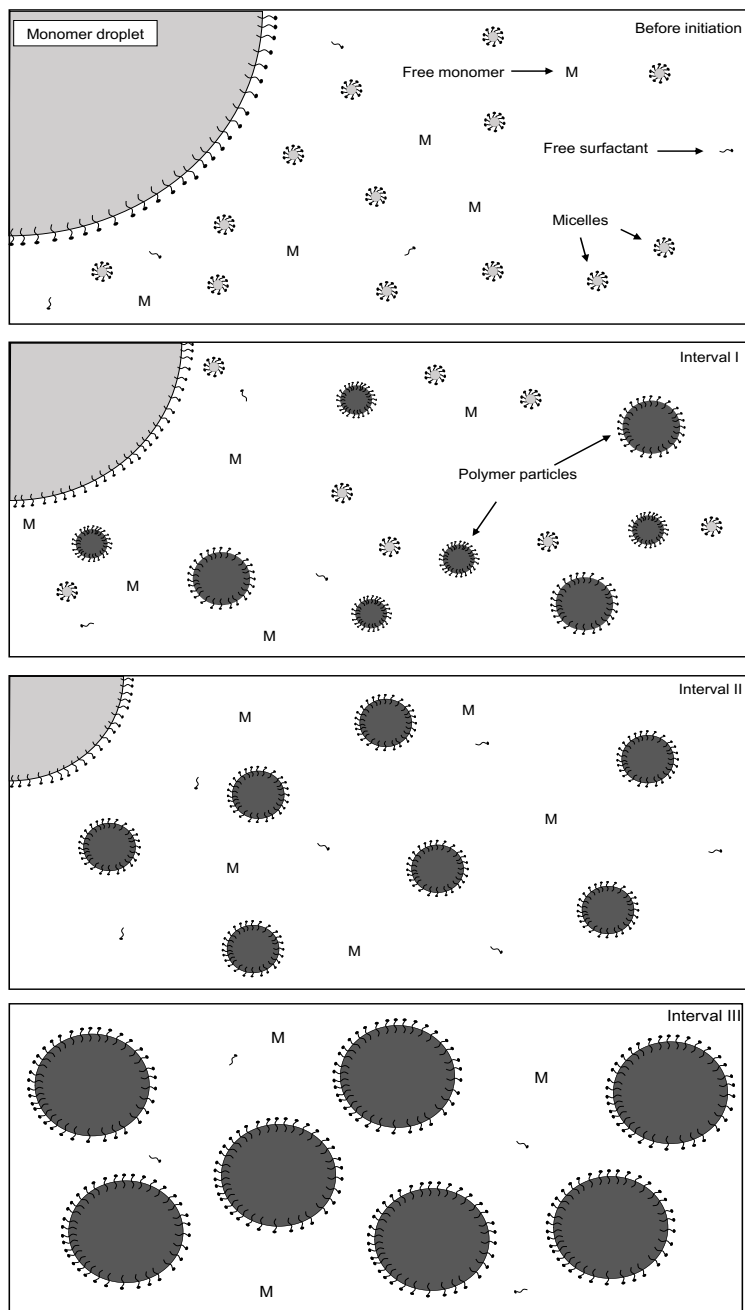


Figure 1. 1 Representation of a batch emulsion polymerization before initiation and during intervals I-III.

1.2.2 Semibatch emulsion polymerization

Batch emulsion polymerization is not an industrially relevant process, as usually semibatch (also known as semi-continuous) processes are preferred. A semibatch process allows a higher flexibility as the process can be controlled by the feed streams of the reactants leading to a safer process because the overall polymerization rate is determined by the feed rate of the monomers. Moreover, the semibatch process gives control over many design variables such as the copolymer composition, particle morphology, or particle size distribution.

In a semibatch polymerization, a fraction of the monomers is gradually added to the reaction medium. The nucleation step is the least reproducible event in emulsion polymerization and it is often circumvented by initiating the polymerization from pre-synthesized small polymer particles and low solids content as initial charge (known as seed) to control the particle size distribution. This is called seeded semibatch emulsion polymerization. During the process, monomers, initiator, surfactant, and water are fed into the reactor. To avoid the accumulation of unreacted monomer in the reactor which ensures the safety of the process, the monomer feed rate must not exceed the polymerization rate. Furthermore, a slow monomer addition in the case of copolymerization of monomers with very different reactivity ratios (such as acrylates with methacrylates [35]) can avoid composition drift in the copolymer that happens in the batch processes [37]. Finally, the correct design of the process allows the preparation of more complex particle morphologies such as core-shell particles.

Control of the surfactant feed is important too. Monomodal particle size distributions are obtained when the surfactant feed rate is low enough to avoid nucleation of new particles. However, the formation of new particles can be desirable for some high solids content applications because a multimodal particle size distribution decreases the viscosity of the latex,

and this can be achieved with the correct design of the surfactant feed or adding a different shot of seeds [38, 39]. After the feeding stage, the system is usually allowed to react for an additional time to ensure complete monomer consumption.

Semibatch emulsion polymerization is often used to synthesize waterborne dispersions of multiphase particles. The performance of these latexes is strongly dependent on particle morphology. To obtain those composite particles, it is necessary to produce at least two polymers that are incompatible that will phase separate. The simplest method involves a two-step polymerization, where the polymers are synthesized one after the other. In the first step, a dispersion of copolymer 1 is produced and this dispersion used as a seed for the polymerization of the second stage monomers. Due to the incompatibility, the second stage copolymer phase separates forming clusters. These clusters can grow due to polymerization within them, by diffusion of polymer formed in the matrix of copolymer 1, and by coagulation with other clusters. In addition, clusters migrate toward the equilibrium morphology, which is determined by the interfacial tension between the various phases [40]. Figure 1.2 presents the evolution of the particle morphology for a two-phase system into the equilibrium morphology [9].

A second approach to form composite particles is the continuous change of monomer ratio in the feed. The chemical composition of the copolymer is changed markedly through the polymerization and creates particles having a gradient of chemical composition and a specific arrangement of the various and distinct polymeric chains [41].

A marked change in crosslinking density or molecular weight can induce a phase separation [41]. Consequently, an alternative to the previous processes is to keep the monomer feed constant and to incorporate steps of crosslinker or chain transfer agents into the feed to induce molecular characteristic changes.

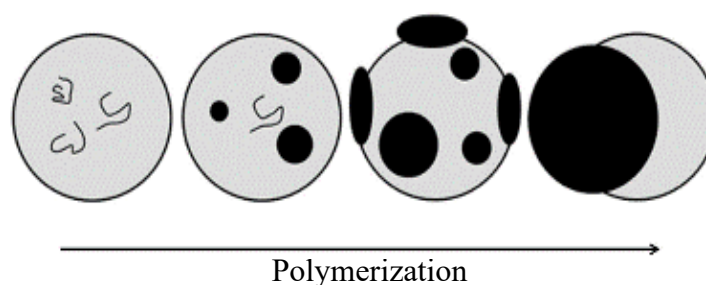


Figure 1. 2 Particle morphology development (Reproduced with permission from John Wiley and Sons) [9]

The final morphology strongly depends on the kinetics of cluster migration. When the movement of the phases is not hindered, equilibrium morphologies are reached. The thermodynamic equilibrium morphology corresponds to the minimum overall surface energy, which depends on the interfacial areas and interfacial tensions between the polymer phases (γ_{12}), and between each polymer phase and the aqueous medium (γ_{13} , γ_{23}) [42]. For two-phase systems, the calculation of the minimum overall surface energy is facilitated by the limited number of possible equilibrium morphologies achievable (core-shell, inverted core-shell and hemispherical) as shown in Figure 1.3 [40]. Inverted core-shell particles are obtained when the second stage polymer is more hydrophobic than the first stage one and the phases are not cross-linked [43]. Hemispherical morphologies are formed when the two polymers have similar hydrophilicities and a relatively high polymer-polymer interfacial tension.

Non-equilibrium particle morphologies result from the hindered movement of the clusters due to the high internal viscosity of the particles. In this case, different particles morphologies can be formed such as: raspberry-like [44, 45] or occluded [46, 47]. Occluded particles are formed when the second stage monomer polymerizes within the matrix formed by the first stage polymer and the viscosity of the matrix is high. Raspberry and multilobed morphologies can result from the high viscosity of the second polymer which forms the lobes.

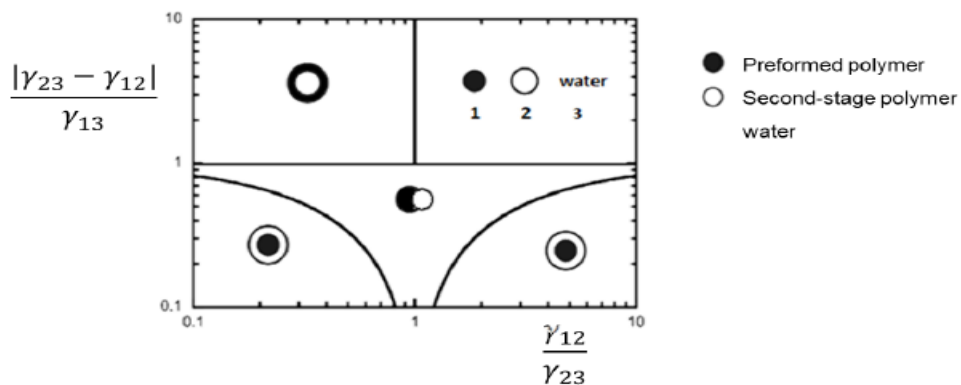


Figure 1. 3 Diagram of thermodynamic equilibrium morphologies for polymer-polymer (Reproduced with permission from American Chemical Society) [40]

1.3 Film formation of waterborne dispersions

1.3.1 Drying process of homogeneous particles

Usually, coatings from waterborne dispersions present worse properties than their solventborne counterparts. One of the most important reasons is that the film formation process is completely different. The formation of film from solventborne resin consists of the evaporation

of the solvent. The chains entangle during evaporation and as the polymer is plasticized by the solvent, hard polymers can be used without having issues with the mobility (diffusion) of the chains [48].

The film formation process from a waterborne dispersion is more complex and it is a crucial step for obtaining good quality cohesive films [49, 50-53]. It consists of four stages as shown in Figure 1.4. At the beginning of the process, stage I, the polymer particles are dispersed in the aqueous media. When water evaporates, the particles get closer, getting in contact with each other and forming a close packed array with water filling the interstices (stage II). The interstitial water evaporates and if the temperature is high enough, the polymer particles deform filling the interstices (stage III) [50, 53]

Particles are deformed under the effect of interfacial and capillary forces, but they remain discrete and maintain their boundaries. The transition from Stage II to Stage III can only happen above the minimum film formation temperature (MFFT). The MFFT only shows the ability of the particles to deform, and it is characterized by the optical clarity of the film. However, this does not imply the disappearance of the particle-particle boundaries. Only when the temperature is above the effective glass transition temperature of the polymer, coalescence between particles and interpenetration of the chains may happen, giving rise to a continuous film (Stage IV).

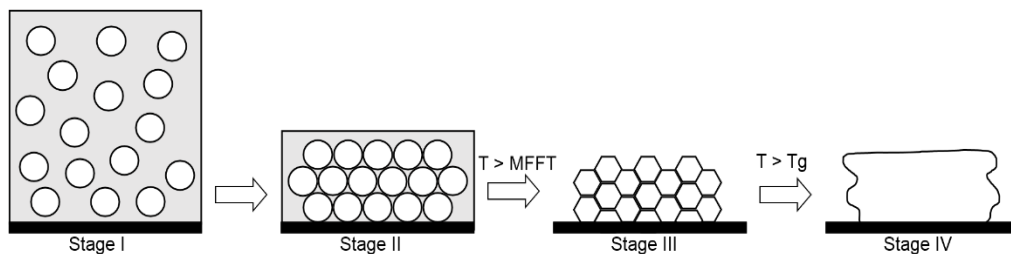


Figure1. 4 Representation of the film formation process.

The last two steps of the film formation process are the reason why waterborne coatings often present worse properties than solvent-borne coatings. The deformation and coalescence steps make it challenging to obtain mechanically stiff films at room temperature because chain mobility (i.e. low T_g) and hardness (i.e. high T_g) are required at the same time. This is known as the film formation dilemma. In addition, during the film formation the species present in the surface of the particles, such as the surfactant and functional monomers can hinder the movement of the chains, decreasing the interpenetration of the chains and leading to films with poorer cohesion.

1.3.2. Drying mechanisms

1.3.2.1. Drying inhomogeneity

Drying could occur non uniformly in both horizontal [53-56] and vertical directions [53, 57], leading to a non-uniform spatial distribution of latex particles that evolves with the drying time.

Two timescales determine the distribution of particles in the film: the one associated with the time required for the water to evaporate in a wet film, and that corresponding to the time needed for a particle to diffuse from the top to the bottom of the film. The time for evaporation is H (wet thickness – dry thickness) (m) divided by the evaporation rate E_{vap} expressed as a velocity (m/s):

$$t_{evp} = \frac{H}{E_{vap}} \quad (1.2)$$

The time for diffusion of a particle for the distance H from the top to the bottom of the film is inversely related to the diffusion coefficient of the particles, D_0 , by the Stokes-Einstein diffusion:

$$t_{diff} = \frac{H^2}{D_0} \quad (1.3)$$

A comparison of the two times is given by the dimensionless Peclet number, P_e as:

$$P_e = \frac{t_{diff}}{t_{evp}} = \frac{HE_{vap}}{D_0} \frac{6\pi\mu R_p H E_{vap}}{KT} \quad (1.4)$$

$$D_0 = \frac{kt}{6\pi\mu R} \quad (1.5)$$

with kT being the thermal energy, μ the viscosity of the aqueous phase and R the particle radius (assuming that they are spherical). For $Pe \gg 1$, diffusion is relatively slow, and therefore a layer of close-packed particles accumulates at the top surface during water evaporation [58]. If the particles deform and coalesce, a skin layer may be formed and the evaporation rate will decrease considerably [59, 60], which results in a poor adhesion to the substrate. For $Pe \ll 1$, the particles order themselves fast enough to avoid being captured at the air-film surface and the particles are predicted to remain uniformly dispersed in the film. That uniform drying can be achieved with slow evaporation rates and thin films.

In addition to non-uniform drying in the vertical direction, latex films do not dry uniformly in the horizontal direction [61]. The particles are dragged by the outward capillary flow due to the pinning of liquid contact line on the substrate. The capillary pressure causes the flow of water towards the dry edge. Moreover, the capillary pressure pushes water towards the end of the film and hence it pins the water at the edge of the film [50]. The film presents different fronts of

different appearances while the film is drying. At least two different fronts can be described as shown in Figure 1.5. The boundary between a dilute dispersion and the packed particles (where water started to evaporate) is called the “particle front”. In a packed particle bed, a boundary is formed between the wet and dry region, which is called the “drying front”. Such drying fronts can lead to poor film levelling and short open time for coating repair. It has to be pointed out that Figure 1.5 is only representative for dilute dispersions, commercial latexes are concentrated and this effect is less pronounced.

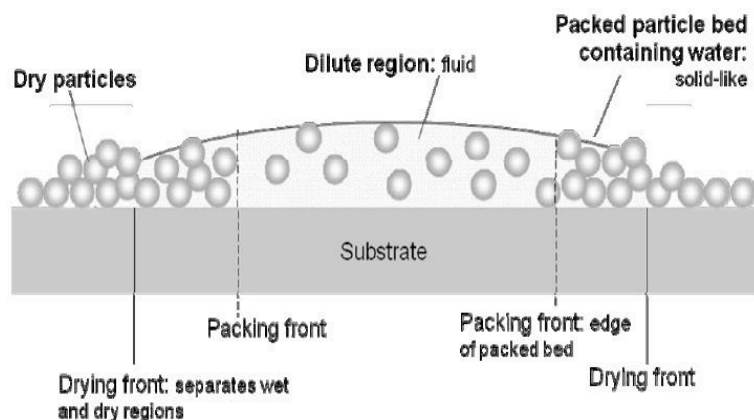


Figure 1.5 Schematic diagram showing the two different types of horizontal fronts (Reproduced with permission from Springer Nature) [50]

While water evaporates, the particles become arranged in a close-packed form. This ordering can be random and the evaporation rate, controlled by temperature and humidity, has an impact on the particle ordering. Indeed, a fast evaporation prevents the formation of a crystal-like structure. On the other hand, crystal-like structures can be formed from monodispersed particles with a slow evaporation [50].

1.3.2.2 Driving forces for particle deformation and coalescence

After close packing of the latex during the first stage, the particles start to deform. This is the second stage of film formation. The ideal result for the deformation is a structure without voids. The compaction and deformation of particles in a face centred cube (FCC) configuration leads to a rhombic dodecahedral structure [54]. This configuration can be reached with a monomodal system and also with bimodal systems if the size of the small particles allows them to fill the voids left by the big size particles during particle ordering [62]. This particle deformation is a result of several forces all of them related to the interfacial tensions (polymer-polymer, polymer-water, polymer-air and water-air). that aim to reduce the surface free energy of the system. These forces should overcome the resistance opposed by the viscoelastic nature of the polymer. Different deformation mechanisms have been proposed [63].

Wet sintering –involves the deformation of particles in the presence of water. The driving force is the interfacial tension between the particles and the water. If the particles fused together in water, the interfacial area between them decreases lowering the surface energy. [64, 65]. Dobler et al. [64] observed particle deformation and compaction only due to the polymer-water interfacial tension. However, the rate of compaction under standard conditions is slow compared to the evaporation of water, so, under common conditions, wet sintering is not a dominant mechanism for film formation.

Dry sintering - the polymer/air surface tension provides the driving force for particle deformation and coalescence takes place in the absence of water. For dry sintering to occur, the water should recede rapidly. [66-68].

Capillary deformation – Brown [63] hypothesised that the air-water interfacial tension dominates particle deformation. As the water evaporates, because of the presence of particles, the curvature of the air/water interface forms a meniscus (curved interface between air and water) that gives rise to a large negative pressure in the fluid (capillary pressure), which in turn compresses the particles below. Under this compression the particles deform. The pressure generated is $12.9 \gamma_{wa}/R_0$, assuming a spherical meniscus within a triangular array of particle with initial radius R_0 . The pressure difference across the meniscus is inversely proportional to its radius of curvature, which depends on the wetting of the particles and the particle diameter. Thus, a more tightly curved water surface will create a greater capillary pressure [69, 70].

Receding waterfront - Keddie [49] identified this inhomogeneous regime whereby deformation is initiated by capillary forces. As the water recedes through the film, leaving dry particles behind the deformation mechanism switch to either dry or moist sintering [49].

Sheetz deformation - The previous models assume a level of homogeneity in the vertical height of the film. If evaporation is fast enough, the particles may form a close packing near the air-latex interface before the particles close to the substrate reach close packing under these conditions, coalescence of the particles accumulated near the top of the latex might form a skin, hindering evaporation of the residual water. Sheetz's model postulated that diffusion of water through this skin causes a large osmotic pressure in the fluid below generating compressive force normal to the film. Routh and Russel offer an alternative explanation which is that the skin slows down the evaporation rate considerably, allowing more time for wet sintering [71].

1.3.3. Modelling film formation

Routh and Russel [71] developed a model for film formation from polymer dispersions. The outputs of the model were summarized in a map that provides the dominant mechanism in terms of two dimensionless control parameters: λ and the Peclet number (Pe) (Figure 1.6). The parameter λ is defined as the ratio between the time required for film compaction (i.e. for complete particle deformation) t_{def} , and the characteristic time for the evaporation of water, t_{evp} , considering that the polymer is viscous

$$\lambda = \frac{t_{def}}{t_{evp}} = \frac{\eta_0 R_0 / \gamma_{wa}}{H/E} = \frac{\eta_0 R_0 E_{vap}}{\gamma_{wa} H} \quad (1.6)$$

where η_0 is the low shear viscosity of the polymer, and γ_{wa} is the water-air interfacial tension. A very high λ value ($> 10^4$) means that the time required for particle deformation is much longer than the evaporation time of water. This implies that the deformation occurs when the water is gone, namely, by a dry sintering mechanism. On the other hand, if λ is low (< 1), the time for water to evaporate is higher than the deformation time of the particles meaning that the deformation occurs by a wet sintering mechanism. If $1 < \lambda < 10^2$, Capillary deformation occurs. Finally, if $10^2 < \lambda < 10^4$, an inhomogeneous regime between capillary and dry sintering is described as a receding water front. On the other hand, when the Peclet number is small ($Pe \ll 1$), the particles order themselves fast enough to avoid being captured at the air-film surface and the particles are predicted to remain uniformly dispersed forming a homogenous film. For $Pe \gg 1$, particle diffusion is relatively slow, and therefore a layer of close-packed particles accumulates at the top surface during water evaporation forming a skin layer.

Although the Routh and Russel model is a valuable tool to improve the performance of the coatings, it is not enough to overcome the film formation dilemma. The approaches aiming at this goal are discussed in the following section.

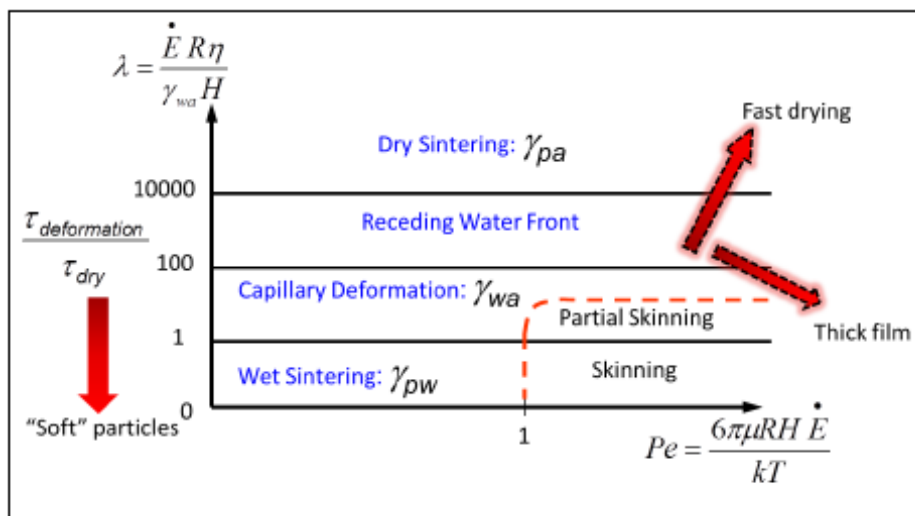


Figure 1.6 Routh-Russel deformation map for latex film formation (Reproduced with permission from American Chemical Society) [71]

1.4 Approaches to overcome film formation dilemma

Strategies to form mechanically strong films from waterborne polymer dispersions include the use of both chemical [72-76] and physical [77-83] crosslinking, but this complicates the chemistry of the system. Another possibility is to blend soft and hard polymer particles [84-90]. However, this often leads to phase separation during film formation. This problem is overcome by including both soft and hard polymers in the same polymer particle resulting in a hybrid polymer latex. Whereas the soft polymer facilitates film formation, the hard polymer provides good mechanical properties like block resistance. In this type of coating, particle morphology plays a critical role. Hard core/soft shell and soft core/hard shell morphologies represent the two

extreme cases. Easy film formation is guaranteed by the first one that will lead to a film of soft polymer reinforced by hard inclusions [91-96]. However, the improvement in properties is limited because the soft phase remains continuous in the film [96, 97].

The soft core/hard shell morphology leads to a honeycomb structure of hard polymer filled with soft polymer that presents much better mechanical properties [52, 65, 98, 99, 100]. It is worth pointing out that sometimes a perfect core-shell morphology is claimed without clear proof [65, 99, 101, 102]. Thus, Dos Santos et al. [65] prepared soft core (poly(butyl acrylate-co-butadiene)-hard "shell" (poly(methyl methacrylate), pMMA) particles with different "shell" ratios (10, 20, 30%). With 10% of hard polymer, the soft core was not well covered by the pMMA. With 20 and 30%, it was stated that most likely the core was well covered, but no clear proof was given. The films were cast at 30°C yielding macroscopically homogeneous and transparent films, which looks in conflict with the existence of perfect hard shells. Nevertheless, the values of the Young's modulus strongly suggest that there was a continuous path of hard polymer in the film. Cao [101] synthesized different soft core-hard "shell" latexes. In one example, the soft core was poly(butyl acrylate), pBA, and the "shell" poly(methyl methacrylate), pMMA. The MFFT increased from about 0°C for 25% of pMMA to about 25°C for 30% of pMMA and to 100 °C for 60% of pMMA. Due to the similar contrast of the two polymers in the transmission electron microscope (TEM), it is difficult to assess the particle morphology, but these results suggest that a certain amount of hard polymer is needed to form a continuous shell. In another example, poly(ethyl acrylate) was used as the soft phase and polystyrene as the hard phase. In this case, the sudden increase (from 0°C to 100°C) of the MFFT when the content of polystyrene passed 62.5% indicates that an acorn-like morphology was obtained and that 62.5% of hard phase was the point for switching from a soft to hard continuous one. Price et al. [99] studied the stress development and film formation of soft core-hard shell latexes with different core/shell ratios,

core and shell T_g s and particle sizes. The latexes were produced by a two-stage semibatch emulsion polymerization in which the hard phase, that was more hydrophilic, was produced first. Methacrylic acid (MAA) was incorporated to the hard phase. Particle morphology was studied by staining the MAA units with uranyl acetate. The presence of MAA at the surface of the particles was taken as proof of the formation of a perfect core-shell morphology. However, it was found that particles containing 50% of hard phase ($T_g = 33.5$ °C) gave a MFFT of only 16.9°C, which was even lower than the T_g of the soft phase (19.5°C). In another example in which a 50% hard phase of $T_g = 56.1$ °C was used, the MFFT was only 34.4°C. This suggests that the particles did not present well-defined soft core-hard shell morphologies. Limousin et al. [36] synthesized composite particles consisting of a soft core with a multilobed hard shell obtaining films with a MFFT close to that of the soft core and a 4.5 times higher Young's modulus.

In the reports summarized above, film formation occurred at low temperature, suggesting that the particles had a thin shell that could be deformed or that they did not have a perfect soft core-hard shell morphology, which would result in the formation of cracks. As thin shells are difficult to produce and patches are naturally produced by seeded emulsion polymerization [103, 104], it is likely that the particles morphology consisted of a soft core covered by patches of hard polymer. This morphology is called soft core-hard "shell" in this PhD Thesis. Even if the hard polymer does not form a continuous shell, its presence at the surface of the particles facilitates the formation of cracks during film formation due to the stress created as a consequence of volume shrinkage and the attachment of the particles to the rigid substrate [105, 106]. This unwanted effect is even more critical in exigent applications (e.g. exterior and anticorrosion coatings) where a thick coating is needed, because crack formation is favoured in thick films [107].

1.5 Formation of cracks during drying of colloidal dispersions

Whereas cracking during drying of dispersions of hard colloids has been extensively studied [108-117], in spite of its practical importance, there are a limited number of articles specifically dealing with cracking during drying of waterborne polymer coatings containing soft and hard polymers.

Blends of soft and hard particles behave in a somehow predictable manner. Increase of the content of the hard particles favours the contact between them, which results in an increase of the minimum film forming temperature (MFFT), and therefore of the cracking formation (MFFT is the minimum temperature needed to avoid crack formation). Colombini et al. [86] used blends of hard and soft particles of different sizes. Above the content of small hard particles that forms a percolating structure, The MFFT increases significantly, which is an indication of occurrence of cracking. In the drying of blends of film forming latexes and silica particles, no crack was mentioned, but the shape of the stress curves suggests that this was the case for silica contents equal or greater than 50% [118]. In blends of soft and hard polymer particles, Lepizzera et al. [119] reported that all films cracked for contents of hard particles greater than 55%. Roberts et al. [120] used a blend of acrylic particles ($T_g = 5\text{ }^\circ\text{C}$) and fumed silica aggregates. Cracks were formed at temperatures lower than $17\text{ }^\circ\text{C}$. Singh et al. [121] used blends of silica and acrylic particles ($T_g = 40^\circ\text{C}$) and measured the critical cracking thickness (CCT, thickness of the dry coating below which no cracks are formed) at $25\text{-}28\text{ }^\circ\text{C}$. Cracking was observed for all silica contents and, surprisingly, the CCT increased with the content of silica.

The behaviour of hard core-soft shell latexes is also predictable with MFFT increasing as the thickness of the soft shell decreased. Thus, Cao [101] reported that hard core-soft shell

particles led to low MFFT until a content of the hard polymer of about 63%. Above this value, MFFT increased sharply.

The analysis of film formation of so-called soft core-hard shell latexes is more complex because as discussed above a perfect core-shell morphology is often claimed without clear proof [65, 99, 101, 102]. Therefore, we will use the term soft core-hard “shell” to describe these systems. Dos Santos et al. [32] prepared soft core (poly(butyl acrylate-co-butadiene)-hard “shell” (poly(methyl methacrylate), pMMA) particles with different “shell” ratios (10, 20, 30%) and no cracking was reported. Cao et al. [101] synthesized different soft core-hard “shell” latexes. They reported that the MFFT increased from about 0°C for 25% of hard phase to 100 °C for 60% of hard phase. As MFFT is the minimum temperature at which no cracking was visually observed, these results show that cracking occurred at room temperature for 60% of hard phase. However, the morphology could not be unambiguously assessed. Petersen et al. [57] prepared 60/40 soft core-hard “shell” particles. Extensive cracks occurred when the casting temperature was lower than 44 °C.

Significant progress has been made in the last three decades in the understanding of the origin of stress and in the prediction of conditions for the failure of drying colloidal films [110, 115-117, 121, 128-130]. For example, Tirumkudulu and Russel [110] developed a model to predict crack formation. In order to calculate the stress-strain relation during film formation, the model combines the constitutive relation of Routh and Russel [131] with the methodology outlined by Xia and Hutchinson [132]. Then, the Griffith’s criterion [125] for the nucleation of cracks (the recovery of the elastic energy equals the energy required to create the surface of the crack) was used. For a system of identical elastic spheres, the critical stress (σ_c) for nucleation of a crack was obtained as

$$\frac{\sigma_c R}{2\gamma} = 0.1877 \left(\frac{2R}{h}\right)^{2/3} \left(\frac{GM\phi_{rcp}R}{2\gamma}\right)^{1/3} \quad (1.9)$$

where R is the radius of the particles, γ is surface tension of the aqueous phase (capillary was assumed to be the main driving force), h is the film thickness at cracking, G is the shear modulus of the particles, M the coordination number (number of contacts of one particle) and ϕ_{rcp} the particle volume fraction at random packing.

Viscoelasticity was considered in a subsequent model [130] in which the constitutive equation was developed based on the Hertzian contact mechanisms between spheres. Using again the Griffith's criterion for cracking [125], the following equation for the capillary pressure necessary for cracking (p_{cap}^{crack}) was obtained

$$-\frac{hp_{cap}^{crack}}{\gamma} \cong 2.06 \left(\frac{\bar{G}h}{\gamma}\right)^{2/5} + \frac{2.91}{\tau} \quad (1.10)$$

where \bar{G} and τ are

$$\bar{G} = \phi_{rcp}MG/2\pi(1-\nu) \quad (1.11)$$

$$\tau = 2\eta E_{vap}(1-\nu)/hG \quad (1.12)$$

Where η is the viscosity of the polymer, E_{vap} is the evaporation rate, and ν is the Poisson's ratio of the polymer.

In order to calculate the CCT from eq 1.10, the capillary pressure is needed. Russel et al. [130] assumed that this pressure is the maximum capillary pressure for hard particles ($-5.3\gamma/R$), which led to

$$\frac{CCT}{R} = 0.05 \left(\frac{\bar{G}R}{\gamma} \right)^{2/3} \quad (1.13)$$

Equation 5 predicts that the CCT increases with both the shear modulus and the particle size. However, this is only strictly valid for hard spheres.

Another attempt to include the deformability of the latex is due to Singh and Tirumkudulu [129] who assumed that the critical stress was equal to the biaxial stress at maximum compressive strain ($\epsilon_{\max}=1-\phi_{rcp}$),

$$\sigma_c = \frac{3}{35} MG \phi_{rcp} (1 - \phi_{rcp})^2 \quad (1.14)$$

Combination of eqs 1.9 and 1.14 leads to

$$CCT = \frac{37\gamma}{GM\phi_{rcp}(1-\phi_{rcp})^3} \quad (1.15)$$

which predicts that CCT decreases with the modulus G. On the other hand, it is independent of the particle size. However, in eq 1.14 it is assumed that there are no holes in the film, namely that the particles are viscous and deform, but this is against the assumption made to develop eq 1.9 (elastic particles).

All the mentioned models were developed for homogeneous particles. Milan and Routh have also developed a model for the film formation of polymer particles that contain a hard inclusion (core) with cylindrical shape with horizontal orientation with a soft polymer shell [133]. According to this model, the presence of the hard core increases the MFFT provided that sufficient drag occurs at the hard-soft interphase.

The applicability of these models to coatings formed from soft core-hard “shell” particles is an open question as a direct link between the morphology of the particle and the film formation properties and mechanical properties of the film cast from the latex dispersion is still missed. In

addition, there are some critical aspects that have not been studied for hybrid particles such as the effects of the thickness of the film, drying conditions, type of substrate, particle size and content of acidic monomers that contributed to hydroplasticization.

1.6. Thesis objectives

The main goal of this project is to obtain a systematic and quantitative understanding of the cracking mechanism and the influence of the composition and morphology of the particles, as well as that of the casting conditions on the formation of cracks. Another goal is to check the performance of existing mathematical models against the experimental data obtained with soft core-hard “shell” latexes and to develop new models if the existing ones fail to fit the trends found experimentally. An additional goal is to improve the performance of the soft core-hard “shell” latexes. It is expected that the knowledge gained in this work will contribute to the progress towards the production of VOC-free, mechanically strong polymer films cast at ambient from curable waterborne dispersions, opening the way for the complete replacement of solvent-based coatings.

1.7. Outline of the thesis

The content of the thesis is divided in eight chapters. **Chapter 1** provides a general introduction and motivation about the work.

Chapter 2 is devoted to the study of the effect of the particle characteristics (size, soft/hard phase ratio, presence of carboxylic moieties, molar mass of the hard phase, glass transition temperature of the soft phase) and drying conditions (temperature, relative humidity, thickness of the film, type of substrate) on the stress generation and crack formation using hybrid

particles containing soft core and hard “shell” synthesized by semi-continuous emulsion polymerization. The morphology of particles and films were characterized in detail and the range of conditions to form a crack-free mechanically strong low temperature film forming coating were determined. Furthermore, the results are compared with the predictions of the mathematical models for cracking available in literature. A data-derived criterion for cracking nucleation is proposed.

Chapter 3 is focused on developing a mathematical model for calculation of drying stress generated during film formation and cracking prediction for soft core hard “shell” hybrid particles cast on a flexible substrate (cantilever in beam bending experiments). The governing incompressible Navier-Stokes and continuity equations were numerically solved using COMSOL Multiphysics. The results were validated with experimental values from Chapter 2 using a scaling down approach that was used to overcome the problem of the unacceptable long computing time needed for a complete film.

Chapter 4 focuses on investigating the effect of blending large and small soft core-hard “shell” particles on MFFT, CCT, mechanical properties, and drying stresses. The amount of small particles was limited (in most cases to 1wt%) to avoid water sensitivity.

Chapter 5 explores a strategy to enhance the mechanical properties of waterborne coatings without compromising the film formation properties of soft core-hard “shell” polymer particles. The strategy is based on a multiphase internal core composed by hard and soft domains.

In **Chapter 6** a coarse graining model was developed to overcome the limitations of the model developed in Chapter 3.

Chapter 7 is dedicated to materials for commercial coating applications. The soft core-hard “shell” latexes are used as binders in paints and stains formulation for decorative and protective wood coatings. The performance of these paints and the stains are compared with that of commercial products.

Finally, in **Chapter 8** the most relevant conclusions of the thesis are summarized.

1.8. References

- [1] A. Goldschmidt; H.-J. Streitberger. BASF Handbook on Basics of Coating Technology **2007**, Hannover, Germany.
- [2] Paints And Coatings Market By Product (High Solids, Powder, Waterborne, Solvent-Borne), By Material (Acrylic, Alkyd, Polyurethane, Epoxy & Polyesters), By Application, And Segment Forecasts 2015-2025. **2017**.
- [3] Businesswire. Water Borne Coatings Global Market Report 2020. Dublin, **2020**.
- [4] G. De With, A. Esteves, L. van der Ven, R. van Benthem, J. Laven and R. Tuinier. Polymer Coatings: A Guide to Chemistry, Characterization and Selected Application **2018**, Wiley-VCH: Weinheim, Germany.
- [5] K. Weiss. Paint and Coatings: A Mature Transition Industry. *Prog. Polym. Sci.* **1997**, 22, 203-245.
- [6] J. Sherman, B. Chin, P. Huibers, R. Garcia-Valls and T. A. Hatton. Solvent Replacement for Green Processing. *Environ. Hea. Pers.* **1998**, 106, 253-271.
- [7] E. Commission. Report on the Implementation and Review of Directive 2004/42/EC of the European Parliament and of the Council on the Limitation of Emissions of Volatile Organic Compounds due to the Use of Organic Solvents in Certain Paints and Varnishes and Vehicle Refin. **2011**.
- [8] E. Commission. Screening Study to Identify Reductions in VOC Emissions due to the Restrictions in the VOC Content of Products. **2002**.
- [9] J. M. Asua. Polymer Reaction Engineering. Wiley – Blackwell **2007**.
- [10] S. Thickett and R. Gilbert. Emulsion Polymerization : State of the Art in Kinetics and Mechanisms. *Polymer* **2007**, 48, 6965–6991.
- [11] D. Myers. Surfaces, interfaces, and colloids. John Wiley & Sons **1999**.
- [12] H. Warson. Emulsion polymerization, a mechanistic approach, London: *Polym. Int.* **1996**, 41, 352-352.
- [13] J. Charmot. Carboxylated styrene-butyl acrylate and styrene-butadiene emulsion copolymers. Modelling the distribution of the acid monomer

- between serum, particle surface and the particle core. *Polymer* **1996**, 37, 5237-5245.
- [14] X. Reynhout, M. Beckers, J. Meuldijk and B. Drinkenburg. Electrosteric Stability of Styrene / Acrylic Acid Copolymer Latices under Emulsion Polymerization Reaction Conditions. *J. Polym. Sci. Part A Polym. Chem.* **2005**, 43, 726–732.
- [15] Z. Aguirreurreta, J. C. de la Cal and J. R. Leiza. Preparation of high solids content waterborne acrylic coatings using polymerizable surfactants to improve water sensitivity. *Prog. Org. Coatings* **2017**, 112, 200–209.
- [16] D. Blackley. Synthetic latices: general principles of production, Dordrecht: Polymer Latices. Springer, **1997**.
- [17] J. M. Barton. Relation of glass transition temperature to molecular structure of addition copolymers. *J. Polym. Sci. Part C Polym. Symp.* **1970**, 30, 573–597.
- [18] H. Schneider, J. Rieger and E. Penzel. The glass transition temperature of random copolymers: 2. Extension of the Gordon-Taylor equation for asymmetric Tg vs composition curves. *Polymer* **1997**, 38, 1323–1337.
- [19] W. Harkins. General Theory of the Mechanism of Emulsion Polymerization. *J. Am. Chem. Soc.* **1946**, 69, 1428–1444.
- [20] W. V. Smith and R. H. Ewart. Kinetics of Emulsion Polymerization Kinetics of Emulsion Polymerization. *J. Chem. Phys.* **1948**, 16, 592–597.
- [21] J. M. Asua. Emulsion Polymerization : From Fundamental Mechanisms to Process Development. *J. Polym. Sci.* **2004**, 42, 1025–1041.
- [22] J. De la Cal, J. Leiza, J. M. Asua, A. Butté, G. Storti and M. Morbidelli. Emulsion Polymerization. in *Handbook of Polymer Reaction Engineering*, Meyer, T., Keurentjes, J., Eds.; Wiley-VCH: Weinheim, **2005**.
- [23] R. M. Fitch and C. J. Tsai. Polymer colloids: particle formation in nonmicellar systems. *J. Polym. Sci. Part B Polym. Lett.* **1970**, 8, 703–710.

- [24] R. M. Fitch and C. H. Tsai. Particle formation in polymer colloids, III: Prediction of the number of particles by a homogeneous nucleation theory. *Polym. Colloids* **1971**, 73–102.
- [25] F. K. Hansen and J. Ugelstad. Particle Nucleation in Emulsion Polymerization . I. A Theory for Homogeneous Nucleation. *J. Polym. Sci. Polym. Chem.* **1978**, 16, 1953–1979.
- [26] J. Ugelstad and F. K. Hansen. Kinetics and Mechanism of Emulsion Polymerization. *Rubber Chem. Technol.* **1976**, 49, 536–609, 1976.
- [27] A. S. Dunn. Kinetics of Emulsifier Adsorption and Nucleation of Latex Particles. *Polym. Int.* **1993**, 30, 547–550.
- [28] N. Ballard, J. Urrutia, S. Eizagirre, T. Schäfer, G. Diaconu, J. C. de la Cal and J. M. Asua. Surfactant Kinetics and Their Importance in Nucleation Events in (Mini)emulsion Polymerization Revealed by Quartz Crystal Microbalance with Dissipation Monitoring, *Langmuir* **2014**, 30, 9053–9062.
- [29] P. Feeney, D. Napper and R. Gilbert. Coagulative Nucleation and Particle Size Distributions in Emulsion Polymerization. *Macromolecules* **1968**, 17, 2520–2529.
- [30] G. Lichti, R. Gilbert and D. Napper. The Mechanisms of Latex Particle Formation and Growth in the Emulsion Polymerization of Styrene Using the Surfactant Sodium Dodecyl Sulfate. *J. Polym. Sci. Polym. Chem.* **1983**, 21, 269–291.
- [31] M. Morton, S. Kaizerman and M. Altier. Swelling of latex particles. *J. Colloid Sci.* **1954**, 9, 300–312.
- [32] I. Maxwell, B. Morrison, D. Napper and R. Gilbert. Entry of Free Radicals into Latex Particles in Emulsion Polymerization **1991**, *Macromolecules*, 24, 1629–1640.
- [33] M. Zubitur, P. Armitage, S. Ben Amor, J. R. Leiza and J. M. Asua. Mathematical Modeling of Multimonomer (Vinyllic, Divinyllic, Acidic) Emulsion Copolymerization Systems Mathematical Modeling of Multimonomer. *Polym. React. Eng.* **2003**, 11, 627–662.
- [34] J. Gordon. Ideal co-polymers and the second order transitions of synthetic rubbers. *Journal of Applied Chemistry* **1952**, 2, 493–500.

-
- [35] G. Arzamendi and J. M. Asua. Monomer Addition Policies for Copolymer Composition Control in Semicontinuous Emulsion Copolymerization. *J. Appl. Polym. Sci.* **1989**, 38, 2019-2036.
- [36] R. Hutchinson, J. McMinn, D. Paquet, S. Beuermann and C. Jackson. Pulsed-Laser Study of Penultimate Copolymerization Propagation Kinetics for Methyl Methacrylate / N-Butyl Acrylate. *Ind. Eng. Chem. Res.* **2002**, 36, 1103–1113.
- [37] N. Othman, G. Févotte and T. McKenna. Nonlinear state estimation and control of a semibatch terpolymerisation reactor. *IFAC Proc. Vol.* **2000**, 33, 515–520.
- [38] FA Mariz. High performance water-borne paints with high volume solids based on bimodal latexes. *Progress in Organic Coatings* **2010**, 68, 225-233.
- [39] FA Mariz. Control of particle size distribution for the synthesis of small particle size high solids content latexes. *Polymer* **2010**, 51, 4044-4052.
- [40] L. J. Gonzalez-Ortiz and J. M. Asua. Development of Particle Morphology in Emulsion. *Macromolecules* **1995**, 28, 3135–3145.
- [41] Y. Sundberg. Latex particle morphology, fundamental aspects: a review. *Polym. React. Eng.* **2003**, 11, 379–432.
- [42] S. Torza and S. Mason. Three-phase interactions in shear and electrical fields. *J. Colloid* **1970**, 33, 67–83.
- [43] S. Kirsch, A. Doerk, E. Bartsch, H. Sillescu, K. Landfester, H. Spiess and W. Maechtler. Synthesis and characterization of highly cross-linked, monodisperse core-shell and inverted core-shell colloidal particles. Polystyrene/ poly(tert-butyl acrylate) core-shell and inverse core-shell particles. *Macromolecules* **1999**, 32, 4508–4518.
- [44] M. Ostovar and H. Eslami. Synthesis of nanostructured confetti-like and mace-like particles via dispersion polymerization of alkyl methacrylates on polystyrene seeds. *Colloid Polym. Sci.* **2016**, 294, 1633–1642.
- [45] H. Huang and H. Liu., Synthesis of the raspberry-like PS/PAN particles with anisotropic properties via seeded emulsion polymerization initiated by X-ray radiation. *J. Polym. Sci. Part A Polym. Chem.* **2010**, 48, 5198–5205.

- [46] D. Blenner, J. Stubbs and D. Sundberg. Multi-lobed composite polymer nanoparticles prepared by conventional emulsion polymerization. *Polymer* **2017**, 114, 54–63.
- [47] J. E. L. Jonsson, H. Hassander, L. H. Jansson and B. Tornell. Morphology of 2-Phase Polystyrene Poly(Methyl Methacrylate) Latex-Particles Prepared under Different Polymerization Conditions. *Macromolecules* **1991**, 24, 126–131.
- [48] V. M. Chesunov and R. M. Vasenin. The Kinetics of Solvent Evaporation during Film Formation from Polymer Solutions. *Polym. Sci. U.S.S.R.* **1967**, 9, 2333–2338.
- [49] J. L. Keddie, P. Meredith, R. Jones and M. Donald. Kinetics of Film Formation in Acrylic Latices Studied with Multiple-Angle-of-Incidence Ellipsometry and Environmental SEM. *Macromolecules* **1995**, 28, 2673–2682.
- [50] J. L. Keddie. Film Formation of Latex. *Mater. Sci. Eng.* **1997**, 21 101–170.
- [51] P. A. Steward, J. Hearn and M. C. Wilkinson. An overview of polymer latex film formation and properties. *Adv. Colloid Interface Sci.* **2000**, 86, 195–267.
- [52] E. Limousin, N. Ballard and J. M. Asua. Soft core–hard shell latex particles for mechanically strong VOC-free polymer films. *J. Appl. Polym. Sci.* **2019**, 136.
- [53] J. L. Keddie and A. F. Routh. Fundamentals of Latex Film Formation: Processe and Properties. Dortecht, The Netherland, **2010**.
- [54] F. Routh and W. B. Russel. Horizontal drying fronts during solvent evaporation from latex films. *AIChE J.* **1998**, 44, 2088–2098.
- [55] E. Sutanto, Y. Ma, H. T. Davis and L. E. Scriven. Cryogenic Scanning Electron Microscopy of Early Stages of Film Formation in Drying Latex Coatings. *ACS Symp. Ser. Film Form. Coatings* **2001**, 174–192.
- [56] J. M. Salamanca, E. Ciampi, D. A. Faux, P. M. Glover, P. J. McDonald, A. F. Routh, A. C. I. A. Peters, R. Satguru and J. L. Keddie. Lateral drying in thick films of waterborne colloidal particles. *Langmuir* **2001**, 17, 3202–3207.

-
- [57] J.-P. Gorce, D. Bovey, P. J. McDonald, P. Palasz, D. Taylor and J. L. Keddie. Vertical water distribution during the drying of polymer films cast from aqueous emulsions. *Eur. Phys. J. E. Soft Matter* **2002**, 8, 421–429.
- [58] Y. Ma, H. T. Davis and L. E. Scriven. Microstructure development in drying latex coatings. *Prog. Org. Coatings* **2005**, 52, 46–62, 2005.
- [59] J. Mallégol, G. Bennett, P. J. McDonald, J. K. Keddie and O. Dupont. Skin Development during the Film Formation of Waterborne Acrylic Pressure- Sensitive Adhesives Containing Tackifying Resin. *J. Adhes.* **2006**, 82, 217–238.
- [60] J. W. Vanderhoff, E. B. Bradford and W. K. Carrington. The transport of water through latex films. *J. Polym. Sci. Polym. Symp.* **1973**, 41, 155–174.
- [61] Deegan, R., Bakajin, O., Dupont, T. et al. Capillary flow as the cause of ring stains from dried liquid drops. *Nature* **1997**, 389, 827–829.
- [62] J. Feng, M. A. Winnik, R. R. Shivers and B. Clubb. Polymer Blend Latex Films: Morphology and Transparency. *Macromolecules* **1995**, 28, 7671–7682.
- [63] G. L. Brown. Formation of films from polymer dispersions. *Journal of Polymer Science*, **1956**.
- [64] F. Dobler, T. Pith, Y. Holl and M. Lambla. Synthesis of model latices for the study of coalescence mechanisms. *J. Appl. Polym. Sci.* **1992**, 44, 1075–1086.
- [65] F. Domingues Dos Santos, P. Fabre, X. Drujon, G. Meunier and L. Leibler. Films from Soft-Core/Hard-Shell Hydrophobic Latexes: Structure and Thermomechanical Properties. *J. Polym. Sci. Part B Polym. Phys.* **2000**, 38, 2989–3000.
- [66] P. Bowen and C. Carry. From powders to sintered pieces: Forming, transformations and sintering of nanostructured ceramic oxides. *Powder Technol.* **2002**, 128, 248–255.
- [67] R. E. Dillon, L. A. Matheson and E. B. Bradford. Sintering of synthetic latex particles. *J. Colloid Sci.* **1951**, 6, 108–117.

- [68] F. Lin and D. J. Meier. A study of latex film formation by atomic force microscopy .2. Film formation vs rheological properties: Theory and experiment. *Langmuir* **1996**, 12, 2774–2780.
- [69] P.A. Steward, J. Hearn, U. M.C. Wilkinson. Formation of films from lattices a theoretical treatment. *Br. Polym. J.* **1973**, 5, 101–108.
- [70] S. T. Eckersley and A. Rudin. The film formation of acrylic latexes: A comprehensive model of film coalescence. *J. Appl. Polym. Sci.* **1994**, 53, 1139–1147.
- [71] A. F. Routh and W. B. Russel. Deformation Mechanisms during Latex Film Formation : Experimental Evidence. *Ind. Eng. Chem. Res.* **2001**, 40, 4302–4308.
- [72] A. Zosel and G. Ley. Influence of crosslinking on Structure, Mechanical Properties, and Strength of Latex Films. *Macromolecules* **1993**, 26, 2222–2227.
- [73] E. C. Galgoci, P. C. Komar and J. D. Elmore. High Performance Waterborne Coatings and an Amine-Functional Curing Agent. *J. Coatings Technol.* **1999**, 71, 45–52.
- [74] M. A. Winnik, P. Pinenq, C. Krüger, J. Zhang and P. V. Yaneff. Crosslinking vs. interdiffusion rates in melamine-formaldehyde cured latex coatings: A model for waterborne automotive basecoat. *J. Coatings Technol.* **1999**, 71, 47–60.
- [75] I. González, J. M. Asua and J. R. Leiza. Crosslinking in Acetoacetoxy Functional Waterborne Crosslinkable Latexes. *Macromol. Symp.* **2006**, 243, 53–62.
- [76] Kessel, N., Illsley, D.R. and Keddie, J.L. The Diacetone Acrylamide Crosslinking Reaction and Its Influence on the Film Formation of an Acrylic Latex. *J. Coatings Technol. Res.* **2008**, 285-297.
- [77] Y. Chen and E. Tunnah. Multiple Hydrogen-Bond Array Reinforced Cellular Polymer Films from Colloidal Crystalline Assemblies of Soft Latex Particles. *ACS Macro Lett.* **2012**, 1, 603–608.
- [78] S. Tungchaiwattana, R. Groves, P. A. Lovell, O. Pinprayoonac and B. R. Saunders. Tuning the Mechanical Properties of Nanostructured Ionomer Films by Controlling the Extents of Covalent Crosslinking in Core-Shell Nanoparticles. *J. Mater. Chem.* **2012**, 22.

- [79] E. González, M. Paulis, M. Barandiarra. Effect of Controlled Length Acrylic Acid-Based Electrosteric Stabilizers on Latex Film Properties. *Eur. Polym. J.* **2014**, 59, 122–128.
- [80] M. S. Musa, A. H. Milani, P. Shaw, G. Simpson, Peter A. Lovell, E. Eaves, N. Hodsonb and B. R. Saunders. Tuning the Modulus of Nanostructured Ionomer Films of Core-shell Nanoparticles Based on Poly(n-Butyl Acrylate). *Soft Matter* **2016**, 12, 8112–8123.
- [81] Jiménez N. Hydrogen Bond-Directed Formation of Stiff Polymer Films Using Naturally Occurring Polyphenols. *Macromolecules* **2019**, 52, 24, 9724–9734.
- [82] N. Ballard. Supramolecularly Reinforced Films from Polyurethane-urea Dispersions Containing the Tris-urea Motif. *ACS Appl. Polym. Mater.* **2020**, 2, 4045-4053.
- [83] Maialen Argai, Fernando Ruipérez, Miren Aguirre and Radmila Tomovska. Ionic inter-particle complexation effect on the performance of waterborne coatings. *Polymers* **2021**, 13, 3098.
- [84] J. L. Keddie, P. Meredith, R. A. L. Jones and A. M. Donald. Film Formation of Acrylic Latices with Varying Concentrations of Non-Film-Forming Latex Particles. *Langmuir* **1996**, 12, 3793–3801.
- [85] D. Kukanja, J. Golob, A. Zupančič-Valant, M. Krajnc. The structure and properties of acrylic-polyurethane hybrid emulsions and comparison with physical blends. *J. Appl. Polym. Sci.* **2000**, 78, 67-80.
- [86] D. Colombini, H. Hassander, O. J. Karlsson and F. H. J. Maurer. Influence of the particle size and particle size ratio on the morphology and viscoelastic properties of bimodal hard/soft latex blends. *Macromolecules* **2004**, 37, 6865–6873.
- [87] Geurts, J., Bouman, J. & Overbeek. New waterborne acrylic binders for zero VOC paints. *Coatings Technol. Res.* **2008**, 5, 57–63.
- [88] J. Pablo Tomba, Xiaodong Ye, Fugang Li, Mitchell A. Winnik, Willie Lau. Polymer blend latex films: Miscibility and polymer diffusion studied by energy transfer. *Polymer* **2008**, 49, 2055-2064.
- [89] J. P. Tomba, D. Portinha, W. F. Schroeder, M. A. Winnik and W. Lau. Polymer diffusion in high-M/low-M hard-soft latex blends. *Colloid Polym. Sci.* **2009**, 287, 367–378.

- [90] Pablo J. Peruzzo, Pablo S. Anbinder, Oscar R. Pardini, Jorge Vega, Carlos A. Costa, Fernando Galembeck, Javier I. Amalvy. Waterborne polyurethane/acrylate: Comparison of hybrid and blend systems. *Prog. Org. Coatings* **2011**, 72, 429–437.
- [91] Michael J. Devon, John L. Gardon, Glen Roberts, Alfred Rudin. Effects of core-shell latex morphology on film forming behavior. *J. app. pol. sci.* **1990**, 39, 2119-2128.
- [92] Heuts, Overbeek. Film Formation of Waterborne Coatings, Washington D.C. : ACS Sym-posium Series 648, 271, T. P. Provder, M. Winnik, M. Urban, ACS, **1996**.
- [93] Y Chevalier, M Hidalgo, J.-Y Cavallé, B Cabane. Small angle neutron scattering studies of composite latex film structure. *Prog. Org. coat.* **1997**, 32, 35-41.
- [94] S. Lepizzera, M. Scheer, C. Fond, T. Pith, M. Lambla, and J. Lang. Coalesced Core/Shell Latex Films under Elongation Imaged by Atomic Force Microscopy. *Macromolecules* **1997**, 30, 7953-795.
- [95] E. Limousin, N. Ballard, J. Asua. The influence of particle morphology on the structure and mechanical properties of films cast from hybrid latexes. *Prog. Org. coat.* **2019**, 129, 69-76.
- [96] K. EH. The elastic and thermo-elastic properties of composite media. *Proc. Phys. Soc. Sect. B.* **1956**, 69, 808.
- [97] Elvis Lopes Brito, Nicholas Ballard. Film formation of hard-core/soft-shell latex particles. *J. Pol. Sci.* **2022** , 1–12.
- [98] F. D. Santos, L. Leibler. Large deformation of films from soft-core/hard-shell hydrophobic lattices. *J. Polym. Sci. Part B:Polym. Phys* **2003**, 41, 224-233.
- [99] Kyle Price, Wenjun Wu, Kurt Wood, Stephanie Kong, Alon McCormick & Lorraine Francis. Stress development and film formation in multiphase composite latexes. *Journal of Coatings Technology and Research* **2014**, 11, 827-839.
- [100] B. Schuler, R. Baumstark, S. Kirsch, A. Pfau, M. Sandor and A. Zosel. Structure and properties of multiphase particles and their impact on the performance of architectural coatings. *Prog. Org. Coatings* **2000**, 40, 139–150.

-
- [101] Cao Tongyu, Xu Yongshen, Su Yuncheng, Long Fu, Li Xing, Hu Yuhong. Study of particle morphology in polymer emulsions and their minimum film formation temperatures. *J. Appl. Polym. Sci.* **1990**, 41, 1965-1972.
- [102] Christian Petersen, Carsten Heldmann, and Diethelm Johannsmann. Internal stresses during film formation of polymer latices. *Langmuir* **1999**, 15, 7745-7751.
- [103] Noushin Rajabalinia, Shaghayegh Hamzehlou, Evgeny Modin, Andrey Chuvilin, Jose R. Leiza, and José M. Asua. Coupling HAADF-STEM Tomography and Image Reconstruction for the Precise Characterization of Particle Morphology of Composite Polymer Latexes. *Macromolecules* **2019**, 52, 5298-5306.
- [104] Noushin Rajabalinia, Shaghayegh Hamzehlou, Jose R. Leiza, José M. Asua. Experimental validation of a mathematical model for the evolution of the particle morphology of waterborne polymer-polymer hybrids: Paving the way to the design and implementation of optimal polymerization strategies. *Chem. Eng. J.* **2019**, 363, 259-269.
- [105] M. Tirumkudulu and W. Russel. Role of Capillary Stresses in Film Formation. *Langmuir* **2004**, 20, 2947-2961.
- [106] H. N. Yow, I. Beristain, M. Goikoetxea, M. J. Barandiaran and A. F. Routh. Evolving Stresses in Latex Films as a Function of Temperature. *Langmuir* **2010**, 26, 6335-6342.
- [107] H. N. Yow, M. Goikoetxea, L. Goehring and A. F. Routh. Effect of Film Thickness and Particle Size on Cracking Stresses in Drying Latex Films. *J. Colloid Interface Sci.* **2010**, 352, 542-548.
- [108] W. F. Jaffe R. Diquarks and exotic spectroscopy. *Phys. Rev. Lett.* **2003**, 91, 232003.
- [109] Wai Peng Lee and Alexander F. Routh. Why do drying films crack?. *Langmuir* **2004**, 20, 9885-9888.
- [110] M. S. Tirumkudulu and W. B. Russel. Cracking in Drying Latex Films. *Langmuir* **2005**, 21, 4938-4948.
- [111] Weining Man and William B. Russel. Direct measurements of critical stresses and cracking in thin films of colloid dispersions. *Physical Review Letters* **2008**, 100, 198302.

- [112] Lucas Goehring, William J. Clegg, and Alexander F. Routh. Plasticity and fracture in drying colloidal films. *Physical review letters* **2013**, 110, 2024301.
- [113] Hanne M. van der Kooij, Gea T. van de Kerkhof and Joris Sprakel. A mechanistic view of drying suspension droplets. *Soft Matter* **2016**, 12, 2858-2867.
- [114] Rajarshi Sengupta and Mahesh S. Tirumkudulu. Dynamics of cracking in drying colloidal sheets. *Soft Matter* **2016**, 12, 3149-3155.
- [115] Monica Schneider, Johannes Maurath, Steffen B. Fischer, Moritz Weiß, Norbert Willenbacher, and Erin Koos. Suppressing crack formation in particulate systems by utilizing capillary forces. *ACS applied materials & interfaces* **2017**, 9, 11095-11105.
- [116] Natalie Birk-Braun, Kamran Yunus, Eric J. Rees, Wilhelm Schabel, and Alexander F. Routh. Generation of strength in a drying film: How fracture toughness depends on dispersion properties. *Physical Review E*. **2017**, 95, 022610.
- [117] Weipeng Meng, Mingchao Liu, Yixiang Gan, Ludovic Pauchard & C. Q. Chen. Cracking to curling transition in drying colloidal films. *The European Physical Journal E*. **2020**, 43, 1-9.
- [118] C. J. Martinez and J. Lewis. Shape Evolution and Stress Development during Latex–Silica Film Formation. *Langmuir* **2002**, 18, 4689–4698.
- [119] S. Lepizzera, C. Lhommeau, G. Dilger, T. Pith, M. Lambla. Film-forming ability and mechanical properties of coalesced latex blends. *J. Pol. Sci. B: Poly. Phy* **1997**, 35, 2093-2101.
- [120] Roberts, C.C., Francis, L.F. Drying and cracking of soft latex coatings. *J. Coat. Technol. Res.* **2013**, 10, 441-451.
- [121] K. B. Singh, L. R. Bhosale and M. S. Tirumkudulu. Cracking in Drying Colloidal Films of Flocculated Dispersions. *Langmuir* **2009**, 25, 4284-4287.
- [122] M. Ward. An Introduction to the Mechanical Properties of Solid Polymers. Chicester UK: John Wiley and Sons, Ltd., **2004**.
- [123] S. Timoshenko. Theory of Elasticity, 3rd Editio, New York: McGraw-Hill College, **1970**.

- [124] W.C. Young, Roark's Formulas for Stress And Strain, 7th Edition, New York : McGraw-Hill, **2002**.
- [125] A. A. Griffith. VI. The phenomena of rupture and flow in solids,” Philosophical transactions of the royal society of london. Series A, containing papers of a mathematical or physical character **1921**, 221, 163-198.
- [126] B. Cotterell. The past, present, and future of fracture mechanics. *Eng. Fract. Mech.* **2002**, 69, 533–553.
- [127] K. Kendall. The adhesion and surface energy of elastic solids. *J. Phys. D. Appl. Phys* **1971**, 4, 1186–1195.
- [128] Arijit Sarkar and Mahesh S. Tirumkudulu. Delamination of drying nanoparticle suspensions. *Soft Matter* **2011**, 7, 8816-8822.
- [129] Karnail B. Singh and Mahesh S. Tirumkudulu. Cracking in drying colloidal films. *Physical review letters* **2007**, 98, 218302.
- [130] William B. Russel, Ning Wu, and Weining Man. Generalized Hertzian model for the deformation and cracking of colloidal packings saturated with liquid. *Langmuir* **2008**, 24, 1721-1730.
- [131] A. F. Routh and W. B. Russel. A Process Model for Latex Film Formation: Limiting Regimes for Individual Driving Forces. *Langmuir* **1999**, 15, 7762-7773.
- [132] H. J. Xia ZC. Crack patterns in thin films. *J. Mech. and Phy. Sol.* **2000**, 48, 1107-1131.
- [133] Milan J. Patel, Venkata R. Gundabala, and Alexander F. Routh. Modeling Film Formation of Polymer-Clay Nanocomposite Particles. *Langmuir* **2010**, 26, 3962–3971.
- [134] M. A. Hayat. Principles and Techniques of Electron Microscopy: Biological Applications. vol. 3, London: Edward Arnold, **1981**.
- [135] Kevin M Scholsky, Robert M Fitch. Examination of small polystyrene latex particles using a negative staining technique. *J. Colloid Interface Sci.* **1985**, 104, 592.
- [136] A. Lee. Control of core-shell latex morphology. in *Polymer Latexes, Preparation, Characterization and Applications*, vol. 234, Washington DC, American Chemical Society, **1992**, 492.

- [137] P. A. Midgley, M. Weyland, J. Meurig Thomas and B. F. G. Johnson. Contrast Tomography: A Technique in Three-Dimensional Nanostructural Analysis Based on Rutherford Scattering. *Chem. Commun.* **2001**, 10, 907–908.
- [138] Z. Liu, T. Epicier, Y. Lefkir, G. Vitrant and N. Destouches. HAADF-STEM Characterization and Simulation of Nanoparticle Distributions in an Inhomogeneous Matrix. *J. Microsc.* **2017**, 266, 60–68.
- [139] J. C. Hindson, Z. Saghi, J.-C. Hernandez-Garrido, P. A. Midgley and N. C. Greenham. Morphological Study of Nanoparticle–Polymer Solar Cells Using High-Angle Annular Dark-Field Electron Tomography. *Nano Lett.* **2011**, 11, 904–909.
- [140] Didier Juhue and Jacques Lang. Effect of surfactant postadded to latex dispersion on film formation: a study by atomic force. *Langmuir* **1993**, 9, 792–796.
- [141] Françoise Sommer, Tran Minh Duc, Rosangela Pirri, Gilles Meunier, and Christian Quet. Surface morphology of poly(butyl acrylate)/poly(methyl methacrylate) core shell latex by atomic force microscopy. *Langmuir* **1995**, 11, 440–448.
- [142] Q. Zhong, D. Inniss, K. Kjoller, V.B. Elings. Fractured polymer silica fiber surface studied by tapping mode atomic-force microscopy. *Surf. Sci.* **1995**, 290, 688–692.
- [143] H. Magonov. Phase imaging and stiffness in tapping-mode atomic force microscopy. *Surf. Sci.* **1997**, 375, 385–391.
- [144] Feldman. Toward a force spectroscopy of polymer surfaces. *Langmuir* **1998**, 14, 372–378.
- [145] Yuyao Zhang, Xiaoying Zhu, Chiheng Chu, Xin Xiao & Baoliang Chen. Applications of atomic force microscopy-based imaging and force spectroscopy in assessing environmental interfacial processes. *Critical Reviews in Environmental Science and Technology* **2022**, 52, 2421–2452.
- [146] Do Ik Lee, Lynn C. Walker, Charles S. Kan. The thermal behaviors of latexes: wet latex glass transition temperatures. *Macromol. Symp.* **1997**, 118, 267–273.

-
- [147] M. Hourston. Modulated differential scanning calorimetry: 6. Thermal characterization of multicomponent polymers and interfaces. *Polymer* **1997**, 38, 1-7.
- [148] D. Song. Modulated differential scanning calorimetry: XI. A characterization method for interpenetrating polymer networks. *Thermochim. Acta* **1997**, 305, 335–346.
- [149] Douglas J. Hourston, Mo Song. Quantitative characterization of interfaces in rubber-rubber blends by means of modulated-temperature DSC. *J. Appl. Polym. Sci.* **2000**, 76, 1791-1798.
- [150] D.J. Hourston, H.X. Zhang, M. Song, M. Pollock, A. Hammiche. Modulated differential scanning calorimetry-VII: Interfacial macromolecular diffusion in core-shell latex particles. *Thermochim. Acta* **1997**, 294, 23-31.
- [151] N. D. Tembou, *Contribution a l'étude de l'interphase des latex coreshell par lat RMN du solide a haute resolution*, Mulhouse, France: Universite de Haute-Alsace, **1992**.
- [152] D. P. Jensen and W. Morgan. Particle Size as it Relates to the Minimum Film Formation Temperature of Latices. *J. Appl. Polym. Sci.*, vol. **1991**. 42, 2845–2849.
- [153] C. Zhonghua and Y. Fei. Coalescing Aid Influences on Acrylic Latexes Property and Film Formation Process. *Indian J. Mater. Sci.* **2016**, 1–8.
- [154] A. A. Tracton, *Coatings Technology Handbook*, Florida: Taylor & Francis, **2006**.
- [155] R. C. Chiu, T. J. Garino, M. J. Cima. Drying of Granular Ceramic Films: I, Effect of Processing Variables on Cracking Behavior. *Journal of the American Ceramic Society* **1993**, 76, 2257-2264.
- [156] S. Bohn, L. Pauchard, and Y. Couder. Hierarchical crack pattern as formed by successive domain divisions. *PHYSICAL REVIEW E* **2005**, 71.
- [157] M. Meincken and R. D. Sanderson. Determination of the influence of the polymer structure and particle size on the film formation process of polymers by atomic force microscopy. *Polymer* **2002**, 43, 4947-4955.

- [158] D. M. Fasano, S. J. Fitzwater, W. Lau and A. C. Sheppard. Diffusion of oligomers in latex systems - A route to low volatile organic compound (VOC) coatings. *Can. J. Chem.* **2010**, 88, 500–513
- [159] Z. Yang and D. Q. M. Craig. Monitoring film coalescence from aqueous polymeric dispersions using atomic force microscopy: surface topographic and nano-adhesion studies. *Asian J. Pharm. Sci.* **2018**, 15, 104–111.
- [160] E. Gonzalez, C. Tollan, A. Chuvilin, M. J. Barandiaran and M. Paulis. Determination of the Coalescence Temperature of Latexes by Environmental Scanning Electron Microscopy. *Appl. Mater. Interfaces* **2012**, 4, 4276–4282.
- [161] J. K. Oh, J. Yang, J. P. Tomba, J. Rademacher, R. Farwaha and M. A. Winnik- Molar Mass Effect on the Rate of Polymer Diffusion in Poly(vinyl acetate-co-butyl acrylate) Latex Films. *Macromolecules* **2003**, 36, 8836–8845.
- [162] E. M. Boczar, B. C. Dionne, Z. Fu, A. B. Kirk, P. M. Lesko and A. D. Koller. Spectroscopic Studies of Polymer Interdiffusion during Film Formation. *Macromolecules* **1993**, 26, 5772–5781.
- [163] M. Soleimani, S. Khan, D. Mendenhall, W. Lau and M. A. Winnik. Effect of molecular weight distribution on polymer diffusion during film formation of two-component high-/low-molecular weight latex particles. *Polymer* **2012**, 53, 2652–2663.
- [164] P. Pinenq and W. Toronto. Polymer Diffusion and Mechanical Properties of Films Prepared from Crosslinked Latex Particles. *J. Coatings Technol.* **2000**, 72, 45–61.
- [165] F. Tronc, W. Chen, M. A. Winnik, S. T. Eckersley, G. D. Rose, J. M. Weishuhn and D. M. Meunier. Epoxy-Functionalized, Low-Glass-Transition-Temperature Latex. II. Interdiffusion versus Crosslinking in the Presence of a Diamine. *J. Polym. Sci. Part A Polym. Chem.* **2002**, 40, 4098–4116.
- [166] H. Zhang and R. P. Wool. Concentration Profile for a Polymer-Polymer Interface. 1. Identical Chemical Composition and Molecular Weight. *Macromolecules* **1989**, 22, 3018–3021.

- [167] K. D. Kim and L. H. Sperling. Reptation Time, Temperature, and Cosurfactant Effects on the Molecular Interdiffusion Rate during Polystyrene Latex Film Formation. *Macromolecules* **1994**, 27, 6841–6850.
- [168] K. Hahn, G. Ley, H. Schuller and R. Oberthür. On particle coalescence in latex films. *Colloid Polym. Sci.* **1986**, 264, 1092–1096.
- [169] J. N. Yoo, L. H. Sperling, C. J. Glinka and A. Klein. Characterization of Film Formation from Polystyrene Latex Particles via SANS. 1. Moderate Molecular Weight. *Macromolecules* **1990**, 23, 3962–3967.
- [170] J. K. Oh, P. Tomba, X. Ye, R. Eley, J. Rademacher, R. Farwaha and M. A. Winnik. Film Formation and Polymer Diffusion in Poly(vinyl acetate-co-butyl acrylate) Latex Films. Temperature Dependence. *Macromolecules* **2003**, 36, 5804-5814.
- [171] P. R. Paxton. Adsorption of emulsifier on polystyrene and poly (methyl methacrylate) latex particles. *J. Colloid Interface Sci.* **1969**, 31, 19.
- [172] Jeffrey M. Stubbs, Yvon G. Durant, and Donald C. Sundberg. Competitive adsorption of sodium dodecyl sulfate on two polymer surfaces within latex blends. *Langmuir* **1999**, 15, 3250–3255.
- [173] Samuel H Maron, Max E Elder, I.N Ulevitch. Determination of surface area and particle size of synthetic latex by adsorption. I. Latices containing fatty acid soaps. *J. Colloid Sci.* **1945**, 9, 89.
- [174] M. Lluaro. NMR Techniques in emulsion polymer investigation. in *3rd International Symposium on Radical Copolymers in Dispersed Media*, Lyon: Groupe Francais des Polymeres, **1994**.
- [175] Masato Ishida , Junji Oshima , Kunio Yoshinaga , Fumitaka Horii. Structural analysis of core-shell type polymer particles composed of poly(butyl acrylate) and poly(methyl methacrylate) by high-resolution solid-state ¹³C NMR spectroscopy. *Polymer* **1999**, 40, 3323–3329.
- [176] K. Landfester, H.W. Spiess. Characterization of interphases in core-shell latexes by solid state NMR. *Chemie-Ingenier-Technik* **1997**, 69, 111–115.
- [177] S. Kirsch, K. Landfester, O. Shaffer, M.S. El-Aasser. Particle morphology of carboxylated poly(n-butyl acrylate)/poly(methyl

- methacrylate) composite latex particles investigated by TEM and NMR. *Acta Polym.* **1999**, 50, 347–362.
- [178] S Kirsch , A Pfau , J Stubbs , D Sundberg. Control of particle morphology and film structures of carboxylated poly (n butylacrylate)/ poly (methyl methacrylate) composite latex particles. *Colloids Surf.* **2001**, 183–185.
- [179] J. Feng, M. A. Winnik, R. R. Shivers and B. Clubb. Polymer Blend Latex Films: Morphology and Transparency. *Macromolecules* **1995**, 28, 7671–7682.
- [180] S. T. Eckersley and B. J. Helmer. Mechanistic Considerations of Particle Size Effects on Film Properties of Hard/Soft Latex Blends. *J. Coatings Technol.* **1997**, 69, p. 97–107.
- [181] A. Tzitzinou and J. L. Keddie. Film Formation of Latex Blends with Bimodal Particle Size Distributions: Consideration of Particle Deformability and Continuity of the Dispersed Phase. *Macromolecules* **2000**, 33, 2695–2708.
- [182] D. C. Sundberg, A. P. Casassa, J. Pantazopoulos and M. R. Muscato. Morphology Development of Polymeric Microparticles in Aqueous Dispersions. I. Thermodynamic Considerations. *J. Appl. Polym. Sci.* **1990**, 41, 1425–1442.
- [183] I. Hasanzadeh, A. R. Mahdavian and H. Salehi-mobarakeh. Particle size and shell composition as effective parameters on MFFT for acrylic core – shell particles prepared via seeded emulsion polymerization. *Prog. Org. Coatings* **2014**, 77, 1874–1882.
- [184] S. Ugur, A. Elaissari and Y. Holl. Film Formation From Polystyrene – Poly (butyl acrylate-co-methyl methacrylate) Latex Blends. *Polym. Compos.* **2006**, 27, 431–442.
- [185] J. Feng, E. Odrobina and M. A. Winnik. Effect of Hard Polymer Filler Particles on Polymer Diffusion in a Low-Tg Latex Film. *Macromolecules* **1998**, 31, 5290-5299.
- [186] D. Juhué and J. Lang. Film Formation from Dispersion of Core-Shell Latex Particles. *Macromolecules* **1995**, 28, 1306–1308.
- [187] D. Maugis, Contact, Adhesion and Rupture of Elastic Solids, New York: Springer, **1999**.

- [188] J. Frenkel. Viscous Flow of Crystalline Bodies Under the Action of Surface Tension. *J. J. Phys.* **1945**, 9, 385.
- [189] K. Johnson, K. Kendall and A. Roberts. Surface energy and the contact of elastic solids. *Proc. R. Soc. Lond. A* **1971**, 324, 301–331.
- [190] R. C. Chiu, T. J. Garino, M. J. Cima, Drying of Granular Ceramic Films: I, Effect of Processing Variables on Cracking Behavior,” *Journal of American Ceramic Society* **1993**, 76, 2257 - 2264.
- [191] M. J. C. Raymond C. Chiu. Drying of Granular Ceramic Films: II, Drying Stress and Saturation Uniformity. *Journal of American Ceramic Society* **1993**, 76, 2769-2777.
- [192] D. Perera and D. Van den Eynde. Considerations on a Cantilever (beam) Method for Measuring the Internal Stress in Organic Coatings. *J. Coatings Technol.* **1981**, 53, 39-44.
- [193] S. G. Croll. Internal stress in a solvent-cast thermoplastic coating. *Journal of Coatings Technology* **1978**, 50, 33-38.
- [194] S. G. Croll. The origin of residual internal stress in solvent-cast thermoplastic coatings. *Applied Polymer* **1979**, 23, 3, 847-858.
- [195] E. Santanach Carreras, F. Chabert, E. E. Dunstan and G. V. Franks. Avoiding “mud” Cracks During Drying of Thin Films from Aqueous Colloidal Suspensions. *J. Colloid Interface Sci.* **2007**, 313, 160–168.
- [196] M. Smith and J. Sharp. Effects of Substrate Constraint on Crack Pattern Formation in Thin Films of Colloidal Polystyrene Particles. *Langmuir* **2011**, 27, 8009-8017.
- [197] H. Lama, T. Gogoi, M. G. Basavaraj, L. Pauchard, and D. K. Satapathy. Synergy between the crack pattern and substrate elasticity in colloidal deposits. *Phys. Rev. E* **2021**, 103, 032602.
- [198] Lucas Goehring, William J. Clegg, and Alexander F. Routh, Wavy cracks in drying colloidal films. *Soft Matter* **2011**, 7, 7984–7987.
- [199] E. R. Dufresne, D. J. Stark, N. A. Greenblatt, J. X. Cheng, J. W. Hutchinson, L. Mahadevan, and D. A. Weitz. Dufresne, Dynamics of fracture in drying suspensions. *Langmuir* **2006**, 22, 7144-7147.
- [200] A. Urretabizkaia, J. R. Leiza and J. M. Asua. On-line terpolymer composition control in semicontinuous emulsion polymerization,” *AIChE J.* **1994**, 40, 1850–1864.

- [201] G. Tillet, B. Boutevin and B. Ameduri. Chemical Reactions of Polymer Crosslinking and Post-Crosslinking at Room and Medium Temperature. *Prog. Polym. Sci.* **2011**, 36, 191–217.
- [202] B. Voogt, H. Huinink, S. Erich, J. Scheerder, P. Venema, J. L. Keddie and O. C. Adan. Film Formation of High Tg Latex Using Hydroplasticization: Explanations from NMR Relaxometry. *Langmuir* **2019**, 35, 2418–2427.
- [203] H.-B. Kim and M. A. Winnik. Factors Affecting Interdiffusion Rates in Films Prepared from Latex Particles with a Surface Rich in Acid Groups and Their Salts. *Macromolecules* **1995**, 28, 2033–2041.
- [204] M. Ooka and H. Ozawa. Recent developments in crosslinking technology for coating resins. *Prog. Org. Coatings* **1994**, 23, 325–338.
- [205] Z.-T. Li and L.-Z. Wu, Hydrogen Bonded Supramolecular Structures, Beijing, China: Springer, **2015**.
- [206] A. Toussaint, M. de Wilde, F. Molenaar and J. Mulvihill. Calculation of Tg and MFFT depression due to added coalescing agents. *Prog. Org. Coatings* **1997**, 30, 179–184.
- [207] Y. Wang and M. A. Winnik. Effect of a Coalescing Aid on Polymer Diffusion in Latex Films. *Macromolecules* **1990**, 23, 4731–4732.
- [208] R. W. Hoffman. Stress Distributions and Thin Film Mechanical Properties. *Surf. Interface Anal.* **1981**, 3, 62–66.
- [209] H. Lei, J. Payne, A. V. McCormick, L. Francis, W. Gerberich and L. Scriven, “Stress Development in Drying Coatings. **2001**, 1000–1013.
- [210] S. W. Tsai. Structural Behavior of Composite Materials. *Philco Corp Newport Beach Ca Space and Re-Entry Systems*, **1964**.
- [211] Ye Xu, Guy K. German, Aaron F. Mertz and Eric R. Dufresne. Imaging stress and strain in the fracture of drying colloidal films. *Soft Matter* **2013**, 9, 3735–3740.
- [212] Alexander M. König, Tecla G. Weerakkody, Joseph L. Keddie, and Diethelm Johannsmann. Heterogeneous drying of colloidal polymer films: Dependence on added salt. *Langmuir* **2008**, 24, 7580–7589.
- [213] M. Winnik. Latex film formation. *Curr. Opin. Colloid Interface Sci.* **1997**, 2.

-
- [214] Mitchell A. Winnik and Jianrong Feng. Latex blends : an approach to zero VOC coatings. *JCT, J. Coat.* **1996**, 68, 39-50.
- [215] Z. Ugur, S. Sunay and P. Önder. Film Formation of Nano-Sized Hard Latex (PS) in Soft Polymer Matrix (PBA): An Excimer Study. *Polym. Compos.* **2010**, 1611–1619.
- [216] V. Lazarusa and L. Pauchard. From craquelures to spiral crack patterns: influence of layer thickness on the crack patterns induced by desiccation. *Soft Matter* **2011**, 7, 2552-2559.
- [217] M. Chekchaki & V. Lazarus. Mechanical stresses induced by evaporation in consolidated colloidal suspensions of hard particles. Poroelasticity theory versus experiments. *Transport in porous media* **2013**, 100, 143-157.
- [218] K J Wallenstein and W B Russel. The theory of delamination during drying of confined colloidal suspensions. *Journal of Physics: Condensed Matter* **2011**, 23, 194104.
- [219] A. Gromer, M. Nassar, F. Thalmann, P. Hébraud, and Y. Holl. Simulation of latex film formation using a cell model in real space: Vertical drying. *Langmuir* **2015**, 31, 10983-10994.
- [220] Ye Xu, Wilfried C. Engl, Elizabeth R. Jerison, Kevin J. Wallenstein, Callen Hyland, Larry A. Wilen, and Eric R. Dufresne. Imaging in-plane and normal stresses near an interface crack using traction force microscopy. *Proceedings of the National Academy of Sciences* **2010**, 107, 14964-14967.
- [221] S. G. Croll. Internal stress in a solvent-cast thermoplastic coating. Ottawa, Canada: Division of Building Research, National Research Council, **1978**.
- [222] S. G. Croll. The origin of residual internal stress in solvent-cast thermoplastic coatings. *Journal of Applied Polymer Science* **1979**, 23, 847-858
- [223] Oldroyd.. On the Formulation of Rheological Equations of State. *Proc. Roy. Soc. Lon. A, Math. Phy. Sci.* **1950**, 200, 523–541.

Chapter 2. Cracking in films cast from soft core/hard shell waterborne polymer dispersions

2.1. Abstract

Soft core-hard “shell” waterborne polymer dispersions are promising to achieve no-VOC mechanically strong coatings able to form films at low temperature. However, the resistance to deformation of the hard phase creates stresses that may lead to cracking of the coating, which is catastrophic for substrate protection. Cracking is what hinders the broad use of soft core-hard shell latexes for demanding applications that require thick coatings. This chapter reports on a study of the effect of the particle characteristics and drying conditions on stress generation and crack formation. The morphology of particles and films are characterized in detail. The range of conditions to form a crack-free mechanically strong low temperature film forming coating are determined. It is shown that the existing mathematical models for cracking are not able to explain the experimental data and reasons for the failure are discussed. A data-derived criterion for crack nucleation is proposed.

2.2. Experimental part

2.2.1. Materials

Technical grade monomers methyl methacrylate (MMA, Quimidroga), n-butyl acrylate (BA, Quimidroga) and styrene (S, BASF) were used without purification. Acrylic acid (AA, >99%, Sigma-Aldrich) and methacrylic acid (MAA, >99%, BASF) were used as received. Potassium persulfate (KPS, Fluka) was used as thermal initiator and Dowfax 2A1(>99%, alkylidiphenyloxide disulfonate, Dow Chemical Co.) as a surfactant. 2-ethylhexyl mercaptoacetate (EHTG, Alfa) was used as a chain transfer agent. 25% ammonia aqueous solution (NH₃) were also used as received. Hydroquinone was used to stop the polymerization reaction in the samples withdrawn from the reactor. Deionised water was used throughout the work.

2.2.2. Synthesis of two-phase particle latex

Several series of soft core-hard “shell” latexes were prepared. All of the latexes were synthesized by two-staged seeded semicontinuous emulsion polymerizations using Dowfax 2A1 as emulsifier and KPS as thermal initiator. The final solids content was 50 wt% for Series 1 and 2 and 45 wt% for Series 3-5. Details of the polymerizations are given in the Appendix I. In the first series (Runs 1-3 in Table 2.1), the core that accounted for 75 wt% of the final particle was a 60/40 (wt/wt) copolymer of BA and MMA. The “shell” was a 1/99 (wt/wt) copolymer of BA and MMA. The glass transition temperature (T_g) of the core was about -5°C and that of the “shell” was about 100 °C. In the second series (Runs 4-6 in Table 2.1) different amounts of acrylic acid (AA) were included in both core and “shell”. These two first series of experiments were used to investigate the effects of drying conditions, type of substrate and AA contents on film formation and cracking. Runs 7 and 8 have different fractions of hard “shell” (35% and 15%).

Table 2.1 Formulations used to synthesize soft core-hard “shell” latexes in Series 1 and 2.

run	seed		core		“shell”		surfactant (wbm)	dp (nm)	PDI
	BA/MMA/AA (wt/wt)	wt%	BA/MMA/AA (wt/wt)	wt%	BA/MMA/AA (wt/wt)	wt%			
1	60/40/0	10	60/40/0	75	1/99/0	25	0.1%	350	0.119
2	60/40/0	10	60/40/0	75	1/99/0	25	0.5%	250	0.094
3	60/40/0	10	60/40/0	75	1/99/0	25	1%	150	0.083
4	60/38/2	10	60/38/2	75	1/97/2	25	0.5%	254	0.084
5	60/37/3	10	60/37/3	75	1/96/3	25	0.5%	259	0.110
6	60/36/4	10	60/36/4	75	1/95/4	25	0.5%	265	0.092
7	60/40/0	10	60/40/0	65	1/99/0	35	0.5%	250	0.126
8	60/40/0	10	60/40/0	85	1/99/0	15	0.5%	250	0.081

With the information gathered in the first two series of experiments, a third series of latexes (Runs 9-17 in Table 2.2) was designed aiming at a broader range of particle sizes that also included smaller particles, which are more common in commercial coatings. The composition of the core was modified by substituting a fraction of the MMA by BA and styrene (S). Therefore, the core was more hydrophobic and slightly softer than in the first two series with T_g about -10°C . On the other hand, the “shell” was made slightly more hydrophilic removing the BA. This was expected to facilitate the formation of core-shell particles [1]. All these latexes contained AA.

Experiments 3-6 in Table 2.1 and 11, 18-21 in Table 2.2 were used to investigate the effect of the content and type of acidic monomer on cracking for particles of different size (250 nm and 90 nm). The effect on cracking of reducing the molar mass of the “shell” by adding a chain transfer agent (EHTG) was studied in Run 22.

In Runs 23-27 (Table 2.3) the fraction of the hard phase was varied maintaining constant the composition of the two phases. Finally, the effect of the T_g of the soft core on film formation and cracking was studied (Table 2.4)

Table 2.2 Formulations used in the third series of experiments.

run	seed		core		"shell"		Dowfax 2A1 (wbm)	dp (nm)	PDI
	BA/MMA/S/AA (wt/wt)	wt%	BA/MMA/S/AA (wt/wt)	wt%	MMA/AA (wt/wt)	wt%			
9	68/15/15/2	10	68/15/15/2	75	97/3	25	4%	55	0.032
10	68/15/15/2	5	68/15/15/2	75	97/3	25	2.89%	70	0.048
11	68/15/15/2	5	68/15/15/2	75	97/3	25	2%	90	0.038
12	68/15/15/2	3	68/15/15/2	75	97/3	25	1.5%	95	0.007
13	68/15/15/2	2	68/15/15/2	75	97/3	25	1.05%	110	0.024
14	68/15/15/2	2	68/15/15/2	75	97/3	25	0.6%	130	0.006
15	68/15/15/2	2	68/15/15/2	75	97/3	25	0.1%	150	0.009
16	68/15/15/2	2	68/15/15/2	75	97/3	25	0.05%	250	0.014
17	68/15/15/2	2	68/15/15/2	75	97/3	25	0.009%	350	0.027
18	68/16/16/0	5	68/16/16/0	75	100/0	25	2%	95	0.026
19	68/16/16/0	5	68/16/16/0	75	98/2	25	2%	94	0.017
20	68/15/15/2	5	68/14/15/3	75	97/3	25	2%	91	0.009
21	68/15/15/2	5	68/15/15/2	75	95/5MAA	25	2%	82	0.003
22	68/15/15/2	5	68/15/15/2	75	95/5MAA/1.5 EHTG	25	2%	83	0.008

Table 2.3 Formulations used in the fourth series of experiments.

run	seed		core		"shell"		Dowfax 2A1 (wbm)	dp (nm)	PDI
	BA/MMA/S/AA (wt/wt)	wt%	BA/MMA/S/AA (wt/wt)	wt%	MMA/AA (wt/wt)	wt%			
23	68/15/15/2	5	68/15/15/2	80	97/3	20	2%	91	0.016
24	68/15/15/2	5	68/15/15/2	77.5	97/3	22.5	2%	92	0.006
25	68/15/15/2	5	68/15/15/2	75	97/3	25	2%	90	0.008
26	68/15/15/2	5	68/15/15/2	72.5	97/3	27.5	2%	89	0.023
27	68/15/15/2	5	68/15/15/2	70	97/3	30	2%	85	0.017

Table 2. 4 Experiments with different T_g of the core polymer

run	seed		core		"shell"		Dowfax 2A1 (wbm)	dp (nm)	PDI
	BA/MMA/S/AA (wt/wt)	wt%	BA/MMA/S/AA (wt/wt)	wt%	MMA/AA (wt/wt)	wt%			
28	64/17/17/2	5	64/17/17/2	75	97/3	25	2%	85	0.026
29	72/13/13/2	5	72/13/13/2	75	97/3	25	2%	89	0.039

2.2.3. Characterization

2.2.3.1. Latex Characterization

In the following, we summarize the methods used to determine the different characteristics. Details are given in Appendix I. Solids contents and monomer conversion were determined gravimetrically. The residual monomers were measured by gas chromatography (GC). The particle size was determined using dynamic light scattering (DLS). Glass transition temperature (T_g) of the polymer was measured by differential scanning calorimetry (DSC) and dynamic mechanical thermal analysis (DMTA). Particle morphology was studied by atomic force microscopy (AFM) and transmission electron microscopy (TEM).

The mechanical properties of the films cast from the synthesized latexes were determined by tensile test measurements. The surface hardness was measured using the pendulum surface hardness test (3° König). The minimum film formation temperature (MFFT) was measured by drying the latexes on a temperature gradient bar. The reported values are the average of 2 repeated measurements. The critical cracking thickness (CCT) was determined visually in a special device (Figure I.2, Appendix I). The development of stress during film formation was determined by means of the beam-bending technique (Figure I.3, Appendix I).

2.3. Results and discussion

2.3.1. Particle morphology

Particle morphology could not be well characterized by TEM because the (meth)acrylic polymer forming the “shell” does not have enough contrast (Figure I.4, Appendix I). Therefore, particle morphology was determined using AFM. Figure 2.1 presents the particle morphology of Latexes 2 and 5. It can be seen that the hard phase (darker areas) formed patches on the surface of the polymer particles, namely they did not have an ideal core-shell morphology. The same morphology was obtained for other particle sizes (Figure I.5, Appendix I).

2.3.2. Effect of the drying conditions

Latex 2 was dried at different temperatures and relative humidity. Figure 2.2 presents the effect of the drying conditions on the formation of cracks for a dry film thickness of 170 μm on a glass substrate. It can be seen that at 55% relative humidity, a crack-free film could only be obtained at 50°C. Avoiding crack formation by increasing drying temperature is an expected result, as higher temperatures will allow an easier flow of the soft phase. The increase in temperature might also affect the fraction of the hard phase at the interphase between the hard and soft phases, where interpenetration is possible due to the chemical similarity of the polymers. However, both the DMTA and the DSC in (Figure I.6, Appendix I) show well defined peaks for each phase with little interpenetration.

The reason for the formation of a homogeneous film at 23°C and 90% relative humidity is the longer drying time (Figure I.7, Appendix I), which allows the deformation of the viscoelastic particles without an increase of the stress generated during film formation as can be seen in Figure 2.3.

This behavior is not predicted by the models developed considering elastic particles [2, 3], but has been experimentally observed for homogeneous particles [4, 5]. This highlights the importance of including the viscoelastic properties of the polymer particles in the modelling of crack formation from waterborne polymer coatings.

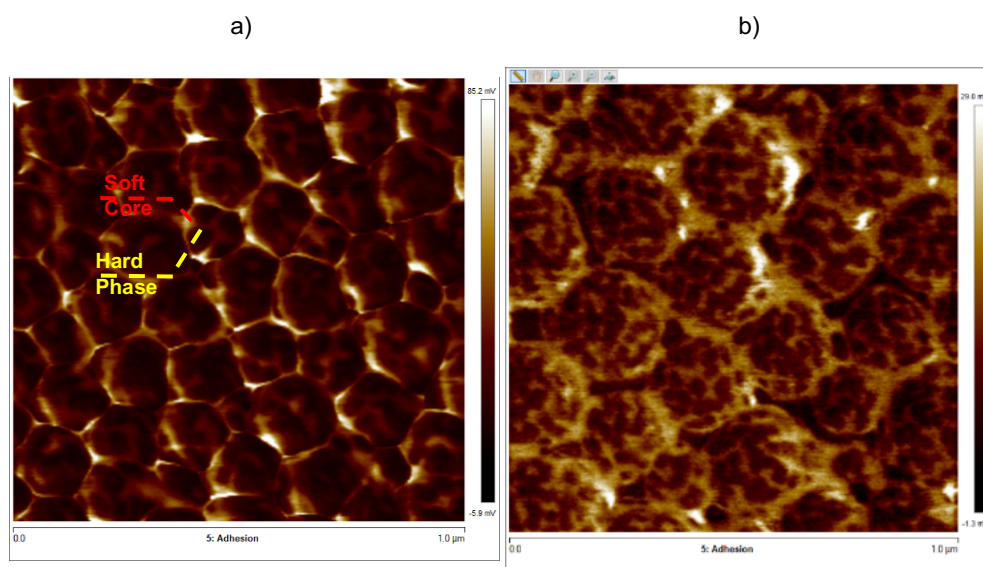


Figure 2.1 Morphology of the particles of Latex 2_0%AA (a) and latex 5_3%AA(b). The images are presenting the adhesion in peak force mode with image scan size of $1\mu\text{m} \times 1\mu\text{m}$. The dark zones are low adhesion zones (hard phase) while the bright zones are high adhesion zones (soft phase). AFM images were obtained using a Bruker Nanoscope V Dimension Icon in Peak Force tapping mode with a silicon nitride cantilever equipped with a rotated super sharp silicon tip. The nominal resonant frequency of the cantilever was 55 kHz and the spring constant was $0.25\text{ N}\cdot\text{m}^{-1}$.






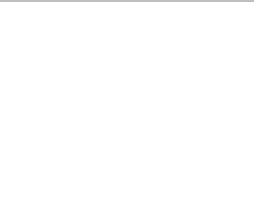

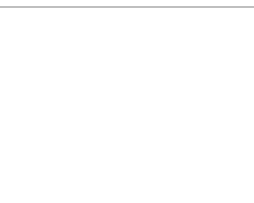
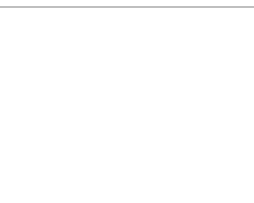
Temp. RH%	23°C	35°C	50°C
55%			
70%			
90%			

Figure 2.2 Effect of drying conditions (drying temperature and relative humidity (RH%) on the formation of cracks for Latex 2 ($d_p = 250\text{nm}$) on a glass substrate. Dry film thickness $170\ \mu\text{m}$. Red lines are added to the images for easy identification of the cracks.

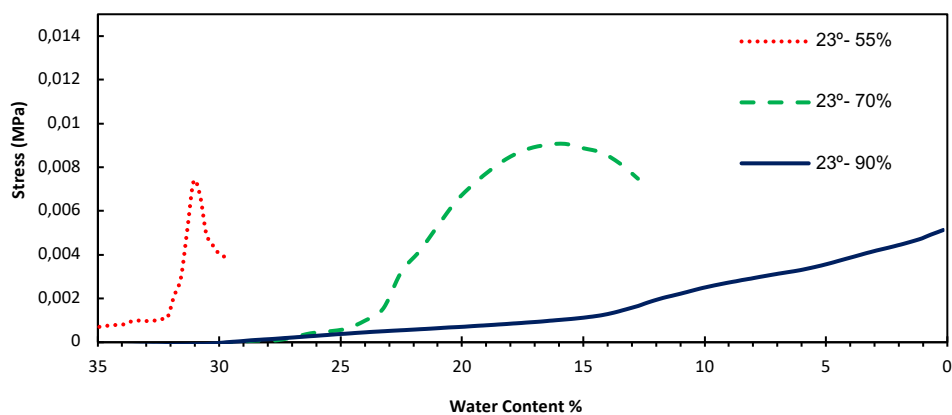


Figure 2.3 Effect of the drying conditions (relative humidity% 55%, 75% and 90%), 23°C on stress evolution during film formation of latex 2 (Table 2.2). Dry film thickness $170\ \mu\text{m}$.

2.3.3. Effect of the type of substrate

Crack formation is due to the tensions caused because of the film shrinkage due to water evaporation and particles deformation in addition to the bond to the substrate [6, 7]. Therefore, the type of substrate is likely to have an effect on cracking. Latex 2 was cast at 23°C and 55% relative humidity on different substrates (silicone (PDMS), glass, a 50/50 pMMA/pBA coating, and a pBA adhesive). Figure 2.4 shows that cracking increased as the substrate became stickier, namely as the strength of the attachment of the particles to the substrate increased. At first sight, it might be surprising that the softest substrate (pBA adhesive) gave the higher concentration of cracks instead of yielding to the stress generated by the shrinkage of the film. However, the modulus of pBA measured in a probe-tack test was 1.5 MPa, which was higher than the stress needed to create cracks.

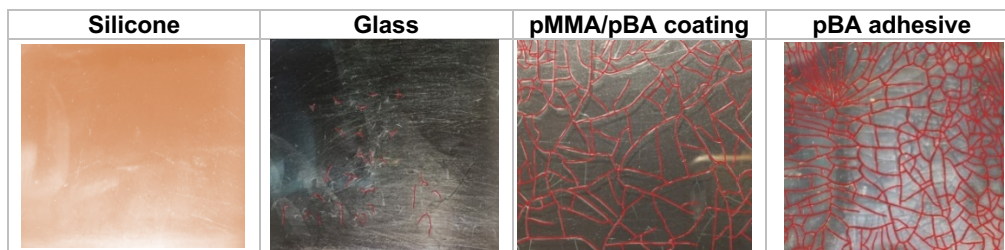


Figure 2.4 Effect of the type of substrate on crack formation during Latex 2 drying at 23°C and 55% RH. Dry film thickness = 100 µm. Red lines are included to facilitate the observation of the cracks.

2.3.4. Effect of the type and content of acidic monomer

The effect of the presence of acidic monomer in the formulation on MFFT and CCT was investigated using two particle sizes (250 and 90 nm). Figure 2.5 presents the results for the 250 nm latexes. It can be seen that up to 3% of AA, the MFFT decreased and the CCT increased with the AA content. For 4% AA, MFFT increased and CCT decreased. The incorporation of AA

in the formulation modifies the interfacial tensions of the system, which in turn might vary the particle morphology [1] Therefore, a possible reason for the effects observed in Figure 2.5 is a modification of the particle morphology. However, Figure I.8, Appendix I shows that particle morphology was not significantly varied by the incorporation of AA and that a soft core-hard "shell" morphology was still obtained. Therefore, the effects observed in Figure 2.5 were attributed to the combined effect of slower drying, hydroplasticization and the higher Tg of poly(acrylic acid).

The presence of AA slows down drying (Figure I.9, Appendix I), due to the hydrophilicity of the carboxylic group that form hydrogen bonds with water molecules, giving more time for deformation to the viscoelastic particles and therefore reducing the stress generated. This effect is somehow similar to effect of increasing the relative humidity (Figure I.7, Appendix I). In addition, hydroplasticization can play a role, which is reduction of the effective Tg of the polymer due to absorption of water that in this case is favored by the presence of AA moieties of the copolymer. The lower effective Tg facilitates deformation of the particles lowering the stress generated. These effects are reflected in the evolution of stress during drying measured by the cantilever (Figure 2.6). It can be seen that up to 3% of AA, the stresses appeared at longer times and that for the same water content, the stress decreased with the AA content. Latex 6 containing 4% of AA deviated from this behavior as for the same water content it gave higher stress than with 3% of AA. A possible reason is that the Tg of the outer part of the "shell" increased due to the high concentration of AA and this compensated the effects of hydroplasticization.

Cracking in films cast from soft core/hard shell waterborne polymer dispersions

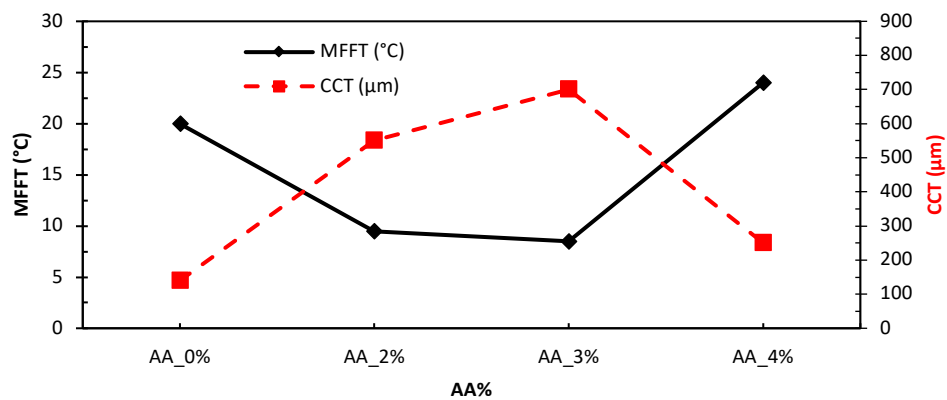


Figure 2.5 Effect of the AA content on MFFT and CCT for the 250 nm latexes (Runs 2, 4-6).

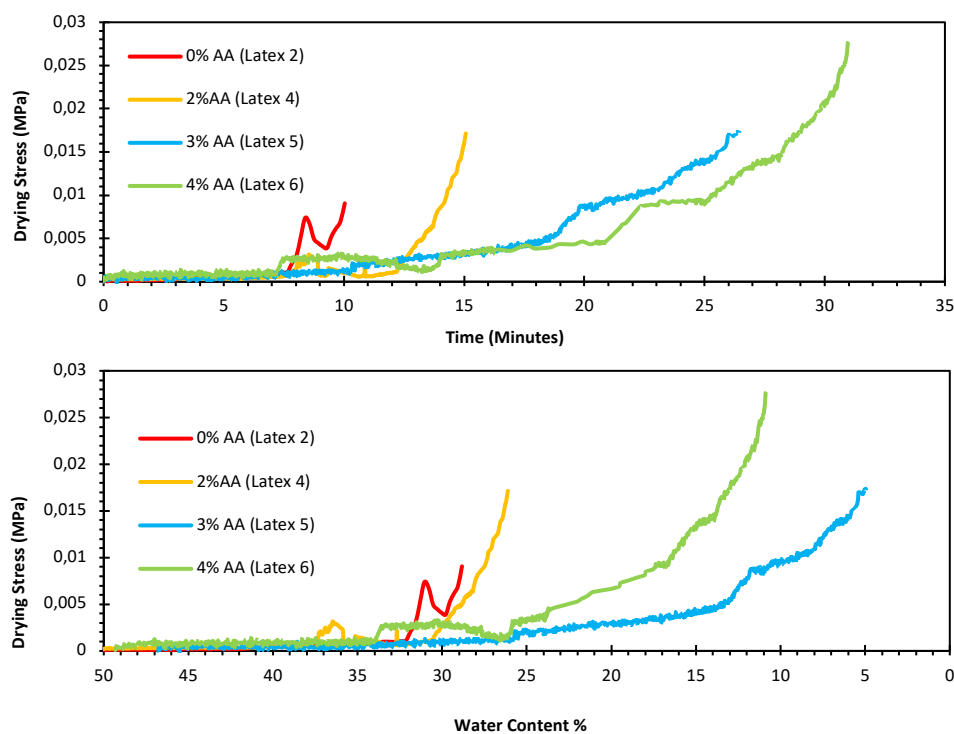


Figure 2.6 Effect of the AA content on the stress evolution as measured in the cantilever using latex 2, 4-6 for a layer 170 μm thick versus a) time and b) water content %.

Figure 2.7 presents the effect of the type and content of acidic monomer on MFFT and CCT for the 90 nm latex. It can be seen that, as in the case of the 250 nm latexes, MFFT decreased and CCT increased with AA contents up to 3%. As discussed above, this is due to the combined effect of hydroplasticization that reduces the effective T_g facilitating particle deformation and the longer drying time that allows more time for deformation. Both effects reduce the generated stress (Figure I.10, Appendix I). The models developed for elastic particles [2, 3] cannot predict this behaviour. On the other hand, the model developed by Russel et al. [8] included a viscous term that could account for the decrease of the effective T_g , but the effect of the drying time was not considered.

When 5% of MAA was used, CCT decreased. Figure I.11, Appendix I shows that T_g for the dry latex containing 5% of MAA was slightly higher, which might explain the lower CCT. However, T_g might be different during film formation due to hydroplasticization. The MFFT measured for Latex 21 (5% of MAA) was low, but it cannot be compared with Latex 20 because the lowest MFFT that can be measured with the equipment used was 5°C (for lower temperatures condensation introduces artefacts in the measurements). In order to shed some light on the effect of the acidic monomers, the cross-sections of the dry films were observed by AFM. Figure 2.8 presents the results for Latexes 11 (2% AA), 20 (3% AA), 21 (5% MAA) and 22 (1.5% EHTG). It can be seen that while Latex 11 presented a quite well-defined honeycomb structure, where the particles maintained their individuality, in Latex 20, a substantial breakage of the particles was observed. The reason for this behaviour might be the combined effect of the longer drying times and the hydroplasticization of the "shell". Latex 21 containing 5% MAA also showed some breakage of particles that might explain the low MFFT.

It is worth pointing out the positive effects of the AA content have consequences on the mechanical properties (Figure I.12, Table I.2, Appendix I). The increase of AA content on one part, lowers the Young's modulus, the stress at break and the surface hardness, and, it increases the elongation at break and the toughness.

In Latex 22, a chain transfer agent (EHTG) was used to reduce the molar mass of the polymer in the "shell". The result was a substantial increase of the CCT (CCT = 1000 μm) due to the easier deformation of the hard "shell", which resulted in a higher destruction of the hard walls in the honeycomb structure of the film (Figure 2.8d). However, the film had poor mechanical properties (Young's modulus = 0.59 MPa; Stress at break = 2.9 MPa; Elongation at break = 270 %; Toughness = 8.2 MPa).

Figure 2.9 presents the evolution of the stress for films of different thickness prepared with Latex 2. It can be seen that the stress generated with 150 μm film was low and no cracking occurred. On the other hand, the stresses generated in 250 μm and 350 μm thick films were higher and both of them cracked, but the cracking stress decreased with the film thickness.

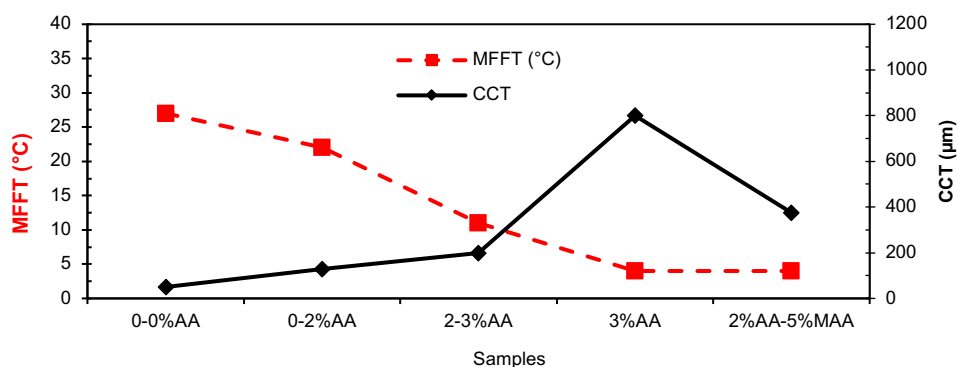


Figure 2.7 Effect of the acidic monomer content on the MFFT and CCT using Latexes 11 and 18-21. The coding has two numbers. They represent the fraction of acidic monomer in the core (first value) and in the "shell" (second number).

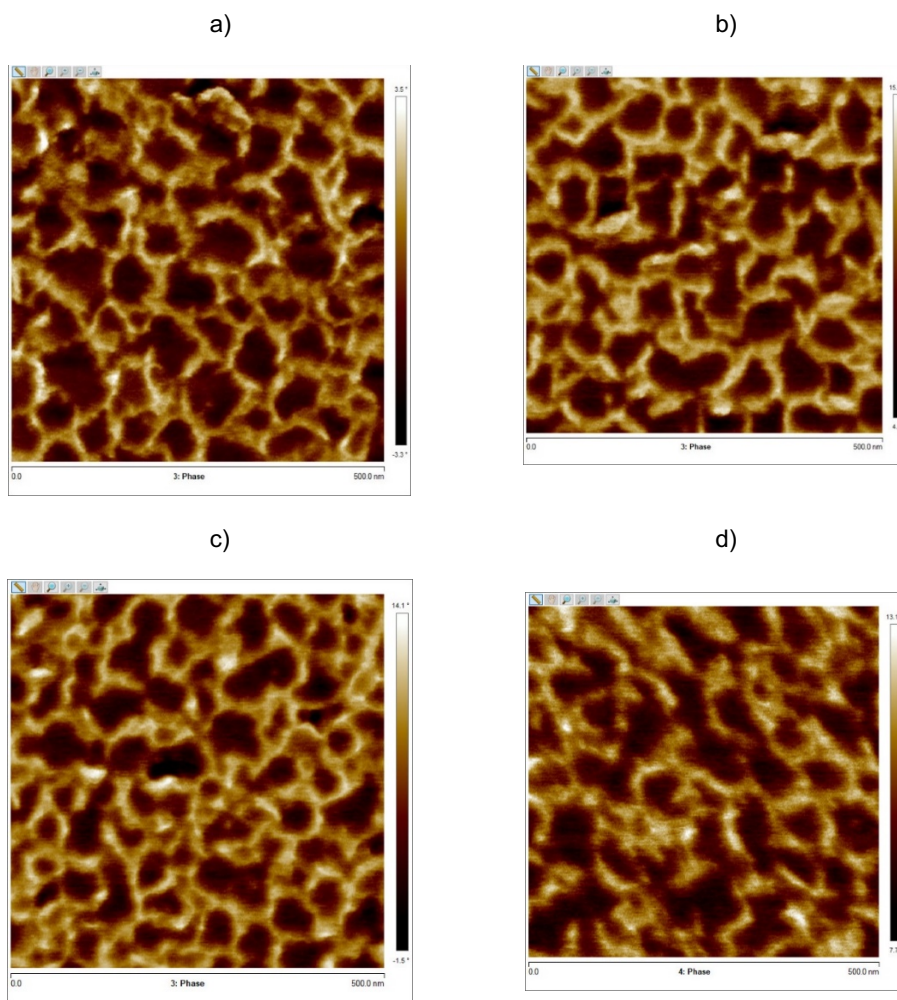


Figure 2.8 AFM Phase images with scan size 500nm × 500nm of the cross-sections of Latexes 9 (a), 2% AA), 20 (b), 3% AA), 21 (c), 5% MAA) and 22 (d), 1.5% EHTG). The AFM analysis was done in tapping mode on films cross section after drying the films at 23°C-55% RH. Then the samples were frozen at -80°C and cut using diamond knife. The bright regions represent the hard phase while the dark regions are the soft phase.

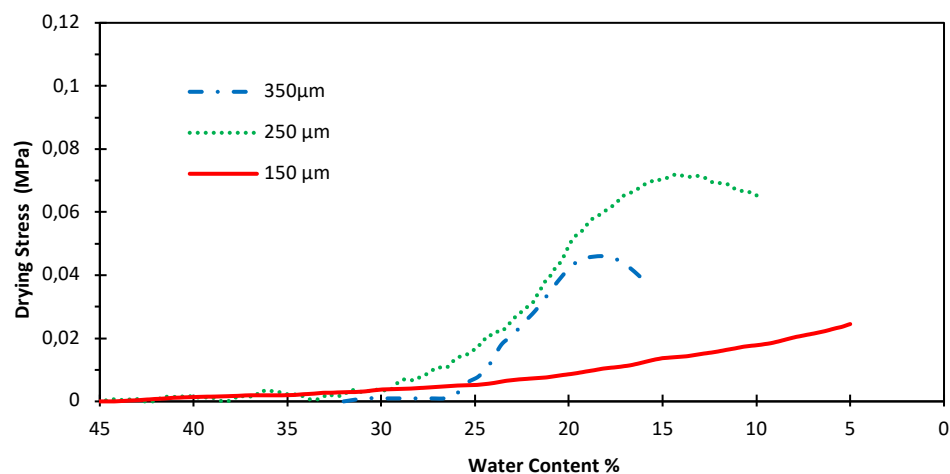


Figure 2.9 Effect of the thickness of the film on the development of stress for Latex 11. It can be seen that the water content at which the stress starts to appear increases with the thickness of the latex layer. A possible reason is that lateral drying creates areas of high solids content earlier in thinner coatings.

2.3.5. Effect of particle size

Figure 2.10-a presents the effect of particle size on MFFT and CCT for Latexes 9-17 containing AA in the formulation. Figure 2.10-b presents the effect of particle size on MFFT and CCT for latexes devoid of acidic monomers (Latexes 1-3). It can be seen that in both cases, CCT decreased with the particle size. This is surprising because the theoretical models predict either that CCT is independent of the particle size [2, 3] or that CCT increases with the particle size [1]. In order to shed some light on this issue, the evolution of the stress was determined by the beam-bending technique. Figure 2.11 shows that the stress generated increased as the particle size decreased, but the critical stress that the films could withstand decreased as particle size increased. This is in conflict with the model predictions [2, 3, 6]. In the beam bending experiments, cracking is detected by the decrease of the stress (formation of cracks release the stress in the film) The figure shows that both films with 250nm and 350nm had cracked, while the films with 150nm and 70nm had no cracks.

In addition to the positive effects on MFFT and CCT, the decrease in particle size led to mechanically stronger films (Figure I.13, Appendix I) that resulted from the better-defined and more closed honeycomb structure of the film (Figure 2.12). The strength at the yield point increased significantly with decreasing particle size from approximately 3 MPa to 9 MPa, but the toughness decreased correspondingly. The mechanical characteristics of the films changes from tough elastic to brittle. Figure 2.13 shows the effect of the particle size on the DMTA curves. When particle size decreased, the interpenetration between the hard and soft phases increased.

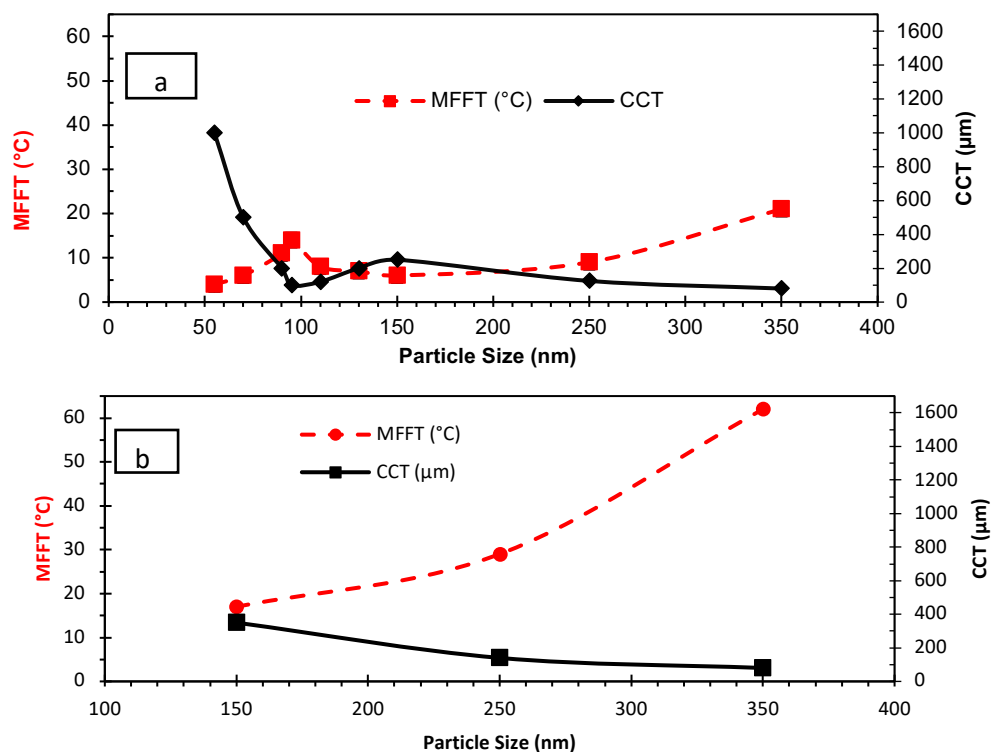


Figure 2.10 The effect of particle size on MFFT and CCT for latexes with AA (a) Latexes 9-17 and without acidic groups (b) Latexes 1-3. MFFT was measured twice obtaining the same value. No replicate experiments for CCT were performed

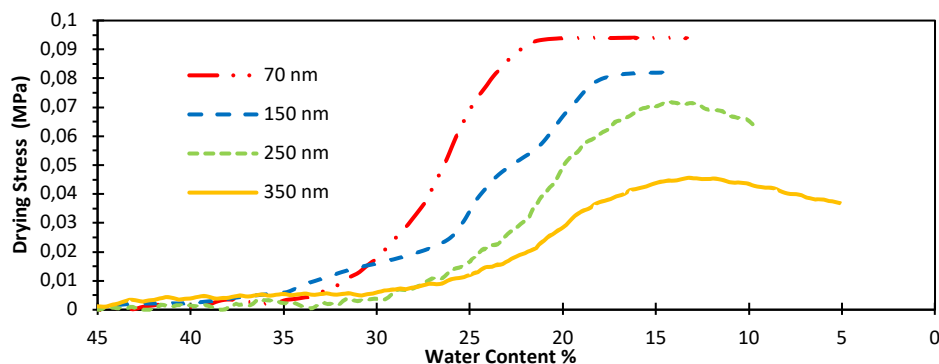


Figure 2.11 Effect of particle size on the stress development during film drying as measured by the beam-bending technique. Latexes 10, 15-17. Film dry thickness = 170 μm.

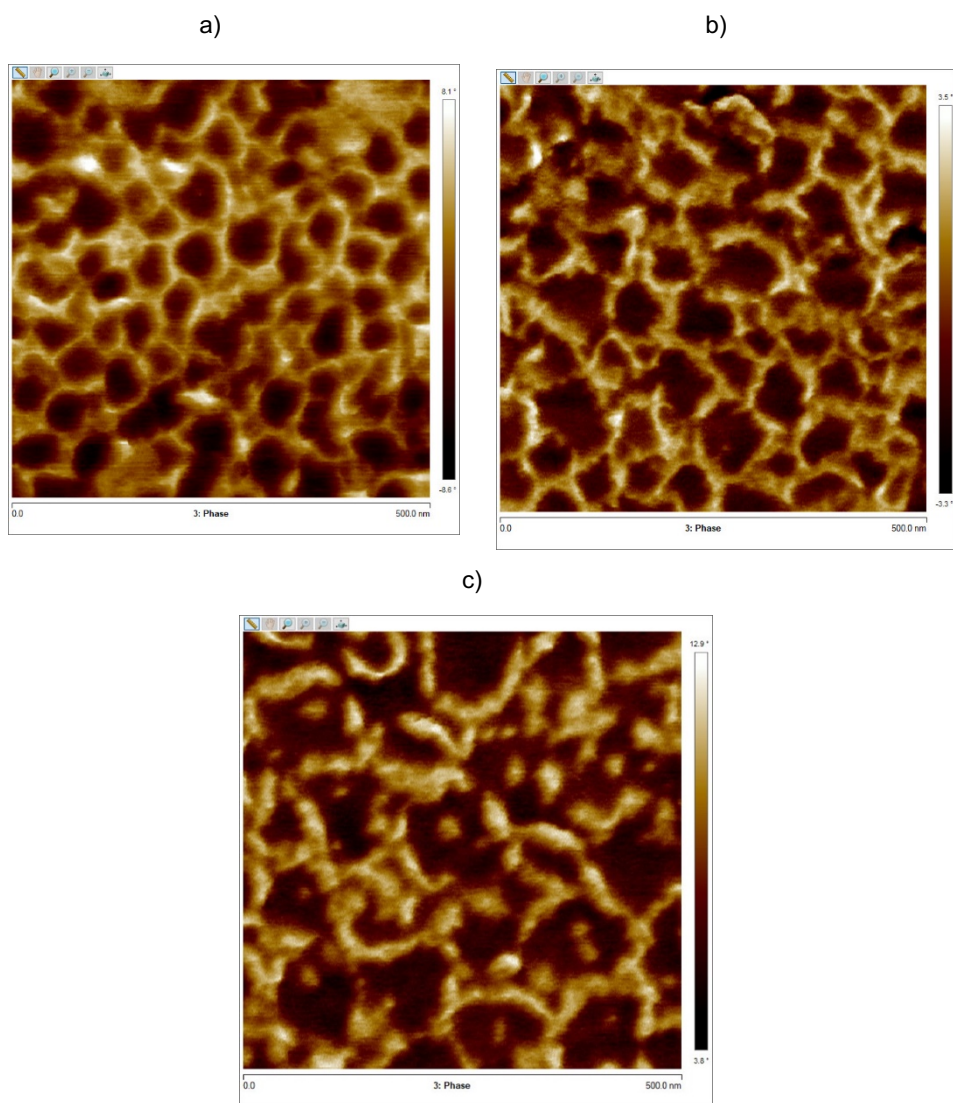


Figure 2.12 Effect of the particle diameter on the film morphology. a) 70 nm (Latex 10); b) 90 nm (Latex 11); c) 150 nm (Latex 15). The AFM analysis with scan size 500nm × 500nm was carried out in tapping mode on films cross section after drying the films at 23°C-55% RH. Then the samples were frozen at -80°C and cut using diamond knife. The bright regions represent the hard phase while the dark regions are the soft phase.

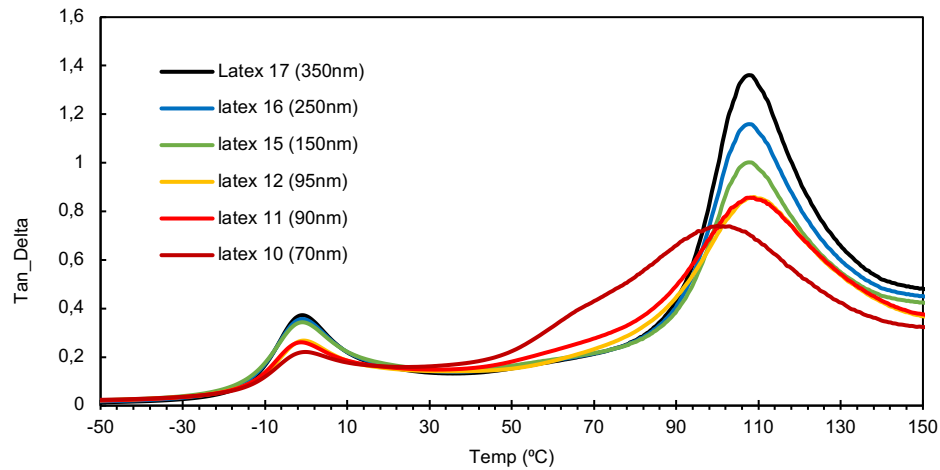


Figure 2.13 DMTA of latexes 10-12, 15-17 showing the effect of particle size.

2.3.6. Effect of the content of hard phase

Figure 2.14 shows the effect of the content of the hard phase on MFFT (determined with a 60 μm dry film) and CCT for Latexes 23-27 in Table 2.3. It can be seen that MFFT increased and CCT decreased as the content of the hard phase increased. The effect of the hard phase was reinforced by the fact that the interpenetration between soft and hard polymers decreased as the content of the hard phase increased (Figure 2.15). Figure 2.16 shows that the hard phase formed a honeycomb structure filled with the soft core and that the thickness of the walls increased with the content of hard phase. The honeycomb structure substantially increased the Young's modulus, the stress at break and the hardness of the film (Figure I.14 Table I.3, Appendix I).

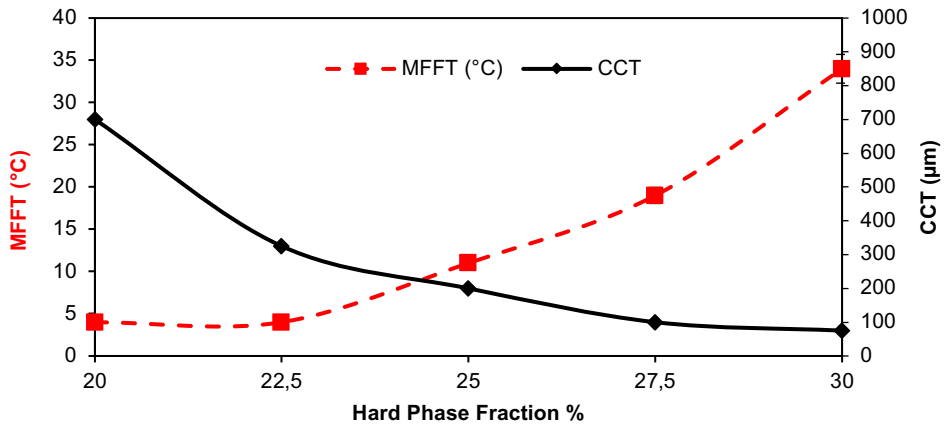


Figure 2.14 Effect of the hard phase content on MFFT and CCT for latexes in Table 2.3 (Latexes 23-27).

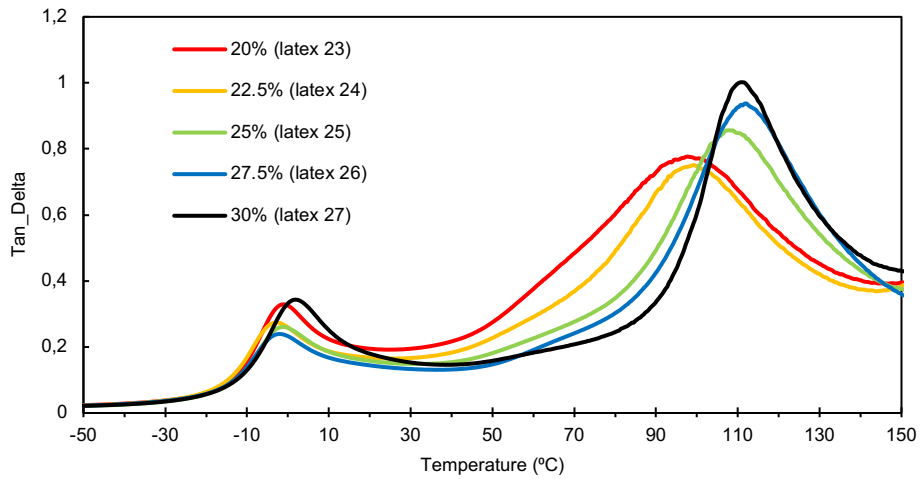


Figure 2.15 DMTA of latexes 23-27 showing the effect of hard phase fraction variation.

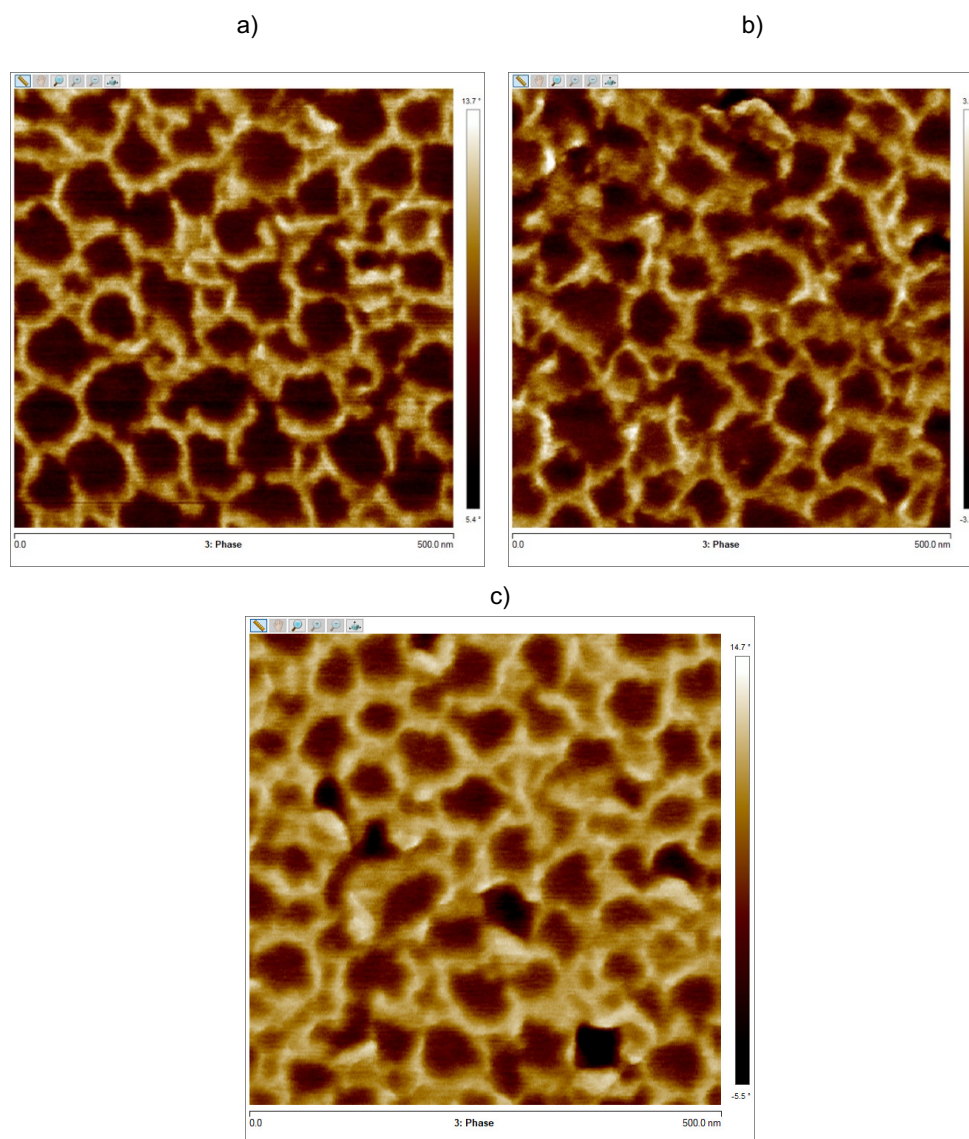


Figure 2.16 Phase images of cross section of films of latexes 23 (a), 11 (b) and 27 (c). Bright regions: Hard phase, Dark regions: Soft phase. The AFM analysis was done in tapping mode on film cross sections after drying the films at 23°C-55% RH. Then the samples were frozen at -80°C and cut using diamond knife.

2.3.7. Effect of the T_g of the soft phase

Soft core-hard “shell” latexes with different T_g s of the soft phase were synthesized (Latexes 28 ($T_g = -5^\circ\text{C}$), 11 ($T_g = -10^\circ\text{C}$) and 29 ($T_g = -5^\circ\text{C}$)). Figure 2.17 presents the effect of the T_g of the core on CCT and MFFT. It can be seen CCT increased and MFFT decreased as the T_g of the core decreased. The softer core slightly decreased the mechanical strength and hardness (Figure 2.18) and (Figure I.15 and Table I4, Appendix I). DMTA experiments carried out on the films of latexes with different T_g s of the soft phase are presented in Figure 2.19. The analysis shows the separation between the two peaks increased with decreasing the T_g of the soft phase. That could be because of the less compatibility between the two phases, which lead to more phase separation.

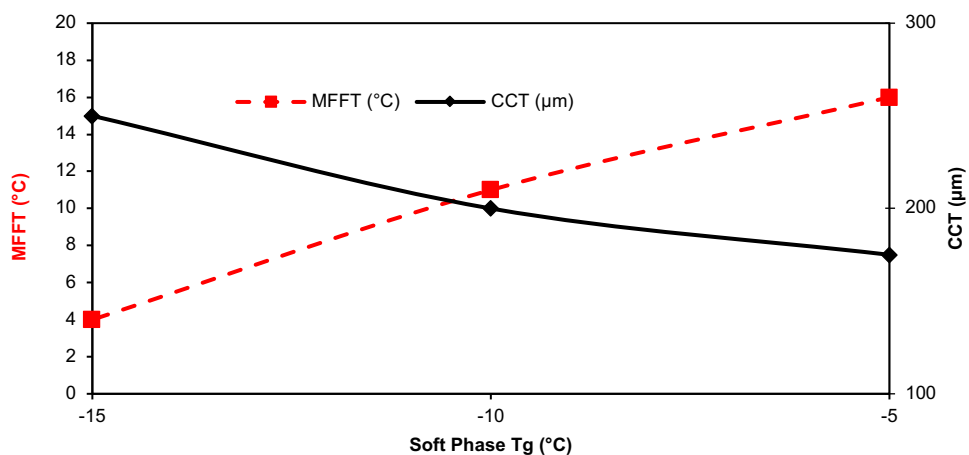


Figure 2.17 Effect of the T_g of the core on CCT and MFFT (Latexes 11, 28 and 29)

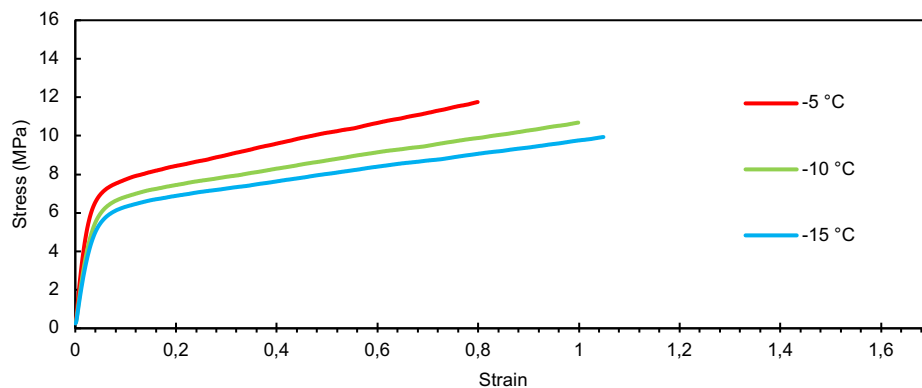


Figure 2.18 Tensile stress vs. strain curves for films cast from Latexes 11, 28 and 29 showing the effect of different hard core T_g .

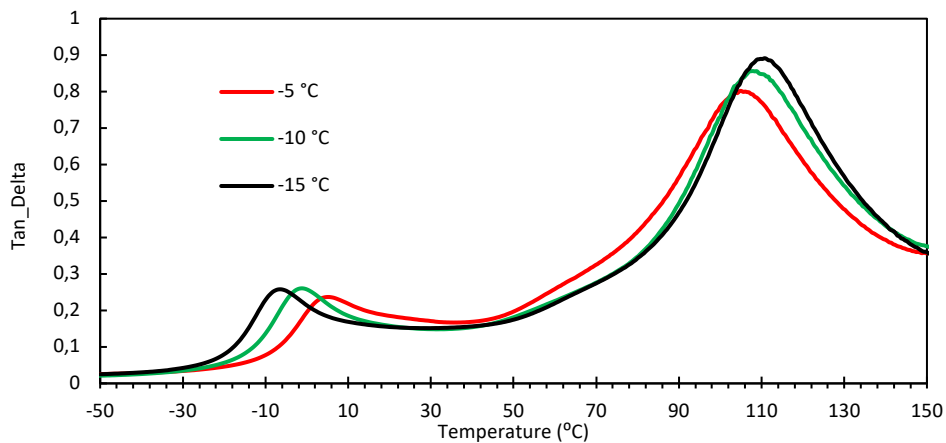


Figure 2.19 DMTA of latexes 28, 11 and 29 showing the effect of the T_g s of the soft phase.

2.3.8. Why current mathematical models for cracking fail to justify the experimental data?

In the preceding sections, it has been shown that the existing mathematical models [5, 3, 6] for crack nucleation during drying of colloidal dispersions do not describe the experimental findings presented in this work. The failure can be attributed to several reasons. The main reason is that the models were developed for homogeneous particles or glassy particles whereas in the present work composite, soft core-hard “shell” particles were used. It is worth to point out that a model for hard core-soft shell particles has been proposed [9], but it does not describe the current soft core-hard “shell” system. A second reason is that usually [2, 3] the models were developed for elastic particles. Even when a viscous term was initially considered [8], the final equations were given for elastic particles. A third reason is that the criterion used for crack formation is based on the Griffith’s criteria that crack nucleation occurs when the recovery of the elastic energy of the film equals the energy required to create the surface of the crack [9], which is associated to the thermodynamic work of adhesion. However, whereas this criterion could be valid for elastic materials if does not take into account the effect of the viscoelasticity on the real work of adhesion. The effect of the viscoelasticity on the work of adhesion is clearly shown in the case of adhesives. The thermodynamic work of adhesion is 2γ (J/m^2), where γ is the surface tension of the polymer in the film. Surface tensions of polymers range from about 0.02 (J/m^2) for fluorinated polymers to 0.05 (J/m^2) for polar polymers [10]. Therefore, the maximum thermodynamic work of adhesion is about 0.1 (J/m^2), which is much lower than the values reported for pressure sensitive adhesives (PSA). For example, Daniloska et al. reported 210 (J/m^2) for a waterborne PSA [11]. The difference is due to the energy spent in the deformation of the viscoelastic polymer during debonding. Therefore, Griffith’s criterion is not a valuable reference for estimation of the stress needed for cracking nucleation.

2.3.9. Criterion for cracking nucleation for the soft core-hard “shell” latexes using in this work

In order to predict the formation of cracks, the mathematical models need some information about the stress necessary for nucleation. As discussed above, the commonly used Griffith’s criterion is not suitable for viscoelastic particles. The goal of this section is to obtain a criterion for the soft core-hard “shell” dispersions used in this work. The beam-bending experiments provide the stress needed to create cracks under different situations, in particular with particles of different sizes and films of different thicknesses. Analysis of this data reveals that the formation of cracks occurred when the tension force per particle was about $3.5 \cdot 10^{-9}$ N (Table 2.5) independent of the particle size and the thickness of the film. The total tension force was calculated by multiplying the cracking stress by the film cross section area. The number of particles in cross section was estimated by dividing film cross section area over the cross sectional area of one particle. The force per particle was calculated by dividing the total tension force over the number of particles per film cross section.

Table 2.5 Force per particle at cracking

Run	Cracking stress (MPa)	Particle size (nm)	Film thickness (μm)	Film width (mm)	Number of particles in cross-section	Tension force per particle (N)
16	0.072	250	170	15	$5.19 \cdot 10^7$	$3.53 \cdot 10^{-9}$
17	0.042	350	170	15	$2.65 \cdot 10^7$	$3.91 \cdot 10^{-9}$
11	0.072	250	250	15	$7.64 \cdot 10^7$	$3.49 \cdot 10^{-9}$
11	0.046	250	350	15	10.710^7	$3.10 \cdot 10^{-9}$

2.4. Conclusions

This chapter explores a solvent-free route of overcoming the film formation dilemma (achieving at the same time film formation at low temperature and good mechanical properties of the film) in waterborne coatings by using soft core-hard “shell” polymer particles. Due to the presence of the hard polymer at the surface of the particles, these composite particles are prone to create cracks in the film, which are more frequent when thick coatings are needed for demanding applications. This work aims at shedding some light on cracking to be able to design soft core-hard “shell” latexes that yield VOC and crack free, mechanically strong coatings that can be cast at low temperatures.

The chapter reports on a study of the effect of the particle characteristics (size, soft/hard phase ratio, presence of carboxylic moieties, molar mass of the hard phase, glass transition temperature of the soft phase) and drying conditions (temperature, relative humidity, thickness of the film, type of substrate) on the stress generation, crack formation and mechanical properties of the films. A detailed characterization of the morphology of both particles and films was used to analyse these macroscopic results.

It was found that the particles consisted of a soft core that was covered with patches of hard polymer. The fact that the hard polymer did not form a continuous shell allowed deformation and coalescence of the particles that yielded mechanically strong films where the soft polymer filled a rather well-defined honeycomb structure of hard polymer.

Cracks can be formed during film formation due to the stress created as a consequence of volume shrinkage and the attachment of the particles to the rigid substrate. Any variable that favours the deformation of the viscoelastic particles decreases the probability of crack formation.

Thus, increasing the drying times by increasing the relative humidity or including acidic moieties in the polymer as well as reducing the T_g of the soft core, the molar mass of the hard phase and the effective T_g of the hard polymer by hydroplasticization resulted in smaller stresses and less cracking. On the other hand, cracking is favoured by increasing the hard phase content and the attachment of the particles to the substrate.

A particularly interesting finding was that CCT increased by decreasing the particle size even though the stress generated was higher for smaller particles. The reason was that the critical stress that the films could withstand increased as particle size decreased. On the other hand, the organization of the honeycomb structure of the hard polymer in the film improved as the particle size decreased, which translated in much higher mechanical strength and hardness, but also in increased brittleness. From a practical point of view, the correlations allow the design of solvent-free latexes able to form crack-free thick coatings of very good mechanical properties.

The experimental results were used to test the existing mathematical models finding that they could not justify the trends observed. Possible reasons for the failure are that the models do not consider the soft core-hard "shell" morphology, that they are mainly developed for elastic particles and the lack of a criterion for crack formation applicable to the present system. In this regard, it is worth to mention that in this work, using with particles of different sizes and films of different thickness, crack appeared when the tension force per particle was about $3.5 \cdot 10^{-9}$ N.

The results presented in this chapter highlight that careful design of soft core-hard "shell" polymer dispersions allows to overcome the film formation dilemma frequently found in waterborne coatings.

2.5. References

1. Gonzalez-Ortiz LJ, Asua JM. Development of particle morphology in emulsion polymerization. 1. Cluster dynamics. *Macromolecules* **1995**, 28, 3135-3145.
2. Tirumkudulu MS, Russel WB. Cracking in drying latex films. *Langmuir* **2005**, 21, 4938-48.
3. K.B. Singh, M.S. Tirumkudulu, Cracking in drying colloidal films, *Phys Rev. Let.* **2007**, 98, 218302.
4. P.R. Sperry, B.S. Snyder, M.L. O'Dowd, P.M. Lesko, Role of water in particle deformation and compactation in latex film formation. *Langmuir*, **1994**, 10, 2619-2628.
5. F. Fin, D.J. Meier, A study of latex film formation by atomic force microscopy 1. A comparison of wet and dry conditions, *Langmuir*, **1995**, 11, 2726-2753.
6. Tirumkudulu MS, Russel WB. Role of capillary stresses in film formation. *Langmuir* **2004**, 20, 2947-2961.
7. Yow HN, Beristain I, Goikoetxea M, Barandiaran MJ, Routh AF. Evolving stresses in latex films as a function of temperature. *Langmuir* **2010**, 26, 6335-6342.
8. W.B. Russel, N. Wu, W. Man Generalized Hertzian model for the deformation and cracking of colloidal packing saturated with liquid, *Langmuir* **2008**, 24, 1721-1730.
9. A.A. Griffith, The phenomena of rupture and flow in solids. *Philos. Trans. R. Soc. Lond. A* 1921, **221**, 163–198.
10. D.V. van Krevelen, K. Te Nijenhuis, *Properties of Polymers* 4th Ed. Elsevier, Amsterdam, **2008**, Ch.8.
11. Daniloska V, Carretero P, Tomovska R, Asua JM. High performance pressure sensitive adhesives by miniemulsion photopolymerization in a continuous tubular reactor. *Polymer* **2014**, 55, 5050-5056.

Chapter 3. Modelling cracking during film formation of soft core/hard shell latexes

3.1. Abstract

As discussed in Chapter 2, waterborne dispersions of hybrid polymer particles consisting of a soft core covered by patches of hard polymer (soft core-hard “shell”) are very promising to overcome the film formation paradox (formation of mechanically strong films at low temperature). However, the presence of a hard phase at the exterior of the particles creates stresses during film formation that often results in cracking of the films. Chapter 1 shows that due to the technological importance, mathematical modelling of cracking has been an active area of research. These models developed analytical expressions that predict cracking for homogeneous and hard core-soft shell dispersions. However, they could not justify the experimental results obtained with soft core-hard “shell” dispersions in Chapter 2. As the development of analytical equations for film formation from soft core-hard “shell” dispersions looks an insurmountable challenge, in this chapter, a different strategy was used and particle deformation and stress generation were calculated by numerically solving the Navier-Stokes equation. A good agreement between experimental results and model predictions was achieved.

3.2. Model description

The model considers an aqueous dispersion of soft core-hard “shell” particles. As the experimental results of Chapter 2 show that the stress starts developing when the particles become in contact upon water evaporation, a system of close packed particles with the interstices filled with water was considered as initial condition. To represent the experimental particle morphology presented in Chapter 2 (Figure 2.1) each particle contained a soft core with patches of hard polymer at the surface (illustrated in 2D in Figure 3.1). The volume fraction of the hard phase was 25%. As an average, 7 hard domains per particle were used. The average volume of the hard domains was 25% of the volume of the particle. A narrow size distribution was imposed and the domains were randomly distributed at the surface of the particles. In the model, the hard phase is embedded in the surface of the particle to maintain the spherical shape of the particles.

Particle deformation and stress generation were calculated by solving a modified Navier-Stokes equation. The modification was necessary to use the Navier-Stokes equation with viscoelastic polymers (in its classical form is only applicable to Newtonian fluids). The modification is presented in eq. 3.1 and consisted in the addition of the stress vector χ . In addition to continuity equation (the total volume of the particles is constant) for the whole system (3.2).

$$\rho \frac{\partial u}{\partial t} + \rho(u \cdot \nabla)u = \nabla \cdot [-\rho I + \chi] + F_g + F_{st} \quad (3.1)$$

$$\rho \nabla \cdot u = 0 \quad (3.2)$$

where, ρ is the density (kg/m^3), u is the flow velocity (m/s), t represents the time (s), F_g is the force per unit volume due to gravity, F_{st} is the force per unit volume due to interfacial tension

(N/m³), and χ is the extra stress tensor, which is defined as a sum of viscous and viscoelastic or elastic contribution,

$$\chi = 2\eta_s(T_0) S + P_e \quad (3.3)$$

$$S = \frac{1}{2}(\nabla u + (\nabla u)^T) \quad (3.4)$$

where, $\eta_s(T_0)$ is the dynamic viscosity of the polymer at room temperature (T_0), S is the strain-rate tensor and P_e is the viscoelastic stress tensor. To describe the flow of a fluid with a complex rheological behaviour, the symmetric stress tensor P_e is represented as a sum of the individual modes. The Oldroyd-B constitutive model was used for the viscoelastic flow. The Oldroyd-B model [1] can be derived from the kinetic theory representing the polymer molecules as a suspension of Hooken springs with Young's modulus (E) in a Newtonian fluid with dynamic viscosity η_s . This model can be regarded as an extension of the upper-convected Maxwell model [2]. The hyperbolic partial differential transport equation of Oldroyd-B is

$$\frac{1}{2\eta_s} P_e^2 + \frac{\tau}{2\mu\eta_s} P_e^\nabla = P_e S \quad (3.5)$$

where the first term represents the material derivative, which is the rate of change of the fluid momentum with time and the second term represents the deformation. P_e^∇ is the upper convective derivative operator defined as

$$P_e^\nabla = \frac{\partial P_e}{\partial t} + (u \cdot \nabla) P_e - [(\nabla u) P_e + P_e (\nabla u)^T] \quad (3.6)$$

In eq. 3.5, τ is a relaxation time, which is related with the viscosity and the Young's modulus (E) as

$$\tau = \frac{\eta_s}{E} \quad (3.7)$$

The interfacial force is

$$F_{st} = \gamma \kappa \delta \mathbf{n} + \delta \nabla_s \gamma \quad (3.8)$$

where, γ is the polymer/water or polymer/air interfacial tension (N/m), δ is a smoothing function, \mathbf{n} is the unit normal to the interface, $\kappa = -\nabla \cdot \mathbf{n}$ is the curvature and ∇_s is the surface gradient operator given by

$$\nabla_s = (I - \mathbf{nn}^T) \nabla \quad (3.9)$$

It was considered that the bottom layer of particles, which is in contact with the substrate is fixed and could not slip, namely that its velocity with respect the substrate was zero ($u = 0$). On the other hand, to simulate the open surrounding boundaries, the boundary normal stress was set equal to zero. This is done by vanishing any tangential stress exerted on the fluid boundary as shown in eq. 3.10.

$$\eta_s \frac{\partial u_t}{\partial n} = 0 \quad (3.10)$$

where, $\frac{\partial u_t}{\partial n}$ is the normal derivative of the tangential velocity field.

No heat balance was included because casting was carried out under isothermal conditions. The equations were solved by means of a finite element method using a software package platform (COMSOL Multiphysics version 5.6) based on the creeping two-phase flow level-set interface coupling with the electrostatic interface and deformed geometry modules. This

commercial software uses a finite element method, and hence the mesh represented in Figure 3.1 was build. During film formation, the driving forces for particle deformation were the interfacial tensions polymer/water (γ_{pw} , wet sintering), polymer/air (γ_{pa} , dry sintering) and air/water (γ_{pw} , capillary deformation). The resistance to deformation arises from the viscoelasticity of the polymer particles, which is characterized by the Young's modulus (E_{soft} , E_{hard}) and the relaxation times (τ_{soft} , τ_{hard}) of the soft and hard phases.

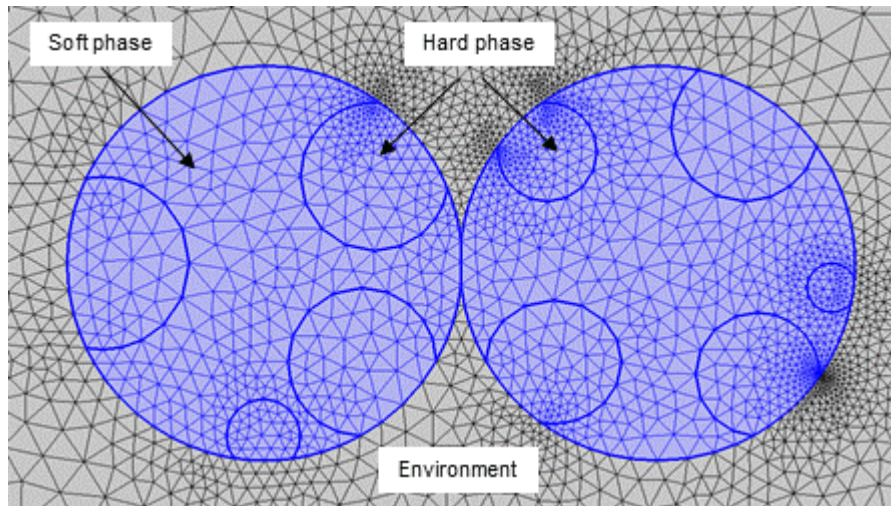


Figure 3.1 Mesh representing two polymer particles and the surrounding medium

Figure 3.2 illustrates the evolution of the deformation calculated for two multiphase particles submerged in water. The Young's moduli and relaxation times used were: hard phase Young's modulus $E_h = 6.8 \cdot 10^7$ Pa, soft phase Young's modulus $E_s = 5.9 \cdot 10^4$ Pa, hard phase relaxation time $\tau_h = 0.109$ s and soft phase relaxation time $\tau_s = 0.0082$ s. The particles were initially tangent to each other with an initial particle size 250 nm. The interfacial tension function was 7mN/m. The driving force for the deformation is the reduction of the surface energy. The

colours in the figure shows the distribution of the stress inside the particle during deformation. The red colour shows higher relative stress, while the blue one presents the lower relative stress. Figure 3.2 shows that the deformation stress varied inside the particles from negative stress close to the deformation zone to compressing stress away from the deformation zone. The black arrows represent the direction of the stress acting on the surface of the particle, hence the direction of the deformation. The black arrows have the same scale for all the images.

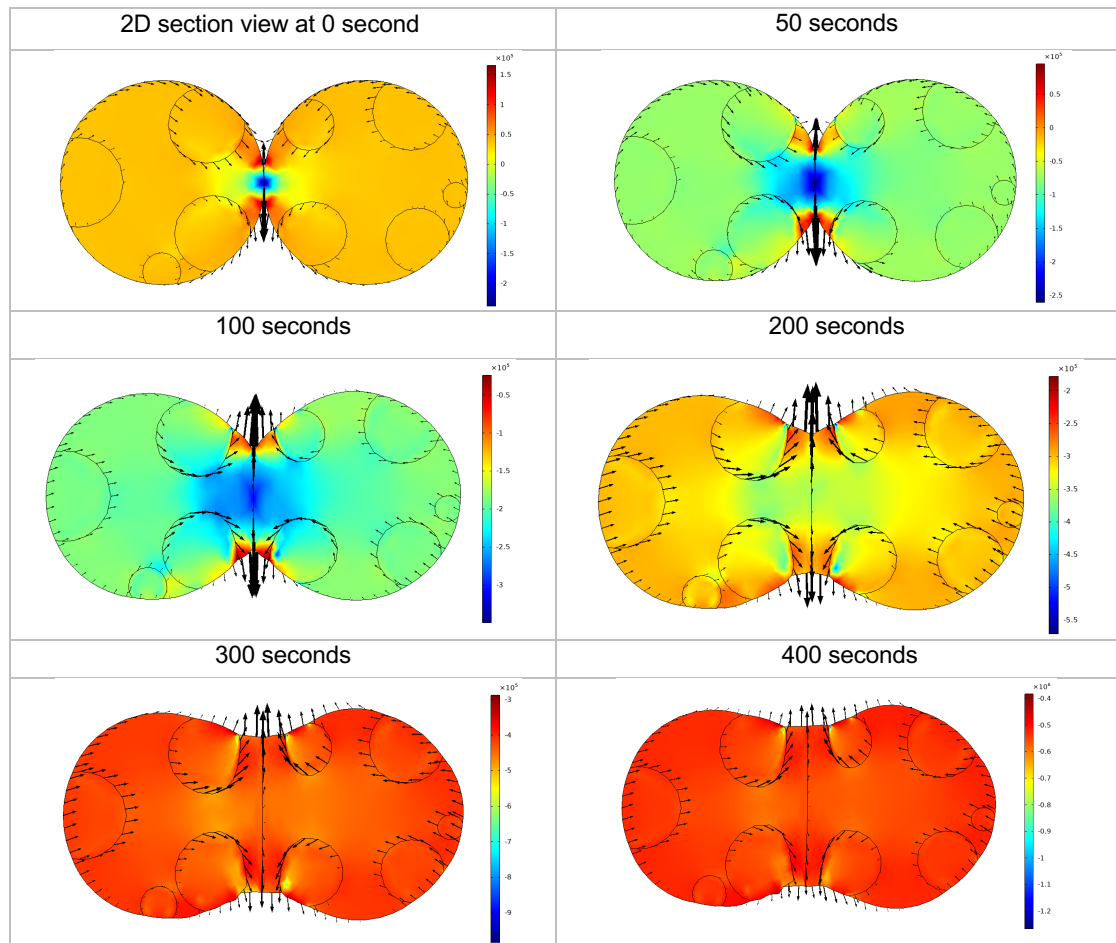


Figure 3.2 Evolution of the deformation of two multiphase particles

To simulate the stress generation during film formation in the beam bending experiments reported in Chapter 2, drying of a film should be considered. In these experiments, the rate of water evaporation was measured and this experimental information was used in the simulations. It has to be pointed out that even though drying of the film in the beam bending device was most likely non-uniform, the stress measured was an average value that was reported as a function of the water content, which also was an average value in the whole film. With these constraints, the model developed in this article considered that the film was uniform.

Figure 3.3 illustrates the effect of water evaporation on the implementation of the model. At time zero, the top layer of particles in the film was subjected to the Laplace pressure generated by the water menisci (capillary deformation) and the rest of layers underwent wet sintering (driven by the polymer/water interfacial tension). Later in the drying process, the level of water was determined by the volume of the gaps between particles (output of the simulation) and the amount of water that had not evaporated (experimental value). The layer of particles that was at the interface air-water suffered capillary deformation, the layers above suffered dry sintering (driven by the polymer/air surface tension) and the layers below underwent wet sintering. At any moment in the simulations, the level of water was determined by the volume of the gaps between particles (output of the simulation) and the amount of water that has not evaporated (experimental result presented in Chapter 2). It was considered that no water remained in the interstices of the particles in the dry zone.

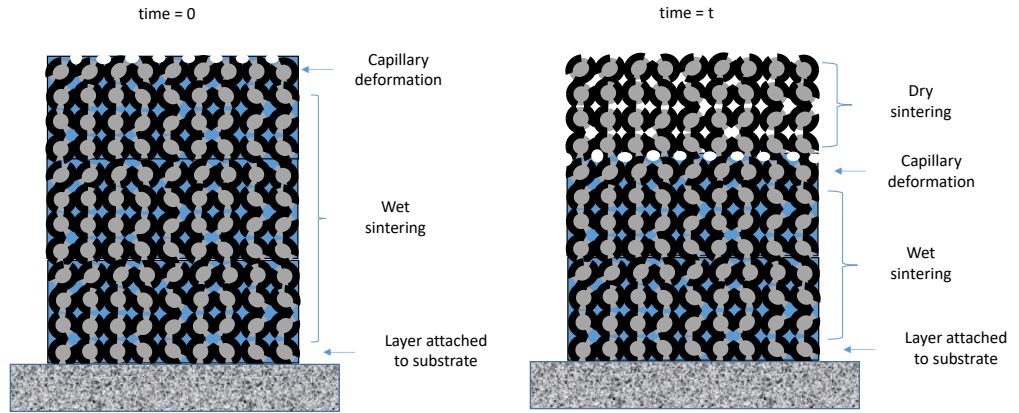


Figure 3.3 Drying stages in the model

The initial simulations revealed that the time needed to solve a real film was unaffordable. To illustrate this, enough is to say that a 20 mm long, 10 mm width and 0.17 mm thick film (typical dimensions of a film in the beam-bending experiments) has about $5 \cdot 10^{12}$ particles and that to simulate a film with 17000 particles, 228 computing hours using a high capability server (one node with 32 cores of 2.3 GHz processing speed with 128 GB Ram) were needed.

To overcome this problem and to be able to solve the model in a reasonable time with the available resources, a double strategy was implemented. First, the beam-bending device (Figure 3.4) was numerically scaled down, namely a smaller system that still provided meaningful results was simulated. The key point is that, at any time, the stress in the real and scaled down systems should be equal.

$$\sigma_{exp} = \sigma_{scaled\ down} \quad (3.11)$$

The stress in the cantilever is given by [2]

$$\sigma = \frac{E_s t^3 d}{3 c L^2 (t+c) (1 - \nu_s)} + \frac{d E_c (t+c)}{L^2 (1 - \nu_c)} \quad (3.12)$$

where, E_s and E_c are the Young's modulus of the substrate and coating, respectively, t is the substrate thickness, d is the cantilever deflection, c is the dried coating thickness, L is the cantilever free length and ν_s and ν_c are the Poisson's ratios of the substrate and film, respectively. In eq. 3.12, the second term of the right-hand side accounts for stress relief due to bending of the coating, but this term can be neglected because the Young's modulus of the coating is small relative to that of the substrate. Furthermore, we impose that the two systems should have the same bending (Figure 3.4), namely that

$$\left(\frac{d_1}{L_1}\right)_{exp} = \left(\frac{d_2}{L_2}\right)_{scaled\ down} \quad (3.13)$$

where the subscripts 1 and 2 refer to the regular and scaled down systems, respectively. Taking this into account, combination of eqs 3.11-3.13 leads to

$$\left(\frac{E_{s1}t_1^3}{c_1 L_1 (t_1+c_1) (1-\nu_{s1})}\right)_{exp} = \left(\frac{E_{s2}t_2^3}{c_2 L_2 (t_2+c_2) (1-\nu_{s2})}\right)_{scaled\ down} \quad (3.14)$$

Table 3.1 presents the values of the dimensions of the variables in eq. 3.14 for the real and scaled down systems. The substrate thickness t and the substrate Poisson's ratio ν_s were kept the same in the scaled down system as to the real system to limit the number of parameters. Even with this scaled downsize of the film, the number of particles for a 0.075 mm wide film is around 200,000,000 particles of 250 nm, far too big to perform the simulation in an acceptable time. Therefore, a second reduction was carried out by limiting the simulation of one slab of the scaled down film of a width equal to the diameter of a particle.

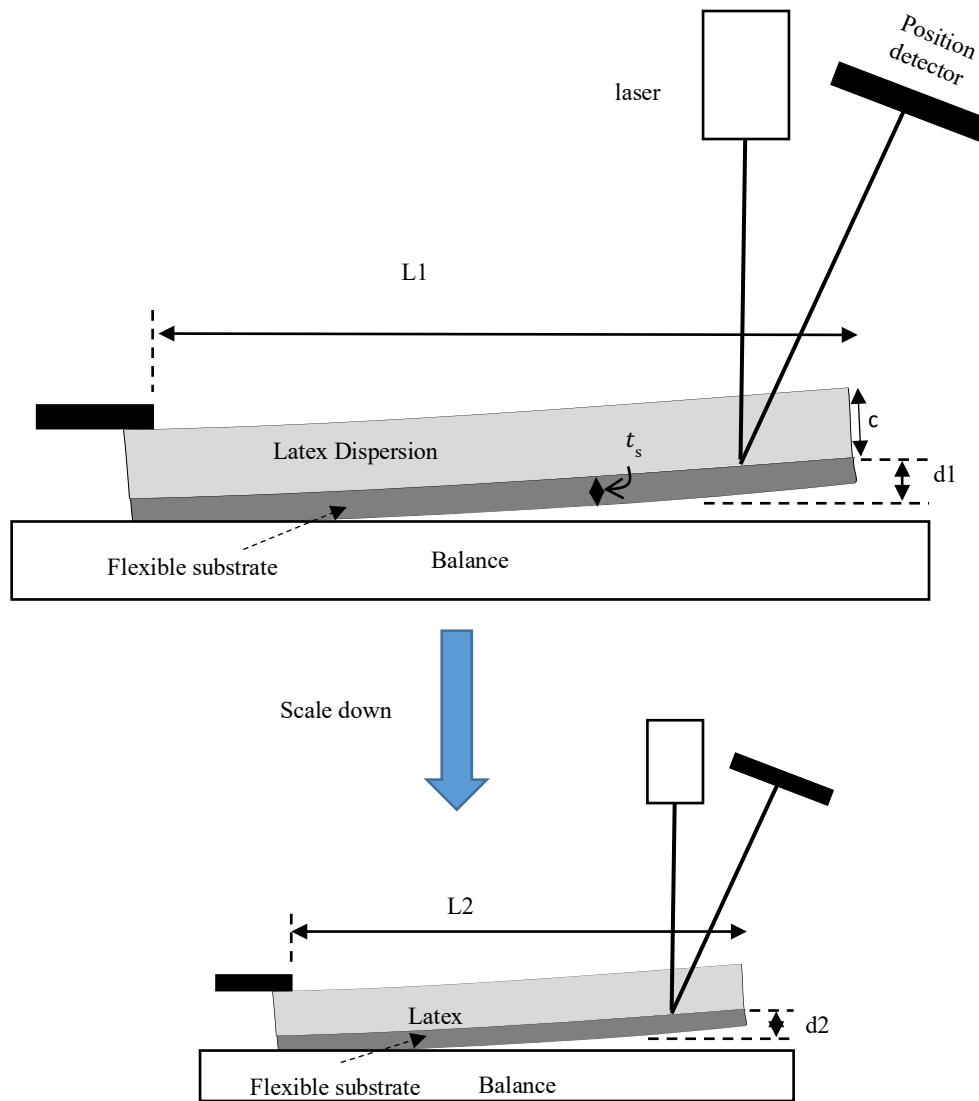


Figure 3.4 Numerical scale-down of the beam-bending experiment

Table 3.1 Real and scaled down systems.

Magnitude	Real system	Scaled down system
E_s	6.429 GPa	0.68 MPa
t	30 μm	30 μm
c	170 μm	11.5 μm
L	10 mm	0.075 mm
ν_s	0.4	0.4

3.3. Model validation

In order to validate the model, the results presented in Chapter 2 on the evolution of the stress generated during film formation from soft core-hard “shell” latexes were used. These data were obtained by means of the beam-bending technique in experiments where the drying conditions (temperature and relative humidity) and the characteristics of the soft core-hard “shell” latexes were varied. For the sake of clarity, the soft core-hard “shell” latexes from Chapter 2 used to validate the model are presented in Table 3.2.

Table 3.2 Latexes from Chapter 2 used for model validation in current chapter. To facilitate the identification of the Latexes, the same number as in Chapter 2 was used.

latex	seed		core		“shell”		dp (nm)
	BA/MMA/AA (wt/wt)	wt%	BA/MMA/AA (wt/wt)	wt%	BA/MMA/AA (wt/wt)	wt%	
2	60/40/0	10	60/40/0	65	1/99/0	25	250
4	60/38/2	10	60/38/2	65	1/97/2	25	254
5	60/37/3	10	60/37/3	65	1/96/3	25	259
6	60/36/4	10	60/36/4	65	1/95/4	25	265
10	68/15/15/2	5	68/15/15/2	70	97/3	25	70
11	68/15/15/2	5	68/15/15/2	70	97/3	25	90
15	68/15/15/2	2	68/15/15/2	73	97/3	25	150
16	68/15/15/2	2	68/15/15/2	73	97/3	25	250
17	68/15/15/2	2	68/15/15/2	73	97/3	25	350
18	68/16/16/0	5	68/16/16/0	70	100/0	25	95
20	68/14/15/3	5	68/14/15/3	70	97/3	25	91

3.3.1. Model parameters

The parameters of the model are summarized in Table 3.3. The interfacial force F_{st} depended on the surface tension of the polymer (γ_p) and the polymer-water interfacial tension ($\gamma_{p/w}$). The values of these parameters were determined experimentally as detailed in Appendix II. The model also needs the viscoelastic properties of the soft and hard polymers of the core-“shell” particles: Young’s moduli and relaxation times. The Young’s moduli of the dry soft and hard polymers devoid of acrylic acid were determined by AFM nanoindentation as detailed in Appendix II. These values were $E_s = 5 \cdot 10^5$ Pa and $E_h = 8.3 \cdot 10^7$ Pa for soft and hard polymers, respectively. It is worth pointing out that these values were obtained for dry polymers with no acrylic acid and that during film formation, the polymers are in the presence of water, namely affected by hydroplasticization, which is enhanced by the AA content. Therefore, the values of the Young’s moduli in the beam-bending experiments should be lower. Consequently, E_s and E_h were considered as estimable parameters of the model, whose maximum value was limited by those determined by AFM nanoindentation. The values of the Young’s moduli and the relaxation times were estimated by fitting the beam-bending experiments carried out with latexes of different particle sizes (Latexes 10-17). The model was also used to fit the data obtained by casting dispersions of the same size but different AA contents. This results in a different hydroplasticization that leads to different Young’s modulus and relaxation times for each AA content (Latexes 11, 18, 20 for a particle diameter of 90 nm; and Latexes 2, 4, 5 and 6 for a particle size of about 255 nm). The values of the Young’s modulus and relaxation times for Latex 11 that contained an intermediate content of AA (2wt% of AA in the soft core and a 3wt% of AA in the hard “shell”) were estimated using the experiments for variation of the particle size. On the other hand, the values of the Young’s moduli for particles devoid of AA were determined by AFM nanoindentation. The Young’s moduli for other AA contents were obtained by inter and

extrapolating from these values (Figure II.6 in Appendix II). On the other hand, the values of the relaxation times obtained for Latex 11 were used for all AA contents.

The critical force per particle for cracking (force needed to overcome the adhesive force between two particles) was determined in Chapter 2 from beam bending experiments in which the particle size (250 nm and 350 nm) and the thickness of the film (170, 250 and 350 μm) were varied. These experiments provide the stress at which the film cracked, which is the force per unit area needed for cracking. As both the particle size and the geometry (thickness and width) of the film were known, the force per particle at the cracking point was calculated (critical cracking force per particle). The latexes used in those experiments (11, 16 and 17 in Table 3.2) contained the same amount of acrylic acid (2 wt% of AA in the core that accounted for 75 wt% of the particle, and 3 wt% of AA in the “shell” that was 25 wt% of the particle, 2.25 wt% as average) and it was found that the critical cracking force per particle was independent of the particle size and the thickness of the film ($3.5 \cdot 10^{-9}$ N). However, when latexes containing different contents of AA are considered, it was found that the critical force per particle for cracking increased with the content of acrylic acid (Figure II.6, Appendix II). A possible reason for the increase of the critical cracking force with the content of acrylic acid is the contribution of the hydrogen bonding due to the carboxylic moieties to the adhesion between particles.

In the beam bending experiments, the time evolution of both the stress generated during drying and the water content of the film were determined. The experimental time evolution of the water content of the film was an input in the model. The data were presented as stress vs. water content in Chapter 2 and this is used in the current chapter to compare the experimental results with the model predictions.

Table 3.3 Parameter of the model

Parameter	Value	Source
γ_P	36.6 mN/m	Determined experimentally in Appendix II
$\gamma_{p/w}$	7.2 mN/m	Determined experimentally in Appendix II
γ_w	53.6 mN/m	Determined experimentally in Appendix II
E_s	$5.9 \cdot 10^4$ Pa	Estimated by fitting the beam-bending experiments with latexes containing an average of 2.25 wt% of AA.
E_h	$6.8 \cdot 10^7$ Pa	Estimated by fitting the beam-bending experiments with latexes containing an average of 2.25 wt% of AA.
τ_s	0.0082 s	Estimated by fitting the beam-bending experiments with latexes containing an average of 2.25 wt% of AA.
τ_h	0.109 s	Estimated by fitting the beam-bending experiments with latexes containing an average of 2.25 wt% of AA.
Force per particle for cracking	Force (N)= $10^{-9} AA^2 - 10^{-9} AA + 2 \cdot 10^{-10}$ (3.15)	Chapter 2 and Chapter 3

3.3.2. Model results

Figure 3.5 presents a comparison between the experimental data and the predictions of the mathematical model for the stress development during drying of soft core-hard “shell” latexes with different particle sizes (Latexes 10, 15-17). These latexes contained an average of 2.25 wt% of acrylic acid and the critical failure force was $F_{crit} = 3.5 \cdot 10^{-9}$ N as shown in Chapter 2. The parameters used are presented in Table 3.3, where E_s , E_h , τ_s and τ_h were estimated by fitting. The solids content of the latex was 45 wt% (55 wt% water) and no significant stress was detected until a water content of about 35-30 wt%. Therefore, the model was applied from this

point. It can be seen that the model agreed quite well with the experimental findings. In the beam bending experiments, cracking is detected by the decrease of the stress (formation of cracks release the stress in the film). In agreement with the experimental results, cracking was predicted for latexes with diameters of 250 and 350 nm. Cracking occurred at lower stress for the 350 nm latex than for the 250 nm one because the number of particles was smaller for the bigger latex and the critical cracking force was $F_{crit} = 3.5 \cdot 10^{-9}$ N per particle. On the other hand, no cracking was predicted for the 70 and 150 nm latexes (in these experiments, measurement was stopped once the plateau was reached). The reason was that the maximum tension between particles at the top layer were $4.23 \cdot 10^{-10}$ N and $1.34 \cdot 10^{-9}$ N for 70 nm and 150 nm, respectively, namely smaller than the critical cracking force for cracking. The results in Figure 3.5 also show that the stress per particle was greater for larger particles.

Figure 3.5 shows that in agreement with the experimental results, the model predicts that the larger the particle size the easier the formation of cracks. This implies that unlike the previous models for cracking [3-5], the present model predicts that, for these viscoelastic soft core-hard "shell" particles, the critical cracking thickness (CCT) decreases with the particle size. Most likely, this will apply to any viscoelastic particle.

Figure 3.6 presents the structure of the film predicted by the model just before cracking and at two stages of the cracking for Latex 16. It can be seen that when the force generated by the stress reached the critical force for cracking, cracks nucleated in the upper layer(s) of the film, where the stress is maximum. This resulted in a relaxation of the stress, but as the thickness of the undamaged film decreased, the force per particle was still high, and cracking propagated.

Figure 3.5a shows that the model overestimated the stress generated for the 70 nm latex. A possible reason is that as shown in Figure 2.13 in Chapter 2, when particle size decreased, the interpenetration between the hard and soft phases increased leading to a softening of the

hard phase. This effect was not accounted for in the simulations, where the same Young's modulus of the hard phase ($E_h = 6.80 \cdot 10^7$ Pa) was used for all the particle sizes.

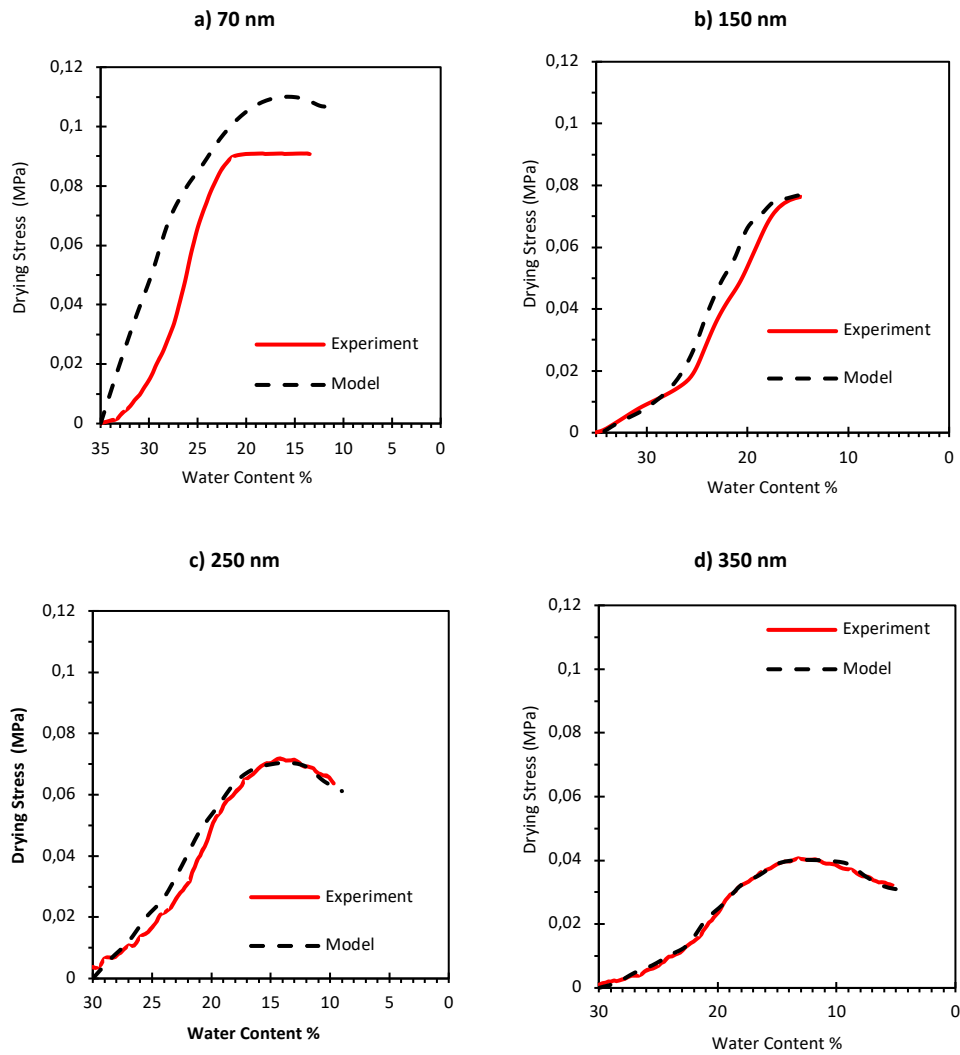


Figure 3.5 Effect of the particle size on the evolution of the stress. Latexes 10, 15-17. Drying conditions: $T = 23$ °C, $RH = 55\%$. Film dry thickness $250\mu\text{m}$. Particle diameters: a) 70 nm; b) 150 nm; c) 250 nm; d) 350 nm.

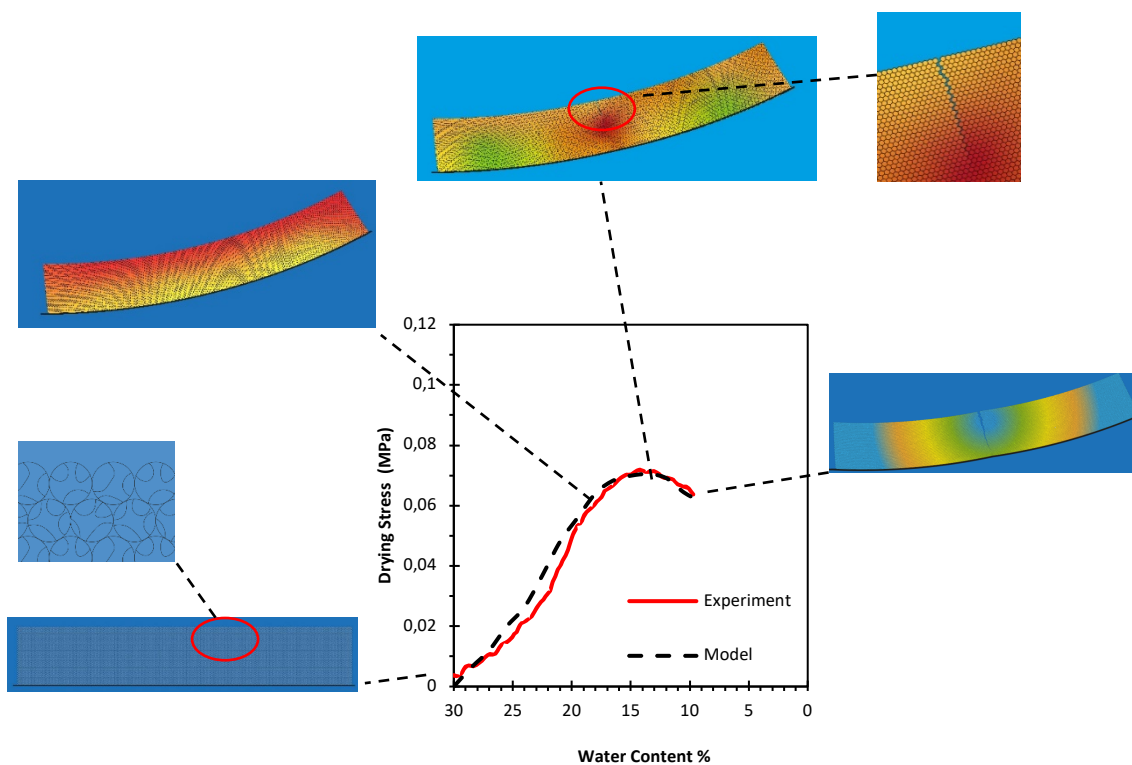


Figure 3.6 Details of stress development and cracking formation in the simulations during drying of Latex 16 ($d_p = 250$ nm) at 23 °C and 55% RH. The color represents the stress in the film. the more red color represents higher tension and the more blue represents lower tension.

Due to computer time limitations, the simulations presented in Figures 3.5 and 3.6 were carried out using a single particle slab and it may be argued that this ignores the effect of the neighbouring slabs. In order to check this effect, a system formed by three slabs was simulated and the stress generated in the middle one was calculated. This simulation was done on a supercomputing server (12 nodes with 32 cores each of 3.6 GHz processing speed with 256 GB

Ram). Figure II.1 shows that the predictions with one and three slabs coincide quite well. Therefore, it was considered that simulation of a single slab was representative enough.

Figure 3.7 presents the comparison of the experimental data and model predictions for the effect of the relative humidity on the stress development during drying of a film cast from Latex 16. The higher the relative humidity, the lower the stress generated because the drying time is longer, giving more time for the particles to deform. It can be seen that the model represented well the evolution of the stress for different relative humidities. For 55% RH, the model predicts cracking as discussed in Figure 3.6. However, for 70% and 90%, the model did not predict cracking. According to the model, for 70% RH, the slight decrease of the stress at water contents less than 15% was due to the stress relaxation of the particles. The difference with respect to 55%RH is that the drying rate decreased when the relative humidity increased giving more time for the particles to deform. It is noteworthy that these data do not match with the macroscopic images reported in Figure 2.2 (Chapter 2) that clearly showed that a film of the same thickness suffered cracking under the same drying conditions (23°C, 70%RH). This could be because of the change of the substrate. The substrate used in Chapter 2 was a rigid glass, whereas here the substrate is a flexible cantilever, which is free to bend, This bending relieves some of the drying shrinkage stress in the layer which allowed formation of a good film at the same conditions. At RH 90%, the model predicted a very low stress and the formation of a sound film with no cracks.

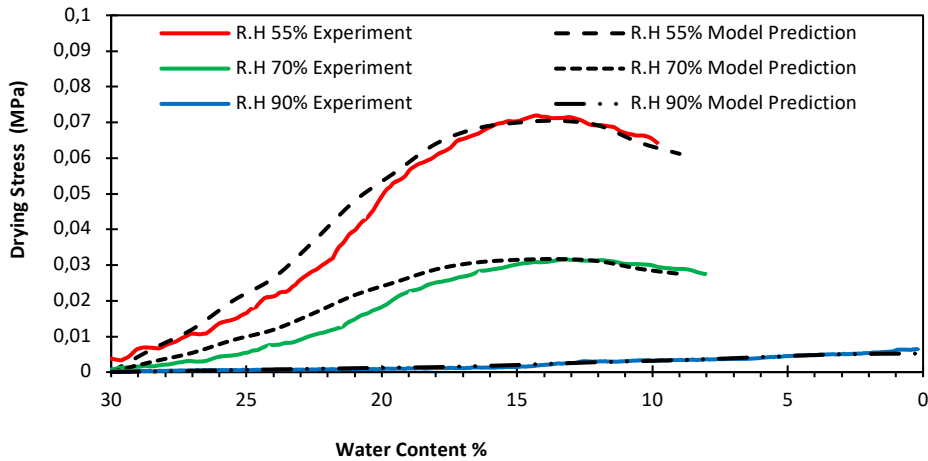


Figure 3.7 Fitting of the experimental evolution of the stress by the model for films cast from Latex 16. Film dry thickness 250 μm . Drying temperature: 23 $^{\circ}\text{C}$. Relative humidity 55%, 70% and 90%.

Figure 3.8 presents the comparison between the experimental results and the predictions of the model for the effect of the drying temperature on the stress generation. Temperature affects the viscoelastic properties of the polymers. In order to account for the effect of temperature on the Young's moduli (E) and the relaxation time (τ), the values of the Young's modulus and the relaxation times at 35 $^{\circ}\text{C}$ were estimated by fitting the stress evolution. Then, the following equations were derived.

$$E_s(T) = E_s(T_0) * (-0.266 \ln(T) + 1.8177) \quad (3.16)$$

$$\tau_s(T) = \tau_s(T_0) * (-0.061 \ln(T) + 1.2116) \quad (3.17)$$

$$E_h(T) = E_h(T_0) * (-0.173 \ln(T) + 1.5236) \quad (3.18)$$

$$\tau_h(T) = \tau_h(T_0) * (-0.151 \ln(T) + 1.4753) \quad (3.19)$$

where the temperature (T) is in Celsius. It can be seen that the model captures the effect of temperature and is in agreement with the experimental results, cracking was only observed when the drying temperature was 23 °C.

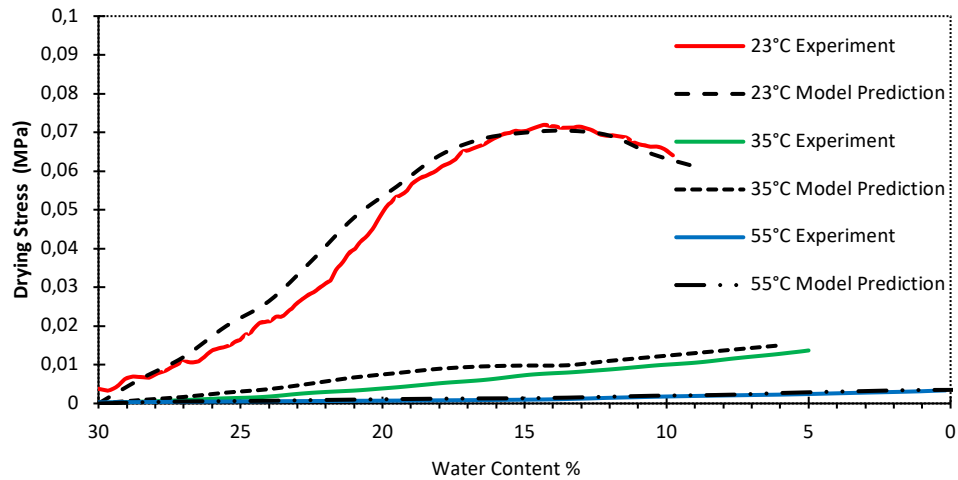


Figure 3.8 Effect of drying temperature on the evolution of stress. Soft core-hard “shell” latex. Latex 16. Particle size 250 nm. Film dry thickness 250 µm. Relative humidity: 55%. Temperature 23 °C, 35 °C and 55 °C.

Figure 3.9 presents the effect of the thickness of the film cast from Latex 16 on the evolution of the stress for beam-bending experiments carried out at 23 °C and 55% relative humidity. It can be seen that, in agreement with the experimental data, the model predicts the formation of cracks for films thicker than 250 µm. Figure 3.9 also shows that the thicker the film

the lower the stress at which the crack is nucleated. Nevertheless, it has to be pointed out that cracks appeared for the same tension force per particle ($3.5 \cdot 10^{-9}$ N).

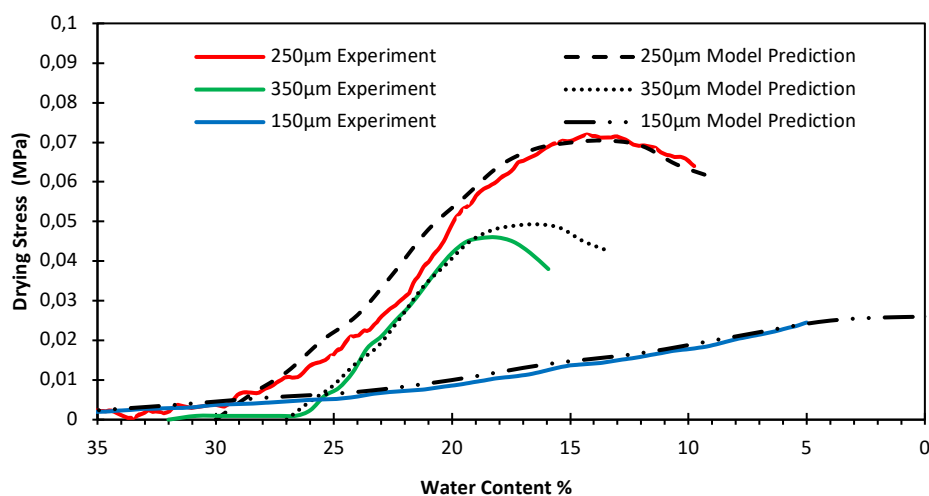


Figure 3.9 Effect of the thickness of the film on the evolution of the stress. Latex 16 ($d_p = 250$ nm). Drying conditions: $T = 23$ °C, $RH = 55\%$. Layer thickness 150 μm , 250 μm and 350 μm .

The effect of the acrylic acid content on the development of the stress in two series of latexes that had different particle diameters was reported in Chapter 2. Latexes 2, 4-6 with a particles size of about 255 nm and Latexes 11, 18 and 20 with 90-95 nm particles. The comparison between the experimental evolution of the stress and the model predictions is presented in Figures 3.10 and 3.11. In the simulations, the critical force for cracking was calculated using eq. 3.15. It can be seen that in agreement with the experimental data, the model predicts cracking for the latexes devoid of acrylic acid and for the 255 nm latex with 2 wt% of AA, whereas in the other cases, no cracking was predicted. For the 90 nm latex also containing 2

wt% of AA, the reason for the resistance to cracking was that the critical force per particle for cracking was not reached. Figures 3.10 and 3.11 show that the tendency to form cracks decreased as particle size decreased and the AA content increased. The effect of particle size is due to the higher number of contacts. Acrylic acid affects in two ways. On one part, the adhesion between particles increased due to the higher number of H-bonds. On the other hand, the acrylic acid reduces the drying rate, allowing more time for the particles to deform (in this regard, the effect is similar to that of the relative humidity).

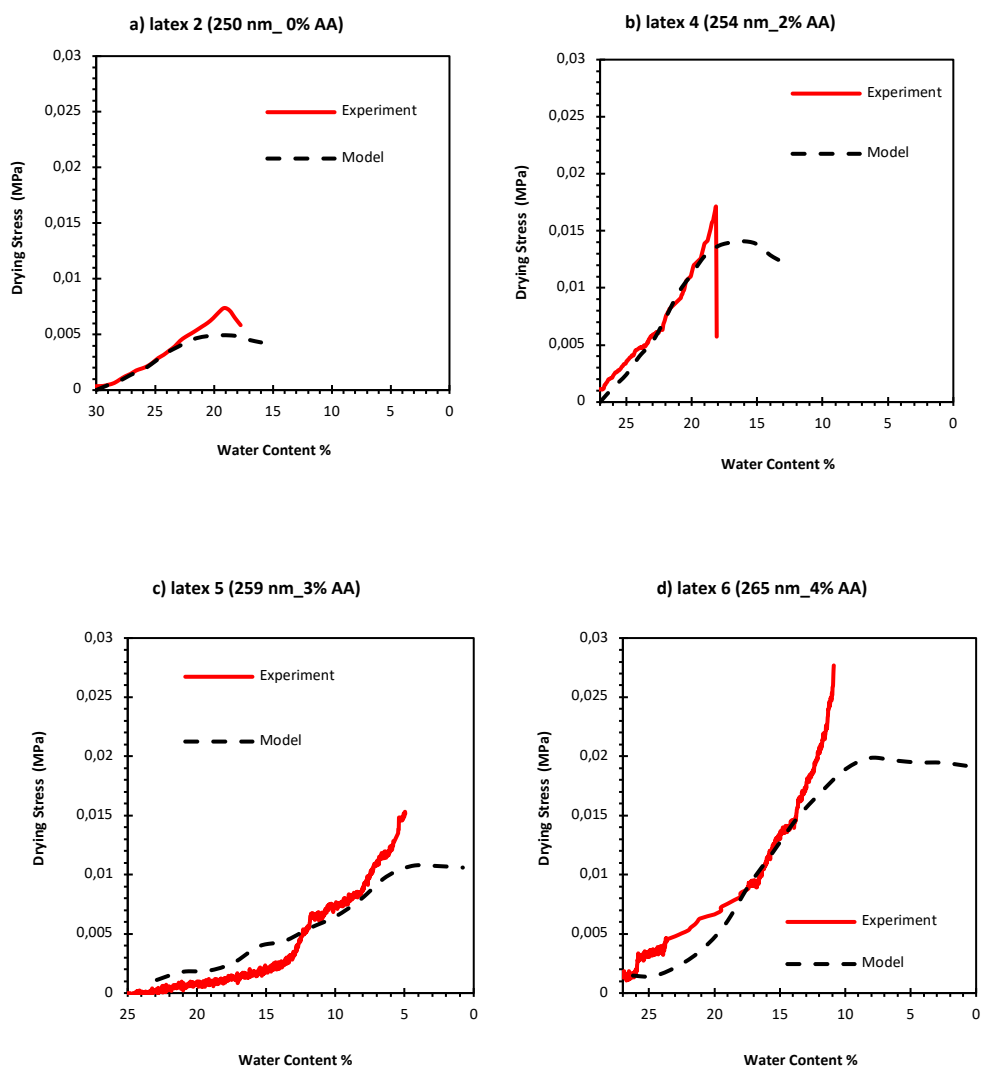


Figure 3.10 Comparison between experiments and model predictions for experiments where the acrylic acid content of the latex was varied. Particle diameter: 250 nm. Latexes 2, 4, 5 and 6. 170 μm dry films. Drying conditions: $T = 23\text{ }^\circ\text{C}$, $\text{RH} = 55\%$. Acrylic acid content: a) 0 %; b) 2 %; c) 3 %; d) 4 %.

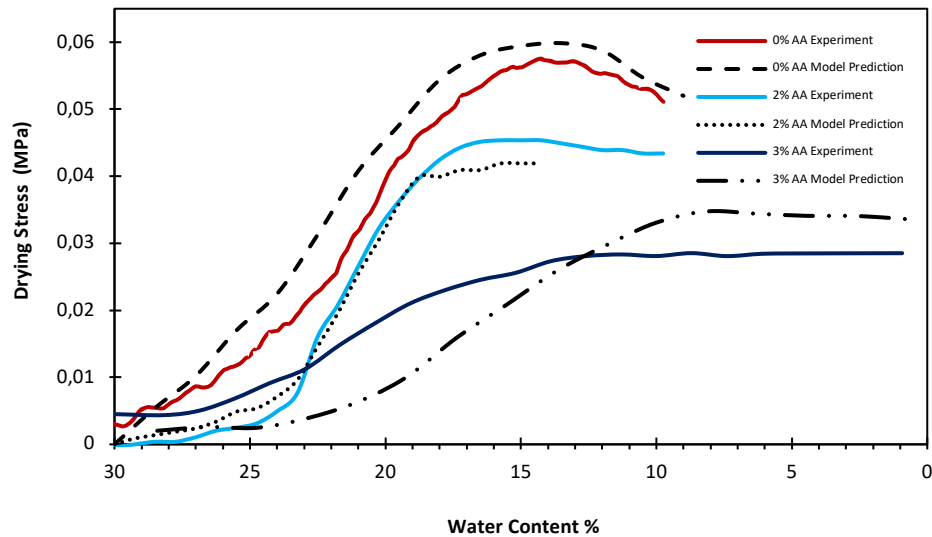


Figure 3.11 Effect of the acrylic acid (AA) content on the evolution of the stress generated during drying. Latexes 11, 18, 20. Particle size 91-95 nm. 170 μm dry films. Drying conditions: $T = 23^\circ\text{C}$, $\text{RH} = 55\%$. Acrylic acid content 0 %, 2 % and 3 %.

3.4. Conclusions

A mathematical model for cracking prediction and stress calculation during drying of aqueous dispersions of soft core-hard “shell” particles is developed. The model solves numerically the incompressible Navier-Stokes and continuity equations using COMSOL Multiphysics. The parameters of the model were either experimentally measured or estimated by fitting the model outputs with the experimental data. The model was validated with experimental data obtained with dispersions having different particle sizes and content of acidic monomers that were formed under different drying conditions (temperature and relative humidity). A very good agreement between experimental results and model predictions was achieved. Unlike the previous models

for film cracking, the present model predicts that, for viscoelastic particles, the critical cracking thickness (CCT) decreases with the particle size.

3.5. References

1. Oldroyd. On the Formulation of Rheological Equations of State. Proc. Roy. Soc. Lon. A, Math. Phy. Sci. **1950**, 200, 523–541.
2. Corcoran EM. Determining stresses in organic coatings using plate beam deflection. J. Paint Technol. **1969**, 41, 635-640.
3. Tirumkudulu MS, Russel WB. Cracking in drying latex films. Langmuir 21, **2005**, 4938-48.
4. W.B. Russel, N. Wu, W. Man Generalized Hertzian model for the deformation and cracking of colloidal packing saturated with liquid, Langmuir 24, **2008**, 1721-1730.
5. K.B. Singh, M.S. Tirumkudulu, Cracking in drying colloidal films, Phys Rev. Let. 98, **2007**, 218302.

Chapter 4. Blends of soft core-hard “shell” particles

4.1. Abstract

Blends of soft core-hard “shell” particles of different sizes have been prepared and it has been observed that adding tiny amounts of small particles (e.g. 1 wt %) to big particles film formation can be substantially improved (lower MFFT and higher CCT). Furthermore, mechanical properties of the films are also improved (higher elongation at break and toughness, maintaining the Young’s modulus and the stress at break), without affecting the water sensitivity of the film. It has been found that that the viscoelastic properties of small particles must be similar to the large ones in order to have a significant effect.

4.2. Introduction

This chapter is an attempt to go beyond the limits of the film formation presented in Chapter 2 using blends of soft core-hard “shell” particles of different sizes. This strategy is somehow inspired by the work of Peters et al. [1] who found that 75/25 (wt/wt %) blends of large and small homogeneous particles gave a minimum in MFFT that was significantly lower than those of the individual components of the blend. Similar results have been recently reported for blends of large and small hard core-soft shell particles [2]. Based on these results, the scope of this chapter is to study if the MFFT could be reduced and CCT increased by adding low quantities of small particles to dispersions of large particles. The reason of limiting the amount of small particles is to reduce the total amount of surfactant in the film, and therefore the water sensitivity of the resulting films.

4.3. Experimental part

4.3.1. Latex Synthesis

Soft core-hard “shell” latexes of different particle size and acrylic acid (AA) content previously synthesized in Chapter 2 were used in blends preparation. For the sake of clarity, the soft core-hard “shell” latexes from Chapter 2 are presented in Table 4.1. In addition, pure poly (methyl methacrylate) and poly (butyl acrylate) latexes of 55 nm in diameter were prepared.

Table 4.1 Characteristics of the soft core/hard “shell” latexes prepared in Chapter 2. To facilitate the identification of the Latexes, the same number as in Chapter 2 was used.

Latex	Soft core		Hard “shell”		dp (nm)
	BA/MMA/S/AA (wt/wt)	wt%	MMA/AA (wt/wt)	wt%	
1	70/15/15/0	75	100/0	25	55
2	68/15/15/2	75	97/3	25	70
3	70/15/15/0	75	100/0	25	70
4	68/15/15/2	75	97/3	25	90
5	70/15/15/0	75	100/0	25	90
16	68/15/15/2	75	97/3	25	250
7	70/15/15/0	75	100/0	25	250
8	68/15/15/2	75	97/3	25	350
9	70/15/15/0	75	100/0	25	350
10	70/15/15/0	70	100/0	30	359

4.3.2. Characterization

Environmental Scanning Electron Microscopy (ESEM) images were acquired on a Quanta 250 FEG ESEM (FEI, Netherlands) equipped with Peltier cooling stage and GSE detector. Particle coalescence was studied following the procedure detailed in [3].

Water uptake of the films dried from the latexes were measured. The films were cast on silicone molds and had a dry thickness of 250 μm . After drying for 7 days at 23 $^{\circ}\text{C}$ / 55% RH, the samples were weighed (w_1) before immersing in water for 72 hours. After that, the samples were dried with paper and then weighed again (w_2). Water uptake % was calculated from equation 4.1.

$$\text{Water Uptake \%} = \frac{w_2 - w_1}{w_1} \% \quad (4.1)$$

4.4. Results and discussion

As a benchmark for checking the effect of blending, the most exigent conditions were tested and the largest latex (350 nm, devoid of AA; Latex 9), which gave the highest MMFT and the lowest CCT, was blended with only 1 wt % of smaller latexes (55, 70 and 90 nm also devoid of AA, Latexes 1, 3, 5). It is worth pointing out that that no stratification is expected for 45 wt% solids content, size ratios (large/small) smaller than 7 and 1 wt% of small particles [4]. Figure 4.1 presents the CCT and MFFT of the blends. The values for the 350 nm latex (Latex 9) are included for comparison. It can be seen that the MFFT is substantially reduced by adding only 1 wt % of the small latex. Thus, MFFT decreased from 62 °C (for the 350 nm latex) to 43 °C adding only 1 wt % of the 90 nm latex, and to 18 °C when 1 wt % of the 70 nm latex was added. In parallel, the CCT increased from 80 μm to 150 μm when 1 wt% of the 90 nm latex was added, and to 260 μm for 1 wt % of the 70 nm latex. Figure 4.1 also shows that similar results were obtained for the 350 nm latex containing 3 % of AA (Latex 8), but due to the hydroplasticization effect, as studied in Chapter 2, the MFFTs were lower and the CCT higher than for the 350 nm latex devoid of acrylic acid. Higher concentrations of the small latexes led to further decreases of the MFFT and increase of the CCT, but the effect was attenuated (Table III.1).

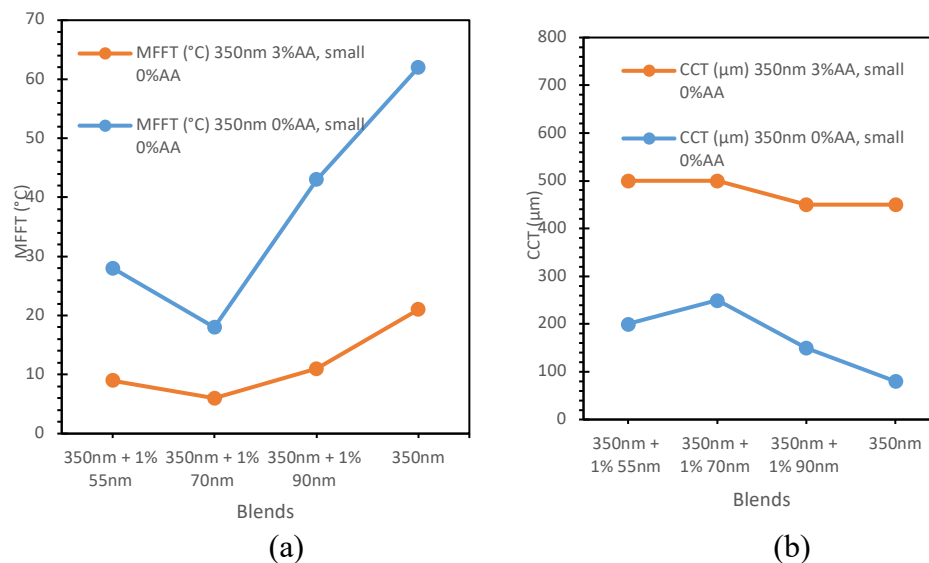


Figure 4.1 Effect of adding 1 wt % of small particles with 55, 70 and 90 nm of diameter (Latexes 1, 3, 5) to a 350 nm latex with (Latex 8) and without (Latex 9) AA on a) MFFT and b) CCT.

It is remarkable that the MFFT increased and the CCT decreased when the size of the small particles was further decreased to 55 nm. In this regard, it is worth pointing out that for blends of the 250 nm latexes with 1 wt % of smaller latexes (55 and 70 nm) the best results were obtained for blends with the 55 nm latex (Table III.2). This suggests that there is an optimal ratio between the sizes of the large and small particles, which is close to five. For 1 wt% of small particles, this ratio results in a similar number of small and large particles. It is worth pointing out that whereas the AA content of the large particles strongly affected the results, the AA content of the small particles had only a small effect (Figure III.1).

It is surprising that only 1wt % of the small latex could produce such a significant effect. In order to investigate this phenomenon, the effect of the presence of small particles on the

formation of the film cast from the blend was investigated by environmental scanning electron microscopy (ESEM). Figure 4.2 shows that whereas the 350 nm particles (Latex 9) maintained their identity at 30 °C (Figures 4.2a and 4.2b), adding only 1 wt % of 70 nm particles (Latex 3) was enough to force sintering of particles at 10 °C (Figures 4.2c and 4.2d) and this temperature was further reduced to 0 °C when a 3 wt % of the 70 nm latex was used (Figures 4.2e and 4.2f). This demonstrated that the presence of a tiny fraction of small particles tremendously facilitates the deformation of the large particles, which likely reduces the generation of stress during film formation.

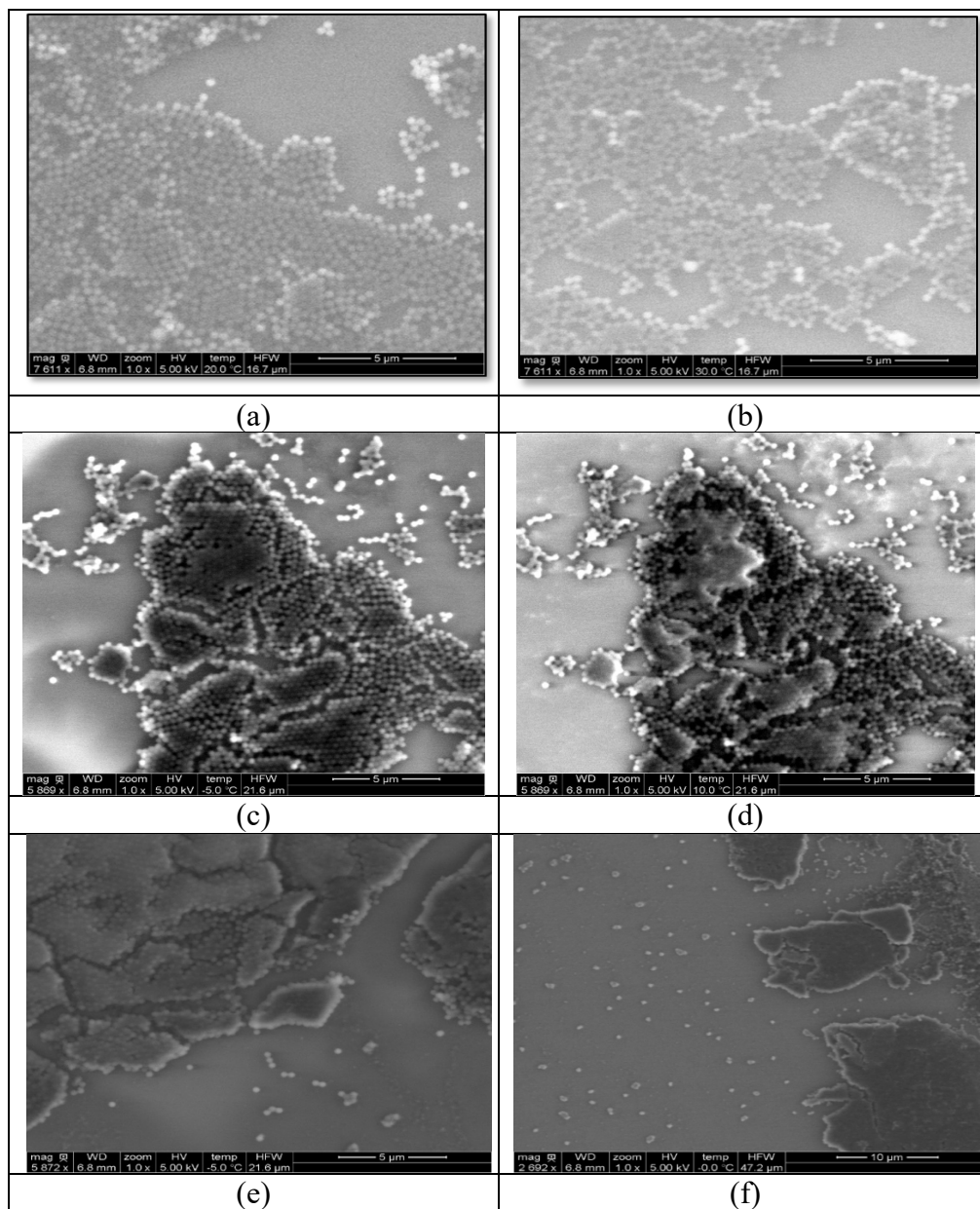


Figure 4.2 ESEM images of Latex 9 (350 nm) and blends of Latex 9 and Latex 3 (70 nm), both of them devoid of AA. (a) Latex 9 at 20 °C, (b) Latex 9 at 30 °C, (c) Latex 9 plus 1 wt % of Latex 3 at -5 °C, (d) Latex 9 plus 1 wt % of Latex 3 at 10 °C, (e) Latex 9 plus 3 wt % of Latex 3 at -5 °C and (f) Latex 9 plus 3 wt % of Latex 3 at 0 °C.

In order to check this point, the stress generated during film formation was determined via the beam-bending technique. Figure 4.3 shows the evolution of the stress for films cast from blends of 350 nm (Latex 9) and 70 nm latexes (Latex 3), both devoid of AA. Cracking was observed for the 350 nm latex as evidenced by the decrease of the stress that is a fingerprint of cracking. The stresses for the individual latexes are included for comparison. It can be seen that contrary to expectations, the presence of small particles resulted in an increase in the stress generated during film formation, but no cracks were formed. These results indicate that the reason for the higher resistance of the films was an increase in the cohesion. One may speculate that this is the result of an increase in the number of contact points due to the presence of small particles. The fact that for the 350 nm particles, the lowest value of the MFFT and the highest one for CCT were obtained with the 70 nm latex (size of the hole between large particles) suggests that this is the case. Another possibility, suggested by the ESEM results, is that the higher deformation led to an increase in the overall contact area between particles.

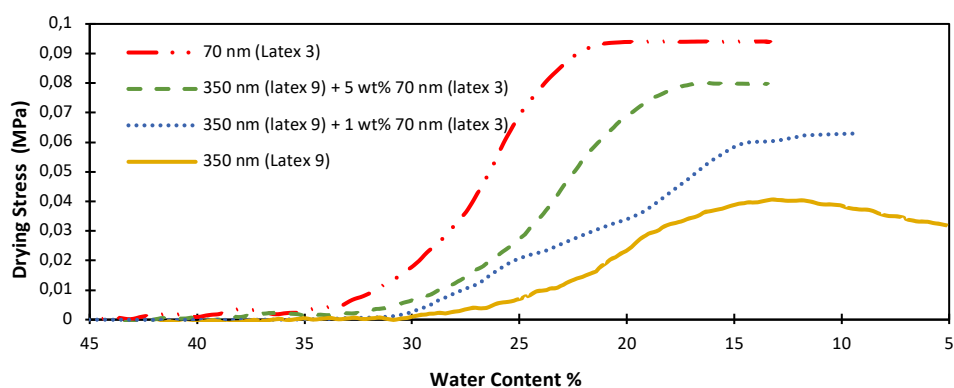


Figure 4.3 Evolution of the stress generated during film formation. Latexes 3 (70 nm) and 9 (350 nm). 1 % wt and 5 % wt blending were used.

It can be speculated that the physicochemical reasons for the increase in stress are linked to the decrease of the contact angles between particles that increase the Laplace pressure accelerating the deformation of the viscoelastic particles. In order to check this hypothesis, the sintering of three soft core-hard “shell” 350 nm particles with and without one interstitial soft core-hard “shell” 70 nm particle was simulated. For that, the Navier-Stokes equations were solved using COMSOL Multiphysics. The polymer/water interfacial tension $\gamma_{p/w}$ is 7.2 mN/m as estimated in Chapter 3. The Young’s moduli and relaxation times used were a weighted average of the values estimated in chapter 3: Young’s modulus $E = 1.7 \cdot 10^7$ Pa and phase relaxation time $\tau = 0.0334$ s. The driving force for the deformation is the reduction of the surface energy. The colours in the figure shows the distribution of the stress inside the particle during deformation. The red colour presents relatively higher compression stress, while the blue one presents relatively higher tension stress. Figure 4.4 presents the evolution of the sintering as well as the values of the deforming stresses. It can be seen that the presence of the small particle almost doubled the value of the particle deforming stress. This phenomenon is linked to the decrease of the contact angles between particles that increase the Laplace pressure accelerating and facilitating the deformation of the viscoelastic particles. The result of the higher deformation stress is that the 350 nm particles deformed faster in the presence of the 70 nm particle (Figure 4.5).

Chapter 4

Time	a) Large particles only (350 nm)		b) Large articles (350 nm) with an interstitial small particle (70 nm)	
	illustration	Max. deforming stress (Pa)	illustration	Maximum deforming stress (Pa)
≅ Zero Sec	<p>Large particles</p> <p>126</p> <p>-263</p>	263	<p>Large particles</p> <p>Small particle</p> <p>778</p> <p>-503</p>	503
≅ 20 Sec	<p>116</p> <p>-275</p>	275	<p>1040</p> <p>-330</p>	330

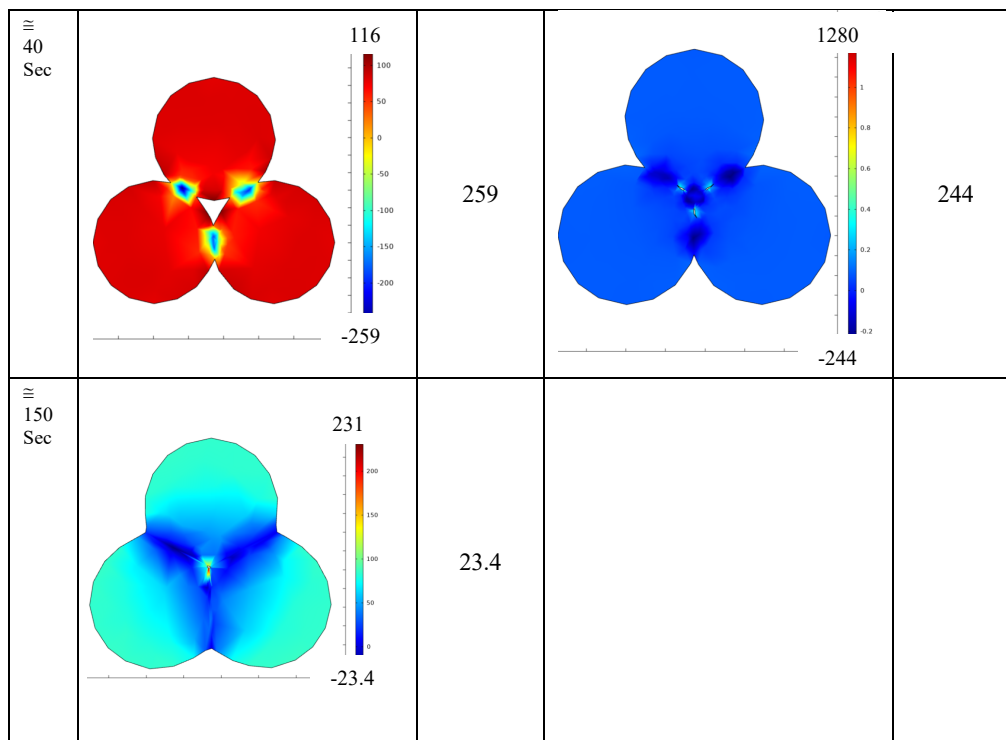


Figure 4.4 Effect of the presence of a 70 nm soft core-hard "shell" particle on the deformation of 350 nm soft core-hard "shell" particles.

Experimental results and model predictions support the hypothesis that the presence of small particles facilitates the deformation of particles due to the decrease of the contact angles between particles that increases the Laplace pressure accelerating the deformation of the viscoelastic particles. In this context, the viscoelastic properties of the small particles might have an effect. To investigate this point, Latex 9 (350 nm, devoid of AA) was blended with different fractions of 55 nm latexes of different glass transition temperatures (poly (butyl acrylate) (PBA), $T_g = -54$ °C; and poly (methyl methacrylate) (PMMA), $T_g = 110$ °C). The results are presented in Table 4.2 where it can be seen that the small latexes behaved as hard and soft fillers, without any significant effect for small fractions of the small particles.

The volume fraction of the small particles was lower than that required to form a continuous phase in the film [5]. This clearly indicates that in order to have a significant effect the small latex should have similar viscoelastic properties to the large one, so the small particles are relatively hard enough to keep contact angle with big particles and on the other side, be able to be deformed to form a homogenous film.

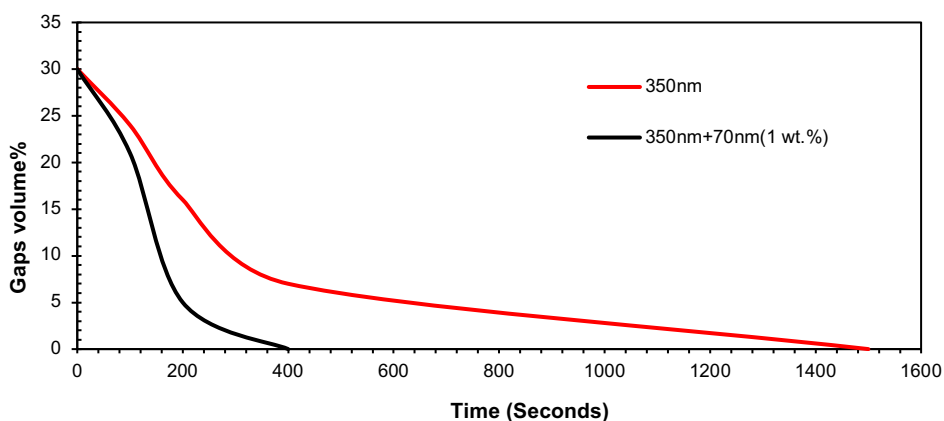


Figure 4.5 Effect of the presence of 1 wt % of 70 nm soft core-hard “shell” particles (Latex 3) on the reduction of the volume of the gaps between 350nm soft core-hard “shell” particles (Latex 9).

Table 4.2 Effect of the viscoelastic properties of the small particles. Blends of Latex 9 (350 nm) with 55 nm particles of PMMA and PBA.

Fraction of small particles	PMMA		PBA	
	MFFT (°C)	CCT (μm)	MFFT (°C)	CCT (μm)
0.5 wt %	62	70	62	80
1 wt %	58	85	62	80
2 wt %	63	50	60	80
4 wt %	68	50	55	120
10 wt %	>70	≅ 0	21	200

The results presented above suggested that the film formation behaviour of a large particle latex can be substantially improved by adding only 1 wt % of small particles (number of big particles to small particles 1:1.2) of similar viscoelastic properties. However, this would be irrelevant if it were accompanied with a detriment in the mechanical properties. Figure 4.6 and Table 4.3 present the effect of blending on the tensile tests. It can be seen that both in the presence and in the absence of AA, blending has a positive effect on the mechanical properties of the films dried from big particles. Blending slightly reduced the Young's modulus and had almost no effect on the maximum strength while it increased the maximum strain and the film toughness. Therefore, blending with a 1 wt % of small particles improved both film formation and mechanical properties.

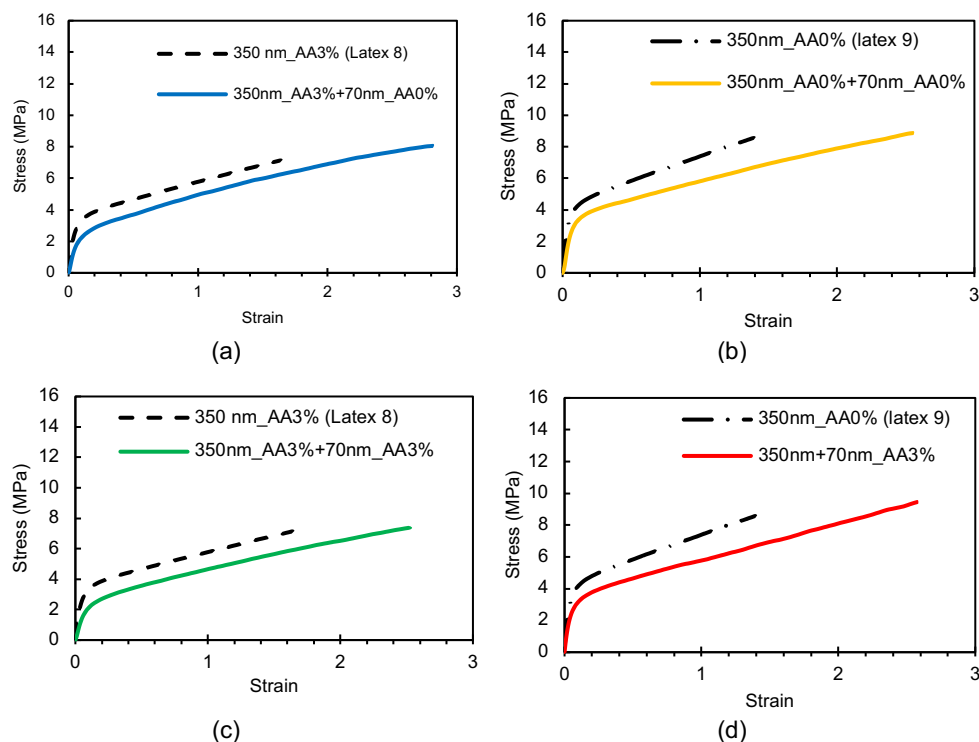


Figure 4.6 Effect of the addition of 1 % wt of 70 nm particles (with and without AA) on the tensile strain curve of films formed with 350 nm particles (with and without AA). (a) Latex 8 (350 nm, 3

% AA) plus 1 wt % of Latex 3 (70 nm, without AA), (b) Latex 9 (350 nm, without AA) plus 1 wt % of Latex 3 (70 nm, without AA), (c) Latex 8 (350 nm, 3 % AA) plus 1 wt % of Latex 2 (70 nm, 3 % AA) and (d) Latex 9 (350 nm, without AA) plus 1 wt % of Latex 2 (70 nm, 3 % AA)

Table 4.3 Effect of the addition of 1 % wt of 70 nm particles (with and without AA) on the tensile strain curve of films formed with 350 nm particles (with and without AA)

Latex	Young's modulus (MPa)	Stress at Break (MPa)	Elongation at break (%)	Toughness (MPa)
Latex 8 (350 nm, AA 3%)	2.7 ± 6%	7.1	160 ± 11%	8.6
Latex 8 + 1 wt % of Latex 2 (70nm, AA 3%)	2.3 ± 4.2%	7.4	250 ± 16%	16.4
Latex 8 + 1 wt % of Latex 3 (70nm, no AA)	1.9 ± 4.7%	7.4	280 ± 13%	14.5
Latex 9 (350 nm, no AA)	3.0 ± 5.8%	10.3	130 ± 9%	9.2
Latex 9 + 1 wt % of Latex 2 (70nm, AA 3%)	2.7 ± 2.7%	9.5	260 ± 14%	16.6
Latex 9 + 1 wt % of Latex 3 (70nm, no AA)	2.7 ± 3.1%	8.9	257 ± 11%	16.1

One of the limitations of using small particles is that they contain higher surfactant contents, which leads to water sensitivity. Therefore, it was important to check the effect of blending on the water uptake. Figure 8 shows that addition of 1 wt % of 70 nm particles with 0% AA had nearly no effect on the water sensitivity of the film after 3 days of immersing in water.

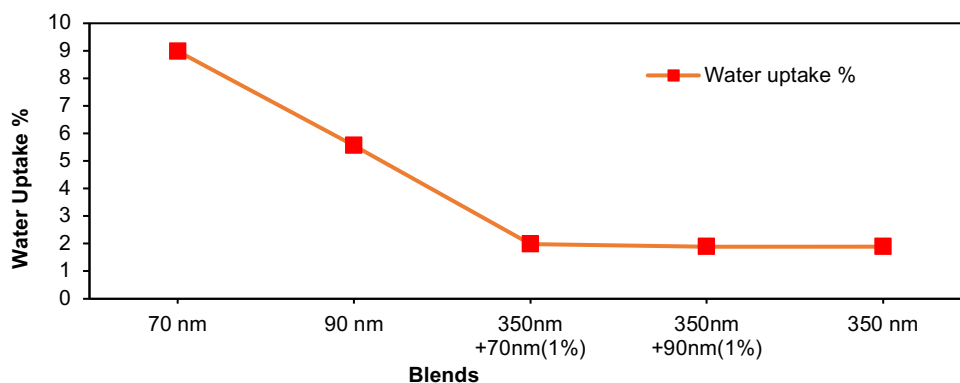


Figure 4.7 Water uptake for monomodal latexes and blends with 0%Aa after 3 days of immersing in water.

In Chapter 2, Section 2.3.6, it was shown that the increase of the hard phase content from 25 wt % to 30 wt % led to a severe increase of the MFFT and to a strong decrease of the CCT, limiting the usefulness of this latex. Table 4.4 shows that the addition of low amounts of small particles to a larger latex having a high amount of hard phase (Latex 10, 30 wt % hard phases, $d_p = 359$ nm) resulted in a substantial reduction of the MFFT and an important increase in CCT. This broadens the range of hard phase/soft phase ratios that can be used.

Table 4.4 Effect of adding small particles to a hard large latex (Latex 10, 30 wt % hard phase, $d_p = 359$ nm) on MFFT and CCT

	MFFT (°C)	CCT (μm)
Latex 10 (30 wt % of hard phase, 359 nm)	78	$\cong 0$
Latex 10 + 1 wt % of Latex 3 (70 nm)	53	100
Latex 10 + 2 wt % of Latex 3 (70 nm)	45	150
Latex 10 + 3 wt % of Latex 3 (70 nm)	31	250

In Chapter 3, the development of stress during film formation can be well described by solving numerically the Navier-Stokes equations using a finite element method implemented in COMSOL. In that case, particles of the same size were used. In the current chapter, this approach was applied to calculate the development of stress during film formation of blends. The scale down concepts developed in Chapter 3 were used. Figure 4.8 presents a comparison between experimental data and model predictions for the evolution of film stress. It can be seen that, in agreement with the experimental data, the model predicted the formation of cracks for pure 350 nm particles. No failure was predicted for both blended films. The parameters used were the same as in Chapter 3, Section 3.3.1, namely, no parameter estimation was performed.

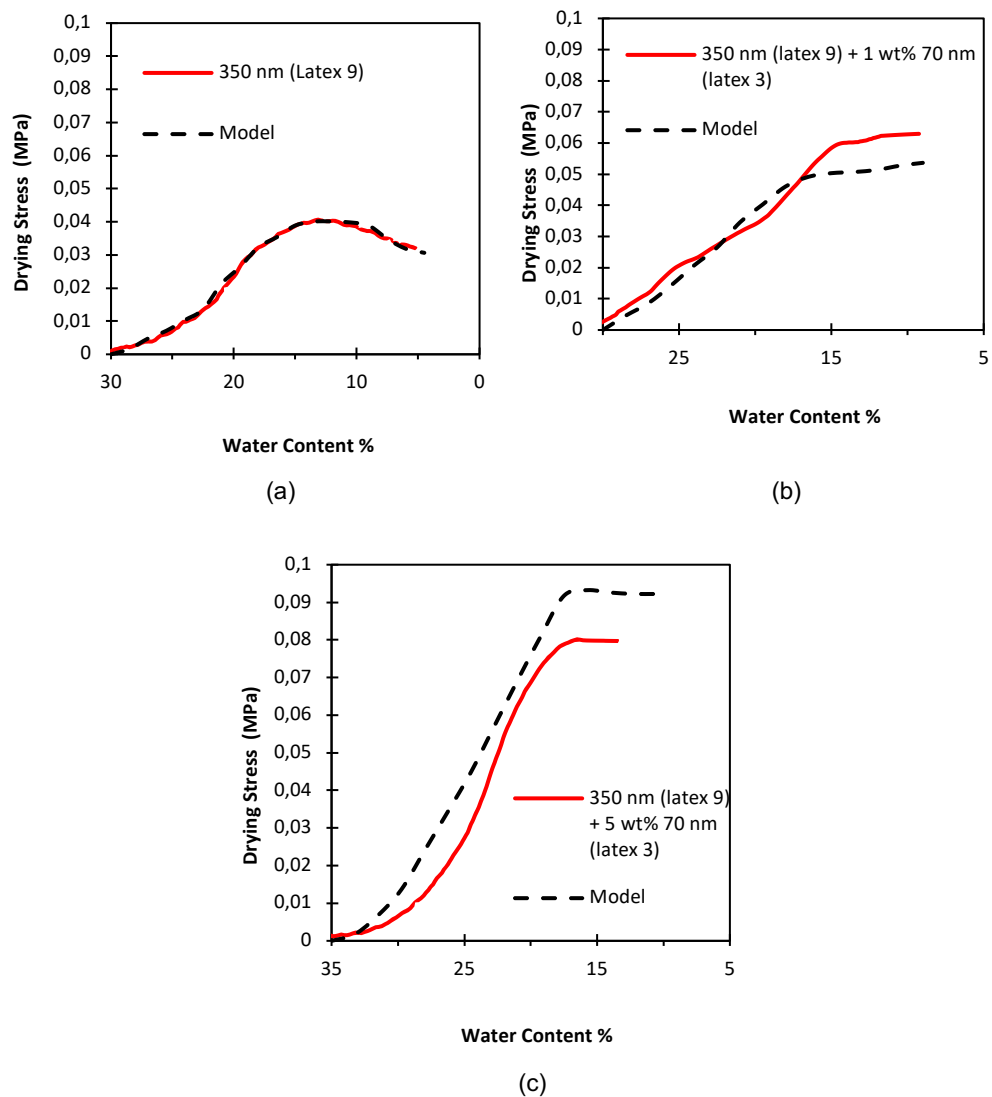


Figure 4.8 Comparison between the modelled and measured stress generated during film formation for Latex 9 (350 nm) (a), and blends of Latex 9 with 1 wt % (b) and 5 wt % (c) of Latex 3 (70 nm).

4.5. Conclusions

This chapter shows that addition of tiny amounts of small particles (e.g. 1 wt %) leads to a substantial improvement of both film formation (strong decrease of MFFT and increase of CCT) and mechanical properties (higher elongation at break and toughness, maintaining the Young's modulus and the stress at break), without any effect on the water sensitivity of the film. An important finding is that in order to have a significant effect, the small particles should have similar viscoelastic properties to the large ones. Furthermore, addition of small particles allows to use high contents of hard phase, broadening the range of hard phase/soft phase ratios that can be used.

4.6. References

1. Peters, A.C.I.A.; Overbeek, G.C.; Buckmann, A.J.P.; Padget, J.C.; Annable, T. Bimodal dispersions in coating applications, *Prog. Org. Coat.* **1991**, 29, 183-194.
2. Brito, E.L.; Ballard, N. Film formation of hard-core/soft-shell latex particles. *J. Pol. Sci.* **2022**, 1–12.
3. Gonzalez E, Tollan C, Chuvilin A, Barandiaran M.J, Paulis M. Determination of the Coalescence Temperature of Latexes by Environmental Scanning Electron Microscopy, *ACS Ap Mater. Interfaces* **2012**, 4, 4276–4282.
4. D. K. Makepeace, A. Fortini, A. Markov, P. Locatelli, C. Lindsay, S. Moorhouse, R. Lind, R. P. Sear, J. L. Keddie, *Soft Matter*, **2017**, 13, 6969-6980
5. Tzitzinou, A.; Keddie, J.L.; Geurts, J.M.; Peters, A.C.I.A.; Satguru, R. Film formation of latex blends with bimodal particle size distributions. Consideration of particles deformability and continuity of the dispersed phase. *Macromolecules*, **2000**, 33, 2695-2708.

Chapter 5. Internally reinforced soft core-hard shell waterborne dispersions for high performance solvent-free coatings

5.1. Abstract

Waterborne polymer dispersions composed of soft core-hard shell particles allow obtaining mechanically robust coatings that can be cast at low temperatures without the use of coalescent agents. However, the presence of a hard phase at the outer of the particle increases the stress generated during film formation leading to cracks. The need of forming film free of cracks limits the mechanical properties of the coating. This chapter explores a strategy of enhancing the mechanical properties of waterborne coatings without compromising the film formation properties of soft core-hard "shell" polymer particles. The approach is based on a multiphase internal core composed by hard and soft domains. This strategy resulted in coatings with higher Young's modulus, stress at break and toughness, without compromising the film formation characteristics.

5.2. Introduction

In Chapter 2, the effect of the characteristics of soft core-hard “shell” latexes (particle size, hard/soft ratio, acrylic acid content) and film application conditions (temperature, relative humidity, type of substrate, thickness of the film) on the minimum film forming temperature (MFFT, minimum temperature at which a crack-free film can be formed), critical cracking thickness (CCT, maximum thickness of the film at which cracks are not formed) and mechanical properties were investigated. It was found that good films could be formed if the hard polymer forms patches on the surface of the particles instead of a continuous shell. This structure is called soft core/hard “shell”. On the other hand, the tendency to crack is reduced by decreasing the particle size, which leads to lower MFFT and higher CCT. In addition, the Young’s modulus, the stress at break and the surface hardness increased. Unfortunately, brittleness increased and therefore, strain at break and toughness decreased.

Ideally, one would like to simultaneously increase the Young’s modulus and the stress at break without damaging the strain at break, the MFFT and the CCT. This chapter aims at achieving this goal. The strategy used was guided by an equation for the elastic modulus in honeycomb structures of a hard material filled with a soft one (Figure 5.1) [1].

$$E_{honeycomb} = E_{wall} + E_{filler} \quad (5.1)$$

where

$$E_{wall} = \frac{t^3}{l^3} \frac{E_{hard\ phase} l \sin\theta}{h (\cos\theta + 1) (\sin^2\theta \left(\frac{t}{l}\right)^2 + \cos^2\theta)} \quad (5.2)$$

and

$$E_{filler} = \frac{E_{soft\ phase} l \sin\theta}{8 (h + l \cos\theta)} \quad (5.3)$$

Where $E_{hard\ phase}$ and $E_{soft\ phase}$ are the elastic modulus of the hard and soft phases, respectively, and h , l , t and θ are geometrical parameters of the honeycomb structure (Figure 5.1).

The structure of the honeycomb structure in Figure 5.1 differs from the (so-called honeycomb) dodecahedral structure of a film cast from soft core/hard “shell” particles, but eq. 5.1 should apply and although the geometrical part of eqs. 5.2 and 5.3 will be different, E_{wall} and E_{filler} will be proportional to $E_{hard\ phase}$ and $E_{soft\ phase}$. Therefore, $E_{honeycomb}$ can be increased by increasing $E_{hard\ phase}$ and $E_{soft\ phase}$. For “shells” formed by patches of hard polymer, the wall of the dodecahedral structure is a blend of soft and hard polymer. The modulus of this blend can be increased by increasing the fraction of hard phase in the particle, but it has already been demonstrated that this leads to an undesired increase of MFFT and decrease of CCT as studied in Chapter 2. Therefore, increasing $E_{hard\ phase}$ is not an option. Another alternative is to increase $E_{soft\ phase}$ using a soft polymer with a higher glass transition temperature (T_g). However, this will likely increase MFFT and decrease CCT.

With these constraints, the strategy explored in this chapter was to create a multiphase internal phase composed by hard and soft domains. In particular, the structures outlined in Figure 5.2 were explored.

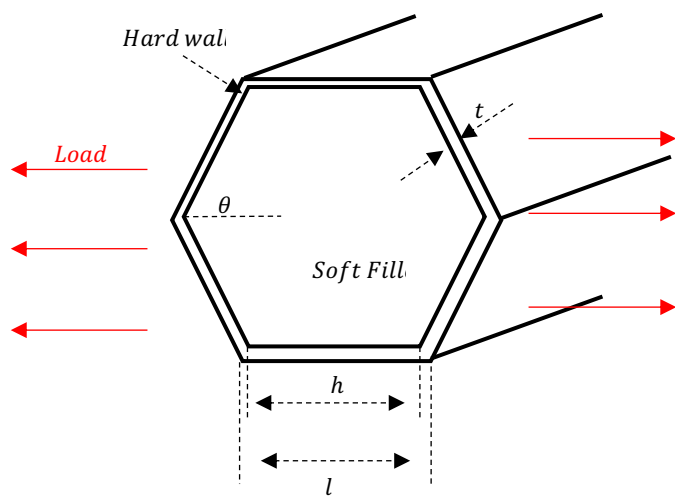
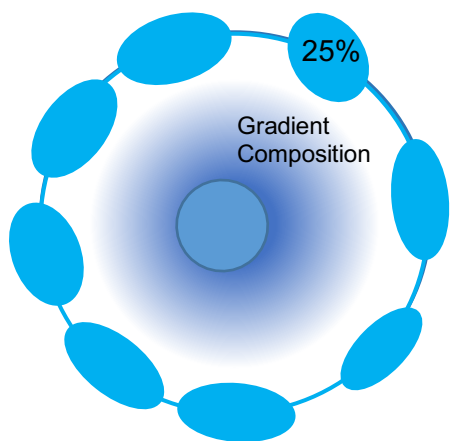


Figure 5.1 Honeycomb structure

a)



b)

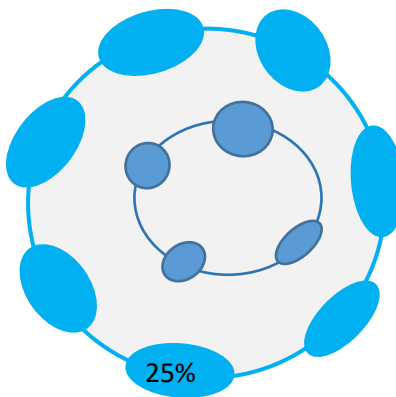


Figure 5.2 Structures of the soft core/hard "shell" particles explored

5.3. Experimental part

Latexes with the structures outlined in Figure 5.2 were synthesized by seeded emulsion polymerization. For the particles with a gradient composition in the core (Figure 5.2a, Latexes 1-3 in Table 5.1), a hard core (styrene/butyl acrylate: 90/10 wt/wt) was initially formed and then the gradient was formed adding semicontinuously styrene (S) and butyl acrylate (BA) in two different streams. The flow rates of these streams were varied so that the flow rate ratio varied from an initial S/BA = 90/10 wt/wt to a final value that was richer in BA. The average composition of the gradient zone was maintained constant (S/BA = 40/60 wt/wt). Then, the hard outer phase (methyl methacrylate (MMA)/BA = 99/1 wt/wt) was formed feeding the monomers semicontinuously. The core/"shell" ratio was in all cases 75/25 wt/wt.

For the latexes with hard internal domains (Figure 5.2b) a soft core (MMA/BA 40/60 wt/wt, $T_g = -10$ °C) was synthesized first. Then, the internal hard inclusions were formed by feeding semicontinuously a mixture of MMA/S/BA (49.5/49.5/1 wt/wt) that yielded a polymer with a $T_g = 100$ °C. The reason for including styrene in the hard domains was to facilitate the identification of these domains in the electron microscope and to control the hydrophilicity of the domains. After that, the formation of the core was finished by feeding a MMA/BA (40/60 wt/wt) monomer mixture. Two latexes with different content of hard inclusions were synthesized. Latex 4 contained 3.5 wt% of hard internal domains and Latex 5 had 5 wt%. Finally, the hard outer "shell" was prepared by feeding a 99/1 MMA/BA mixture of monomers. The core/"shell" ratio was in all cases 75/25 wt/wt. In addition, a regular soft core/hard "shell" latex (Latex 6) was synthesized for comparison. Details of the polymerizations are given in Appendix IV. For the sake of clarity, the synthesized latexes are summarized in Table 5.1.

Details about the characterization methods are given in Appendices I and IV. Solids contents and monomer conversion were determined gravimetrically. The particle size was determined using dynamic light scattering (DLS). Glass transition temperature (T_g) of the polymer was measured by differential scanning calorimetry (DSC). Particle morphology was studied by electron tomography (ET). The mechanical properties of the films, cast from the synthesized latexes were determined by tensile test measurements.

Table 5.1 Summary of synthesized latexes

Latex	Morphology of the core		dp (nm)
1	Gradient core	Hard region in core 10%	173
2	Gradient core	Hard region in core 5%	230
3	Gradient core	Hard region in core 2%	245
4	Multiphase core	3.5% hard domains	210
5	Multiphase core	5% hard domains	210
6	Standard soft core		250

5.4. Results and discussion

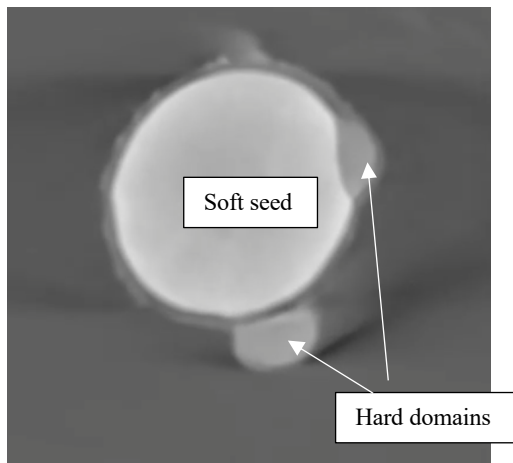
Table 5.2 summarizes the MFFT and CCT of the different latexes. The standard soft-core-hard “shell” latex was included as a reference. It can be seen that out of the latexes with a composition gradient in the core, only the one having the smallest hard region in the core (Latex 3) presented MFFT and CCT that were as good as those of the standard soft core-hard “shell” reference latex (Latex 6). Latexes 1 and 2 were too hard. On the other hand, the latexes containing hard inclusions in the soft core (Latexes 4 and 5) gave the same MFFT than the reference and a slightly better CCT. Therefore, the rest of the study was focused on Latexes 3, 4 and 5.

Table 5.2 Summary of synthesized latexes

Latex	Morphology of the core	dp (nm)	MFFT (°C)	CCT (µm)
1	Gradient core Hard region in core 10%	173	65	25
2	Gradient core Hard region in core 5%	230	25	150
3	Gradient core Hard region in core 2%	245	22	250
4	Multiphase core 3.5% hard domains	210	21	300
5	Multiphase core 5% hard domains	210	21	300
6	Standard soft core	250	21	250

In order to check if the morphology depicted in Figure 5.2b for the particles containing hard domains in the core was achieved, Latex 5 was analysed by electron tomography (ET). First, the soft seed after formation of the hard domains was studied. Figure 6.3a presents the image taken from the reconstructed video. It can be seen that the hard domains were located at the surface of the soft seed. Then, electron tomography was applied to the whole particle. Measurement in this case was more difficult due to the small size of the hard domains relative to the size of the particle (5wt%) and to the interpenetration of the polymers in the soft core and the hard domains that decrease the contrast between the phases (see Figure 5.4). Nevertheless, the presence of hard domains can be seen in Figure 5.3b that presents the image obtained from the reconstructed videos. Therefore, the morphology of the particle was that depicted in Figure 5.2b, namely that the particle contained hard domains in the soft core.

a) Soft seed with hard domains ($d_p = 87$ nm)



b) Full particle ($d_p = 203$ nm)

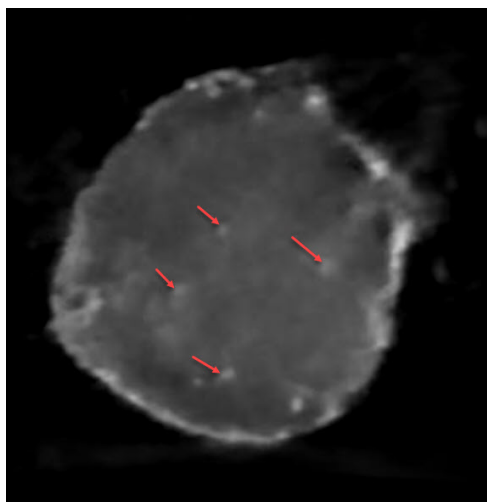


Figure 5.3 ET images of Latex 5. a) soft seed with hard domains at the surface. b) whole particle consisting of a soft core with hard inclusions and a hard “shell” that is not clearly visible)

The results of the tensile tests for Latexes 3-6 are presented in Table 5.3 and Figure 5.4. Comparison with the standard soft core-hard “shell” Latex 6 shows that the presence of hard

phase in the soft core led to stiffer films. The gradient Latex 3 was too brittle and presented a small elongation at break (47%), which resulted in a low toughness. On the other hand, in comparison with the standard Latex 6, Latexes 4 and 5 which contained hard inclusions in the soft core, showed substantially higher Young's moduli and stress at break, while maintaining good elongation at break. For Latex 5, this combination resulted in a higher toughness. Therefore, the inclusion of hard domains in the soft core led to a substantial improvement of the mechanical properties whilst maintaining and even slightly improving the film formation characteristics (MFFT and CCT).

Table 5.3 Mechanical properties of Latexes 3-6

Latex	Young's Modulus (MPa)	Stress at Break (MPa)	Elongation at break (%)	Toughness (MPa)
Latex 3	5.6	7.4	47	2.9
Latex 4	5.2	9.0	135	10.3
Latex 5	9.9	14.4	120	14.7
Latex 6	3.3	6.4	240	12.6

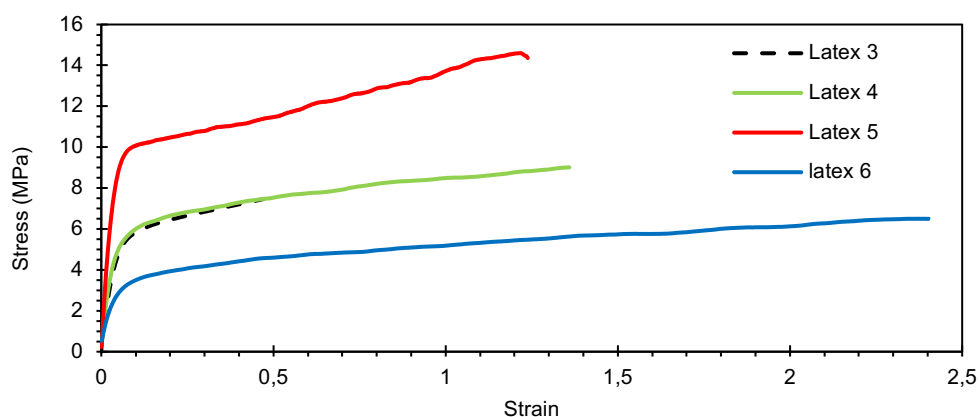


Figure 5.4 Tensile tests for the films of Latexes 3-6

In an attempt to shed some light on these findings, the glass transition temperatures of Latex 5 were determined by DSC and compared with those of Latex 6 (standard). Figure 5.5 shows that both latexes presented a high T_g at about 100 °C that corresponded to the external hard polymer. On the other hand, the low T_g was completely different. Whereas, the standard Latex 6 had a relatively narrow T_g at about 5 °C, Latex 5 presented a very broad T_g that extended from 0 °C to about 40 °C. This was attributed to the interpenetration of the polymer of the soft core with that of the hard inclusions. Quite likely, this diffused structure of the core is responsible for the very good properties of Latex 5, as on one part it is soft enough to allow an easy deformation of the particles during film formation, and on the other, it increased the Young's modulus of the core and consequently that of the honeycomb structure (eq. 5.1).

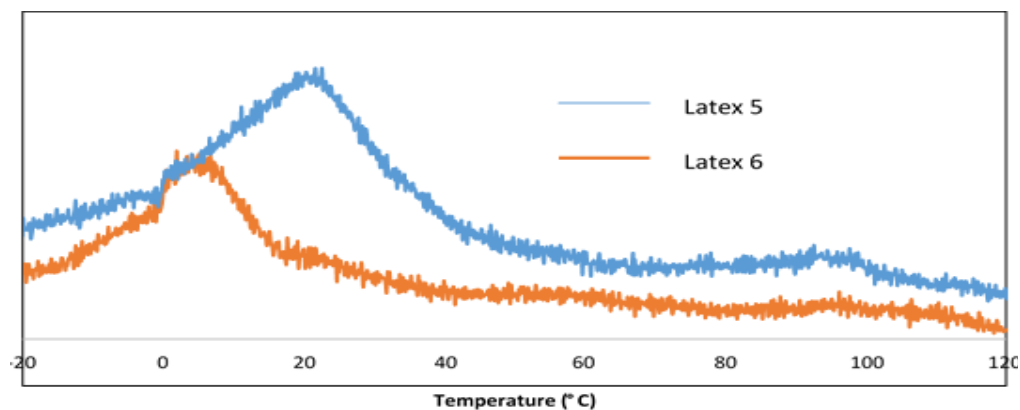


Figure 5.5 DSC curves of latexes 5 and 6

5.5. Conclusions

It is shown that soft core-hard "shell" waterborne dispersions with a core reinforced with discrete domains of hard polymer resulted in a solvent-free coating with improved mechanical properties maintaining and even slightly improving the film formation characteristics (MFFT and CCT). This was attributed to the interpenetration of the polymers of the soft core and hard inclusions. This resulted in a diffuse structure of the core that on one part, it was soft enough to allow an easy deformation of the particles during film formation, and on the other, increased the Young's modulus of the core and consequently that of the honeycomb structure.

5.6. References

1. Hedayati, R, Sadighi, M, Mohammadi Aghdam M, Zadpoor AA. Mechanical properties of additively manufactured thick honeycombs. *Materials*. 2016, 9, 613.

Chapter 6. Coarse graining modelling of the film formation from soft core-hard shell waterborne dispersions

6.1. Abstract

Soft core-hard shell waterborne polymer coating is a promising way to overcome the film formation paradox, but they are prone to suffer cracking leaving the substrate unprotected. Modelling of crack formation during drying of colloidal dispersions has received plenty of attention, but the existing models are unable to justify the behavior of these coatings. In Chapter 3, modified Navier-Stokes equations were used to model the stresses generated during film drying on flexible substrates using a scaling down technique to limit the computing time. This chapter overcomes this limitation by solving the modified Navier-Stokes equations through a coarse graining approach. The model is validated by comparing its predictions with experimental results of the critical cracking thickness (CCT) obtained for soft core-hard “shell” latexes with different particle size, acrylic acid content and soft/hard phase ratio dried under different conditions on hard substrates. It is worth pointing out that the values of the parameters used were those of Chapter 3, namely, no parameter estimation was performed. The potential of the approach to handle more complex cases is demonstrated by simulating the film formation of a blend of large and small soft core-hard “shell” latexes.

6.2. Model description

The coarse graining model is illustrated in Figure 6.1. It consists of dividing the three dimensional films into a number of horizontal layers (five layers for the simulations presented in this chapter). The number of the layers remained fixed during the simulation, but each layer was free to change in the three dimensions under the effect of the drying shrinkage of the layer. In order to limit the computing requirements, the width of the layers was made equal to their thickness (height).

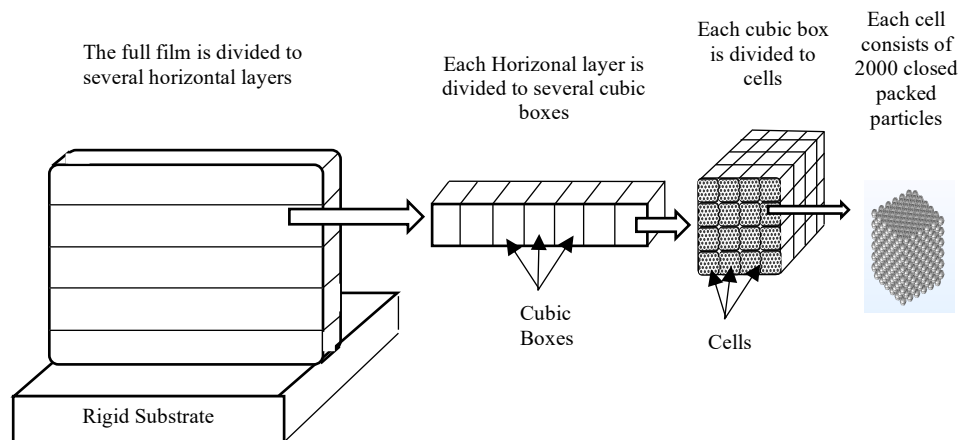


Figure 6.1 Illustration of the coarse graining strategy.

Each horizontal layer was divided into 50 cubic boxes. Each cubic box had the same height and width as the horizontal layer. The boxes were formed by cubic cells, each of them containing 2000 particles that initially were in hexagonal close packing, therefore, the size of the cell increased with the particle size. As the size of the box was given by the thickness of the layer, the number of cells per box depended on the particle size. Table 6.1 presents an example of the effect of the particles size on the number of cells per box for a 100 μm thick layer.

It is worth mentioning that although the concept of cell appears in both models, the present model has nothing to do with the one reported by Gromer et al. for latex film formation [1]. In Gromer's model, the cells defined a fixed space along the vertical axis of the film. Therefore, a cell that initially contained particles could be empty if the water level decreased. Gromer et al. [1] did not consider stress generation and crack formation.

Table 6.1 Effect of the particle size on the number of cells per cubic box. Thickness of the film = 100 μm . 5 horizontal layers. Size of the box = $20 \times 20 \times 20 \mu\text{m}^3$. 2000 particles/cell.

dp (nm)	Length of each size of the cubic cell (μm)	Number of cells per cubic box	Particles per box
70	0.786	25^3	31,250,000
150	1.684	12^3	3,456,000
250	2.807	7^3	686,000
350	3.929	5^3	25,000

The boxes forming the bottom layer are attached to the rigid substrate and neither shrinkage nor deformation was allowed in this attachment. Solid mechanics rules (full attachment) were applied between each cell/box and its surrounding neighbours, which is responsible for the transfer of stresses and deformation between the adjacent cells/boxes. The cells/boxes changed in the three dimensions during the simulation due to drying shrinkage, but the number of particles per cell/box remained the same.

Initially, the film was filled with water. In this moment, the particles were deformed due to the effect of the polymer/water interfacial tension, i.e. wet sintering. As soon as evaporation of water started, the top layer was considered to be under capillary deformation, namely under forces created by the water-air surface tension. In the rest of the layers, particle deformed under

wet sintering. When the level of the water reached the second layer from the top, the particles of the top layer continued deforming under dry sintering (driving force due to polymer surface tension). In the second layer from the top, the particles deformed under capillary deformation, and the rest of the layers were under wet sintering. The process continued as the level of liquid decreased.

The kinetics of water evaporation used in the simulations was that experimentally measured. The values of surface and interfacial tensions used in this work were determined experimentally in Chapter 3. The polymer surface tension γ_p was 36.6 mN/m and the polymer/water interfacial tension $\gamma_{p/w}$ was 7.2 mN/m.

In order to apply the coarse graining approach, the equivalent physical properties functions (strain rate, Young's modulus, E , and relaxation time, τ) of one cell per horizontal layer (reference cell in that layer) were calculated as a function of time. Particle deformation and stress generation were calculated by solving the classical incompressible Navier-Stokes equation and the continuity equation. The Oldroyd-B constitutive model [2] was used for the viscoelastic flow. The equations were solved by means of a finite element method using a software package platform (COMSOL Multiphysics) based on the creeping two-phase flow level-set interface coupling with the electrostatic interface and deformed geometry modules (As explained in Chapter 3).

As each horizontal layer follows a different history, at any moment in time, the physical properties of the cells in different layers were different. Once the properties of the reference cell in each layer were obtained, those of the boxes in the layer were calculated by interaction between cells. Finally, the properties of each layer were calculated by interaction between the boxes in that layer. Due to the coarse graining approach, there will be a sharp change of the

interfacial tension values between the layers depending on the drying stage (wet sintering or dry sintering) of each layer. To avoid this sudden change, a smoothing function was applied to gradually change the interfacial surface tension for air/polymer and the interfacial tension for polymer/water values between the borders of the layers. That was done by changing the value of the interfacial surface tension applied to the last 10% of layer thickness to gradually reach the average interfacial tension of the two adjacent layers.

This approach allowed to simulate the film formation of soft core-hard “shell” latexes with film thickness comparable to the experimental values. The potential of the approach to handle more complex cases was demonstrated by simulating the film formation of a blend of large and small soft core-hard “shell” latexes.

6.3. Model validation

In order to validate the model, the data reported in Chapter 2 on the effect of particle size, acrylic acid (AA) content and soft/hard ratio of soft core-hard “shell” latexes on the critical cracking thickness (CCT) obtained under different drying conditions were used. In addition, a blend of large soft core-hard “shell” particles with a tiny amount (1wt%) of smaller particles of the same morphology (Chapter 4) was simulated. Tables 6.2 and 6.3 present the latexes used and the values of CCT obtained experimentally for those latexes.

Coarse graining modelling of the film formation from soft core-hard shell waterborne dispersions

Table 6.2 Soft core- hard “shell” latexes used for validation of the coarse graining model.

latex	seed		core		“shell”		dp (nm)	CCT (μm)
	BA/MMA/AA	wt%	BA/MMA/AA	wt%	BA/MMA/AA	wt%		
	(wt/wt)		(wt/wt)		(wt/wt)			
2	60/40/0	10	60/40/0	65	1/99/0	25	250	140
4	60/38/2	10	60/38/2	65	1/97/2	25	254	550
5	60/37/3	10	60/37/3	65	1/96/3	25	259	700
6	60/36/4	10	60/36/4	65	1/95/4	25	265	250
10	68/15/15/2	5	68/15/15/2	70	97/3	25	70	500
11	68/15/15/2	5	68/15/15/2	70	97/3	25	90	200
15	68/15/15/2	2	68/15/15/2	73	97/3	25	150	250
16	68/15/15/2	2	68/15/15/2	73	97/3	25	250	125
17	68/15/15/2	2	68/15/15/2	73	97/3	25	350	80
18	68/16/16/0	5	68/16/16/0	70	100/0	25	95	50
20	68/14/15/3	5	68/14/15/3	70	97/3	25	91	800
27	68/15/15/2	5	68/15/15/2	65	97/3	30	85	75

Table 6.3 Blends used for validation of the coarse graining model

latex	seed		core		“shell”		dp (nm)	CCT (μm)
	BA/MMA/AA	wt%	BA/MMA/AA	wt%	BA/MMA/AA	wt%		
	(wt/wt)		(wt/wt)		(wt/wt)			
17	68/15/15/2	2	68/15/15/2	73	97/3	25	350	80
10	68/15/15/2	5	68/15/15/2	70	97/3	25	70	500
Blend latex 17 + latex 10 (1 wt.%)								250

In the simulations, the values of the properties of the particles (Young's modulus E and relaxation time τ) and the critical cracking force per particle either measured or estimated in Chapter 3 were used, namely no parameter estimation was carried out in the present chapter. The values of the parameter are summarized in Table 6.4. These parameters were obtained at 23°C. At other temperatures, the values of the Young's moduli and relaxation times estimated in Chapter 3 were

$$E_s(T) = E_s(T_o) * (-0.266 \ln(T) + 1.8177) \quad (5.1)$$

$$\tau_s(T) = \tau_s(T_o) * (-0.061 \ln(T) + 1.2116) \quad (5.2)$$

$$E_h(T) = E_h(T_o) * (-0.173 \ln(T) + 1.5236) \quad (5.3)$$

$$\tau_h(T) = \tau_h(T_o) * (-0.151 \ln(T) + 1.4753) \quad (5.4)$$

Where T is the temperature in Celsius.

Figure 6.2 presents an example of the evolution of the equivalent strain and equivalent Young's modulus in the top layer of the film during drying of Latexes 10, 15 and 17. Figure 6.2a shows the effect of the particle size on the evolutions of the strain and Young's modulus for one cell of 2000 particles surrounded by other cells (reference cell). Figures 6.2b and 6.2c present the evolutions for a cubic box and the top layer, respectively. The figure shows that the equivalent Young's modulus increased with deformation. That is because of closing the gaps between the particles. The relaxation time τ was taken as a fixed average value equal to 0.083s for each cell at 23°C, 55% RH. That is because the coarse graining to cell scale has no significant effect on

the relaxation time with relative deformation time, so the average value (0.083 s) is applied to each cell all over the deformation time.

Coarse graining resulted in a substantial reduction in the computational time that passed from 228 computing hours for simulating 17000 particles to 20 minutes for simulating $1.7 \cdot 10^8$ particles. The simulations were carried out using the same server (one node with 32 cores of 2.3 GHz processing speed with 128 GB Ram)

Table 6.4 Parameters used in the simulation as measured or estimated in Chapter 3.

Parameter	Value	Determination mode
γ_P	36.6 mN/m	Determined experimentally
$\gamma_{p/w}$	7.2 mN/m	Determined experimentally
E_s	$5.9 \cdot 10^4$ Pa	Estimated by fitting the beam-bending experiments with latexes containing an average of 2.25 wt% of AA.
E_h	$6.8 \cdot 10^7$ Pa	Estimated by fitting the beam-bending experiments with latexes containing an average of 2.25 wt% of AA.
τ_s	0.0082 s	Estimated by fitting the beam-bending experiments with latexes containing an average of 2.25 wt% of AA.
τ_h	0.109 s	Estimated by fitting the beam-bending experiments with latexes containing an average of 2.25 wt% of AA.
Force per particle for cracking	$3.5 \cdot 10^{-9}$ N	Determined experimentally

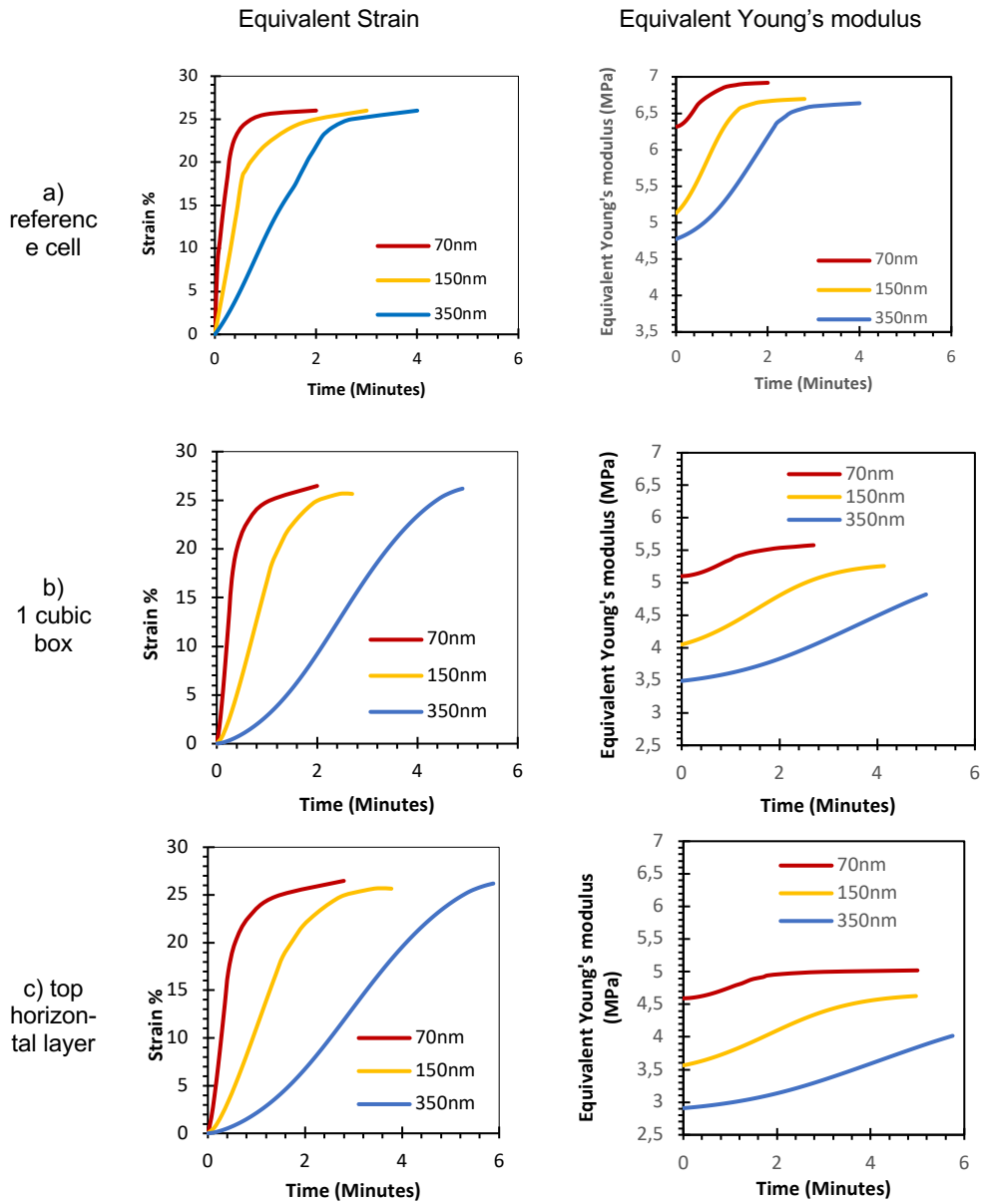


Figure 6.2 Simulation of the effect of the particle size on the evolution of the strain and equivalent Young's modulus in the top layer of the film during drying of Latex 10, 15 and 17 dried at 23 °C and 55% relative humidity. (a) 2000 particles reference cell, (b) a cubic box and (c) top horizontal layer.

Figure 6.3 presents the predictions of the mathematical model for the stress development during drying of films with different film thickness (100, 200, 300, 500 and 1000 μm) of soft core-hard "shell" latexes with different particle sizes (Latexes 10, 11, 15-17). These latexes contained an average of 2.25 wt% of acrylic acid and the critical failure force considered was $F_{\text{crit}} = 3.5 \cdot 10^{-9}$ N. In these figures, cracking appeared as a sudden decrease of the stress. The predicted CCT was the largest thickness for which cracking was not predicted. This means that for Latex 10 (70 nm, Figure 6.3a), the CCT was considered to be 500 μm .

Table 6.5 presents a comparison between the predicted and experimentally measured CCT. It can be seen that the model agreed quite well with the experimental CCTs. Stress increased with film thickness, and at a given thickness, the tension force per particle was higher than the critical value ($3.5 \cdot 10^{-9}$ N) and cracking occurred. Figure 6.3 shows that cracking occurred at lower stress for larger particles, simply because the cohesion of the films (contact points per unit volume) was lower. Therefore, although the stress generated increased as particle size decreased, the films did not crack because they were more cohesive.

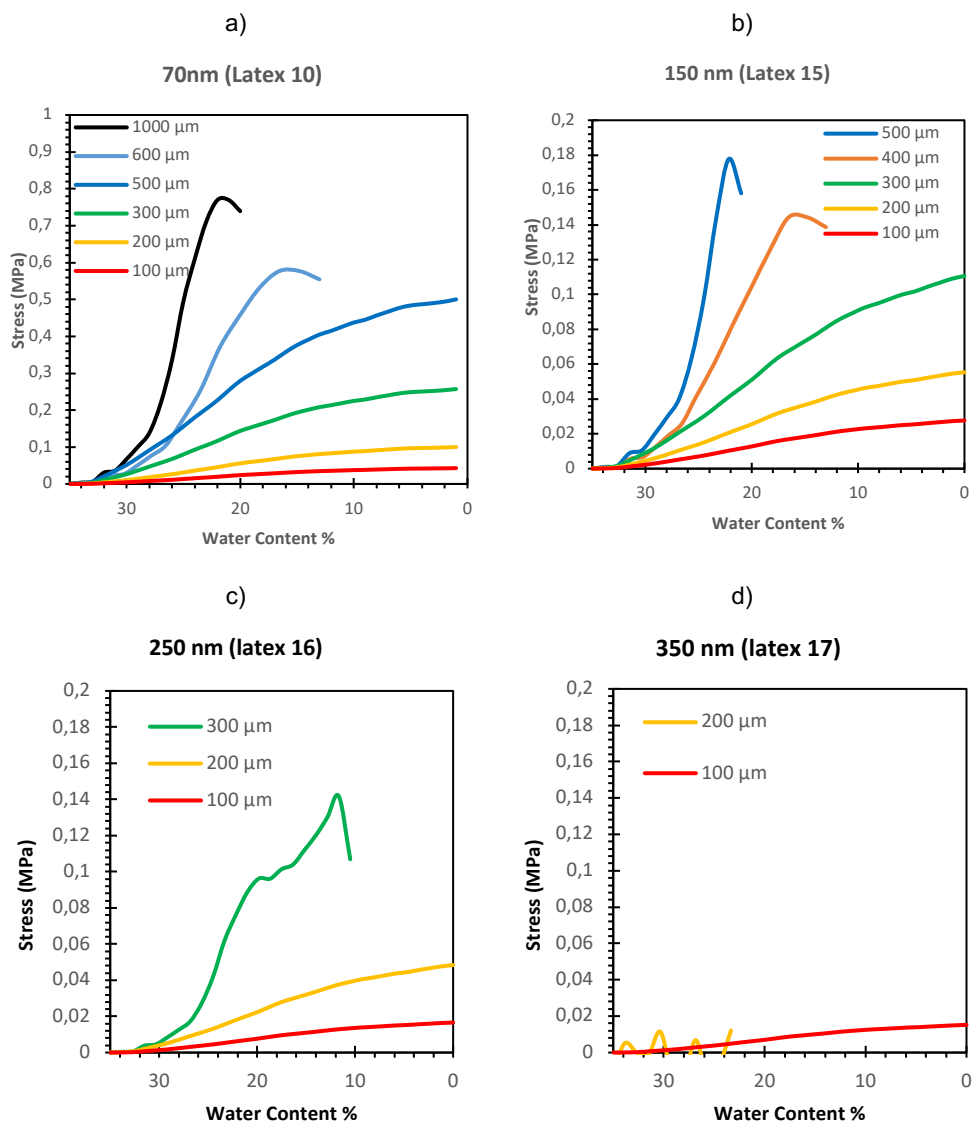


Figure 6.3 Stress development predictions during drying of soft core-hard “shell” latexes with different particle sizes (Latexes 10, 15-17) with different film thickness (100, 200, 300, 500 and 1000 μm). Drying conditions: 23 $^{\circ}\text{C}$, 55% RH.

Table 6.5 Comparison between the predicted and the experimentally measured CCT for experiments where the particle size and AA content were varied.

latex	dp (nm)	AA% Core	AA% shell	measured CCT (μm)	Predicted CCT (μm)
10	70	2	3	500	500
11	90	2	3	200	300
15	150	2	3	250	300
16	250	2	3	125	200
17	350	2	3	80	100
18	95	0	0	50	50-100
20	91	3	3	800	900

Figure 6.4 presents the model predictions for the effect of the relative humidity on the stress development during drying of a 300 μm thick film cast from Latex 16. The higher the relative humidity, the lower the stress generated because the drying time was longer, giving more time for the particles to deform. It can be seen that whereas for 55% RH, the model predicted cracking, for 70% and 90% RH, the model predicted the formation of crack-free films, while the experimental results revealed that cracking was formed only at 70% RH on glass substrate, as shown in Chapter 2. That shift in results could be because of the change of the used substrates.

Figure 6.5 presents the predictions of the model for the effect of the drying temperature on the stress generation on a rigid substrate for Latex 16. Equations 6.1-6.4 obtained in Chapter 3 were used to account for the effect of the temperature on Young's modulus and relaxation time. It can be seen that the model predicted cracking only when the drying temperature was 23 $^{\circ}\text{C}$. No cracking was predicted neither at 35 $^{\circ}\text{C}$ nor at 50 $^{\circ}\text{C}$. On the other hand, the experimental observations presented cracking at 35 $^{\circ}\text{C}$, while no cracking was observed at higher temperatures (Chapter 2).

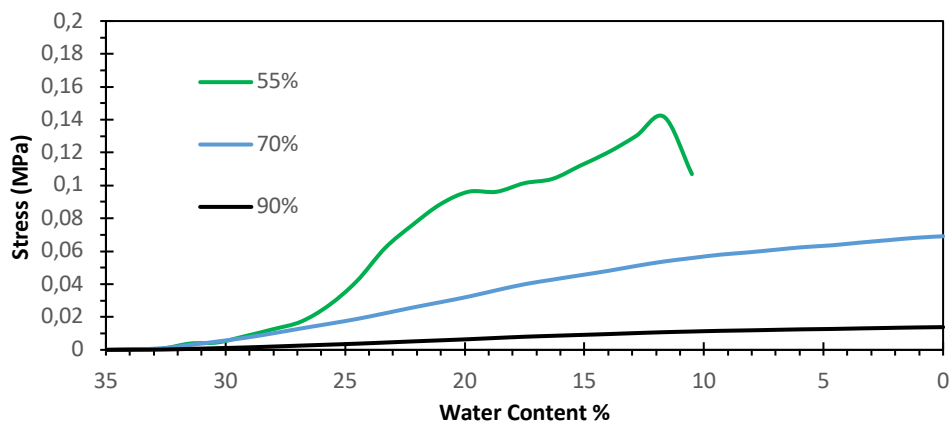


Figure 6.4 Stress development predictions during drying of soft core-hard “shell” latex 16 ($d_p = 250\text{nm}$) at drying temperature 23°C with film thickness $300\ \mu\text{m}$.

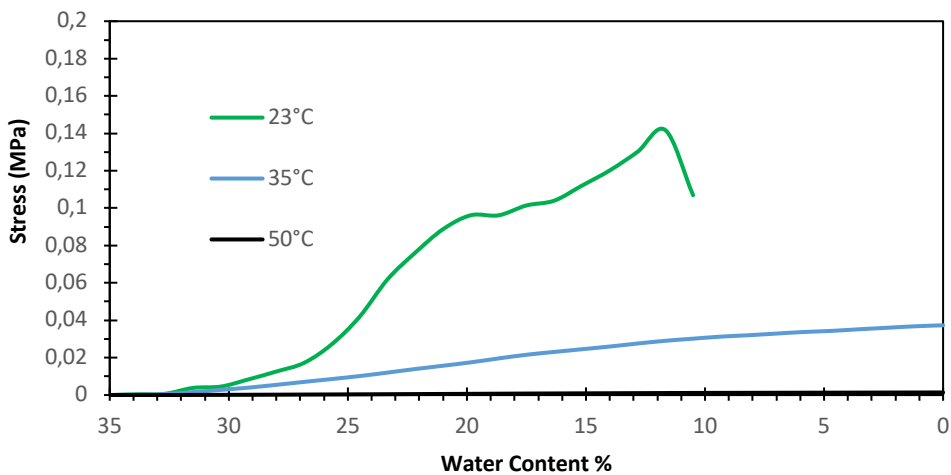


Figure 6.5 Stress development predictions during drying of soft core-hard “shell” latex 16 ($d_p = 250\text{nm}$) at $55\% \text{RH}$ with film thickness $300\ \mu\text{m}$. Experimentally, the film cracked at 23°C and didn’t crack at 35°C nor at 50°C .

The coarse graining strategy was also applied to analyse the effect of the acrylic acid (AA) content on CCT. Latexes 18, 11 and 20 respectively containing 0%, 2% and 3% of AA (Table 6.2) were compared. The experimental values of the CCT were 50, 200 and 800 μm , respectively. The effect of the AA is complex as shown in Chapters 2 and 3. On one hand, the adhesion between particles increases because the high number of H-bonds. This resulted in an increase of the critical force for cracking that in Chapter 3 was quantified as

$$\text{Force} = 10^{-9} \text{AA}^2 - 10^{-9} \text{AA} + 2 \cdot 10^{-10} \quad (5.5)$$

where AA is the acrylic acid content (%). Another effect is that AA reduces the drying rate, allowing more time for the particles to deform, and hence reducing the stress generated. Finally, the acrylic acid may induce hydroplasticization, which would reduce the Young's moduli. As no data on the effect of the hydroplasticization on the Young's moduli are available, in order to avoid any parameter estimation, it was decided to neglect this effect and to use the Young's moduli and relaxation times given in Table 6.4.

Figure 6.6 presents the predictions of the model for different AA contents. The model predicts that the stress increased as AA content decreased, and as the critical force for cracking also decreased (eq. 6.5), this led to lower CCTs. In addition, the predicted CCTs agree quite well with the experimental values (Table 6.2). For 0% AA (Latex 18) the predicted was more than 50 μm and less than 100 μm , which is in well agreement with the experimental findings (50 μm). For 2.3% AA (Latex 11) the predicted CCT (300 μm) was higher than the experimental value (200 μm) and 3% AA (Latex 20) CCT= 900 μm was predicted, while the experimental value was 800 μm .

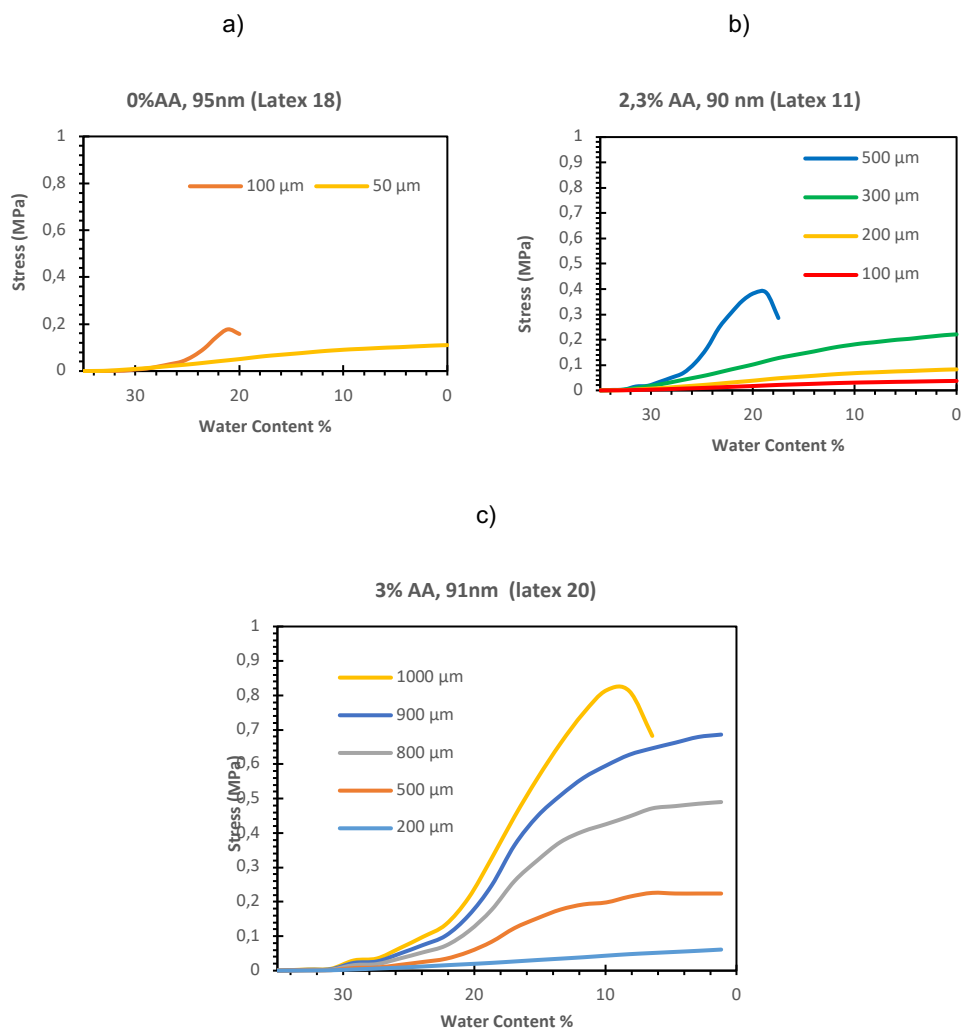


Figure 6.6 Stress development predictions during drying of soft core-hard “shell” a) Latex 18 ($dp=95m$, 0% AA); b) Latex 11 ($dp=90m$, 2-3% AA); and c) Latex 20 ($dp=95m$, 0% AA).

Figure 6.7 presents the predictions of the model for the effect of the film thickness on the evolution of the stress for soft core-hard “shell” latexes of different soft/hard ratios (75/25 for Latex 11 and 70/30 for Latex 27). The increase of the hard phase fraction resulted in a fast

increase of the drying stress due in part to the lower coalescence between the particles, which led to failure of the film at lower CCT. For the 30% of hard phase (Latex 27), there was a very good agreement between experimental results (Table 6.2) and model predictions. Thus, the predicted CCT was less than 100 μm , while the experimental value is equal to 75 μm . On the other hand, for 25% of hard phase, the model predicted a higher CCT (300 μm) than the experimental one (200 μm).

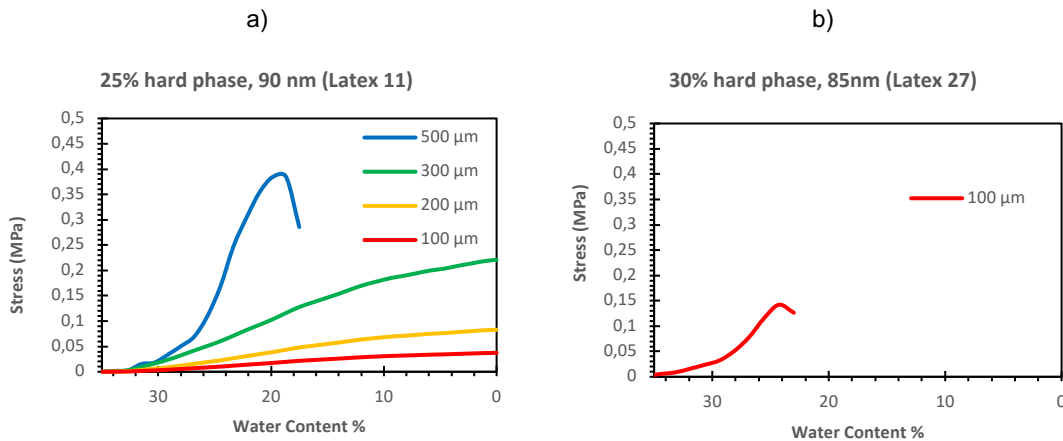


Figure 6.7 Stress development predictions during drying of soft core-hard “shell” a) latex 11 (dp 90m) 25% hard phase fraction and b) latex 27 (dp 85m) 30% hard phase fraction.

It has been reported in Chapter 4 that addition of 1wt% of a small particle size latex to a large latex of the same soft core-hard “shell” morphology resulted in a substantial increase of the CCT. In order to check the versatility of the present approach to simulate complex systems, the film formation of a blend of small (70 nm, 1 wt%) and large (350 nm, 99 wt%) soft core-hard “shell” particles were studied. The small particles were randomly distributed in each cell by

starting the simulation with a 45 wt% solid content (water content 55 wt%, Figure 6.8a). Then, the cell was let to dry until reaching full packing with a solids content of 65% (water content 35%) (Figure 6.8b). Figure 6.9 presents the prediction of the model. It can be seen that the presence of the small particles increased the stress generated during drying, but no cracking was observed for film thickness equal or lower than 300 μm because the film was more cohesive due to the higher number of contacts between particles. The predictions agreed quite well with the experimental data. For 350 nm particles, the CCT was predicted to be 100 μm (experimental value 80 μm). For the blend, the CCT predicted was 300 μm while the experimental value was 250 μm , as shown in Chapter 4.

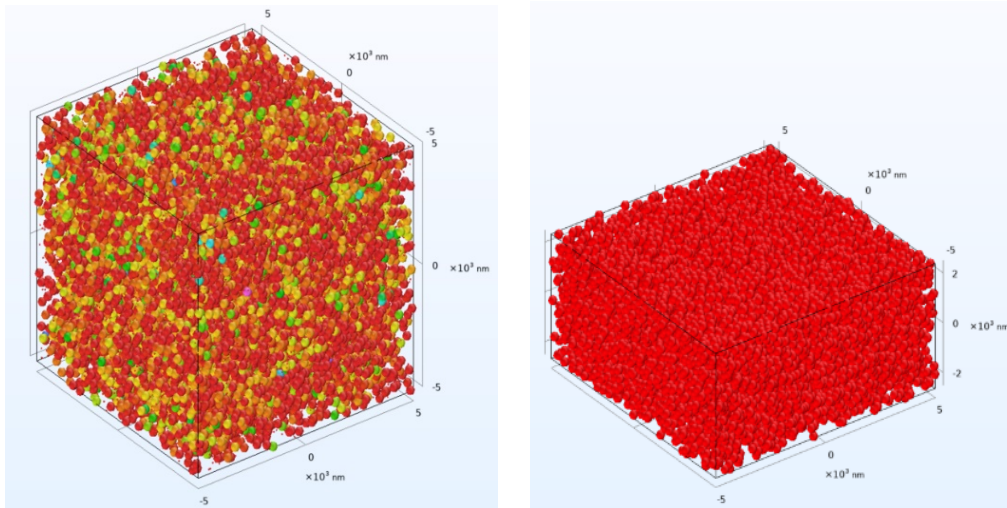


Figure 6.8 The reduction of the cell height from a) 45% S.C to b) 65% S.C to random distribute the small particles (70nm – 1 wt.%) across 350nm particles.

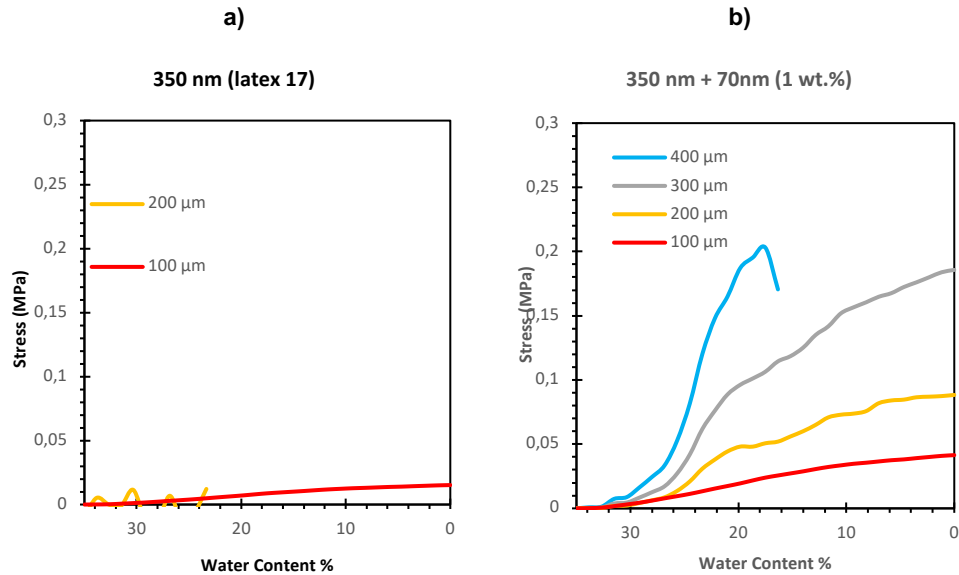


Figure 6.9 The stress evolution for a) pure 350nm latex and b) 350nm+70nm (1 wt. %) layers.

6.4. Conclusions

In this chapter, a new approach to predict crack formation is presented. The model solves the Navier-Stokes and continuity equations in a coarse graining scheme. The model is validated by comparing its predictions with experimental results reported in literature of crack formation during drying of soft core-hard “shell” latexes with different particle size, acrylic acid content and soft/hard phase ratio. Different drying conditions were also considered. It is shown that the model captured remarkably well the experimental findings even though no parameter estimation was carried out. The potential of the approach to handle more complex cases is demonstrated by simulating the film formation of a blend of large and small soft core-hard “shell” latexes.

6.5. References

1. Gromer A. Simulation of Latex Film Formation Using a Cell Model in Real Space: Vertical Drying. *Langmuir*. **2015**, 13, 10983-94
2. Oldroyd. On the Formulation of Rheological Equations of State. *Proc. Roy. Soc. Lon. A, Math. Phy. Sci.* **1950**, 200, 523-541.

Chapter 7. Soft core hard “shell” latex for industrial coatings applications

7.1. Abstract

Acrylic polymer particle latexes are used as binders in architectural or protective paints. The coatings contain pigments and different additives, and the final properties of the paints are affected by the interaction between the binder and other components of the formulation. This may modify the effects observed in the previous chapters for neat films of the latexes. The goal of this chapter is to study the behaviour of the soft core hard “shell” latexes developed in Chapter 2 as binder in waterborne industrial coatings such as wood stains and white paints using industrial formulations. This work of this chapter was carried out at BASF SE in Ludwigshafen, Germany.

7.2. Experimental part

7.2.1. Materials

Tego Foamex 823 (EVONIK) as defoamer, Hydropalat WE3221 (BASF) as a wetting agent, Butyldiglycol (BDG, BASF) as a coalescent agent, Rhevois Pu 1291 (BASF) as hydrophobically modified polyurethanes rheology modifier and Luconyl Yellow 1916 (iron oxide hydrate, BASF) as yellow pigment were used as received. Demineralized water was used throughout the work. The used formula is a commercial formula which is used widely for wood staining and coatings applications application. A commercial wood latex binder is included in the comparison and denoted with CL (commercial latex).

7.2.2. Preparation of waterborne stains and coatings

The previously prepared acrylic hybrid latexes prepared in Chapter 2 were used as binders in the preparation of glossy stains and white paint. For the sake of clarity, the soft core-hard “shell” latexes from Chapter 2 used in the present chapter are presented in Tables 7.1 and 7.2.

- Preparation of glossy stains

The preparation of the glossy stain coatings was done according to the formulation shown in Table 7.3. The latex was mixed with defoamer (Tego Foamex 823), wetting agent (Hydropalat WE3221), coalescent agent (BDG), rheology modifiers (Rhevois Pu 1291), yellow pigment (Luconyl Yellow 1916) and water while stirring at 200 rpm using a disperser (Disperlux). At the end, ammonia was added to adjust the pH to 8 to avoid coagulation during mixing later at higher speed. Then, the dispersion was mixed for 4 minutes at 1000 rpm. The formula was adjusted to

have a viscosity higher than 80KU after 24 hours of mixing. The final solids content (S.C) of all the stains was 35%. For the denomination of the stains, letter **S** was added at the name of the corresponding latex used as binder in the stain. A commercial latex (CL) was used for comparison. The coalescent agent (BDG) was used in the formula because the used formulation is an commonly used industrial formula.

Table 7.1 Latexes with particle size and acidic monomer variations from Chapter 2 used for industrial formulations.

run	seed		core		"shell"		Dowfax 2A1 (wbm)	dp (nm)
	BA/MMA/S/AA (wt/wt)	wt%	BA/MMA/S/AA (wt/wt)	wt%	MMA/AA (wt/wt)	wt%		
10	68/15/15/2	5	68/15/15/2	70	97/3	25	2.89%	70
11	68/15/15/2	5	68/15/15/2	70	97/3	25	2%	90
13	68/15/15/2	2	68/15/15/2	73	97/3	25	1.05%	110
15	68/15/15/2	2	68/15/15/2	73	97/3	25	0.1%	150
20	68/15/15/3	5	68/14/15/3	70	97/3	25	2%	91
21	68/15/15/2	5	68/15/15/2	70	95/5MAA	25	2%	82
22	68/15/15/2	5	68/15/15/2	70	95/5MAA/1.5 EHTG	25	2%	83

Table 7.2 Latexes with different hard phase fraction from Chapter 2 used for industrial formulations.

run	seed		core		"shell"		Dowfax 2A1 (wbm)	dp (nm)
	BA/MMA/S/AA (wt/wt)	wt%	BA/MMA/S/AA (wt/wt)	wt%	MMA/AA (wt/wt)	wt%		
23	68/15/15/2	5	68/15/15/2	75	97/3	20	2%	91
24	68/15/15/2	5	68/15/15/2	72.5	97/3	22.5	2%	92
25	68/15/15/2	5	68/15/15/2	70	97/3	25	2%	90
26	68/15/15/2	5	68/15/15/2	67.5	97/3	27.5	2%	89
27	68/15/15/2	5	68/15/15/2	65	97/3	30	2%	85

Table 7.3 Stain Formulation

Compound	Product	wt. %
Latex	Binder	79.40
Defoamer	Tego Foamex 823	0.50
Wetting agent	Hydropalat WE3221	0.10
Coalescent agent	BDG	2.50
Rheology modifiers	Rhevois Pu 1291	1.90
Yellow pigment	Luconyl Yellow 1916	2.00
Water		13.50
Ammonia	PH adjuster	0.1

- Preparation of white paints

The preparation of the white paint coatings was done using the formulation shown in Table 7.4 by mixing the latex particles with defoamer (Tego Foamex 810), dispersing agent (Dispex CX 4320), coalescent agent (BDG), rheology modifiers (Rhevois Pu 1291), white pigment (Kronos 2190), Filler (omyacrb 5GU), PH adjuster (AMP 90) and water. The mixing was carried out using centrifugal mixer as follows; 800 rpm for 30 sec, then 1000 rpm for 30 sec, then 1250 rpm for 90 sec, then 1600 rpm for 90 sec and finally 1250 rpm for 30 sec. The pH was adjusted to be higher than 8.5 and the viscosity to be higher than 80 KU after 24 hours of mixing. The final solids content of all the white paints was 25%. For the denomination of the stains, letter **P** was added at the name of the corresponding latex used as binder in the paint. A commercial latex (CL) was used for comparison.

Table 7.4 Paint Formulation

Compound	Product	wt. %
Latex	Binder	55.00
Defoamer	Tego Foamex 813	0.60
Dispersing agent	Dispex CX 4320	1.00
Coalescent agent	BDG	2.0
Rheology modifiers	Rhevois Pu 1291	1.13
White pigment	TiO ₂ - Kronos 2190	20.00
Filler	Omyacrb 5GU	5.00
Water		15.22
AMP 90	PH adjuster	0.05

7.2.3.Characterization

1.2.3.1. Latex Characterization

The viscosity was measured using a Stormer Rotation Viscometer at constant speed (200 rpm). The surface hardness was measured using Pendulum surface hardness test (3° König) after 1, 7 and 14 days of drying at 22 °C and 55% relative humidity (RH) The tensile tests were carried out on films with 100 µm dry thickness after 7 days of drying at 22 °C and 55% RH.

The MFFT was measured by applying a film of 100 µm thickness on an aluminium substrate with a gradient in temperature from 0°C to 30°C and visually observing the location of cracking. Each measurement was repeated twice and no noticeable differences were observed. The critical cracking thickness (CCT) on wood was measured by applying different layer thickness 100 µm, 300 µm, 600 µm, 900 µm and 1200 µm on Pine wood and checking visually

at which thickness the cracking appeared. The CCT was taken as the highest thickness that did not present cracks. The cracking density was calculated by applying the layer on an adhesive substrate, which accelerates the cracking tendency (mud cracking) [1]. Five images for each sample were taken using optical microscope at 10X. ImageJ software was used to measure the cracked area and the total image area as shown in Figure 7.1. The cracking density was the ratio between the cracked area over the total area.

Blocking test was carried out by applying a 300 μm wet thickness layer on two identical pieces of wood and leaving them to dry for 24 h at 22 °C / 55% RH. After that, the two pieces were flipped on each other. A weight of 10kg was used to press the two pieces together (resulting in a pressure of 400 g/cm^2) and left for 24 hours at 22 °C/55% RH and 45 °C/55% RH. Then, the samples were separated manually to evaluate the separation and the damage. The separation power has a scale from one to five. One means that the separation was done with no force and five means that the adhesion was extraordinarily strong, and it was impossible to separate the two pieces of wood without breaking the substrate. The damage has a scale from one to five. One means no damage and five means that the layer was totally damaged.

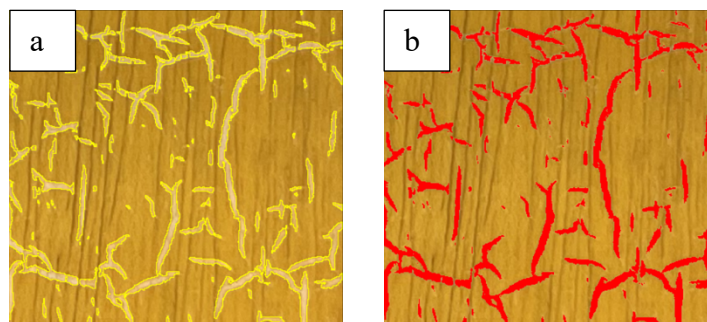


Figure 7.1 An example of measuring the cracking area using image processing of area 1cm X 1cm. a) shows the cracking. Yellow lines were added for clarification. b) shows the measured cracking area. Red areas are added to clarify the measured area.

7.3. Results of wood stains

7.3.1. Effect of the type and content of acidic monomer

In this section, the focus was on investigating the effect of the type and content of carboxylic monomer and the effect of using EHTG as CTA (Latexes 11 and 20-22, Table 7.1) used as binder on the properties of a glossy stain industrial coating.

The MFFT for all the films was less than 4 °C due to the use of a coalescent agent (BDG). Figure 7.2 shows that the CCT increased from 900 μm for 2-3% AA to more than 1200 μm for 3% AA. It should be pointed out that the maximum value for CCT in this test is 1200 μm . Using 5% MAA in the hard phase increased the CCT to more than 1200 μm . Adding 1.5% EHTG as CTA to the hard shell also resulted in a CCT higher than 1200 μm . Mud cracking test was carried out by applying the stain layer on an adhesive substrate with wet thickness 300 μm . Figure 7.3 shows that cracking density decreased with the content of carboxylic monomer. Adding 1.5% EHTG avoided the formation of cracks.

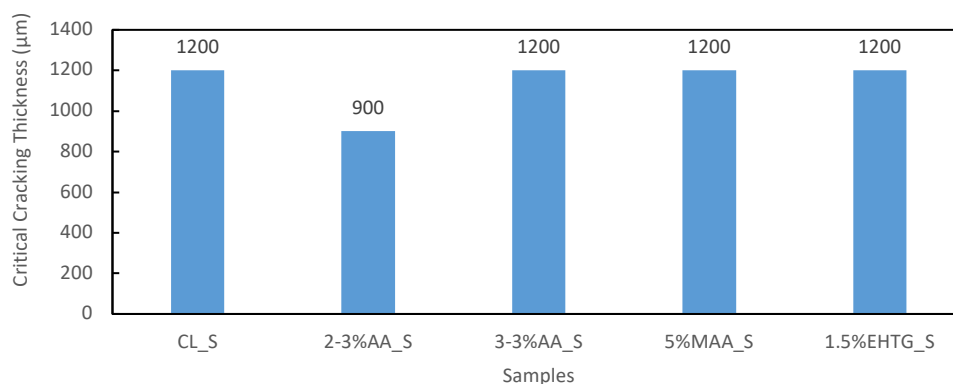


Figure 7.2 Effect of acidic monomer (Stain 11 (2-3% AA), 20 (3-3% AA), 21 (5% MAA) and 22 (1.5% EHTG), Table 7.1) on CCT on pine wood of stains compared to the commercial stain.

The maximum applied layer thickness is 1200 μm .

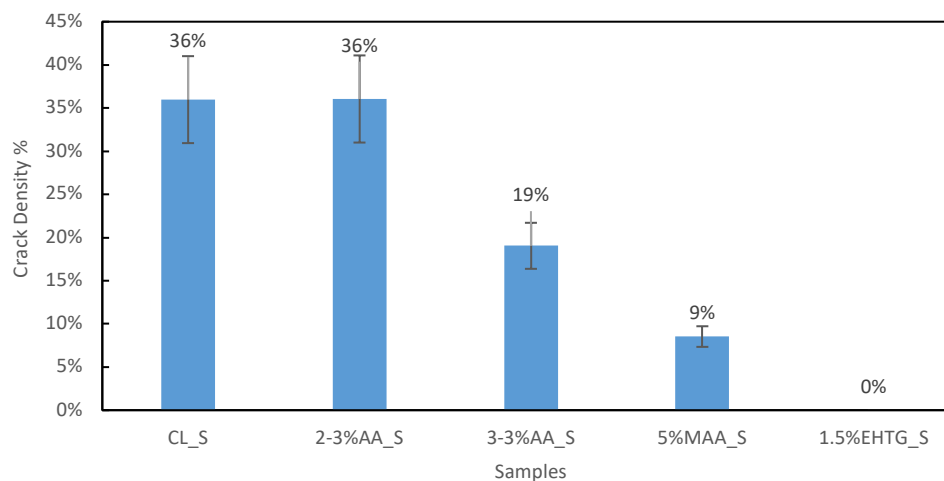


Figure 7.3 Effect of acidic monomer (Stain 11 (2-3% AA), 20 (3-3% AA), 21 (5% MAA) and 22 (1.5% EHTG), Table 7.1) on mud cracking test. Film wet thickness = 300 μ m

Figure 7.4 presents the effect of the acid content on the blocking test at (a) at 22 °C / 55% RH and (b) at 45 °C / 55% RH. It can be seen that at room temperature, there was no effect of the type and content of carboxylic monomer. The samples presented low separation force and no damage. Adding 1.5% EHTG made the latex too sticky and increased the separation power to 3 and the layer damage to 2 at 22 °C. At 45°C, the sample with 3%AA, increased the damage to 2 compared to 1 with 2%AA. The sample with 5%MAA had the same blocking properties than the 2%AA sample. The sample with 1.5% EHTG showed very poor blocking properties.

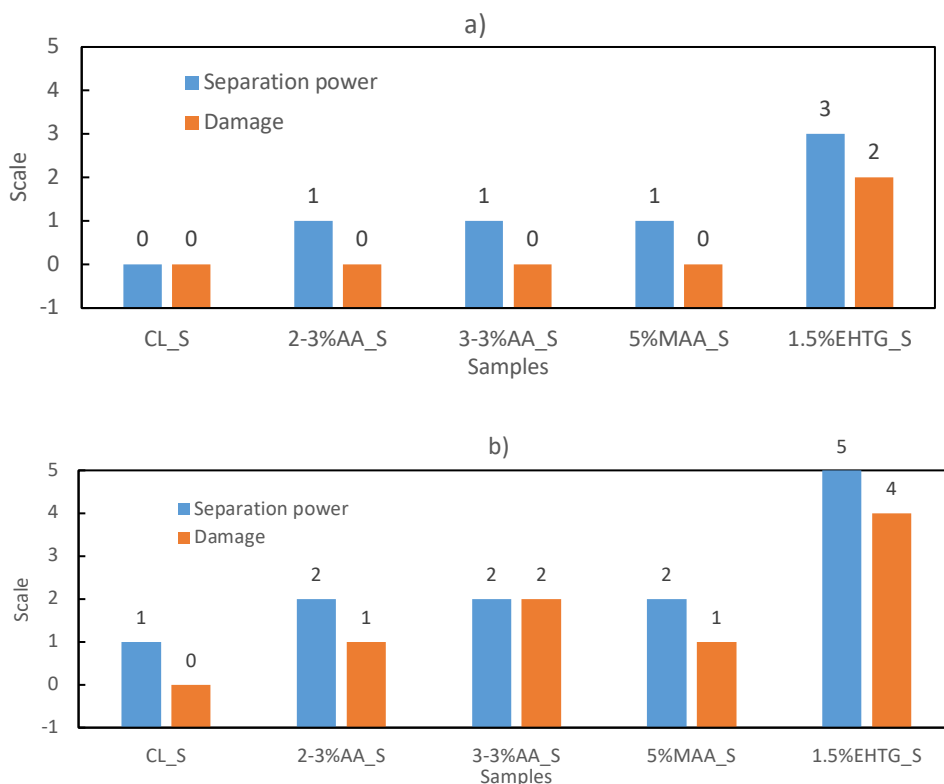


Figure 7.4 Effect of acidic monomer (Stain 11 (2-3% AA), 20 (3-3% AA), 21 (5% MAA) and 22 (1.5% EHTG), Table 7.1) on blocking at a) 22°C / 55% RH and b) 45°C / 55% RH

The mechanical properties of the films are presented in Figure 7.5. The results of the tensile tests are shown in Figure 7.5-a. The Ultimate Tensile Strength (UTS – N/mm²) of the films decreased from 7.62 MPa to 6.81 MPa by increasing the AA% from 2-3% to 3%. That could be due to a small amount of water moieties trapped in the film even after drying because the films were dried at 23°C / 55% RH without vacuum. On the other side, using 5% MAA increased the UTS to 8.67 MPa and decreased the maximum strain % from 173% to 153.72%. Using 1.5% EHTG decreased the UTS to 2.25 MPa and increased the maximum strain to 409%. The surface hardness (Figure 7.5-b) is measured after 1, 7 and 14 days. It shows that the surface hardness

of the layers increased with time. It can be seen that surface hardness decreased with the AA content. 5% of MAA provided the same surface hardness than that of 2%AA, the stiffer backbone of the MAA seems to compensate the effect of the higher content of carboxylate moieties. Adding 1.5% EHTG severely decreased the surface hardness.

From these experiments, it can be seen that the soft core-hard “shell” latexes containing 5% of MAA presented a nice set of properties. It is less prone to form cracks that the reference commercial latex has a higher surface hardness and similar maximum strain. It presents slightly worse Ultimate Tensile Strength (UTS) and blocking properties.

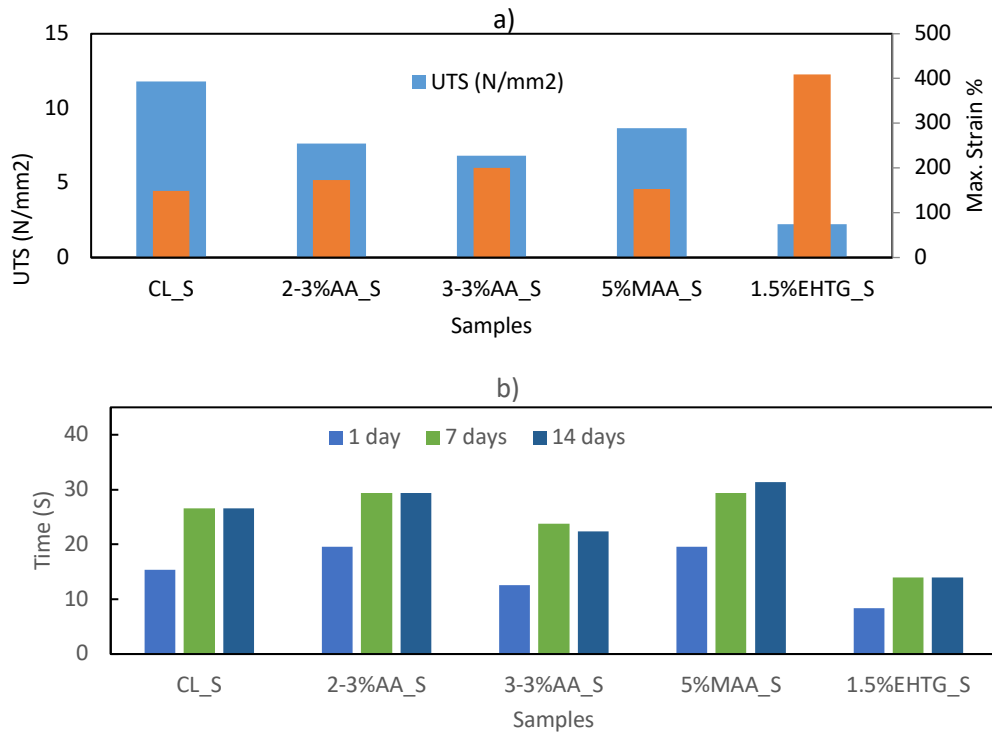


Figure 7.5 Effect of acidic monomer (Stain 11 (2-3% AA), 20 (3-3% AA), 21 (5% MAA) and 22 (1.5% EHTG), Table 7.1) on a) Tensile test mechanical properties and b) Surface hardness test using Pendulum Test (3° Koenig (s)) after 1day, 7 days and 30 days of drying.

7.3.2.Effect of particle size

In this section, the focus was on investigating the effect of the particle size (latex 10-15, Table 7.1) used as binder on the properties of a glossy stain industrial coating.

The MFFT for all the films was less than 4°C. Figure 7.6 shows the effect of particle size on CCT on pine wood. The CCT decreased with increasing the particle size. CCT was more than 1200 µm for 70 nm particle size decreasing to 300 µm for 150 nm. This is in agreement with the observations in Chapter 2 for the neat latexes.

Figure 7.7 shows the effect of the particle size on the cracking density of the mud cracking test. It shows that it was easier to form cracks as particles size increased. The film formation behaviour is not the same on pine wood as on the adhesive substrate. That could be because the smaller particles have more contact points with the adhesive substrate, which hinders their movement under drying shrinkage due to water evaporation, which generated higher tensile stress between the particles. That leads to a higher cracking tendency (higher cracking density) in the dried film.

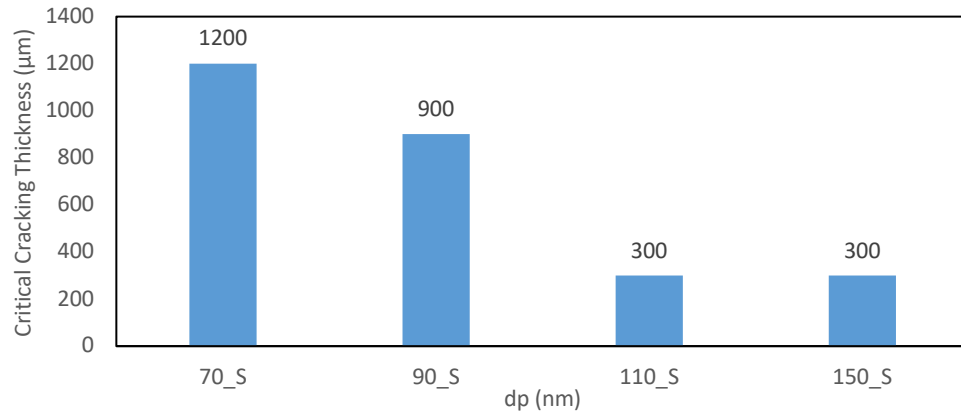


Figure 7.6 Effect of particle size (Stain 10 (70nm), 12 (90nm), 13 (110nm) and (150nm) 15, Table 7.1) on CCT on pine wood of stains

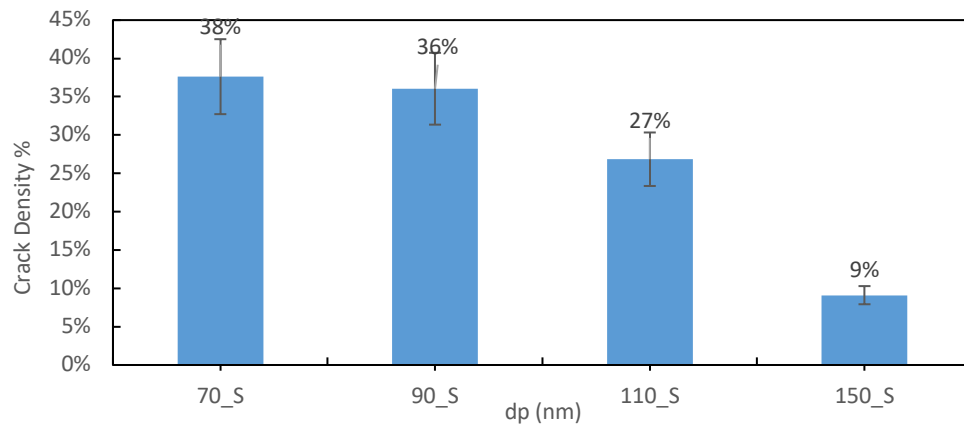


Figure 7.7 Effect of the particle size (Stain 10 (70nm), 12 (90nm), 13 (110nm) and (150nm) 15, Table 7.1) on the cracking density of mud cracking test.

Figure 7.8 presents the effect of the particle size on the blocking test at 22 °C / 55% RH and at 45 °C / 55% RH. It can be seen that there was no effect of the particle size on the separation power and the damage at 22 °C. All the samples presented low separation force and no damage at 22 °C. On the other side, all the samples needed moderate separation power 3 of the scale 1-5 at 45°C. The smallest particles size (70 nm) showed higher damage compared to

the larger particles. That may be because in this latex the hard phase has higher contact area between the soft phase, then the interdiffusion between the soft phase and the hard phases is higher with reduces the hardness of the hard phase. As shown in Figure 2.13, the peak of the hard phase T_g is shifter to lower T_g when the particle size is decreased.

The mechanical properties of the films are presented in Figure 7.9. The surface hardness (Figure 7.9 - a) is measured after 1, 7 and 14 days. It shows that the surface hardness of the layers increased with time, and it reached a plateau after 7 days. It also shows that the surface hardness decreased with increasing the particle size. This may be because the smaller particle sizes have a closer hard phase honeycomb structure which did not allow the flow of the soft phase outside of the structure (Figure 2.12 - a). For bigger particle sizes, the hard phase presents a lose hard honeycomb structure which may allow to the soft phase to flow outside reducing the surface hardness (Figure 2.12 - c). The results of the tensile test are shown in Figure 7.9 – b. There was no significant effect of the particle size on the Ultimate Tensile Strength (UTS – N/mm²) of the films. On the other side, the maximum strain % of the film increased from 173% for 70nm particle size to 237% for 150 nm particle size. That was due to the smaller size of the honeycomb structure has stiffer properties, which is hindering the elongation or the deformation of the film.

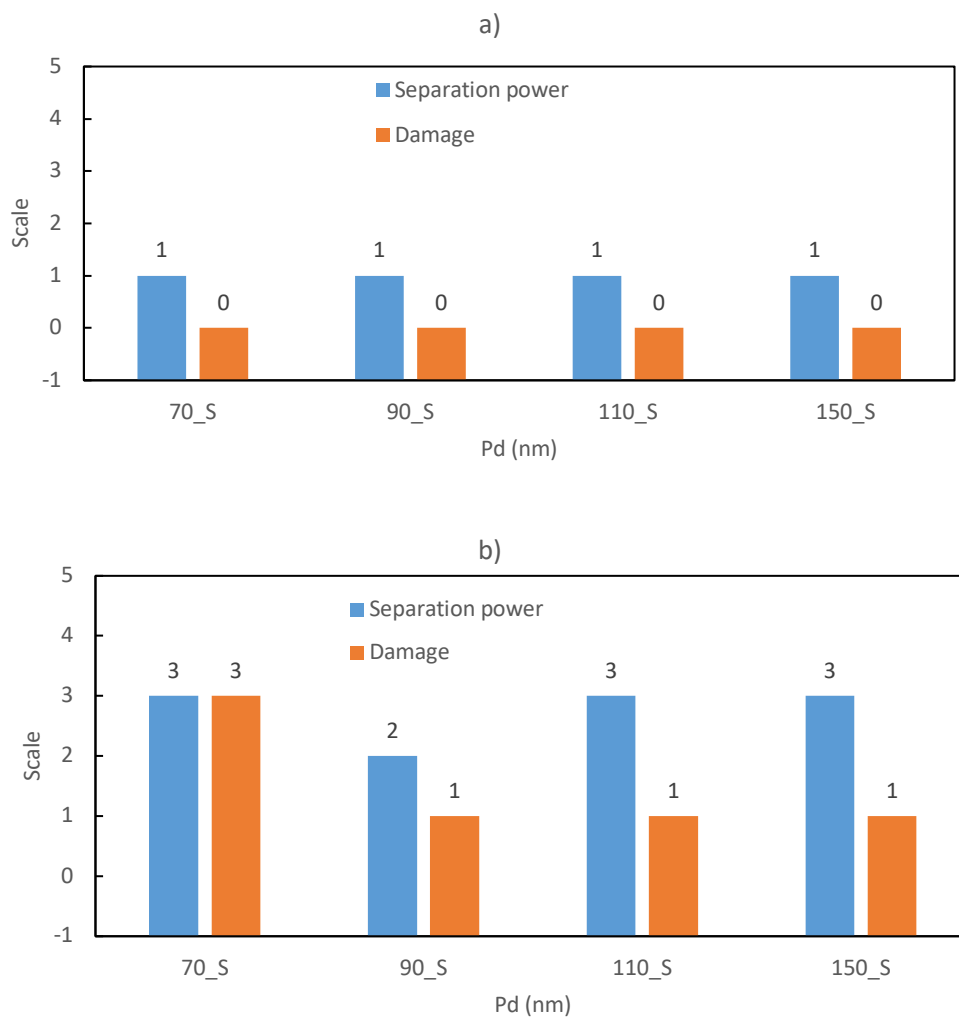


Figure 7.8 Effect of the particle size (Stain 10 (70 nm), 12 (90 nm), 13 (110 nm) and (150 nm) 15, Table 7.1) on blocking at a) 22°C / 55% RH and b) 45°C / 55% RH

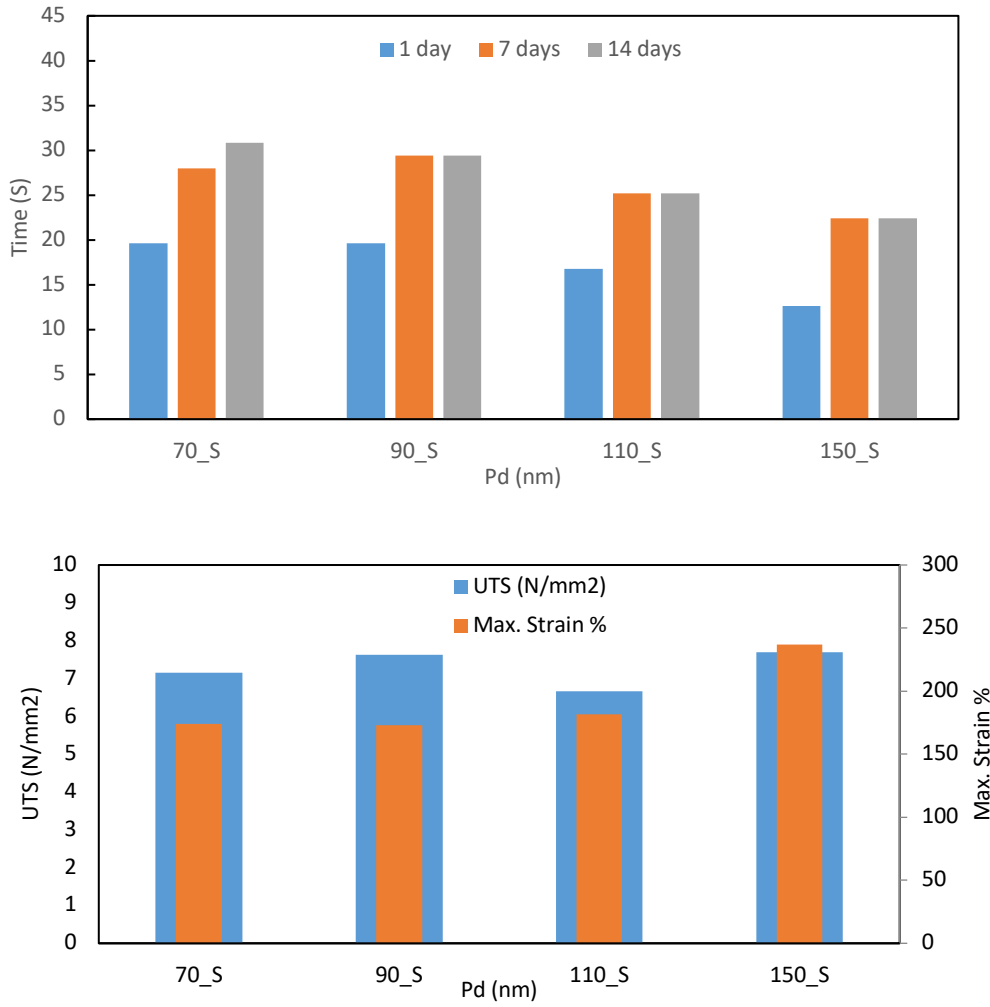


Figure 7.9 Effect of the particle size (Stain 10 (70 nm), 12 (90 nm), 13 (110 nm) and (150 nm) 15, Table 7.1) on a) Surface hardness test using Pendulum Test (3° Koenig (s)) after 1day, 7 days and 30 days of drying and b) Tensile test mechanical properties.

7.3.3. Effect of hard phase content

In this section, the focus was on investigating the effect of the hard phase fraction in the polymer particles (Latex 23-27, Table 7.2) used as binder on the properties of a glossy stain industrial coating.

The MFFT for all the films was less than 4°C for 100µm thick films. Figure 7.10 shows that the CCT of the stain cast on pine wood decreased with the hard phase content. Figure 7.11 shows that the cracking density increased with the hard phase when its content was higher than 22.5%.

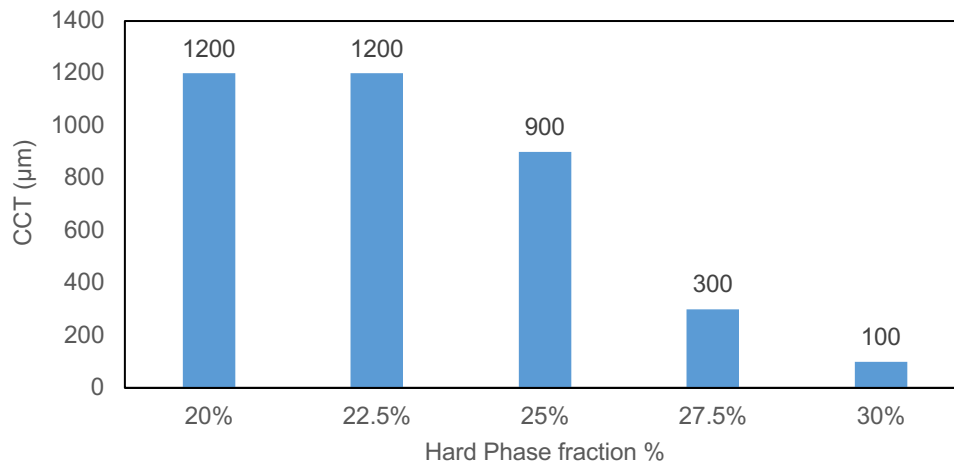


Figure 7.10 Effect of hard phase fraction (Stain 23 (20% hard phase) – 27 (30% hard phase), Table 7.2) on CCT on pine wood of stains

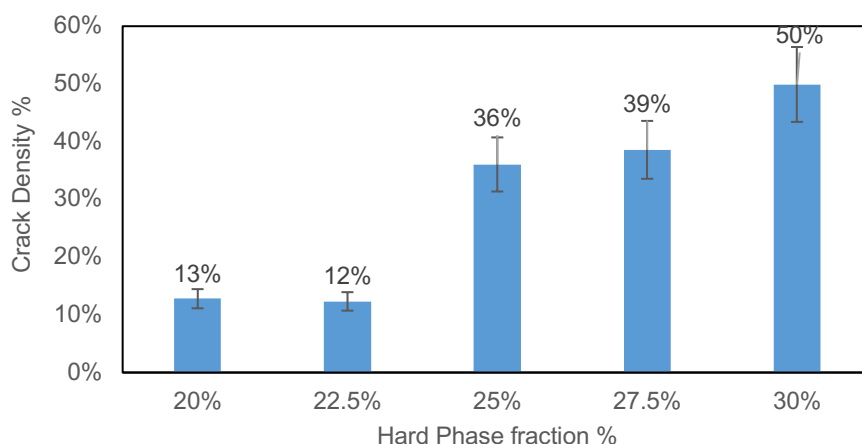


Figure 7.11 Effect of hard phase fraction (Stain 23 (20% hard phase) – 27 (30% hard phase), Table 7.2) on the cracking density of mud cracking test. Film wet thickness 300 μ m.

Figure 7.12 presents the effect of the hard phase content on the blocking test at 22 °C / 55% RH and at 45 °C / 55% RH. The figure shows that latexes containing 20 and 22.5% of hard phase did not present good blocking characteristics, mainly at 45°C. Samples with higher hard phase content showed relatively better results. The mechanical properties of the films are presented in Figure 7.13. The surface hardness (Figure 7.13-a) is measured after 1, 7 and 14 days. It shows that the surface hardness increased with the content of hard phase %. The hardness reached stability after 7 days for all the samples. The results of the tensile test are shown in Figure 13-b. The Ultimate Tensile Strength (UTS – N/mm²) increased from 5.5 MPa for 20% hard phase film to 12 MPa for 30% hard phase film. On the other side, the maximum strain % decreased from 340% for 20% hard phase film to 110% for 30% hard phase film.

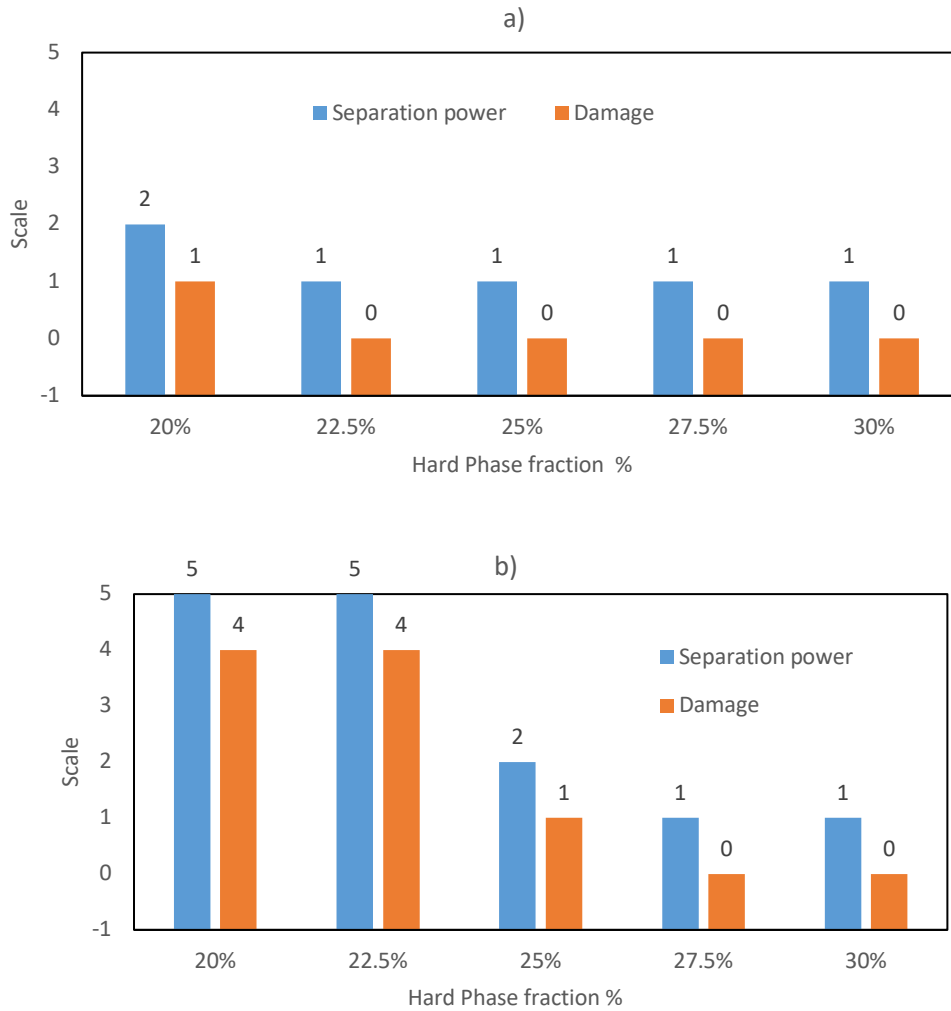


Figure 7.12 Effect of hard phase fraction (Stain 23 (20% hard phase) – 27 (30% hard phase), Table 7.2) on blocking at a) 22°C / 55% RH and b) 45°C / 55% RH

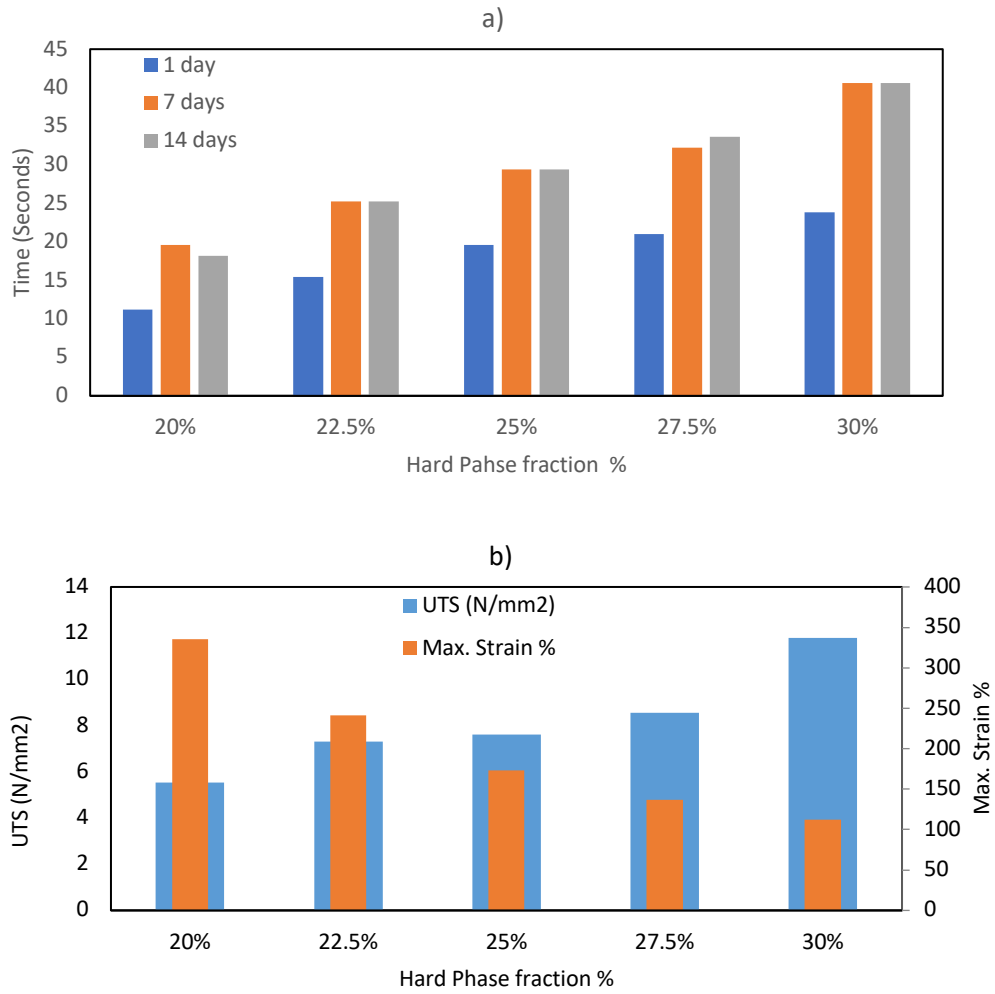


Figure 7.13 Effect of hard phase fraction ((Stain 23 (20% hard phase) – 27 (30% hard phase), Table 7.2) on a) Surface hardness test using Pendulum Test (3^o Koenig (s)) after 1 day, 7 days and 30 days of drying and b) Tensile test mechanical properties.

7.4. Results from white paints

Regarding the white paints, we found that only the type and content of carboxylic monomer and the use of EHTG as CTA (latex 11 and 20-22, Table 7.1) had a significant effect on the properties of the white paint industrial coating.

The MFFT for all the films was less than 4 °C for 100 µm thick films due to the use of a coalescent agent (BDG). Moreover, the CCT on pine wood was higher than 1200 µm for all the samples. The mud cracking test was carried out by applying the paint on an adhesive substrate with a wet thickness 300 µm. Figure 7.14 shows that all samples have a comparable cracking density to the commercial paint around 40%, except for Paint 22 (1.5% EHTG). It had a lower cracking density % (5%), due to the easy flow of hard phase chains because of the lower molecular weight.

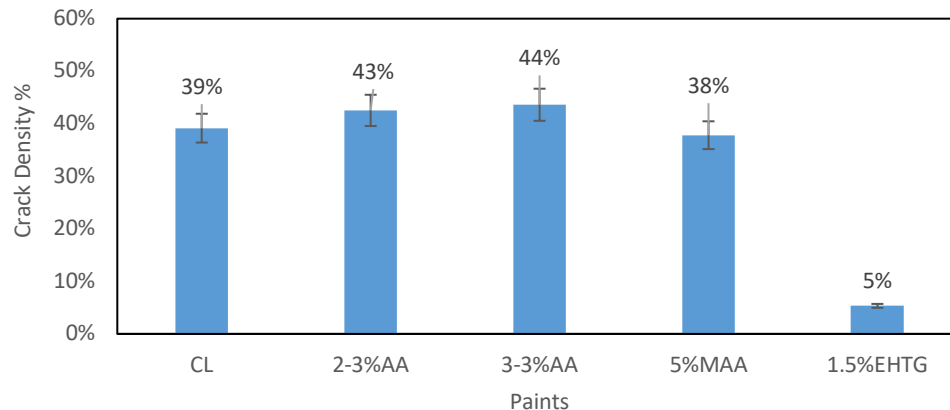


Figure 7.14 Effect of acidic monomer (Paint 11 (2-3% AA), 20 (3-3% AA), 21 (5% MAA) and 22 (1.5% EHTG), Table 7.1) on cracking density

Figure 7.15 presents the results of the blocking test at 22 °C/55% RH and at 45 °C/55% RH. It can be seen that except for the latex produced with CTA, all the latexes had a very good blocking performance. The latex with 1.5% EHTG was softer due to the easier movement of the lower molecular weight hard phase chains and showed a higher separation power and some damage at 45 °C.

The mechanical properties of the coatings are presented in Figure 7.16. The surface hardness (Figure 7.16-a) is measured after 1, 7 and 14 days. The surface hardness increased with time. Increasing the AA5 from 2% to 3% has no significant effect on the surface hardness, while 5% MMA has slightly increased the surface hardness. Reduction of the molecular weight of hard phase polymer chains by using a CTA resulted in a severe decrease of the surface hardness. The results of the tensile test are shown in Figure 7.16-b. The Ultimate Tensile Strength (UTS – N/mm²) of the film increased with the content of carboxylic monomer. Interestingly, the UTS and the maximum strain increased with increasing the AA5 to 3%. 5% MMA has increased the UTS but decreased the maximum strain. Using 1.5% EHTG decreased the UTS to 7.5 MPa and increased the maximum strain to 179%.

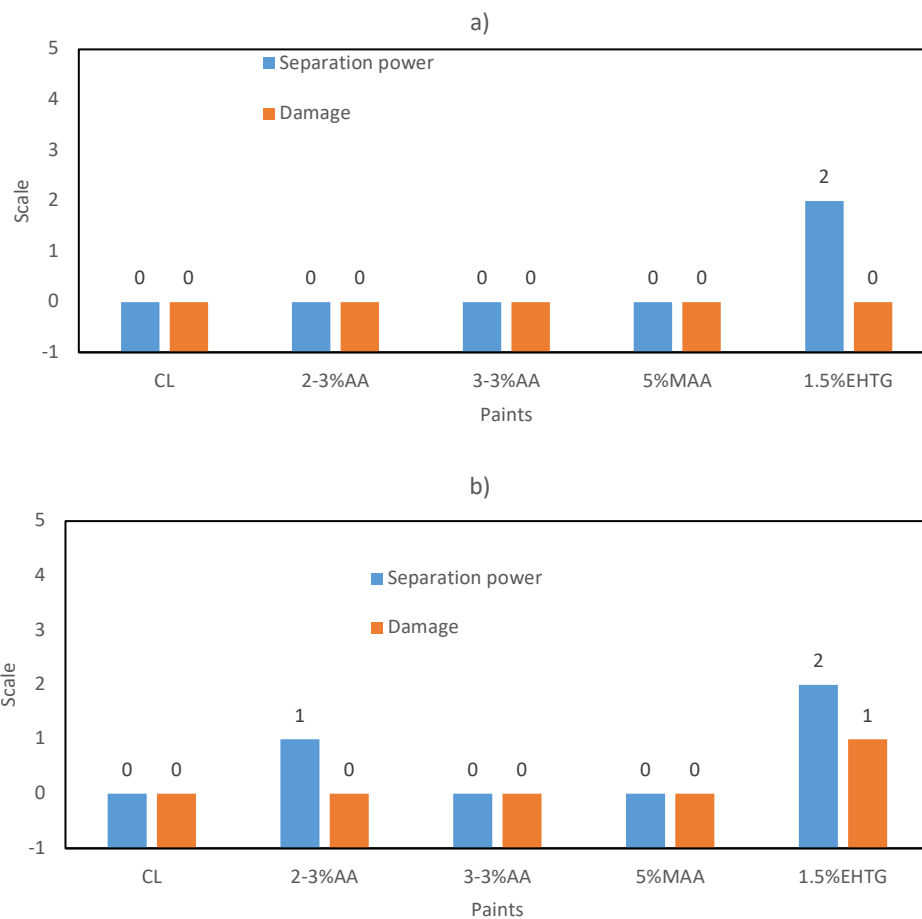


Figure 7.15 Effect of acidic monomer (Paint 11 (2-3% AA), 20 (3-3% AA), 21 (5% MAA) and 22 (1.5% EHTG), Table 7.1) on blocking at a) 22°C / 55% RH and b) 45°C / 55% RH

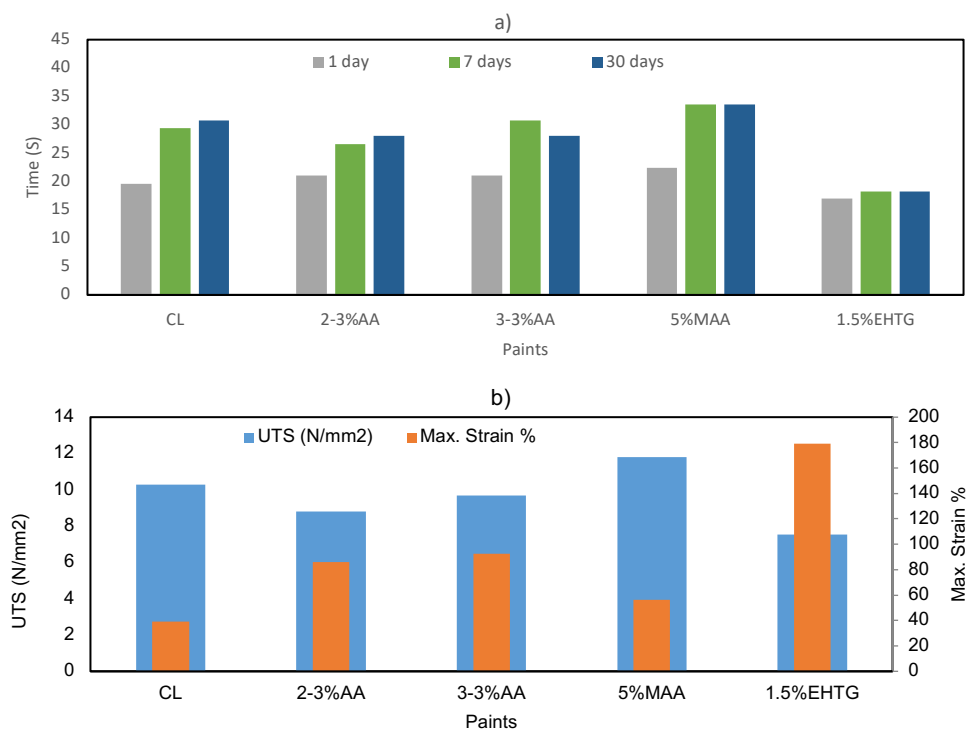


Figure 7.16 Effect of acidic monomer (Paint 11 (2-3% AA), 20 (3-3% AA), 21 (5% MAA) and 22 (1.5% EHTG), Table 7.1) on a) Surface hardness test using Pendulum Test (3^o Koenig (s)) after 1day, 7 days and 30 days of drying and b) Tensile test mechanical properties.

7.5. Conclusions

Latexes with soft core hard / "shell" particles were synthesized by two stage semicontinuous emulsion polymerization with different particle characteristics like variation of acidic monomer, particle size and hard phase fraction and previously characterized as neat latex in Chapter 2. In this chapter, the behaviour of those latexes was evaluated as a binder in waterborne industrial wood stains and white paints using commercial formulations. The results were compared with an industrial latex. The behaviour of the neat latexes translated quite well to those of the stains and the paints. It was found that increasing the AA%, reduced the tendency

for cracking and made softer the films. Increasing the particles size, decreased the CCT and the surface hardness with no significant effect on the film ultimate strength. Finally, increasing the hard phase content increased the tendency for cracking and also increased the film surface hardness and the mechanical properties. The studied latexes have presented competitive results compared to the commercial one. In the context of the work of this thesis, this is a significant result as it suggests information about the structure / property relation of latex films can be directly translated into the formulated product.

7.6. References

1. H. Abdeldaim, B. Reck, K.J. Roschmann, J.M. Asua, Cracking in films cast from soft core-hard shell waterborne dispersions, *Macromolecules* 2023, 56, 9, 3304–3315.

Chapter 8. Conclusions

With the aim of reducing VOC emissions and producing more sustainable coatings and adhesives, solventborne polymers are gradually being replaced by water-based alternatives. However, the mechanical properties of waterborne systems are typically not as good as those of solventborne products due to differences in the film formation process and this has limited the widespread use of waterborne polymers in some demanding applications that require high mechanical strength. Industrially, volatile plasticizing agents are commonly added to enable film formation of high T_g dispersions and produce mechanically resistant polymer films. However, the need for a volatile plasticizer brings back the environmental concerns related to the release of VOCs to the atmosphere. Another possibility is to use hybrid particles with soft and hard polymer domains. Whereas the soft polymer facilitates film formation, the hard polymer provides good mechanical properties like block resistance. In this type of coatings, particle morphology plays a critical role. Hard core/soft shell and soft core/hard shell morphologies represent the two extreme cases. Easy film formation is guaranteed by the first one that will lead to a film of soft polymer reinforced by hard inclusions. However, the improvement of the mechanical properties is limited because the soft phase is the continuous medium of the film. Soft core-hard shell waterborne dispersions lead to better mechanical properties because the hard phase formed a honeycomb structure filled with soft polymer. However, the presence of hard phase at the surface of the

particles creates stress during film formation that often leads to cracking, which is catastrophic for substrate protection

This work aims at shedding some light on cracking to be able to design soft core-hard "shell" latexes that yield VOC and crack free, mechanically strong coatings that can be cast at low temperatures. These are particles consisting of a soft core covered by patches of hard polymer. This morphology is less prone to cracking than the perfect core-shell morphology. In Chapter 2, the work reports on a thorough study of the effect of the particle characteristics (size, soft/hard phase ratio, presence of carboxylic moieties, molar mass of the hard phase, glass transition temperature of the soft phase) and drying conditions (temperature, relative humidity, thickness of the film, type of substrate) on the stress generation, crack formation and mechanical properties of the films. A detailed characterization of the morphology of both particles and films was used to analyse these macroscopic results. It was found that the particles consisted of a soft core that was covered with patches of hard polymer. The fact that the hard polymer did not form a continuous shell allowed deformation and coalescence of the particles that yielded mechanically strong films where the soft polymer filled a rather well-defined honeycomb structure of hard polymer.

Cracks can be formed during film formation due to the stress created because of volume shrinkage and the attachment of the particles to the rigid substrate. Any variable that favours the deformation of the viscoelastic particles decreases the probability of crack formation. Thus, increasing the drying times by increasing the relative humidity or including acidic moieties in the polymer as well as reducing the T_g of the soft core, the molar mass of the hard phase and the effective T_g of the hard polymer by hydroplasticization resulted in smaller stresses and less

cracking. On the other hand, cracking is favoured by increasing the hard phase content and the attachment of the particles to the substrate.

A particularly interesting finding was that CCT increased by decreasing the particle size even though the stress generated was higher for smaller particles. The reason was that the critical stress that the films could withstand increased as particle size decreased. On the other hand, the organization of the honeycomb structure of the hard polymer in the film improved as the particle size decreased, which translated in much higher mechanical strength and hardness, but also in increased brittleness. From a practical point of view, the discovered correlations allow the design of solvent-free latexes able to form crack-free thick coatings of very good mechanical properties.

The experimental results were used to test the existing mathematical models finding that they could not justify the trends observed. Possible reasons for the failure are that the models do not consider the soft core-hard “shell” morphology, that they are mainly developed for elastic particles and the lack of a criterion for crack formation applicable to the present system. In this regard, it is worth to mention that in this work, using with particles of different sizes and films of different thickness, crack appeared when the tension force per particle was about $3.5 \cdot 10^{-9}$ N.

In Chapter 3, a mathematical model for cracking prediction and stress calculation during drying of aqueous dispersions of soft core-hard “shell” particles was developed. The model solved numerically the incompressible Navier-Stokes and continuity equations using COMSOL Multiphysics. The model calculated the stresses generated during film drying on flexible substrate using scaling down technique to limit the solving time. The parameters of the model were either experimentally measured or estimated by fitting the model outputs with the experimental data. The model was validated with experimental data obtained with dispersions

having different particle sizes and content of acidic monomers that were formed under different drying conditions (temperature and relative humidity). A good agreement between experimental results and model predictions was achieved.

In Chapter 4, blends of soft core-hard “shell” particles of different sizes were prepared to go beyond the limits of the film formation which was reached in Chapter 2. It has been observed that adding tiny amounts of small particles (e.g. 1 wt %) to big particles film formation can be substantially improved (lower MFFT and higher CCT). Furthermore, mechanical properties of the films are also improved (higher elongation at break and toughness, maintaining the Young’s modulus and the stress at break), without affecting on the water sensitivity of the film. It has been found that that the viscoelastic properties of small particles must be similar to the large ones in order to have a significant effect.

Chapter 5 explored a strategy of enhancing the mechanical properties of waterborne coatings without compromising the film formation properties of soft core-hard “shell” polymer particles. The approach was based on a multiphase internal core composed by hard and soft domains. This strategy resulted in coatings with higher Young’s modulus, stress at break and toughness, without compromising the film formation characteristics. This was attributed to the interpenetration of the polymers of the soft core and hard inclusions. This resulted in a diffuse structure of the core that on one part, it was soft enough to allow an easy deformation of the particles during film formation, and on the other, increased the Young’s modulus of the core and consequently that of the honeycomb structure.

Chapter 6 overcame the limitation of time needed for solving the Navier-Stokes equations as presented in Chapter 3 through a coarse graining approach. It consists of dividing the three dimensional films into a number of horizontal layers. The number of the layers remained fixed

during the simulation, but each layer was free to change in the three dimensions under the effect of the drying shrinkage of the layer. The model is validated by comparing its predictions with experimental results of soft core-hard “shell” latexes with different particle size, acrylic acid content and soft/hard phase ratio dried under different conditions on hard substrates. It is worth pointing out that the values of the parameters used were those of Chapter 2, namely, no parameter estimation was performed. The potential of the approach to handle more complex cases is demonstrated by simulating the film formation of blend of large and small soft core-hard “shell” latexes. It is found that the model captured remarkably well the experimental findings even though no parameter estimation was carried out. The potential of the approach to handle more complex cases is demonstrated by simulating the film formation of blend of large and small soft core-hard “shell” latexes.

The goal of Chapter 7 was to study the behaviour of the soft core hard “shell” latexes developed in Chapter 2 as binder in waterborne industrial coatings such as wood stains and white paints using industrial formulations. This work of this chapter was carried out at BASF SE in Ludwigshafen, Germany. The properties of the stains and the paints were in the same orders as the latexes films in most of cases. The latexes have presented competitive results compared to the commercial one. In the context of the work of this thesis this is a significant result as it suggests information about the structure / property relation of latex films can be directly translated into the formulated product.

The results presented in this work highlight that careful design of soft core-hard “shell” polymer dispersions allows overcoming the film formation dilemma frequently found in waterborne coatings.

List of publications and conference presentations

Parts of this thesis will be published soon. The list of papers that would be issued from this work is as follows (variation in the paper title might be possible):

H. Abdeldaim, B. Reck, K.J. Roschmann, J.M. Asua, Cracking in films cast from soft core hard shell waterborne dispersions, *Macromolecules* 2023, 56, 9, 3304–3315.

H. Abdeldaim, J.M. Asua, Modelling cracking during film formation of soft core/hard shell latexes

H. Abdeldaim, Edurne González, Noé Duarte, J.M. Asua. Solving the film formation dilemma: blends of soft core-hard “shell” particles

H. Abdeldaim, J.M. Asua, Internally reinforced soft core-hard shell waterborne dispersions for high performance solvent-free coatings

H. Abdeldaim, J.M. Asua, Coarse graining modelling of the film formation from soft core-hard shell waterborne dispersions

Resumen y conclusiones

Con el objetivo de reducir las emisiones de Compuestos orgánicos Volátiles (COV) y producir recubrimientos y adhesivos más sostenibles, los polímeros en base de disolventes se están reemplazando gradualmente por alternativas en base agua. Sin embargo, las propiedades mecánicas de los sistemas acuosos generalmente no son tan buenas como las de los productos en base de disolventes debido a las diferencias en el proceso de formación de películas, lo que ha limitado el uso generalizado de polímeros en base agua en algunas aplicaciones exigentes que requieren una alta resistencia mecánica. En la industria, se suelen agregar agentes plastificantes volátiles para permitir la formación de películas de dispersiones de alta Tg y producir películas de polímero resistente mecánicamente. Sin embargo, la necesidad de un plastificante volátil vuelve a plantear preocupaciones ambientales relacionadas con la liberación de COV a la atmósfera. Otra posibilidad es utilizar partículas híbridas con dominios de polímero blando y duro. Mientras que el polímero blando facilita la formación de la película, el polímero duro proporciona buenas propiedades mecánicas como resistencia al bloqueo. En este tipo de recubrimientos, la morfología de las partículas desempeña un papel crítico. Las morfologías de núcleo duro/corteza blanda y núcleo blando/corteza dura representan los dos casos extremos. La primera garantiza una fácil formación de películas que conducirá a una película de polímero blando reforzada por inclusiones duras. Sin embargo, la mejora de las propiedades mecánicas es limitada porque la fase blanda es el medio continuo de la película. Las dispersiones acuosas de núcleo blando/corteza dura conducen a mejores propiedades mecánicas porque la fase dura forma una estructura de panal de abeja llena de polímero blando. Sin embargo, la presencia de la fase dura en la superficie de las partículas crea tensiones durante la formación de la película que a menudo resultan en grietas, lo que es catastrófico para la protección del sustrato.

Este trabajo tiene como objetivo arrojar luz sobre la formación de grietas para poder diseñar látex de núcleo blando/corteza dura que produzcan recubrimientos mecánicamente fuertes, libres de COV y sin grietas que puedan ser aplicados a bajas temperaturas. Estas partículas consisten en un núcleo blando cubierto por parches de polímero duro. Esta morfología es menos propensa a agrietarse que la morfología perfecta de núcleo-corteza. En el Capítulo 2, se realiza un estudio exhaustivo del efecto de las características de las partículas (tamaño, relación entre la fase blanda/dura, presencia de grupos carboxílicos, masa molar de la fase dura, temperatura de transición vítrea de la fase blanda) y las condiciones de secado (temperatura, humedad relativa, espesor de la película, tipo de sustrato) en la generación de tensiones, formación de grietas y propiedades mecánicas de las películas. Se utilizó una caracterización detallada de la morfología de las partículas y las películas para analizar estos resultados macroscópicos. Se encontró que las partículas consistían en un núcleo blando cubierto con parches de polímero duro. El hecho de que el polímero duro no formara una corteza continua permitió la deformación y coalescencia de las partículas, lo que resultó en películas mecánicamente fuertes donde el polímero blando llenaba una estructura de panal bastante definida de polímero duro.

Las grietas pueden formarse durante la formación de películas debido al estrés creado debido a la contracción de volumen y la adhesión de las partículas al sustrato rígido. Cualquier variable que favorezca la deformación de las partículas viscoelásticas disminuye la probabilidad de formación de grietas. Por lo tanto, aumentar los tiempos de secado aumentando la humedad relativa o incluyendo grupos ácidos en el polímero, así como reducir la temperatura de transición vítrea del núcleo blando, la masa molar de la fase dura y la temperatura de transición vítrea efectiva del polímero duro mediante hidroplastificación, resultó en tensiones más pequeñas y

menos grietas. Por otro lado, el aumento del contenido de fase dura y la adhesión de las partículas al sustrato favorecen la formación de grietas.

Un hallazgo particularmente interesante fue que la temperatura crítica de contracción (CCT) aumentó al disminuir el tamaño de las partículas, aunque el estrés generado fue mayor para partículas más pequeñas. La razón fue que el estrés crítico que las películas podían soportar aumentaba a medida que el tamaño de las partículas disminuía. Por otro lado, la organización de la estructura de panal del polímero duro en la película mejoraba a medida que el tamaño de las partículas disminuía, lo que se traducía en una resistencia mecánica y dureza mucho mayores, pero también en mayor fragilidad. Desde un punto de vista práctico, las correlaciones encontradas permiten el diseño de látex sin disolventes capaces de formar recubrimientos gruesos sin grietas y con muy buenas propiedades mecánicas.

Los resultados experimentales se utilizaron para probar los modelos matemáticos existentes y se encontró que no podían justificar las tendencias observadas. Las posibles razones de la falla son que los modelos no consideran la morfología de núcleo blando/corteza dura, que están principalmente desarrollados para partículas elásticas y la falta de un criterio para la formación de grietas aplicable al sistema actual. A este respecto, vale la pena mencionar que, en este trabajo, utilizando partículas de diferentes tamaños y películas de diferentes espesores, las grietas aparecieron cuando la fuerza de tensión por partícula fue de aproximadamente $3,5 \times 10^{-9}$ N.

En el Capítulo 3, se desarrolla un modelo matemático para la predicción de grietas y el cálculo de tensiones durante el secado de dispersiones acuosas de partículas de núcleo blando/corteza dura. El modelo resuelve numéricamente las ecuaciones de Navier-Stokes y continuidad incompresibles utilizando COMSOL Multiphysics. El modelo calcula las tensiones

generadas durante el secado de películas sobre un sustrato flexible utilizando la técnica de escalamiento para limitar el tiempo de resolución. Los parámetros del modelo fueron medidos experimentalmente o estimados mediante el ajuste de los resultados del modelo con los datos experimentales. El modelo se validó con datos experimentales obtenidos con dispersiones de diferentes tamaños de partículas y contenido de monómeros ácidos que se formaron bajo diferentes condiciones de secado (temperatura y humedad relativa). Se logró una buena concordancia entre los resultados experimentales y las predicciones del modelo.

En el Capítulo 4, se prepararon mezclas de partículas de núcleo blando/corteza dura de diferentes tamaños para superar los límites de la formación de películas alcanzados en el Capítulo 2. Se observó que al agregar pequeñas cantidades de partículas pequeñas (por ejemplo, 1% en peso) a las partículas grandes, se puede mejorar sustancialmente la formación de películas (menor temperatura mínima de formación de película y mayor temperatura crítica de contracción). Además, las propiedades mecánicas de las películas también mejoran (mayor elongación en el punto de quiebre y resistencia al impacto, manteniendo el módulo de Young y la resistencia al quiebre), sin afectar la sensibilidad al agua de la película. Se encontró que las propiedades viscoelásticas de las partículas pequeñas deben ser similares a las de las grandes para tener un efecto significativo.

El Capítulo 5 explora una estrategia para mejorar las propiedades mecánicas de los recubrimientos acuosos sin comprometer las características de formación de películas de las partículas de núcleo blando/corteza dura. El enfoque se basa en un núcleo interno de varias fases compuesto por dominios duros y blandos. Esta estrategia dio como resultado recubrimientos con un módulo de Young, resistencia al quiebre y resistencia al impacto más altos, sin comprometer las características de formación de películas. Esto se atribuyó a la

interpenetración de los polímeros del núcleo blando y las inclusiones duras. Esto resultó en una estructura difusa del núcleo que, por un lado, era lo suficientemente blanda como para permitir una fácil deformación de las partículas durante la formación de la película, y, por otro lado, aumentaba el módulo de Young del núcleo y, en consecuencia, el de la estructura de panal.

El Capítulo 6 supera la limitación del tiempo necesario para resolver las ecuaciones de Navier-Stokes presentadas en el Capítulo 3 a través de un enfoque de granulado grueso. Consiste en dividir las películas tridimensionales en una serie de capas horizontales. El número de capas se mantuvo fijo durante la simulación, pero cada capa era libre de cambiar en las tres dimensiones bajo el efecto de las tensiones interfaciales generadas por las capas adyacentes. Las ecuaciones de balance de momento y masa se resolvieron para cada capa en función del movimiento vertical de las capas adyacentes. Se consideraron las fuerzas viscosas, las fuerzas de tensión superficial y la contracción del volumen de las capas.

En el Capítulo 7 se resumen las conclusiones generales del trabajo y se presentan las perspectivas futuras para continuar la investigación en este campo.

En resumen, este trabajo proporciona un estudio exhaustivo sobre la formación de grietas en recubrimientos en base agua con partículas de núcleo blando/corteza dura y propone estrategias para mejorar las propiedades mecánicas de estos recubrimientos sin comprometer su capacidad de formación de películas. Los resultados experimentales y los modelos matemáticos desarrollados contribuyen al conocimiento fundamental en este campo y pueden ser utilizados para el diseño y la optimización de recubrimientos acuosos más sostenibles y mecánicamente fuertes.

Appendix I. Supporting information for Chapter 2

I.1 Polymerization

The polymerizations were carried out in 1.5L glass reactors fitted with a reflux condenser, a sampling tube, a nitrogen inlet, a feeding inlet, thermocouple, and a stainless-steel anchor stirrer at 150 rpm. The reactor temperature was controlled by an automatic control system.

Firstly, a 5 wt% solids content soft seed (2%-10% of the final particle volume) was synthesized by batch emulsion polymerization of a mixture of monomers (the composition of the mixture is given in Tables 2.1-2.4). An initial charge of water and surfactant was placed in the reactor and heated to 70°C under stirring. The reactor was purged with nitrogen and the monomer mixture and the initiator solution (KPS – 7wt%) were added as shots. The temperature was increased to 80 °C and the reaction was held for 15 minutes. The soft core, which forms 65-85% of the final particle volume, was prepared by feeding the monomer pre-emulsion for two hours. In parallel, a second portion of the initiator solution (KPS) was fed for three hours. The goal of the last hour when no monomer was fed, was to ensure high monomer conversion (Figure I.1). The hard shell (T_g about 100°C), which formed between 20% to 30% of the final particle volume, was synthesized by feeding the pre-emulsion of second monomers and the remaining initiator solution for forty-five minutes. At the end of the feeding, the reaction temperature (80°C) was held for one additional hour to ensure monomer consumption (residual monomers in Run 11 as measured by gas Chromatography were 300 ppm of MMA, 260 ppm of BA and 10 ppm of styrene). At the end of the reaction, the pH was adjusted to 8-8.5 by adding an ammonia solution

(NH3 – 25wt%). The recipe used in the synthesis of Latex 11 (Table 2.2) is given in Table I.1 as an example.

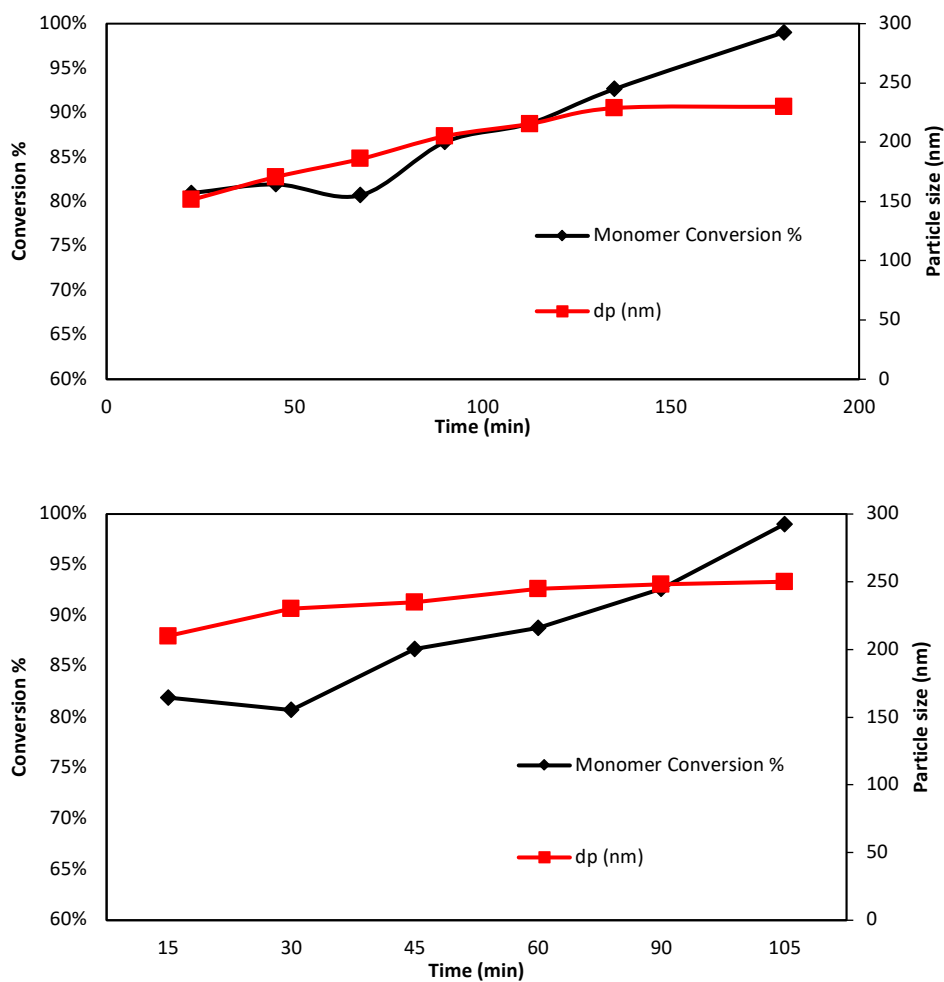


Figure I.1 Time evolution of the monomer conversion and particle size during the synthesis of the core (a) and “shell” (b) of Latex 2 (Table 2.1)

Table I.1 Recipe used in Latex 11 (Table 2.2)

		Seed	core	“shell”
	Compounds	Weight (g)	Weight (g)	Weight (g)
Initial charge	water	217.5	---	---
	Dowfax 2A1	14.1	---	---
Pre-emulsion	water	23.2	442.5	155.2
	Dowfax 2A1	0.7	13.3	2.9
	S	3.9	74.8	---
	MMA	3.9	74.8	169.7
	BA	17.8	339.1	---
	AA	0.5	9.9	5.2
Initiator solution	KPS	0.35	1.05	
	water	4.65	13.95	

I.2 Characterization

The monomer conversion defined as the weight of polymer in the reactor (m_{pol}) divided by the weight of monomer added to the reactor (m_{mon}) was determined gravimetrically. About 2 mL of latex were withdrawn from the reactor and the polymerization was immediately quenched with the addition of ≈ 0.1 mL of an aqueous solution of hydroquinone (HQ, 1 wt %). The samples were dried in aluminium caps at 65 °C until constant weight, and monomer conversion was determined as

$$X_m = \frac{m_{pol}}{m_{mon}} = \frac{S.C * m_{latex} - NPF}{m_{mon}} \quad (I.1)$$

where m_{latex} is the weight of the latex, NPF is the non-polymeric solid fraction of the sample (it includes the initiator, surfactant and HQ), and SC the solids content given by

$$S.C (\%) = \frac{\text{Dry solid (g)}}{\text{Latex (g)}} 100 \quad (1.2)$$

The particle size of the polymer dispersions was measured with dynamic light scattering (DLS) using a Zetasizer Nano Z (Malvern Panalytical, UK). The latex was diluted with deionized water until a transparent dispersion was obtained to avoid multiple scattering.

The particle morphology was determined using atomic force microscopy (AFM, Bruker Nanoscope V Dimension Icon) in Peak Force tapping mode with a silicon nitride cantilever equipped with a rotated super sharp silicon tip. The nominal resonant frequency of the cantilever was 55 kHz and the spring constant was 0.25 N m⁻¹. The analysis was done by drying one droplet of a diluted latex (0.1% SC). The samples cross section analysis was analysed using AFM in tapping mode on films cross section after drying the films at 23°C-55% RH. Then the samples were frozen at -80°C and cut using diamond knife. The bright regions represent the hard phase while the dark regions are the soft phase. In some cases, transmission electron microscopy (TEM, JEOL TM-1400 Plus series 120 kV) was used. A drop of the diluted latex (0.1% SC) was deposited on carbon-coated copper grid (300 Mesh) and let to dry at -70°C to maintain the spherical shape of the particle. Then, the sample was stained with a vapor of RuO₄ for 20-30 minutes to increase the contrast of the aromatic rings. The ruthenium complexes with the aromatic rings and therefore the contrast of the image darkens the styrene-rich areas.

The minimum film formation temperature (MFFT) was measured using a Rhopoint-Model 90 MFFT device with aluminum substrate and temperature range from 0°C to 90°C. The range of temperature used for all experiments included in this work was from 5°C to 40°C. Film

thickness 100 μm . The MFFT was observed visually as the point where the film became optically clear without visible cracks. Each measurement was repeated twice and no noticeable differences were observed.

Critical cracking thickness (CCT) is the thickness at which the layer starts to crack. CCT was measured using the device shown in Figure I.2. This device is made of anodized aluminium and has a thickness gradient between 0 μm and 2000 μm . The device is filled with latex and upon drying, the critical cracking thickness was determined visually at the point where the cracking started. The experiments were done as 23°C and 55% RH.

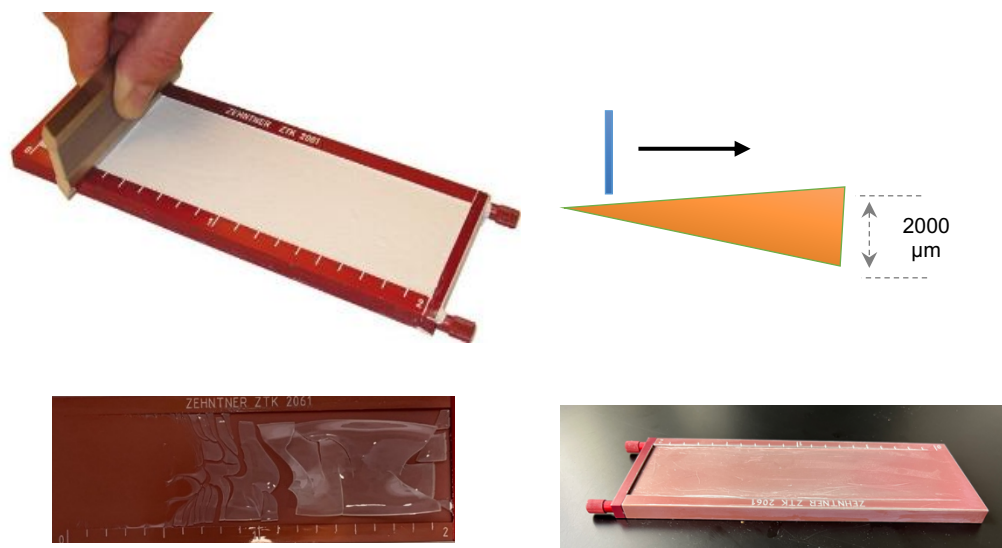


Figure I.2 Device used to determine the critical cracking thickness.

The stress evolution during film formation was examined via the beam bending technique. Figure I.3 depicts a schematic diagram for the experimental setup. The latex was cast manually using a stainless-steel applicator with film dimensions 30mm × 10mm on a 0.03 mm thick flexible polyethylene terephthalate (PET) substrate with dimensions of 40 mm × 15 mm in a controlled climate chamber. As the latex dried, the shrinkage induced tension stresses bent the substrate upwards. This curvature change was monitored using a quadrant position detector (Micro-Epsilon with) with accuracy of 10 μm using Helium–Neon laser beam (JDSU) reflected from the end of the substrate onto the detector. Data were collected immediately after casting (i.e. as soon as the substrate was placed in its position below the laser measurement point) and subsequently once every 0.1s.

The stress was determined by using equation I.3 [1] that is a modification of the Stoney's equation [2] derived by Corcoran using the plate theory [3]. In the development of this equation the following assumptions were made: i) the coating undergoes uniform stress, ii) the substrate and coating have isotropic mechanical properties, iii) good adhesion exists between coating and substrate, iv) the deflection of the cantilever beam is spherical, v) the spherical bending for both substrate and coating is within the elastic limits of the materials, and vi), the deflection of the coated beam is much bigger than the thickness of the substrate. For polymer coatings, these assumptions are reasonable.

$$\sigma = \frac{E_S t^3 d}{3 c L^2 (t+c) (1-\nu_S)} + \frac{d E_C (t+c)}{L^2 (1-\nu_C)} \quad (1.3)$$

where, E_S and E_C are the substrate and coating Young's moduli, t is the substrate thickness, d is the cantilever deflection, c is the dried coating thickness, L is the cantilever free length, and ν_C and ν_S are the coating and substrate Poisson's ratios.

It is worth to point out that the stress provided by this equation is an in-plane biaxial stress averaged across the coating thickness. Therefore, it does not provide any information about variations in stress through the coating thickness or laterally across the substrates. The second term of the right-hand side member of eq. I.3 accounts for film stress relief due to bending of the cantilever, but this term can be neglected because the Young's modulus of the coating is small relative to those of the substrate.

The measurement of the loss of water during film formation was carried out simultaneously with the measurement of the stress using a Sartorius Entris 124-1S analytical balance (resolution 0.1 mg) coupled to a computer that recorded the weight as a function of time every 0.05 s.

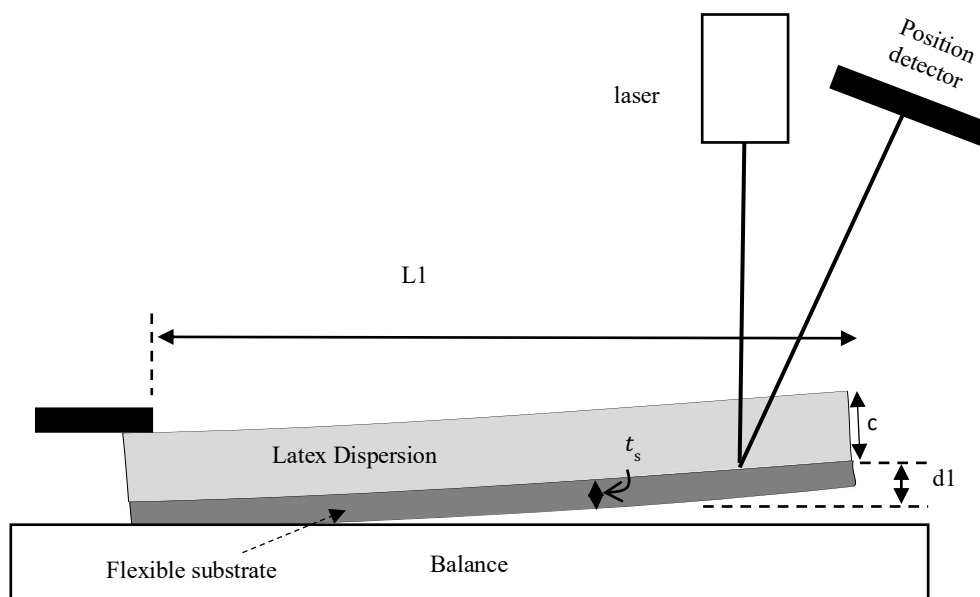


Figure I.3 Schematics of the cantilever beam bending device used for stress measurements.

The glass-transition temperature (T_g) of the polymers were measured using a commercial differential scanning calorimeter (DSC, Q1000, TA Instruments). The procedure consisted of four scanning cycles: cooling, heating, cooling and heating. The temperature range employed for the analysis was from -50°C to 150°C at a heating rate of $10^{\circ}\text{C}/\text{min}$. The results from the second heating run are presented.

Tensile tests were carried out on films produced by casting 0.5 g of latex (45% SC) in rectangular silicone moulds ($10 \times 40 \text{mm}^2$) and let to dry at 23°C and 55% RH for 72h. The tests were carried out using a TA.HD.plus Texture Analyzer (Stable Micro Systems Ltd., Godalming, UK) with a constant velocity of 0.42 mm/s, using samples of dog-bone shape with 25mm gauge length and 3.5mm gauge width. The reported results are the average of 5 repeated measurements. The Young's modulus was determined as the slope of the curve at low strain (before the yield point) and the toughness as the area under the tensile curve.

The surface hardness was measured using a Byko-swing Pendulum surface hardness device (3° König) on films forming upon drying a $300\mu\text{m}$ thick layer of latex for 7 days at 23°C / 55% RH. The results are presented in seconds, which represent the time needed for the pendulum to oscillate an angle of less than 3° degrees. If the sample is hard, the time will be high and vice versa.

The dynamic mechanical thermal analysis (DMTA) measurements were carried out in a Triton 2000 DMA (Triton Technology) equipped with a liquid nitrogen cooling system. The measurements were performed in tension mode at 1 % deformation and a single frequency of 1 Hz. The samples were cooled down to $\approx -50^{\circ}\text{C}$ and heated with a rate of $4^{\circ}\text{C}/\text{min}$ until $\approx 150^{\circ}\text{C}$.

I.3 Results

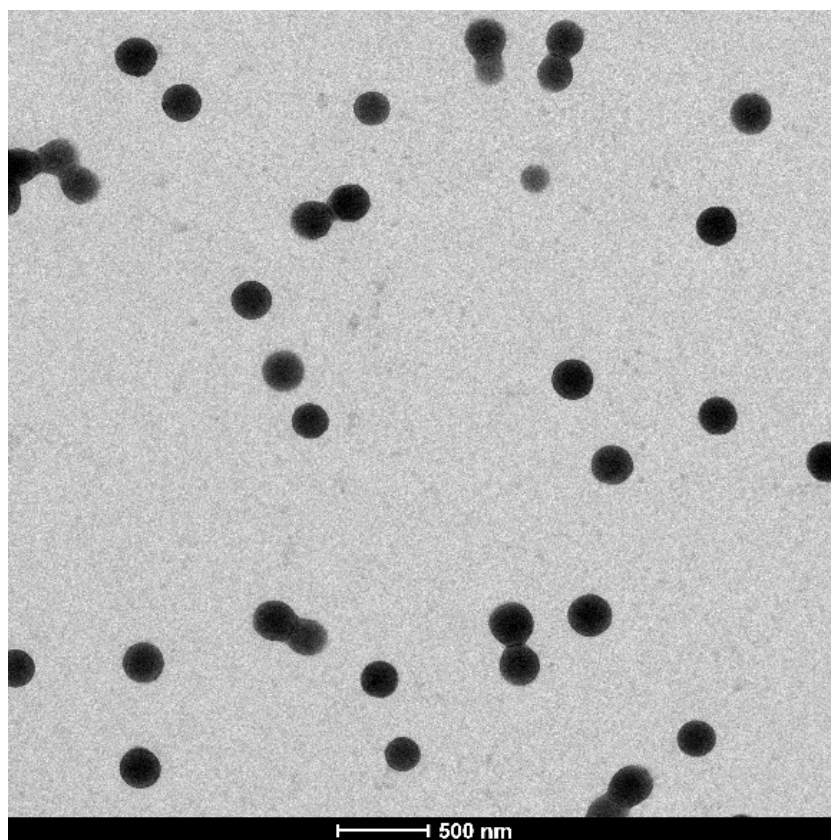
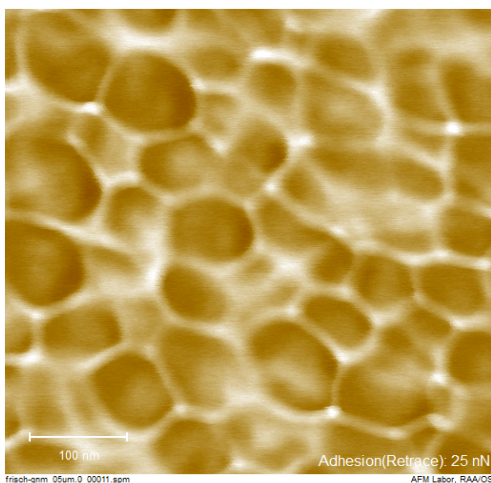


Figure I.4 TEM image of Latex 2 (250nm).

a) Latex 11_90 nm (25% hard phase)



b) Latex 3_150 nm (25% hard phase)

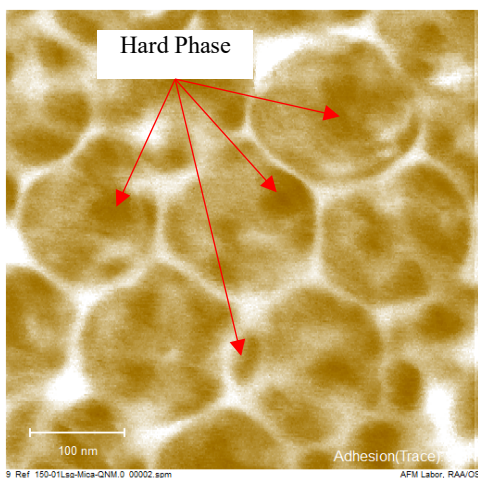


Figure I.5 Particle morphologies for latexes 11 (a) and 3 (b). The AFM images present the adhesion. Dark zones are low adhesion zones (hard phase) while bright zones are high adhesion zones (soft phase). The AFM measurement was carried out in QNM mode (Quantitative Nanomechanics) on diluted (0.1 wt%) particles and shortly tested after dropping on mica substrate.

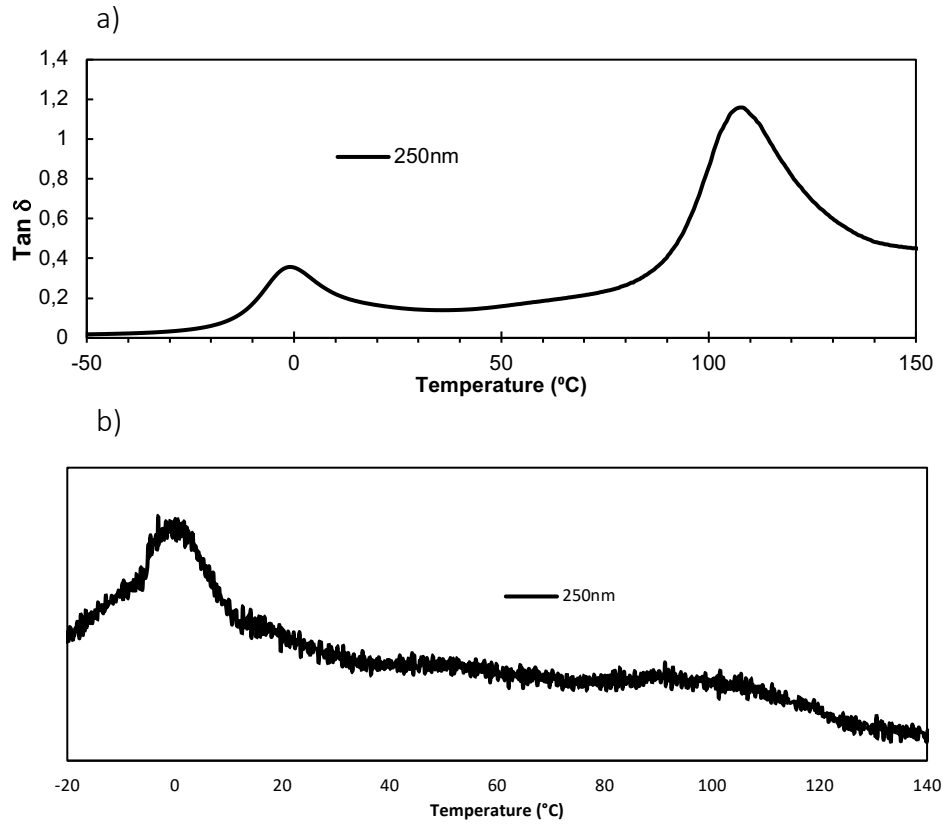


Figure I.6 DMTA(a) and DSC (b) of Latex 2 (250nm).

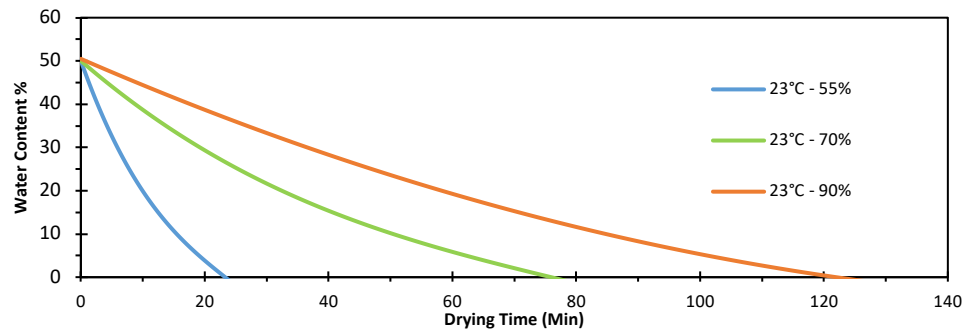


Figure I.7 The effect of the relative humidity (55%, 70% and 90%) on Evaporation rates and drying time

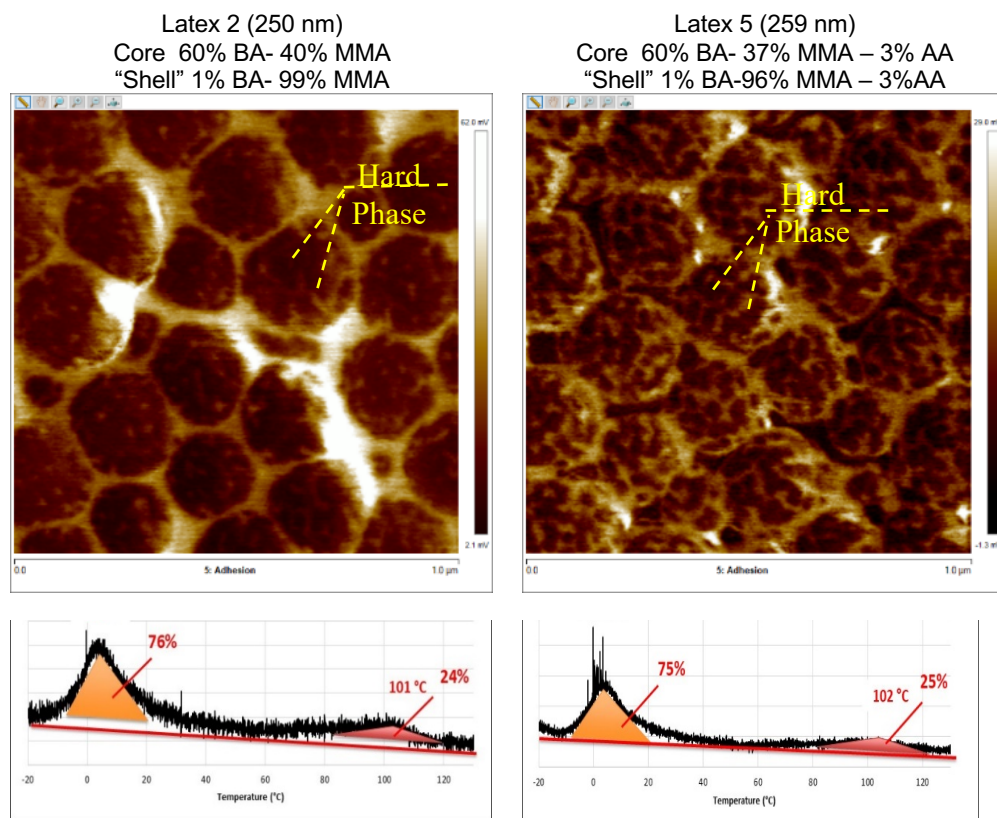


Figure I.8 Effect of the AA content on particle morphology and T_g s. The images are presenting the adhesion in peak force mode. The dark zones are low adhesion zones (hard phase) while the bright zones are high adhesion zones (soft phase). AFM images were obtained using a Bruker Nanoscope V Dimension Icon in Peak Force tapping mode with a silicon nitride cantilever equipped with a rotated super sharp silicon tip. The nominal resonant frequency of the cantilever was 55 kHz and the spring constant was 0.25 N.m^{-1} .

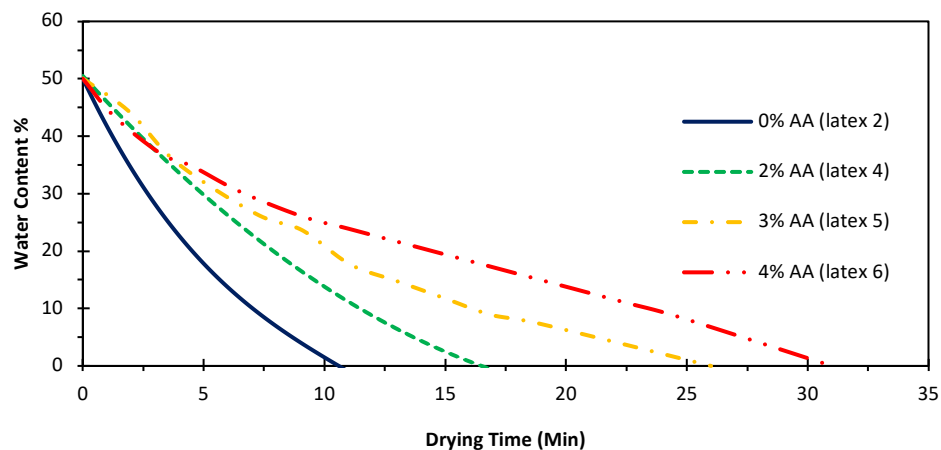


Figure I.9 Effect of AA content on drying time.

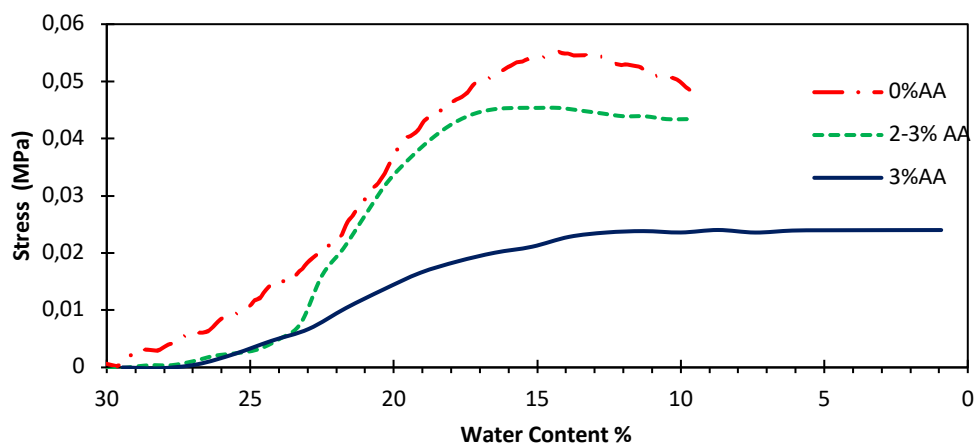


Figure I.10 Effect of the acrylic acid (AA) content on the evolution of the stress generated during drying of Latexes 11, 18 and 20. Particle size 91-95 nm, 170 μm dry films. Drying conditions: 23 $^{\circ}\text{C}$, 55% relative humidity

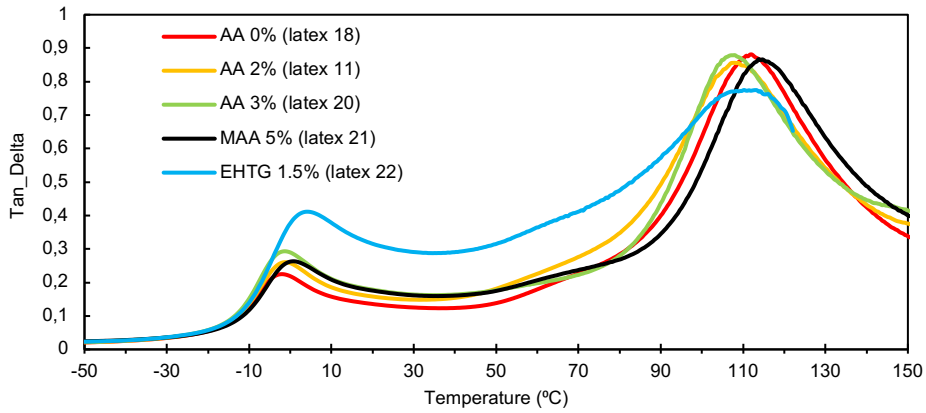


Figure I.11 DMTA of latexes 11, 18 and 20-22 showing the effect of AA content and type of acidic monomer.

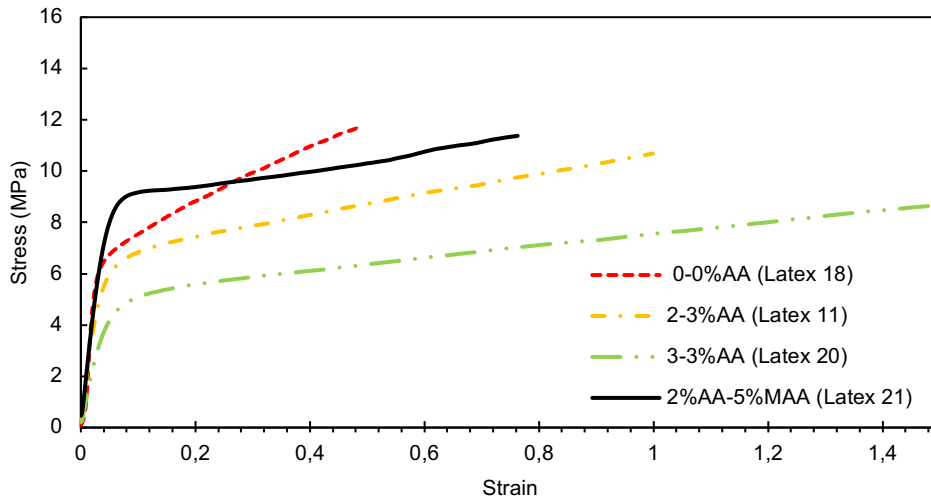
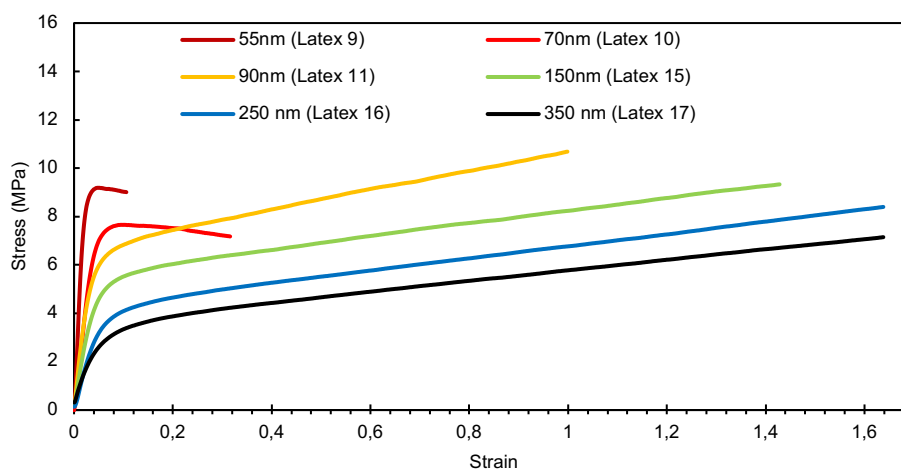


Figure I.12 Tensile tests for the films containing different types and content of acidic monomer (Latexes 11, 18, 20, 21)

Table I.2 Effect of the acidic monomer on the mechanical properties

Latex	Acidic monomer% core-shell	Young's modulus (MPa)	Stress at Break (MPa)	Elongation at break (%)	Toughness (MPa)	Hardness 3° Koenig (s)
Latex 18	0%AA-0%AA	5.9	11.7	49%	4.4	44
Latex 11	2%AA-3%AA	5.2	10.6	100%	8.2	35
Latex 20	3%AA-3%AA	3.9	8.9	150%	10.3	31
Latex 21	2%AA-5%MAA	7.9	11.3	76%	7.4	29



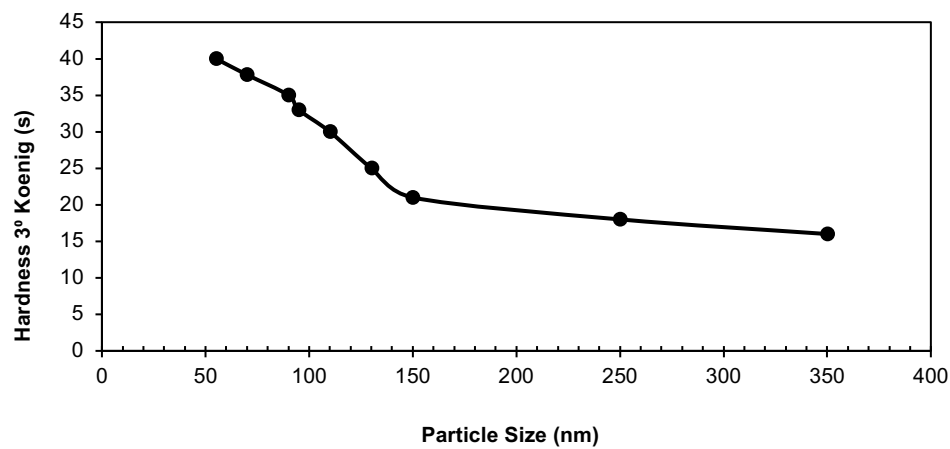


Figure I.13 Tensile test (a) and surface hardness (b) of films cast from latexes with different particle diameters (Latexes 9-11 and 15-17).

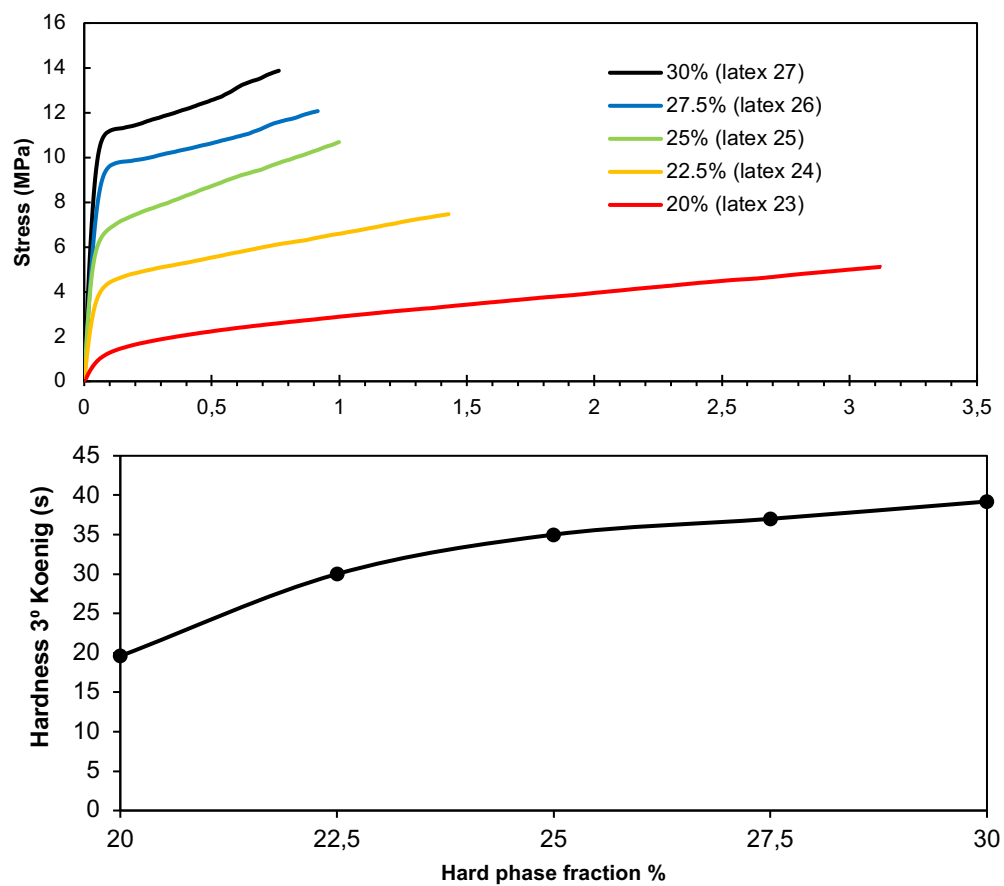


Figure I.14 Tensile test (a) and surface hardness (b) for films cast from latexes 23-27 showing the effect of different hard “shell” fractions.

Table I.3 Effect of the hard “shell” on Young’s modulus, and stress and elongation at break for films cast from latexes 23-27.

Latex	Hard “shell” %	Young’s modulus (MPa)	Stress at Break (MPa)	Elongation at break (%)	Toughness (MPa)
23	20	0.4	3.5	163%	10.6
24	22.5	2.7	7.4	144%	8.4
25	25	5.2	10.6	100%	8.2
26	27.5	7.8	12.1	91%	7.9
27	30	9.1	13.8	76%	7.4

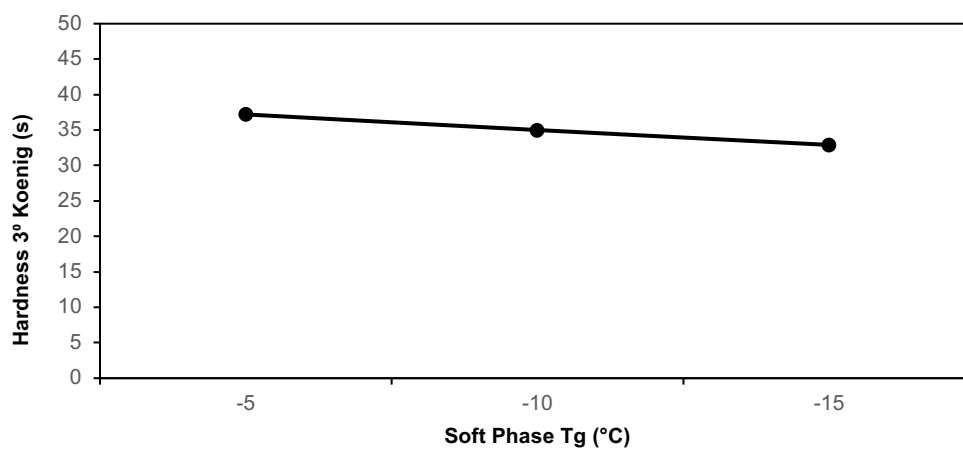


Figure I.15 Effect of soft phase T_g variation on surface hardness of films dried from Latexes 11, 28 and 29.

Table I.4 Effect of the soft core T_g on Young's modulus, and stress and elongation at break for films cast from Latexes 11, 28 and 29.

Latex	Soft core T_g (°C)	Young's modulus (MPa)	Stress at Break (MPa)	Elongation at break (%)
28	-5	5.6	11.7	80%
11	-10	5.1	10.7	100%
29	-15	4.9	9.9	105%

I.4 References

- [1] Corcoran EM. Determining stresses in organic coatings using plate beam deflection. J. Paint Technol. **1969**, 41, 635-640.
- [2] Stoney GG. The tension of metallic films deposited by electrolysis. Proceedings of the Royal Society of London. Series A, Containing Papers of a Mathematical and Physical Character. **1909**, 82,172-175.
- [3] Timoshenko SP, Gere JM. Theory of elastic stability. Dover Publications; **2009**, Mineola, New York.

Appendix II. Supporting information for Chapter 3

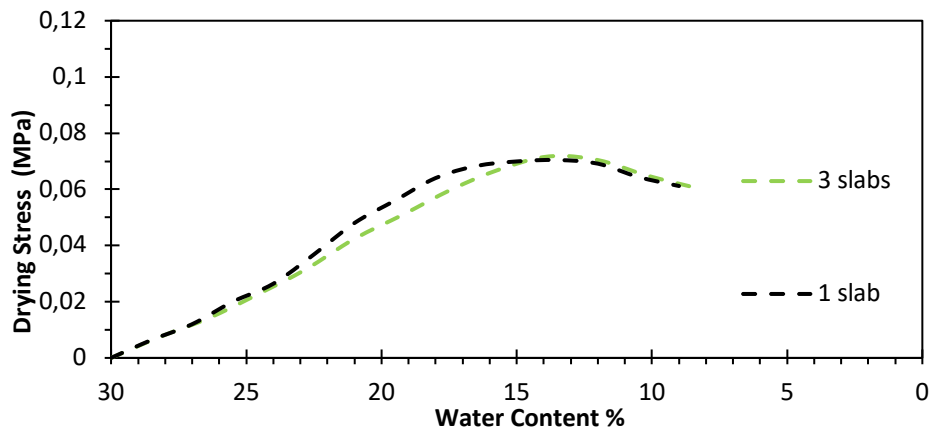
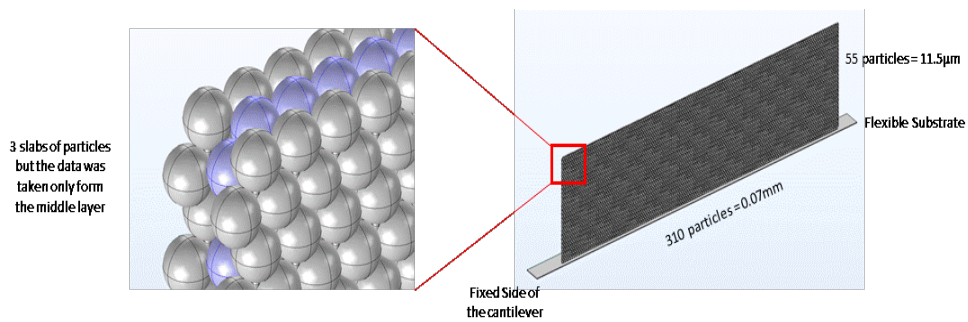


Figure II.1 Comparison of the predictions of the stress with one and three slabs for Latex 16.
Drying: 23 °C, 55% RH

Surface and interfacial tensions calculation

The surface tension of the polymer (γ_p) and the interfacial tension polymer-water ($\gamma_{p/w}$) are parameters of the model. However, the determination of these magnitudes is not straightforward. They are related through the Young equation

$$\gamma_p = \gamma_{p/w} + \gamma_w \cdot \cos\theta \quad (\text{II.1})$$

where γ_w is the surface tension of the aqueous phase and θ is the three-phases contact angle (Figure II.2).

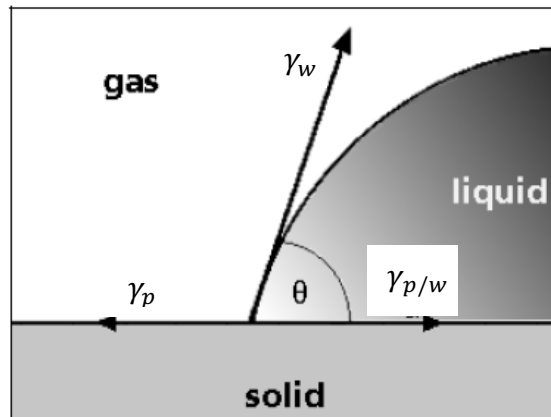


Figure II.2 Three-point contact angle

The surface tension of each phase can be split up into a polar and disperse fraction.

$$\gamma_w = \gamma_w^P + \gamma_w^D \quad (\text{II.2})$$

$$\gamma_p = \gamma_p^P + \gamma_p^D \quad (\text{II.3})$$

The interfacial tension can be expressed in terms of the polar and dispersive fractions of the liquid and solid surface tensions.

$$\gamma_{p/w} = \gamma_p + \gamma_w - 2 \left(\sqrt{\gamma_p^D \cdot \gamma_w^D} + \sqrt{\gamma_p^P \cdot \gamma_w^P} \right) \quad (\text{II.4})$$

For a purely dispersive liquid (e.g. hexane), eq. II.4 reduces to

$$\gamma_{p/h} = \gamma_p + \gamma_h - 2 \sqrt{\gamma_p^D \cdot \gamma_h^D} \quad (\text{II.5})$$

Combination of eqs II.1 and II.5 leads to

$$\cos \theta = 2 \sqrt{\gamma_p^D \cdot \frac{1}{\sqrt{\gamma_h^D}}} - 1 \quad (\text{II.6})$$

Therefore, measuring the contact angle for different purely dispersive polymers, γ_p^D can be determined. In this work, hexane and hexadecane were used as dispersive liquids. The surface tensions of the liquids were measured using a Sigma 700/701 NANOSCIENCE instrument with a Du Nouy platinum ring. The surface tensions of hexane and hexadecane were 18.4 mN/m and 27.47 mN/m, respectively. The contact angles were determined using Data Physics OCA 20 model goniometer. The value of the dispersive component of the surface tension of the polymer was $\gamma_p^D = 17.2$ mN/m.

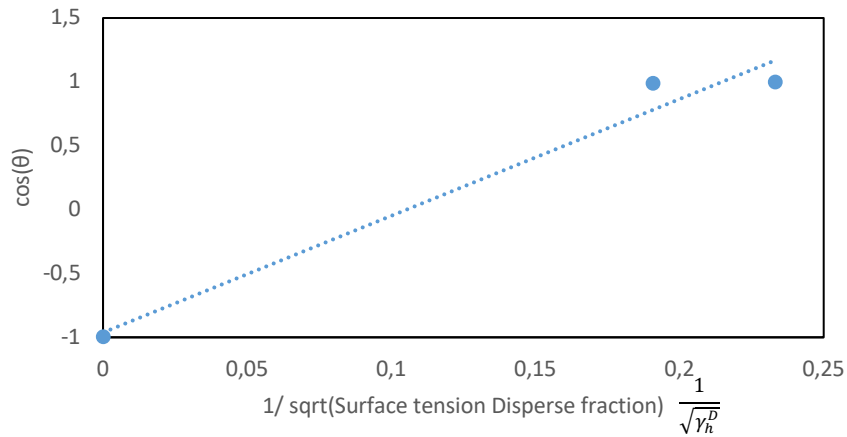


Figure II.3 calculation of polymer surface tension polar fraction

On the other hand, combination of S1 and S4 for a general liquid (*l*) leads to

$$\gamma_l (\cos\theta + 1) - 2 \sqrt{\gamma_p^D \cdot \gamma_l^D} = W_{pl}^P = 2 \sqrt{\gamma_l^P} \sqrt{\gamma_p^P} \quad (\text{II.7})$$

As γ_p^D is known, measuring the contact angle with a liquid of known dispersive and polar components allows determining of the polar component of the surface tension of the polymer (γ_p^P). The liquid used was water. The surface tension polar and disperse components for water are 52.2 mN/m and 19.9 mN/m, respectively. The value of the polar component of the surface tension of the polymer was $\gamma_p^P = 19.5$ mN/m. The surface tension of the polymer was then calculated from eq II.3 giving $\gamma_p = 36.7$ mN/m.

Young's modulus measurement

The Young's moduli of the soft and hard phase were determined by nanoindentation using a Bruker Nanoscope V Dimension AFM in Peak Force tapping mode with a silicon nitride cantilever equipped with a rotated super sharp silicon tip. The nominal resonant frequency of the cantilever was 55 kHz and the spring constant was 0.25 N m^{-1} . A diluted drop (0.1% S.C) of a composite the latex (soft core BA/MMA/AA 60/40/0 wt/wt– hard "shell" BA/MMA/AA 1/99/0 wt/wt) was placed on a mica substrate, dried, and introduced into the AFM stage. The AFM cantilever approached the particle from a few micrometres above, made a contact with the particle, indented the particle until that the cantilever deflection reached a preselected set point; and then pulled away from the particle. During this process the cantilever deflection is recorded as a function of its location for both hard phase (Figure II.4a) and soft phase (Figure II.4b). Before contacting the particle, the cantilever moved in air without any apparent deflection. When indenting on the particle, the cantilever bent and the deflection signal increased till reaching the set maximum magnitude of force applied (20nN). The cantilevers are modelled as elastic beams so that their deflection is proportional to the force applied to the particle. The probe spring constant was 0.999 N/m, Tip half angle was 18° , Tip radius was 0.999 nm and the Poisson's ratio of the tip was 0.3.

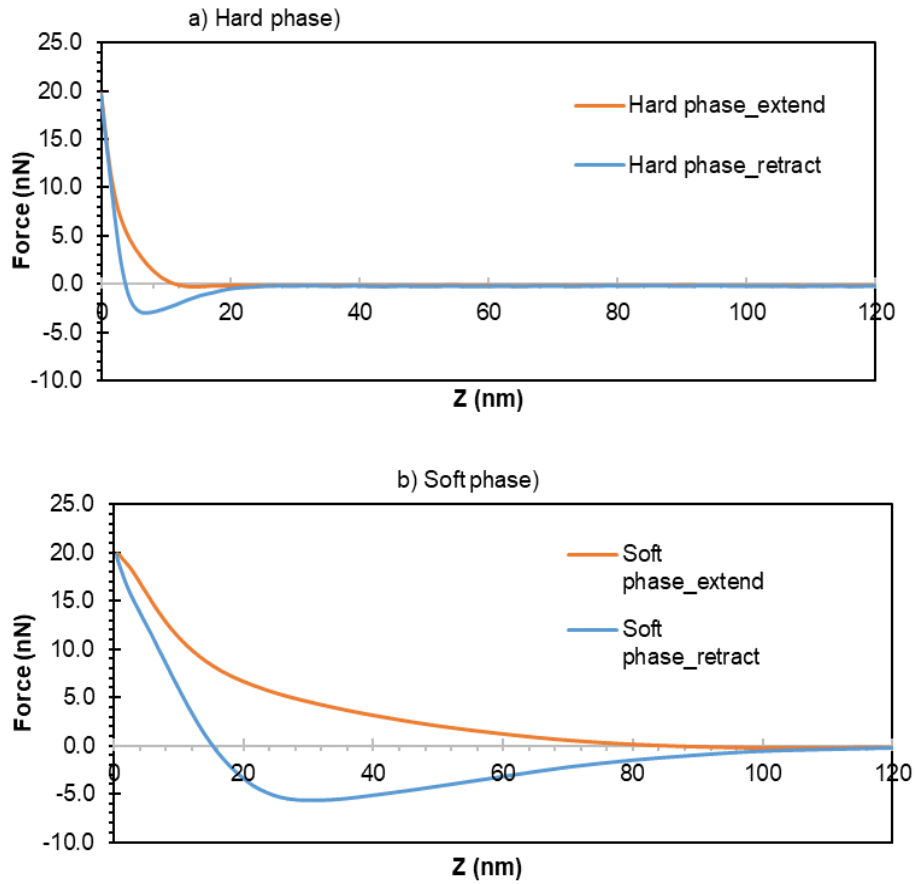


Figure II.4 Force vs. deflection in the AFM nanoindentation. Composite latex (soft core BA/MMA/AA 60/40/0 wt/wt– hard “shell” BA/MMA/AA 1/99/0 wt/wt)

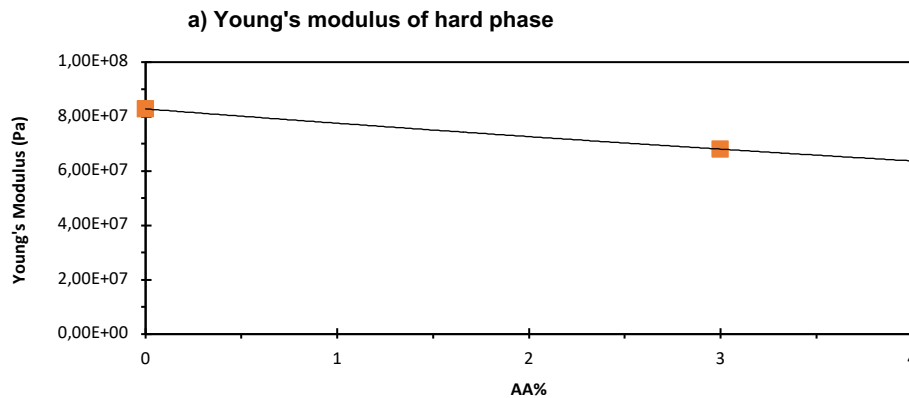
The Young's moduli were calculated using the Hertz model

$$F = \frac{2 E \tan\phi}{\pi (1-\nu^2)} \delta^2 \quad (\text{II.8})$$

where, F is the applied force, E is the Young's modulus, θ is the tip half cone angle, ν is the Poisson's ratio of the tip and δ is the deformation under the applied force F .

It was found that the dry Young's modulus of hard phase was $E_h = 8.3 \cdot 10^7$ Pa and dry Young's modulus of soft phase was $E_s = 5 \cdot 10^5$ Pa. It should be pointed out that these values correspond to dry polymers. During film formation the polymers are in contact with water and hence they may suffer hydroplasticization, which will be more pronounced for polymers containing acrylic acid. Consequently, it is expected that the Young's moduli during film formation will be lower than those obtained in the nanoindentation experiments and that these values will decrease as the AA content increases.

Effect of the AA content on the Young's moduli



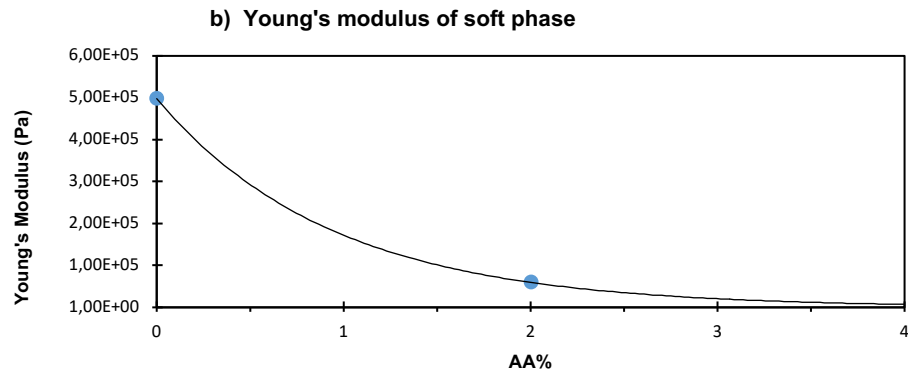


Figure II.5 Effect of the AA content on the Young's moduli. Notice that the AA content of the soft and hard phases of the latex used to estimate the Young's moduli from the beam-bending experiments were different (2 wt% in the soft phase and 3 wt% in the hard phase)

Effect of the acrylic acid content on the critical tension force for cracking

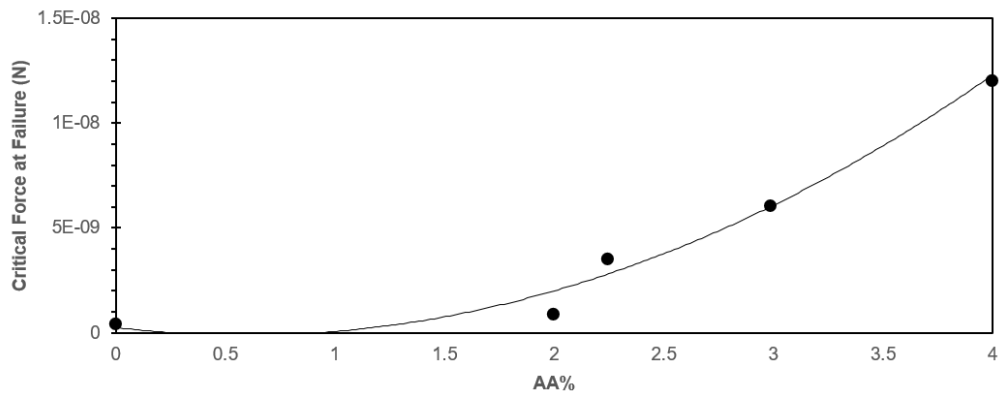


Figure II.6 Effect of the AA content of the critical tension force for cracking. The critical force is calculated for Latexes: 2 (0wt% AA); 4 (2wt% AA); 11, 16 and 17 (2.25wt% AA) using beam-bending experiment, while the trend is extrapolated to estimate the critical force for latex 5 (3wt% AA) and latex 6 (4 wt% AA).

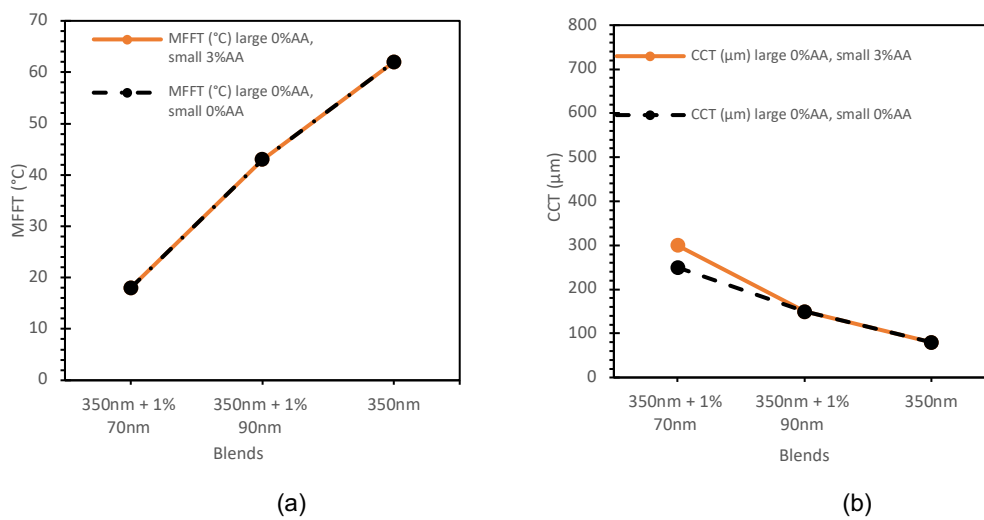
Appendix III. Supporting information for Chapter 4

Table III.1 Effect of the addition fraction of 55 nm particles (Latex 1) to 350 nm particles (Latex 9)

% 55 nm latex	MFFT (°C)	CCT (μm)
0	62	80
1	28	200
2	16	350
4	8	800
10	< 4	>1000

Table III.2 Effect of the addition of 1 wt % of small particles of 55 and 70 nm to big particles of 250 nm with (Latex 7) and without AA (Latex 6)

Blending particle size and ratio	250 nm (latex 7)		250 nm, 3 % AA (Latex 6)	
	MFFT (°C)	CCT (μm)	MFFT (°C)	CCT (μm)
0 wt %	21	140	8.5	700
55 nm, 1 wt % (Latex 1)	14	300		
70 nm, 1 wt% (Latex 2)	14	250	<5	900
70 nm, 3 %AA, 1 wt % (Latex 3)	14	250	<5	850



(a) (b)
Figure III.1 Effect of the AA content of the small particles on a) MFFT and b) CCT

Appendix IV. Supporting information for Chapter 5

IV.1 Polymerization

The polymerizations were carried out in 1.5L glass reactors fitted with a reflux condenser, a sampling tube, a nitrogen inlet, a feeding inlet, thermocouple, and a stainless-steel anchor stirrer at 150 rpm. The reactor temperature was controlled by an automatic control system.

Firstly, a 5wt% solids content seed (2%-10% of the final particle volume) was synthesized by batch emulsion polymerization of a mixture of seed monomers. An initial charge of water and surfactant was placed in the reactor and heated to 70°C under stirring. The reactor was purged with nitrogen and the monomer mixture and the initiator solution (KPS – 7wt%) were added as shots. The temperature was increased to 80 °C and the reaction was held for 15 minutes. For latexes with hard domains (Latex 4 and 5), a shot of hard monomer mixture and initiator solution (KPS – 7wt%) were done after seed polymerization. Then, the reaction was held for another 15 minutes. The soft core, which forms 65-75% of the final particle volume, was prepared by feeding the monomer pre-emulsion for two hours (for gradient latex (1-3), two parallel monomer feedings with gradient feedings rate were used, Table IV). In parallel, a second portion of the initiator solution (KPS) was fed for three hours. The goal of the last hour when no monomer was fed, was to ensure high monomer conversion. The hard shell (T_g about 100°C), which formed between 25% of the final particle volume, was synthesized by feeding the pre-emulsion of second monomers and the remaining initiator solution for forty-five minutes. At the end of the feeding,

the reaction temperature (80°C) was held for one additional hour to ensure monomer consumption. At the end of the reaction, the pH was adjusted to 8-8.5 by adding an ammonia solution (NH₃ – 25wt%).

Table IV.1 Gradient particles

	Gradient latex											
	Latex 1			Latex 2			Latex 3					
	Hard Seed	Gradient Soft Core		Hard Shell	Hard Seed	Gradient Soft Core		Hard Shell	Hard Seed	Gradient Soft Core		Hard Shell
% of the particle	10%	65%		25%	4%	71%		25%	2%	73%		25%
Composition	S/BA 90/10	S/BA 40/60		MMA/BA 99/1	S/BA 90/10	S/BA 40/60		MMA/BA 99/1	S/BA 90/10	S/BA 40/60		MMA/BA 99/1
T _g (°C)	75 °C			100 °C	75 °C			100 °C	75 °C			100 °C
Composition (average)		Inside	Outside			Inside	Outside			Inside	Outside	
		S/BA 90/10	S/BA 25/75			S/BA 90/10	S/BA 35/65			S/BA 90/10	S/BA 35/65	
		75	-25			75	-15			75	-15	
dp (nm)	80	157 nm		173 nm	56	209 nm		230 nm	40	230 nm		243 nm

IV.2 Characterization

Three-dimensional (3D) particle morphology was characterized by HAADF-STEM electron tomography technique using Talos F200i electron microscope operated at acceleration

voltage of 200 kV. HAADF-STEM imaging mode provides the contrast that is strongly dependent on the atomic number ($\sim Z^2$) and thus stained polymer phase looks much brighter at HAADF-STEM images. Tilt series were acquired automatically at angles between -74° and $+74^\circ$ at 2° tilt step. The fiducial-less tilt-series alignment and tomographic reconstructions with weighted back-projection (WBP) and simultaneous iterative reconstruction (SIRT) techniques were done using software. The analysis was done on a drop of the diluted latex (0.1% SC) was deposited on carbon-coated copper grid (300 Mesh) and let to dry at -70°C to maintain the spherical shape of the particle. Then, the sample was stained with a vapor of RuO₄ for 60 minutes.

List of acronyms and abbreviations

AA	acrylic acid
AFM	atomic force microscopy
BA	butyl acrylate
BDG	Butyldiglycol
CCT	Critical cracking thickness
CL	commercial latex
<i>d</i>	cantilever deflection
DLS	dynamic light scattering
DMTA	dynamic mechanical thermal analysis
Dowfax 2A1	alkyldiphenyloxide disulfonate
DSC	differential scanning calorimetry
EHTG	2-ethylhexyl mercaptoacetate
ESEM	Environmental Scanning Electron Microscopy
ET	electron tomography
Fext	external contributions to the free energy
Fg	force due to gravity
Fst	interfacial tension force
γ	Surface tension
GC	gas chromatography
KPS	Potassium persulfate
MAA	methacrylic acid
MFFT	minimum film formation temperature
MMA	methyl methacrylate
NH3	ammonia

PBA	poly (butyl acrylate)
Pe	Peclet number
PET	polyethylene terephthalate
PMMA	poly(methyl methacrylate)
PS	polystyrene
PSA	pressure sensitive adhesives
PSD	particle size distribution
RH%	relative humidity
S	styrene
S	strain-rate tensor
SC	Solids content
SEM	scanning electron microscope
T	temperature
t	time
T ₀	room temperature
TEM	transmission electron microscopy
T _g	glass transition temperature
TiO ₂	titanium dioxide
u	flow velocity
VOC	volatile organic compound
ρ	density
	extra stress tensor
η_s	dynamic viscosity
P_e	viscoelastic stress tensor
	Young's modulus
	relaxation time
δ	smoothing function
ν_s	Poisson's ratios of the substrate
ν_c	Poisson's ratios of the film
γ_P	surface tension of the polymer
$\gamma_{p/w}$	interfacial tension polymer-water

